

AD-A257 969



IDENTIFICATION PAGE

Form 10-100
OMB No. 0700-0100

WARNING: This document contains information which, if disclosed, could result in the identification of sources, methods, and procedures used in the collection of information. This document is to be controlled and its disclosure to unauthorized persons is prohibited. This document is the property of the Office of Management and Budget, Paperwork Reduction Project (0700-0100), Washington, DC 20503.

2. REPORT DATE		3. REPORT TYPE AND DATES COVERED ANNUAL 15 Sep 91 TO 14 Sep 92	
4. TITLE AND SUBTITLE RADAR INTERFEROMETER INVESTIGATIONS OF THE HORIZONTAL WINDS, VERTICAL VELOCITIES, VORTICITY, AND DIVERGENCE AROUND FRONTAL ZONES AND IN MESOSCALE WAVES		5. FUNDING NUMBERS AFOSR-91-0384 61102F 2310 CS	
6. AUTHOR(S) Dr Miguel F. Larsen		2	
7. PERFORMING ORGANIZATION NAME(S) AND ADDRESS(ES) Dept of Physics Clemson University Clemson, SC 29634 AFOSR-TR-91-02			
8. SPONSORING/MONITORING AGENCY NAME(S) AND ADDRESS(ES) Lt Col James G. Stobie AFOSR/NL Building 410 Bolling AFB DC 20332-6448		9. SPONSORING/MONITORING AGENCY REPORT NUMBER	
10. SUPPLEMENTARY NOTES			
12a. DISTRIBUTION/AVAILABILITY STATEMENT Approved for public release; distribution unlimited		12b. DISTRIBUTION CODE	
13. ABSTRACT (Maximum 200 words) The goal of the research has been to use the state-of-the-art, phased-array MU radar facility in Kyoto, Japan, to study the perturbation winds and turbulence associated with frontal zones and mesoscale waves. There are four critical parameters in the dynamical studies. They include unbiased estimates of the horizontal winds, unbiased estimates of the vertical velocities, the location and strength of turbulent layers within the scattering volume, and the vorticity and divergence within the flow. Standard beam-swinging Doppler measurements lead to large biases in the vertical velocities and possible biases in the horizontal winds, the location of the scattering layers can only be determined with the uncertainty of the pulse volume, and vorticity measurements are not possible. Research during the first year has focused on the development of techniques for eliminating large biases in vertical velocity measurements that result when standard vertical beam Doppler methods are used, for eliminating biases in horizontal wind measurements that result with Doppler beam swinging techniques due to horizontal gradients in the flow. We have also worked on developing new techniques for measuring the vorticity and divergence in the flow. The MU radar operates at a frequency close to 50 MHz and has a transmitting/receiving antenna array			
14. SUBJECT TERMS		15. NUMBER OF PAGES	
		16. PRICE CODE	
17. SECURITY CLASSIFICATION OF REPORT (U)	18. SECURITY CLASSIFICATION OF THIS PAGE (U)	19. SECURITY CLASSIFICATION OF ABSTRACT (U)	20. LIMITATION OF ABSTRACT (UL)

103 m in diameter. The beam can be steered from pulse to pulse, and the receiving array can easily be divided into sub-arrays for reception. All the system parameters are under software control so that changes can easily be implemented, and different experimental configurations can be tested quickly. The design of the MU radar system makes it possible to apply various techniques that require spatially separated receiving antennas, such as radar interferometry, spaced antenna measurements, and post-statistic beam steering. The results of applying the different techniques can be compared to each other, and results from standard Doppler measurements can be compared to the spatial receiving array techniques by interlacing such observations. The MU radar is the only facility in the world where the range of comparisons and new technique implementations described above can be implemented quickly.

First Annual Technical Report:

Radar Interferometer Investigations of the
Horizontal Winds, Vertical Velocities,
Vorticity, and Divergence around
Frontal Zones and in Mesoscale Waves

AFOSR Grant # AFOSR-91-0384

P.I.: M. F. Larsen
Dept. of Physics
Clemson University
Clemson, SC 29634
Tel. 803-656-5309

October 27, 1992

92-30162



185pg

29 OCT 1992

92 11 24 026

Contents

1	Introduction	1
2	Research Progress	2
2.1	Multiple receiver horizontal wind measurement techniques . . .	2
2.2	Corrected vertical velocity measurements	2
2.3	Frequency domain interferometry	3
2.4	Vorticity and divergence measurements	3
2.5	Observations of a vertical velocity reversal around the jetstream	4
2.6	Interferometry observations of precipitation	5
3	Forecast	5
A	Cumulative List of Publications (September 15, 1991 - October 14, 1992	7

DTIC QUALITY INSPECTED 4

Accession For	
NTIS	CRA&I
DTIC	TAB
Unannounced	
Justification	
By	
Distribution /	
Availability	
Dist	Availability
A-1	Special

1 Introduction

The goal of the research has been to use the state-of-the-art, phased-array MU radar facility in Kyoto, Japan, to study the perturbation winds and turbulence associated with frontal zones and mesoscale waves. There are four critical parameters in the dynamical studies. They include unbiased estimates of the horizontal winds, unbiased estimates of the vertical velocities, the location and strength of turbulent layers within the scattering volume, and the vorticity and divergence within the flow. Standard beam-swinging Doppler measurements lead to large biases in the vertical velocities and possible biases in the horizontal winds, the location of the scattering layers can only be determined with the uncertainty of the pulse volume, and vorticity measurements are not possible.

Research during the first year has focused on the development of techniques for eliminating large biases in vertical velocity measurements that result when standard vertical beam Doppler methods are used, for eliminating biases in horizontal wind measurements that result with Doppler beam swinging techniques due to horizontal gradients in the flow. We have also worked on developing new techniques for measuring the vorticity and divergence in the flow.

The MU radar operates at a frequency close to 50 MHz and has a transmitting/receiving antenna array 103 m in diameter. The beam can be steered from pulse to pulse, and the receiving array can easily be divided into sub-arrays for reception. All the system parameters are under software control so that changes can easily be implemented, and different experimental configurations can be tested quickly.

The design of the MU radar system makes it possible to apply various techniques that require spatially separated receiving antennas, such as radar interferometry, spaced antenna measurements, and post-statistic beam steering. The results of applying the different techniques can be compared to each other, and results from standard Doppler measurements can be compared to the spatial receiving array techniques by interlacing such observations. The MU radar is the only facility in the world where the range of comparisons and new technique implementations described above can be implemented quickly.

2 Research Progress

Most of the details of the research results to date are described in the publications which were produced under funding from the grant. The list of publications is given in the Appendix. A general overview of the results in each of the main research areas is given below.

2.1 Multiple receiver horizontal wind measurement techniques

The multiple receiver radar techniques for measuring horizontal winds include radar interferometry, imaging Doppler interferometry, spaced antenna wind measurements, and poststatistic beam steering. The potential advantages of the techniques are that both horizontal wind components can be measured from measurements made within the volume illuminated by the vertically-pointing transmitter beam so that biases due to horizontal gradients in the flow can be eliminated. Only recently have the various techniques been applied to measurements of the tropospheric and stratospheric flow parameters. We have developed the theory for the frequency-domain equivalent of the spaced antenna technique, and we have compared the other techniques both experimentally and theoretically. The results are described in *Larsen et al.* [1992], *Palmer et al.* [1992c], and *Sheppard et al.* [1992]. Our work has shown that the various multiple receiver techniques give equivalent results, and we have suggested practical procedures for carrying out routine data analysis and signal processing using various combinations of the multiple receiver techniques.

In addition to the analytic and experimental work, we have also developed a numerical model of the scattering process [*Sheppard and Larsen*, 1992] which has been used to elucidate the sources of bias in the various measurement techniques.

2.2 Corrected vertical velocity measurements

Since VHF radar measurements are subject to aspect sensitivity, the strongest backscatter comes from a direction normal to the refractivity layers within the medium. As long as the refractivity layers are aligned horizontally, the backscatter from a nominally vertically-pointing beam will come from the

vertical direction. However, such layers are typically inclined by up to a few tenths of a degree. Since the backscatter is coming from a slightly off-vertical direction within the beam, the measured Doppler shift will have contributions from both the vertical and horizontal velocities. Since the horizontal velocities are several orders of magnitude larger than the vertical velocities in almost all atmospheric conditions, the errors in the measurements introduced by the inclined refractivity layers often exceed 100%, *i.e.*, the apparent vertical velocity has the wrong direction.

The multiple receiver techniques can be used to correct the inclined refractivity layer effect because the phases of the signals received in the spatially separated receivers provide information about the location of the strongest backscatter within the illuminated volume. Once the incidence angle of the signals is known, the horizontal velocity contribution can be subtracted to yield the true vertical velocity. The articles that show the effect of the biases or errors and the methods for correcting the measurements include the studies by *Larsen et al.* [1991], *Larsen et al.* [1992], *Larsen and Röttger* [1991], and *Palmer et al.* [1991].

2.3 Frequency domain interferometry

The frequency domain interferometry technique involves the use of two transmitting frequencies separated slightly from the central frequency of the radar. The two offset frequencies are transmitted on alternate pulses and the phase differences between the received signals are used to determine the location of the scattering layer within the pulse volume with a height resolution that is much better than the standard pulse volume resolution. The technique has especially great potential in determining the location and characteristics of turbulent layers generated by gravity waves or low-frequency inertia-gravity waves breaking in the upper troposphere and lower stratosphere.

The articles describing our preliminary work with the frequency domain interferometry technique include *Palmer et al.* [1992a] and *Palmer et al.* [1992b].

2.4 Vorticity and divergence measurements

Our interest in making vorticity and divergence measurements using turbulent scatter radar techniques stems from the fundamental nature of the

two quantities in understanding atmospheric flows. In particular, measurements of vorticity and divergence can be used to separate the contributions of turbulence and waves, respectively, to the total flow. Measurements of the wind alone show when perturbations are present, but contributions from a spectrum of turbulent fluctuations cannot be separated unambiguously from contributions due to a spectrum of waves. Distinguishing between the two types of flow is critical since rotational flow will produce mixing of momentum and trace constituents but divergent flow will not.

A standard Doppler radar can be used to measure divergence with a dual elevation VAD technique, for example, but the vorticity cannot be measured regardless of the number of beam directions that are used. We have carried out experiments using two new techniques to attempt to measure the flow vorticity. One technique involves oblique, *i.e.*, off-vertical, spaced antenna measurements. The other involves off-vertical Doppler measurements with beams slightly displaced from the center of the array. One can show analytically that such displaced beam positions will lead to a vorticity measurement if the uncertainties in the velocity determinations are sufficiently small. At the MU radar, we have carried out both oblique spaced antenna measurements and the displaced beam Doppler measurements. The latter experiment was carried out over a three-day period in May 1992, and the data is presently being analyzed. The experimental set-up was such that the antenna was divided into thirds, approximately. The thirds were used sequentially for both transmission and reception at zenith angles of 5° and 15° and vertical. Dual-elevation VAD's were interspersed with the displaced Doppler measurements to provide an alternative measurement of the divergence for comparison with the new measurement technique.

2.5 Observations of a vertical velocity reversal around the jetstream

Observations with the MU radar show a persistent vertical velocity feature around the tropopause when the jetstream is overhead. In particular, the vertical velocities change sign at the peak in the horizontal wind profile, and the magnitude of the vertical circulation is between 10 and 20 cm s^{-1} . We have analyzed three years of such measurements obtained with the MU radar, and have shown the relationship of the feature to the location of the jetstream

and the slopes of the isentropes in the vicinity of the radar. The study has been described in the article by *Fukao et al.* [1991]. The conclusions of the study were that the circulation was in good agreement with the more recent theoretical predictions of the circulation around jetstream/frontal zone regions. Our study represents the first extensive direct observation of such a feature. The sense of the circulation was found to be such that it would tend to maintain the strength of the jet.

2.6 Interferometry observations of precipitation

We carried out a new experiment with the MU radar last May to make radar interferometric observations of precipitation. During the period of observation, regions of both stratiform and convective precipitation passed the radar site. The preliminary data analysis has been completed and an article describing the results was submitted to and accepted for publication in *Geophys. Res. Let.* [*Chilson et al.*, 1992]. The advantage of the interferometric technique for observations of precipitation is that the vertical and horizontal air velocities can all be determined within the volume illuminated by the transmitted beam. In standard Doppler measurements, the beams have to be moved off-vertical in order to measure the horizontal wind component. However, that implies that the horizontal velocity is being measured in a different volume than the vertical velocity. In clear air conditions, the latter is not a significant problem but the large flow gradients in a precipitation environment can lead to unreliable measurements. A further advantage of interferometric precipitation observations is that the high angular resolution within the beam can be used to determine the horizontal spatial structure of the observed precipitation.

3 Forecast

Our plan is to continue the analysis of the interferometer data obtained so far. Last May we made observations over a ten-day period. The first half was characterized by two frontal passages and periods of precipitation. The second half was characterized by a stable air mass. The data analysis will include a study of the vertical circulations around the fronts, and the characteristics of lower stratospheric inertia gravity waves present during

the stable period. There is evidence to suggest that the lower-stratospheric oscillations evident in the data are associated with orographically-generated waves. The vertical momentum fluxes will be calculated to determine if the waves are depositing their momentum in the mean flow. The relationship between the waves and the mean winds in the lower troposphere will also be examined.

Since spring and fall are the best times for observing frontal passages at Kyoto, we plan to carry out observations during those two periods next year in order to obtain a more extensive data set suitable for studying frontal zone/jetstream circulations.

As soon as the initial analysis of the data from the vorticity experiments carried out last spring is completed, planning will begin for the next set of observations using the vorticity measurement technique. The first set of measurements was limited in extent since the new technique was untested. Once we have confidence in the measurement, efforts will be made to make such measurements in a range of background conditions.

Finally, we are planning to expand the numerical model which we have been using to study the scattering processes to include more complicated horizontal flow gradients. The model results will be used to assess and refine the multiple receiver techniques for measuring horizontal winds and flow gradients.

The forecast is consistent with the research plan outlined in the original proposal.

A Cumulative List of Publications (September 15, 1991 - October 14, 1992)

References

- [1] Chilson, P. P., R. D. Palmer, M. F. Larsen, C. W. Ulbrich, S. Fukao, M. Yamamoto, T. Tsuda, and S. Kato, The use of spatial interferometry for the study of precipitation, *Geophys. Res. Lett.*, *in press*, 1992.
- [2] Fukao, S., M. F. Larsen, M. D. Yamanaka, H. Furukawa, T. Tsuda, and S. Kato, Observations of a reversal in long-term average vertical velocities near the jetstream wind maximum, *Mon. Wea. Rev.*, *119*, 1479-1489, 1991.
- [3] Larsen, M. F., S. Fukao, O. Aruga, M. D. Yamanaka, T. Tsuda, and S. Kato, A comparison of VHF radar vertical-velocity measurements by a direct vertical-beam method and by a VAD technique, *J. Atmos. Ocean. Tech.*, *8*, 766-776, 1991.
- [4] Larsen, M. F., R. D. Palmer, S. Fukao, R. F. Woodman, M. Yamamoto, T. Tsuda, and S. Kato, An analysis technique for deriving vector winds and in-beam incidence angles from radar interferometer measurements, *J. Atmos. Ocean. Tech.*, *9*, 3-14, 1992.
- [5] Larsen, M. F., and J. Röttger, VHF radar measurements of in-beam incidence angles and associated vertical-beam radial velocity corrections, *J. Atmos. Ocean. Tech.*, *8*, 477-490, 1991.
- [6] Palmer, R. D., S. Fukao, M. F. Larsen, M. Yamamoto, T. Tsuda, and S. Kato, Oblique frequency domain interferometry measurements using the middle and upper atmosphere radar, *Radio Sci.*, *27*, 713-720, 1992a.
- [7] Palmer, R. D., M. F. Larsen, C. Heinselman, and I. S. Mikkelsen, Frequency domain interferometry using the 1290 MHz Sondrestrom radar: first results, *J. Atmos. Ocean. Tech.*, *submitted*, 1992b.
- [8] Palmer, R. D., M. F. Larsen, E. L. Sheppard, S. Fukao, M. Yamamoto, T. Tsuda, and S. Kato, Poststatistic-steering wind estimation in the troposphere and lower stratosphere, *Radio Sci.*, *submitted*, 1992c.

- [9] Palmer, R. D., M. F. Larsen, R. F. Woodman, S. Fukao, M. Yamamoto, T. Tsuda, and S. Kato, VHF radar interferometry measurements of vertical velocity and the effect of tilted refractivity surfaces on standard Doppler measurements, *Radio Sci.*, 26, 417-427, 1991.
- [10] Sheppard, E. L., and M. F. Larsen, Analysis of model simulations of spaced antenna/radar interferometer measurements, *Radio Sci.*, 27, 759-768, 1992.
- [11] Sheppard, E. L., M. F. Larsen, R. D. Palmer, S. Fukao, M. Yamamoto, T. Tsuda, and S. Kato, A statistical comparison of spaced antenna and spatial interferometry wind estimation, *Radio Sci.*, in press, 1992.
- [12] Yoe, J. G., M. F. Larsen, and E. J. Zipser, VHF wind profiler data quality and comparison of methods for deducing horizontal and vertical air motions in a mesoscale convective system, *J. Atmos. Ocean. Tech.*, in press, 1992.

THE USE OF SPATIAL INTERFEROMETRY FOR THE STUDY OF PRECIPITATION

P.B. Chilson, R.D. Palmer, M.F. Larsen, C.W. Ulbrich

Department of Physics and Astronomy, Clemson University

S. Fukao, M. Yamamoto, T. Tsuda, and S. Kato

Radio Atmospheric Science Center, Kyoto University

Submitted to Geophysical Research Letters: September 1992

Abstract. This paper presents the initial results of a study of precipitation using spatial interferometry (SI) at the MU radar in Japan. On April 30, 1992, data were collected using the VHF Doppler radar at the facility during the passage of a frontal system. A linear variation in the phase was identified in the cross-spectra of the returned signal in the frequency ranges corresponding to both the turbulence and the precipitation peaks. The portions of the spectra which are attributed to the precipitation are broadened by the range of particle sizes and the presence of turbulence. This leads to a larger underestimation in the slope of the phase than would be attributed to turbulent fading alone. The results present the first radar interferometry study of precipitation.

1 Introduction

The effectiveness of using spatial interferometry (SI) for investigating atmospheric dynamics has been well established [e.g., Meek and Manson, 1987; Larsen and Röttger, 1991]. Although the technique was first devised for studying the inclination of the geomagnetic field [Woodman, 1971], the method was quickly shown to be useful in observing *soft targets* such as turbulence in the lower atmosphere. By analyzing the phase of the returned signal, SI can be used to generate the three dimensional wind within the sampling volume. The technique has been described by Palmer *et al.* [1991], Van Baelen and Richmond [1991],

and *Larsen et al.* [1992], and has been shown to be the Fourier transform equivalent of the spaced antenna (SA) technique. Of course, the estimated SI wind vector was equivalent to the so-called SA *apparent* velocity and a scheme for obtaining the *true* velocity from the frequency domain has been derived [*Briggs and Vincent*, 1992; *Sheppard and Larsen*, 1992] using a Fourier transform equivalent of the full correlation analysis (FCA) called full spectral analysis (FSA).

The potential advantage of using SI for precipitation studies is that the location of the particles within the beam can be determined. Also, as will be shown later, the phase information may be useful in estimating the effect of turbulent broadening. To date, no observations of precipitation been made using SI. Indeed it has been unknown whether SI would work in such an analysis. The spectra formed by the backscattered signal from clear air turbulence follow a Gaussian distribution in velocity space. The strength of the signal, the Doppler velocity and the estimate of turbulence intensity can be determined from the spectral moments of the Doppler spectra. The precipitation spectra, however, follow a distribution which varies as a function of the particle sizes. The form of the precipitation spectra in velocity space is then dependant on the fall speeds of the particles as a function of diameter. Furthermore, the motion of the precipitation is influenced by the presence of any turbulence and wind. These factors will be seen to affect the cross-spectra and will be discussed later.

2 Spatial Interferometry

Following the discussion by *Larsen et al.* [1992], the relevant equations for SI will be outlined here. If two spatially separated receivers, i and j , detect the returned signal from a common scatterer or scattering medium, the difference in phase measured by the two receivers will be related to the radar wavenumber k , their separation d_{ij} and the zenith angle δ through

$$\phi_{ij} = kd_{ij}\sin\delta \quad (1)$$

The angle δ is measured relative to the vertical plane containing the two receivers. In the case of a vertically pointing radar, the range of the sampled zenith angles is determined by

the width of the transmitted beam. If the scatterers are moving horizontally through the sampling volume with a uniform speed and the direction of the wind is parallel to a baseline of the receivers, then the detected radial velocity will vary from $-v \sin \delta$ to $+v \sin \delta$, where v is the actual horizontal wind speed. In this analysis, the common assumption has been made that the Taylor hypothesis is valid.

By taking the Fourier transform of two signals, obtained from two spatially separated receiving arrays, the cross-spectrum can be obtained

$$C_{ij}(\omega) = F_i(\omega)F_j^*(\omega) = A_i(\omega)A_j^*(\omega)e^{i[\phi_i(\omega)-\phi_j(\omega)]} \quad (2)$$

where the * denotes the complex conjugate. The amplitude of the cross-spectrum should be very nearly the same as that of the auto-spectra since $F_i(\omega)$ and $F_j(\omega)$ are obtained from essentially the same scattering volume. The Doppler sorting process leads to a linear variation in the phase of the cross-spectrum.

Larsen *et al.* [1992] derived the equations relating the wind velocity to the slope and intercept of the phase variation in the cross-spectra. If the wind vector is decomposed into a horizontal component, v_h , and a vertical component, w , then the radial Doppler velocity v_r can be expressed as

$$v_r = v_h \frac{\sin \delta}{\cos(\alpha_{ij} - \theta)} + w \quad (3)$$

where α_{ij} and θ are the azimuth angles for the baseline and the wind vector, respectively. By using Eqs. (1) and (3) and solving for ϕ_{ij} one finds

$$\phi_{ij} = \frac{kd_{ij} \cos(\alpha_{ij} - \theta)}{v_h} (v_r - w) \quad (4)$$

i.e., a linear equation for the slope of the line defining the variation of the phase in the cross-spectrum. In obtaining Eq. (4) δ has been assumed to be small, allowing the approximation to be made that $\cos \delta \sim 1$ and $\sin \delta \sim \tan \delta$. Substituting the slopes and intercepts found from the cross-spectra of two pairs of baselines along with their azimuth angles, the magnitude and direction of the apparent wind can be obtained.

The velocities given by Eq. (4) are the apparent velocities in that turbulent fading has not been taken into account. Another assumption is that w is not affected by aspect sensitivity, i.e., the scattering is isotropic within the sampling volume. Any layering of the atmosphere would give rise to specular backscatter at VHF frequencies [e.g. Tsuda *et al.*, 1986], leading in turn to an erroneous estimation of the vertical wind if the layers are inclined with respect to horizontal. However, Larsen *et al.* [1992] have shown that the effects of aspect sensitivity can also be handled easily with an SI analysis only slightly more complicated than the one presented here. The estimation of the horizontal wind is not affected by the layers. Since the primary concern of this work has been to show the variations in the phase of the cross-spectra seen in the signal associated with the precipitation, no efforts have been made to correct for the effect of specularity in the present analysis.

3 Description of the Experiment

The data presented in this paper were taken on April 30, 1992, at the MU radar located at Shigaraki, Japan (34.85° N, 136.10° E). A front which passed the radar site resulted in heavy, stratiform rain. The entire array was used for transmission, but was partitioned into three separate subarrays for reception. The receiving arrays are shown in Fig. 1. A more detailed description of the MU radar can be found in [Fukao *et al.*, 1985a, 1985b].

A pulse width of 1 μ s was used during transmission giving a height resolution of 150 m. Furthermore, 64 range bins were sampled beginning at 0.15 km, resulting in height coverage from 0.15 to 9.6 km ASL. The recovery time of the T/R (transmit/receive) switch, however, caused the data below approximately 1.8 km to be unreliable. The inter-pulse period (IPP) was 400 μ s and 256 samples were used for the coherent integrations, resulting in a sampling period of 0.1024 s and a Nyquist velocity of 16 ms^{-1} . The spectral resolution was 0.063 ms^{-1} . The data presented in this work were obtained using 16 incoherent integrations which translates into approximately 8 minutes of real time data. A long integration time was chosen to facilitate the phase analysis of the precipitation signal, which will be discussed below.

An example of the auto-spectra resulting from the 256-pt FFT is presented as a func-

tion of height in Fig. 2a. The spectra are shown using a linear-linear scale and they have been normalized to the peak at each altitude. The corresponding power profile is shown in Fig 2b. The radar return has not been calibrated with the transmitted power, so the power profile indicates only the relative change in the backscattered signal. An interesting feature of the profile is the abrupt increase in echo power at 3 km. In addition, below 3 km, a bimodal pattern establishes itself in the spectra, and the two peaks are seen to separate in velocity. The peaks in the spectra associated with the negative velocities (towards the radar) are attributed to the falling precipitation. The height where the spectral peaks begin to separate and where the enhanced reflectivities occur is indicative of the location of the melting layer or *bright band* [Battan, 1973]. In the transition region in which the spectra become bimodal (3.0 – 3.6 km), the precipitation return is much stronger than the turbulent return causing the turbulent peak to be lost in the spectral noise. Although the presence of a bright band at VHF is not well documented, a similar pattern has been seen at 53.5 MHz by Yoe [1990].

4 Analysis and Results

As shown above, the SI analysis involves using the phase of the cross-spectra. Only those regions of the cross-spectra where the echo power is strong should exhibit consistency in the phase. When examining the phase, it is therefore important to choose a spectral window broad enough to provide adequate data for the statistics without including the noise. The method chosen for this analysis was to fit one or two Gaussian distributions to the spectra and use the fitted parameters as an estimate of the widths. All data within $\pm 2\sigma$ of the peak or peaks of the distribution were used in the phase analysis. This also provided a method of isolating the two peaks in those cases where the spectra were bimodal. Although the spectra resulting from turbulence are well approximated by a Gaussian, the normalized precipitation spectra observed with a vertically pointing radar is better represented by

$$S_p(v_r) = \frac{1}{Z} D^6 N(D) \frac{dD}{dv_r} \quad (5)$$

where Z is the radar reflectivity factor, $N(D)$ is a distribution function of the diameters D of the precipitation particles, and v_r is their fall speed. Eq. (5) is the form the spectra would assume if the particles were falling through a quiescent atmosphere in the absence of any turbulence or vertical wind. The actual observed spectra are a convolution of the precipitation spectra with the turbulence spectra [Wagasaki *et al.*, 1987; Gossard *et al.*, 1990], leading to observed precipitation spectra of the form

$$S_o(v_r) = P_p S_p(v_r - w) \otimes S_t(v_r) + P_t S_t(v_r - w) \quad (6)$$

where P_p and P_t are the spectral powers for the precipitation and turbulence, respectively, and $S_t(v_r)$ is the Gaussian spectrum for the turbulence. The convolution operator is indicated by \otimes . Because of the convolution, a Gaussian distribution can be used sufficiently well to fit the precipitation spectra for the purpose of separating the two peaks and establishing a width for the precipitation spectra.

Having defined the spectral window, a line was fitted to the phase as a function of velocity (see Eq. 4). As can be seen in Fig. 3, a linear variation of the slope can be identified separately for both the turbulence and precipitation. The cross-spectra obtained for all three receiver combinations at a height of 2.1 km are shown for comparison. As is true for the winds, the consistency of the phase is most pronounced when the baseline is parallel to the wind vector. Calculations using the phase from the turbulence peak show the winds to be southerly at this altitude. Since the 2-3 baseline is almost perpendicular to the wind vector (Fig. 3c), the phase shows a small slope. As was mentioned earlier, near the melting layer, the precipitation signal dominates the spectra making the turbulence signal difficult to resolve in the spectral amplitude. Although the echo power from the turbulence is significantly less than that of the precipitation, in many cases the phase variations from both returns can still be detected, providing information about the winds which would have been lost without the use of interferometry.

Since no correction has been made in this analysis for the effects of turbulent fading, the slopes shown in Fig. 3 are underestimated, i.e., the corresponding wind magnitude will be overestimated. Furthermore, it can be seen that the slopes of the phase from the precipitation

return have still smaller values than those obtained from the turbulence signals. The slope is a measure of the apparent horizontal winds and the quotient of slope and intercept for the fitted line is a measure of the vertical wind if there are no aspect sensitivity effects [Palmer *et al.*, 1991]. The Doppler velocities of the precipitation particles result not only from their fall speeds, but to some extent from the presence of the winds as well. Under the assumption that the precipitation particles are carried along by the winds, the slopes in the phase from the rain and the turbulence should be approximately the same. The primary difference in the two would be in the intercepts which are affected by the magnitude of the vertical velocity. The data shown in Fig. 3 clearly indicate that the phase slopes associated with the turbulence signals are more steeply inclined than those associated with the precipitation. A process similar to that which leads to turbulent fading could result in the underestimation of the precipitation phase slopes. Doppler spectra from precipitation particles are broadened by turbulence as well as by the particle size distributions. The distribution of particle diameters consequently results in a broadening of the spectra in velocity space. Any broadening of the spectra in SI tends to decrease the lag time in the cross-correlation function, which is analogous to reducing the phase slope in the cross-spectra.

In the present analysis, long integration times were chosen for the sake of showing the linear variation of the phase associated with the precipitation. This was done at the cost of losing the structure in the phase which is apparent with less averaging. With a beamwidth of 3.6 /degr, the sampling volume at 2.1 km has a diameter of approximately 132 m. The calculated SI apparent horizontal wind at 2.1 km is $\sim 40 \text{ ms}^{-1}$ indicating the radar is detecting a new volume of space every 3.3 seconds. The stratiform nature of the precipitation, however, makes the lengthy averaging of the data justifiable. The phase information represents the general properties of the precipitation particles filling the radar beam. A more detailed study of the data will require integration times of 30 seconds or less.

5 Conclusions

The data collected at the MU radar during the passage of a frontal system demonstrate the applicability of spatial interferometry to precipitation environments. A height profile

of the spectra reveals a bimodal pattern developing near the melting layer. In those cases where both the precipitation and the winds are present in the Doppler spectra and sufficiently well separated in velocity space, the slopes from each contribution can be identified. It is interesting to note that the variation in the phase can often be seen even when the magnitude of the spectra is weak. This is particularly useful when analyzing the spectra near the melting layer where the precipitation contribution is dominant. Without the phase information, an estimate of the vertical wind in this case would be impossible.

Although precipitation should follow the horizontal wind approximately, the data show the slopes in the phase associated with the rain and the wind to be different. It is known that turbulence can decorrelate the signal recorded at two separate receivers, thus reducing the slope in the phase. The turbulent fading can be removed [Briggs and Vincent, 1992] to yield the *true* SI horizontal wind, but this has not been done in the present analysis. The precipitation peak of the spectra should also be influenced by turbulent fading as seen in Eq. 6. This does not, however, account for the enhanced reduction of the slope. The further decorrelation of the signal might result from the distribution of the precipitation particles contained within the radar sampling volume. The spectral peak attributed to the precipitation is broadened in velocity space through the spatial and temporal averaging of the particle fall speeds. Any temporal decorrelation resulting from this averaging would lead to an underestimation of the slope. A more thorough analysis of the data is needed to address this topic.

Acknowledgements. PBC and CWU were supported by the NSF under grant #ATM9003448, and RDP under NSF grants #ATM9121526, #ATM9006846 and #ATM9003448. MFL was supported by AFOSR grant AFOSR-91-0384. The MU radar belongs to and is operated by the Radio Atmospheric Center of Kyoto University, Japan.

References

Battan L. J., *Radar Observations of the Atmosphere*, 324 pp., The University of Chicago Press, Chicago, 1973.

- Briggs, B. and R. A. Vincent, Spaced-antenna analysis in the frequency domain, *Radio Sci.*, **27**, 117-129, 1992.
- Fukao, S., T. Sato, T. Tsuda, S. Kato, K. Wagasuki and T. Makihira, The MU radar with an active phased array, 1, Antenna and power amplifiers, *Radio Science*, **20**, 1155-1168, 1985a
- Fukao, S., T. Tsuda, T. Sato, S. Kato, K. Wagasuki and T. Makihira, The MU radar with an active phased array, 1, In house equipment, *Radio Science*, **20**, 1169-1176, 1985b
- Gossard, E. E., R. G. Strauch and R. R. Rogers, Evaluation of drop-size-distributions in liquid precipitation observed by ground-based Doppler radar, *J. Atmos. Oceanic Tech.*, **7**, 815-828, 1990
- Larsen, M. F. and J. Röttger, VHF radar measurements of refractivity layer tilt angles and associated vertical-beam radial velocity corrections, *J. Atmos. Ocean Tech.*, **8**, 477-490, 1991.
- Larsen, M. F., R. D. Palmer, S. Fukao, R. F. Woodman, M. Yamamoto, T. Tsuda and S. Kato, An analysis technique for deriving vector winds and in-beam incidence angles from interferometer measurements, *J. Atmos. Ocean Tech.*, **9**, 3-14, 1992.
- Meek, C. E. and A. H. Manson, Mesospheric motions observed by simultaneous medium-frequency interferometer and spaced antenna experiments, *J. Geophys. Res.*, **92**, 917-930, 1987.
- Palmer, R. D., M. F. Larsen, R. F. Woodman, S. Fukao, M. Yamamoto, T. Tsuda and S. Kato, VHF Radar Interferometry measurements of vertical velocities and the effect of tilted refractivity surfaces on standard Doppler measurements, *Radio Sci.*, **26**, 417-427, 1991.
- Sheppard, E. L. and M. F. Larsen, Analysis of model simulations of spaced antenna/radar interferometer measurements, *Radio Sci.*, in press, 1992.
- Tsuda, T., T. Sato, K. Hirose, S. Fukao and S. Kato, MU radar observations of the aspect sensitivity of backscattered VHF echo power in the troposphere and lower stratosphere, *Radio Sci.*, **21**, 971-980, 1986.
- Van Baelen, J. S. and A. D. Richmond, Radar interferometry technique: Three-dimensional

wind measurement theory, *Radio Sci.*, **26**, 1209–1218, 1991.

Wagasuki, K., A. Mitzutani, S. Fukao and S. Kato, Further discussions on deriving drop-size distribution and vertical air velocities from VHF Doppler radar spectra, *J. Atmos. Oceanic Technol.*, **3**, 623–639 1987

Woodman, R., Inclination of the geomagnetic field measured by an incoherent scatter radar technique, *J. Geophys. Res.*, **76**, 178–184, 1971.

Yoe, J. G., *Analysis and comparison of several methods for processing VHF Doppler radar wind profiler data obtained during a mesoscale convective storm*, Ph.D. dissertation, Clemson University, Clemson SC, 132pp.

P. B. Chilson, M. F. Larsen, R. D. Palmer, and C. W. Ulbrich, Department of Physics and Astronomy, Clemson University, Clemson, SC 29634.

S. Fukao, S. Kato, T. Tsuda, and M. Yamamoto, Radio Atmospheric Science Center, Kyoto University, Uji, Kyoto 611, Japan.

(Received September x, 1992;

revised X x, 1992;

accepted X x, 1992)

Copyright 1992 by the American Geophysical Union.

Chilson et al.: Precipitation Study Using Spatial Interferometry

Chilson et al.: Precipitation Study Using Spatial Interferometry

Chilson et al.: Precipitation Study Using Spatial Interferometry

Fig. 1. Antenna configuration used for the interferometry experiment conducted on April 30, 1992. The entire array was used for transmission but subdivided into three subarrays labeled 1, 2 and 3 for reception.

Fig. 2. (a) Doppler spectra obtained at 0530 LT plotted over the range of sampled heights. The spectra, which have been normalized to the peak power at each height, are displayed using a linear scale. (b) The corresponding relative echo power.

Fig. 3. An example of the cross-spectra for data obtained at 2.1 km. This corresponds to the data shown in Fig. 2. The magnitude and phase of the cross-spectra are shown in the upper and lower rows, respectively. Vertical lines have been included to indicate the range of data used to find the slope of the displayed fits. The cross-spectra obtained from baselines 1-2, 1-3 and 2-3 are shown in (a), (b) and (c), respectively.

Fig. 1

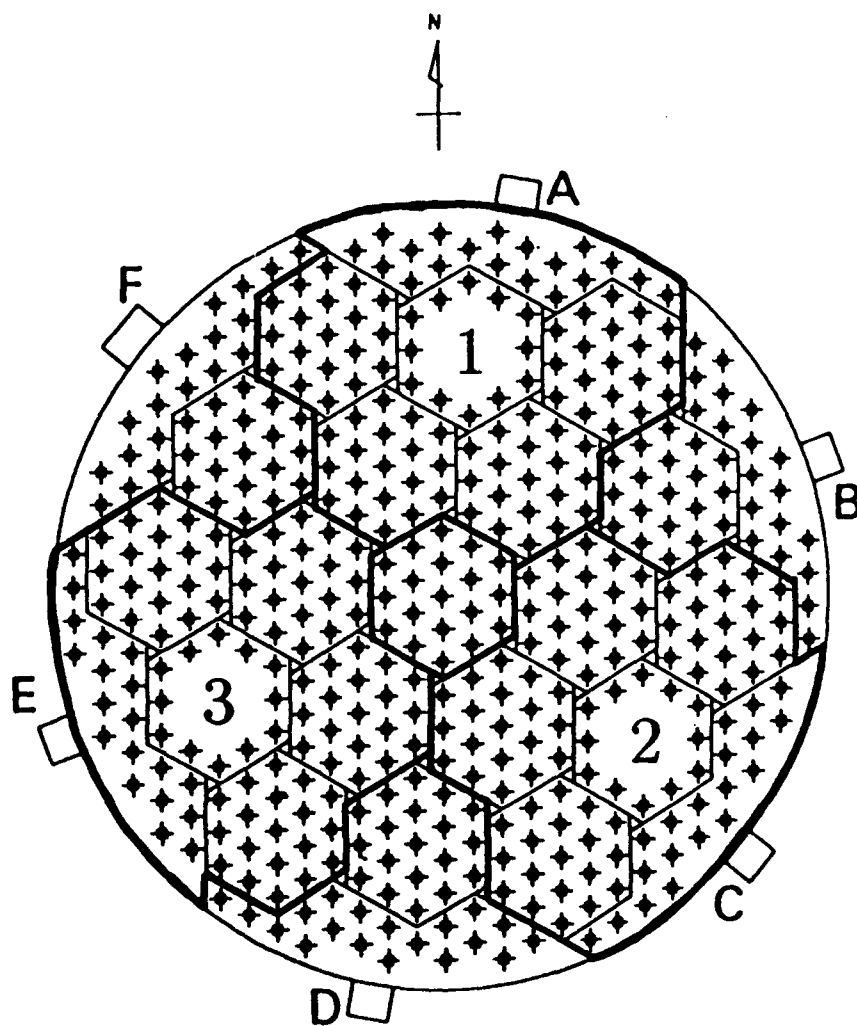
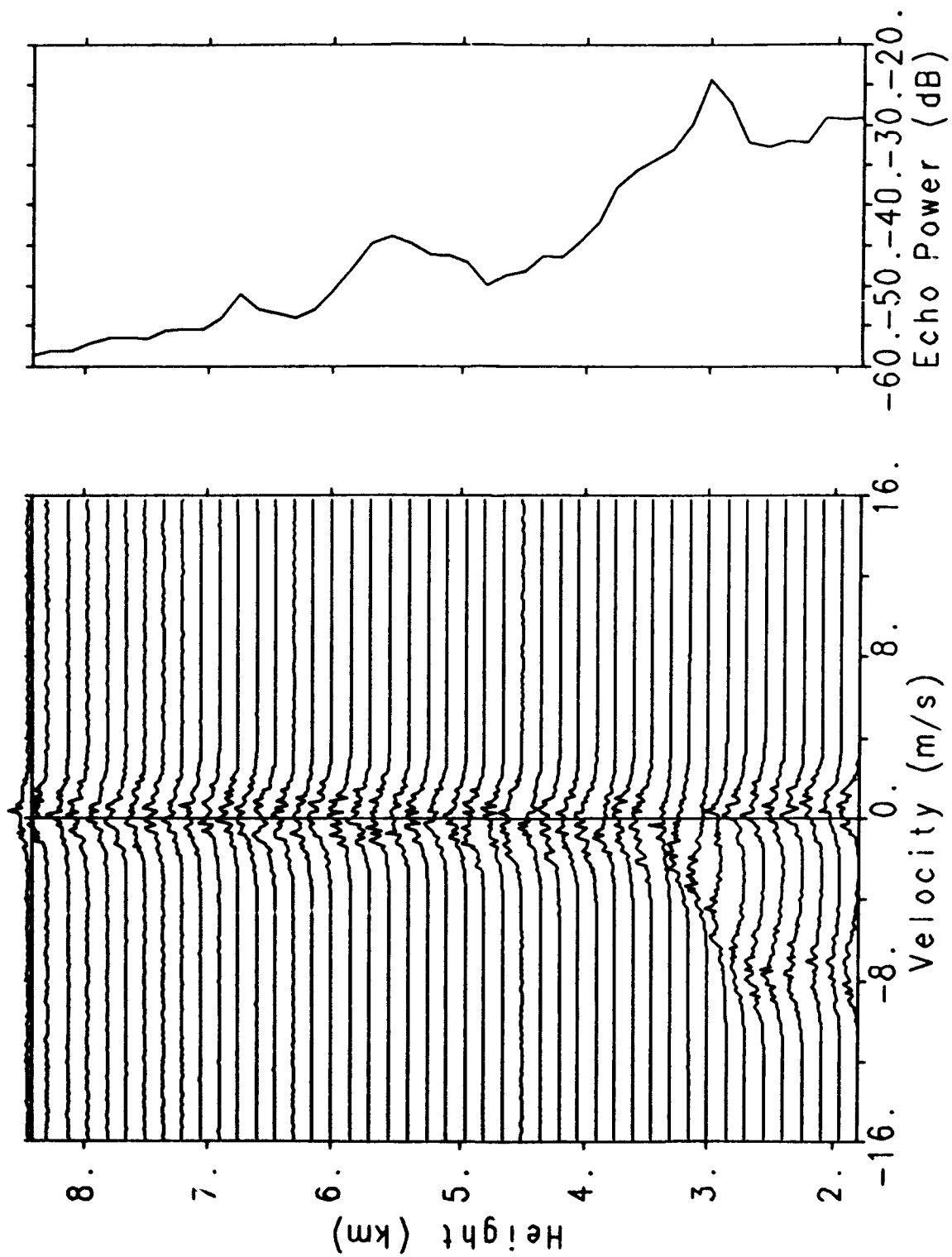
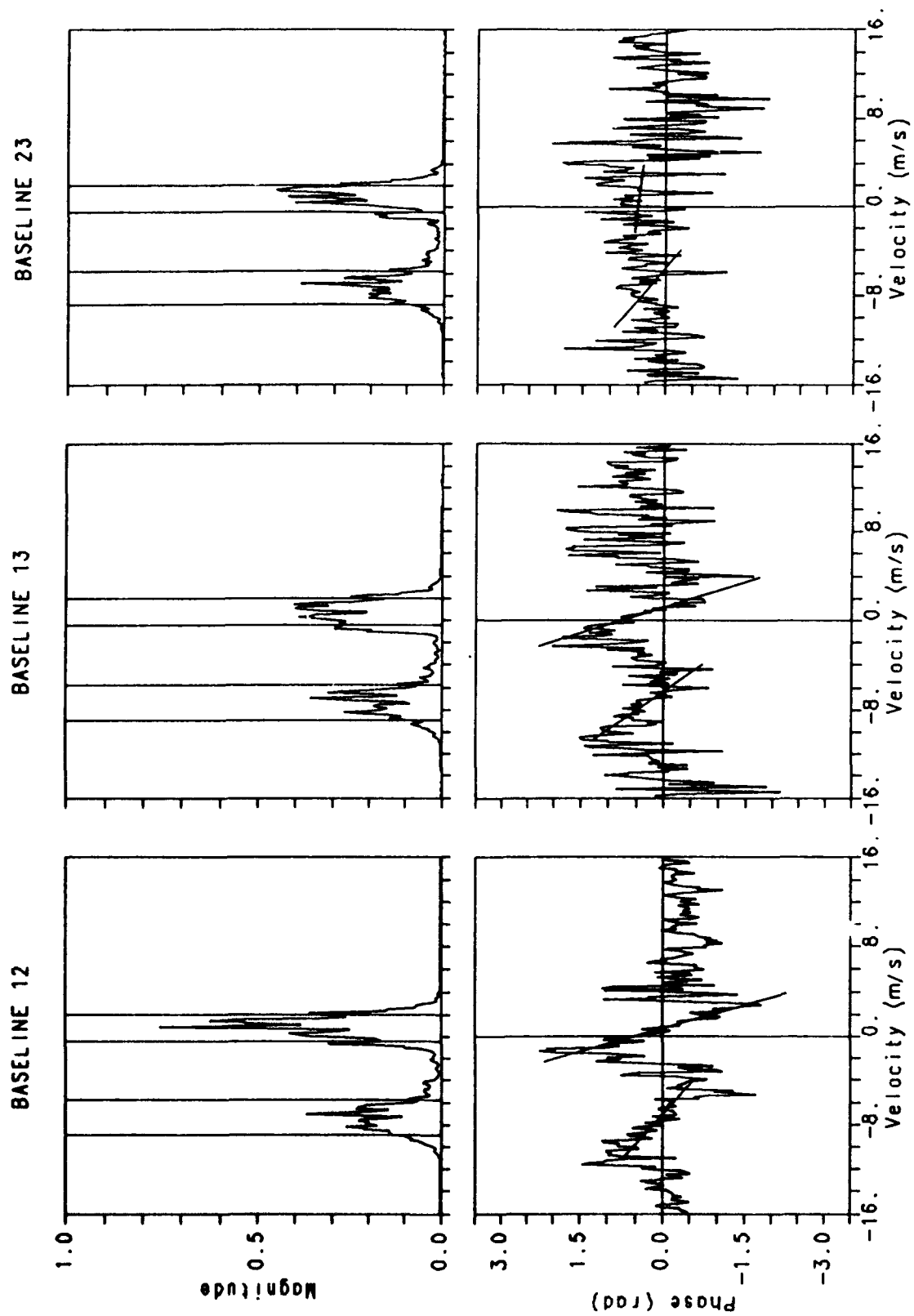


Fig. 2



(a)

(b)



(a)

(b)

(c)

Fig. 3

Observations of a Reversal in Long-Term Average Vertical Velocities near the Jet Stream Wind Maximum

S. FUKAO, M. F. LARSEN*, M. D. YAMANAKA, H. FURUKAWA, T. TSUDA AND S. KATO

Radio Atmospheric Science Center, Kyoto University, Kyoto, Japan

5 August 1990 and 12 December 1990

ABSTRACT

Analysis of vertical velocity measurements made for four days each month over the period from 1986 to 1988 by the MU radar in Japan shows a reversal in direction near the peak in the zonal wind profile during the winter months. More specifically, the reversal is noted during periods when the peak horizontal wind speeds exceed 60 m s^{-1} . The vertical velocities associated with the circulation have magnitudes of $10\text{--}20 \text{ cm s}^{-1}$, and the depth of the circulation is of the order of several kilometers. In 6 out of 14 cases when the feature was observed, the direction of the vertical circulation, although not the magnitude, could be explained by adiabatic ascent or subsidence along the average potential temperature surface slopes for the observation intervals. The direction of the circulation was such that it would tend to produce cooling and heating for the ascent and subsidence, respectively, that would tend to strengthen or at least maintain the jet. In the remaining eight cases, the direction of the vertical circulation could not be explained by the slope of the time-averaged potential temperature surfaces alone since the combination of the horizontal winds and the slopes of the isentropic surfaces would have led to a prediction of a circulation directly opposed to that observed. Thus, either the local tendency in the time-averaged potential temperature must have been significant, structure with scales smaller than the rawinsonde station separation must have been present, or diabatic effects may have played a role in the dynamics of the vertical velocity feature.

1. Introduction

Vertical velocity measurements in the troposphere and stratosphere are rare in general, and measurements over extended periods are even more uncommon. The MU radar located near Kyoto, Japan, has now been carrying out routine wind observations for four days each month since December 1985, in addition to the many other experiments and observations carried out at the facility. The parameters derived from the measurements include the horizontal and vertical winds, as well as the power profiles and Doppler spectral widths. The time chosen for the 4-day observation periods was constrained primarily by the general observing schedule rather than an attempt to observe specific phenomena. Thus, the profiles represent a more or less random sampling.

The goal of our study is to examine the average vertical velocity profiles for each year separately in order to look for long-term trends and for each 4-day period during the individual months to look for seasonal ef-

fects. In addition we will present what we believe to be the first extensive measurements of the vertical velocity profiles obtained in the vicinity of jet stream-frontal zone regions. The latter are associated primarily with the period from October to May. Mattocks and Bleck (1986) and Sechrist et al. (1986), for example, have discussed the importance of the vertical circulation around jet streaks in relation to cyclogenesis and the transport of ozone.

In the next section, we summarize the experimental procedure used in the standard observations. Section 3 describes the yearly average data, the relationship between the 4-day averages for each month and the background wind profiles, and the potential temperature cross sections for some of the periods. Section 4 describes the implications of the inferred vertical circulations.

2. Details of the observing procedure

a. Description of the MU radar system

The MU radar is located at Shigaraki near Kyoto, Japan (34.85°N , 136.10°E), and is operated by the Radio Atmospheric Science Center of Kyoto University as a dedicated facility for atmospheric observations. The radar is a 46.5-MHz system using an active phased array. The antenna is composed of 475 Yagis and an equivalent number of solid-state power amplifiers or

* On leave from the Department of Physics and Astronomy, Clemson University, Clemson, SC 29631.

Corresponding author address: Professor Miguel F. Larsen, Dept. of Physics and Astronomy, Clemson University, Clemson, SC 29634-1911.

transmitter-receiver (TR) modules (Fukao et al. 1985a,b). Each Yagi antenna is driven by a TR module with peak output power of 2.4 kW. All the Yagi antennas and TR modules are grouped into 25 subarrays in such a way that each group of 19 Yagis and associated electronics constitutes one subarray. The nominal peak and average radiated power are 1000 and 50 kW, respectively. The beam can be steered anywhere within 30° of zenith from pulse to pulse. The basic parameters of the system are given in Table 1.

b. Method for measuring vertical velocities

The monthly 4-day observations were made by steering the antenna beam every interpulse period (IPP) in a cycle that included the five directions north, west, south, east, and zenith. The zenith angle for the oblique beams was 10°. The horizontal distance from the zenith beam to the other beams ranged from 1 to 3.5 km in the height range considered, which stretched from 5.32 to 20 km. The transmitted pulse was a 16-element complementary code with 1-μs pulse width, corresponding to 150-m height or range resolution. The use of the coded pulse limits the lowest height of observation to 5.3 km AGL or 5.7 km MSL. The radial wind velocity was obtained approximately every 2.5 min in the five beam directions. The specific beam-pointing directions are listed in Table 2, along with other specific radar parameters used in the observations.

For the vertical beam measurements, the Doppler spectra were calculated, and the frequency offset of a Gaussian curve fitted nonlinearly in the least-squares sense to each spectrum was taken to be the mean Doppler shift in the radial direction. The latter was

TABLE 2. Observational parameters for VAD observations.

Altitude range:	5–24 km		
Height resolution:	150 m		
Pulse coding:	16-bit complementary code		
IPP:	400 μs		
Coherent integrations:	38		
Incoherent integrations:	6		
Interval to construct Doppler spectrum:	150 s		
Beam directions:	5		
(zenith angle, azimuth)	(0,0)	(10,0)	
	(10,90)	(10,180)	(10,270)

attributed to the vertical air velocity. The Doppler spectra were also calculated for each of the four off-vertical beam directions, and Gaussian curves were fitted in the same way as was done for the vertical beam

TABLE 3. Periods of MU radar observations and times and dates of corresponding meteorological analyses.

Case	Date/LST	Duration (h)	Meteorological analysis (Date/UTC)
1985			
December (●)	9 Dec/1156–13 Dec/1257	96	11 Dec/0000
1986			
January (●)	6 Jan/1109–10 Jan/1303	98	08 Jan/0000
February	10 Feb/1304–14 Feb/1547	99	
March	17 Mar/0800–21 Mar/1542	103	
April (●)	7 Apr/1134–11 Apr/1528	100	09 Apr/0000
May	6 May/1123–9 May/1535	76	
June	2 Jun/1200–6 Jun/1426	98	
July	7 Jul/1156–11 Jul/1329	98	
August	18 Aug/0117–22 Aug/1416	100	
September	1 Sep/1201–5 Sep/1639	100	
October (●)	18 Oct/1120–17 Oct/1535	100	15 Oct/0000
November (●)	10 Nov/2357–14 Nov/1536	88	12 Nov/1200
1987			
January (●)	5 Jan/1316–9 Jan/1530	98	07 Jan/0000
February	3 Feb/0053–6 Feb/1529	86	
March (●)	2 Mar/1201–6 Mar/1536	99	04 Mar/0000
April	6 Apr/1104–10 Apr/1536	100	
May	11 May/1344–15 May/1536	98	
June	22 Jun/1200–26 Jun/1200	96	
July	6 Jul/1723–11 Jul/0544	108	
August	3 Aug/1217–7 Aug/1220	96	
September	7 Sep/1151–11 Sep/1634	101	
October	5 Oct/1207–9 Oct/1454	99	
November	26 Oct/1135–30 Oct/1505	99	
December (●)	7 Dec/1037–11 Dec/1517	100	09 Dec/0000
1988			
January (●)	5 Jan/0818–8 Jan/1434	78	06 Jan/1200
February (●)	15 Feb/1214–19 Feb/1517	99	17 Feb/0000
March (●)	7 Mar/0823–11 Mar/1537	103	09 Mar/0000
April	18 Apr/0915–22 Apr/1530	102	
May (●)	9 May/0847–13 May/1521	102	11 May/0000
June	6 Jun/1156–10 Jun/1641	101	
July	18 Jul/1559–22 Jul/1637	96	
August	8 Aug/1137–12 Aug/1628	101	
September	29 Aug/1237–2 Sep/1532	99	
October (●)	24 Oct/1146–28 Oct/1527	99	26 Oct/0000
November (●)	14 Nov/1501–18 Nov/1527	96	16 Nov/0000

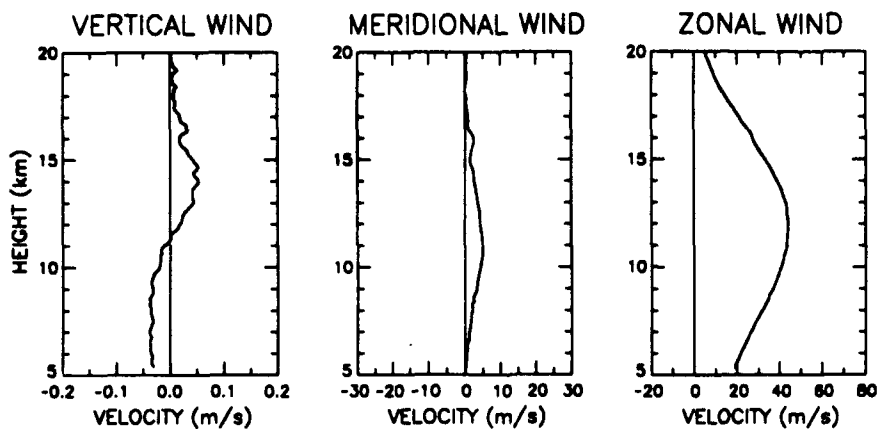
(●) Case showing vertical-velocity reversal.

TABLE 1. Basic parameters of the MU radar (Fukao et al. 1985a).

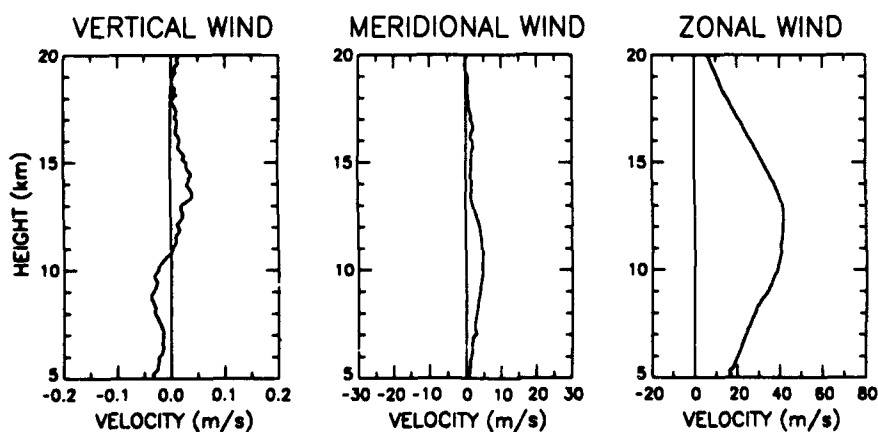
Radar system:	Monostatic pulse radar; active phased array system
Operational frequency:	46.5 MHz
Antenna:	Circular array of 475 crossed Yagi antennas
Aperture:	8330 m ² (103-m diameter)
Beamwidth:	3.6° (half power for full array)
Steerability:	Steering is completed in each IPP
Beam directions:	1657; 0°–30° off-zenith angle
Transmitter:	475 solid-state amplifiers (TR modules) each with output power of 2.4 kW peak and 120 W average
Peak power:	1000 kW (max)
Average power:	50 kW (duty ratio 5%) maximum
Bandwidth:	1.65 MHz (max) (pulse width: 1–512 μs variable)
IPP:	400 μs to 65 ms (variable)
Receiver:	
Dynamic range:	70 dB
A/D converter:	12 bits × 8 channels
Pulse compression:	Binary phase coding up to 32 elements (Barker and complementary codes presently in use)

AVERAGE WIND VELOCITY

JAN 1986-NOV 1986



JAN 1987-DEC 1987



JAN 1988-NOV 1988

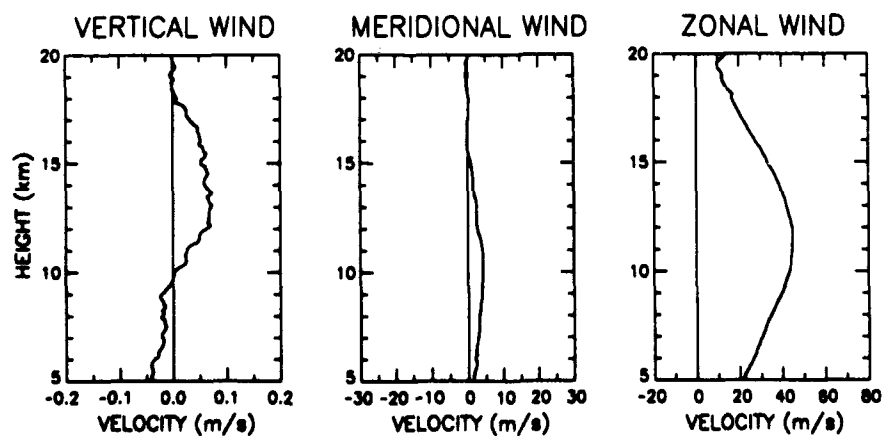


FIG. 1. Profiles of the average vertical, meridional, and zonal velocities derived from four days of measurements during each month in the period from January 1986 to November 1986 (top frame), for the period from January 1987 to December 1987 (center frame), and for the period from January 1988 to November 1988 (bottom frame).

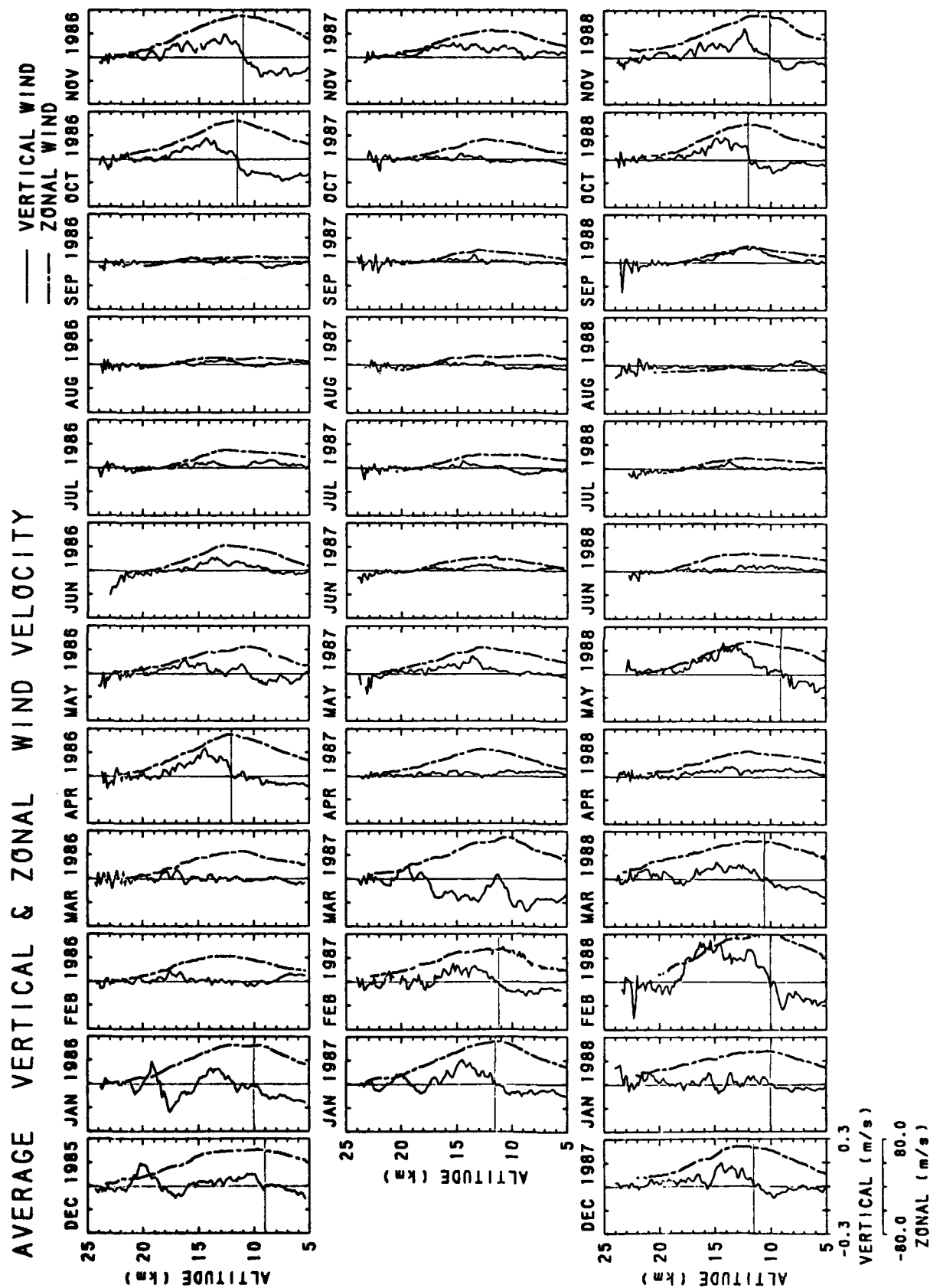


FIG. 2. Four-day average vertical and zonal velocity profiles for the period from December 1985 to November 1988. The height of the vertical-velocity profile reversals is indicated in some of the panels by a thin horizontal line.

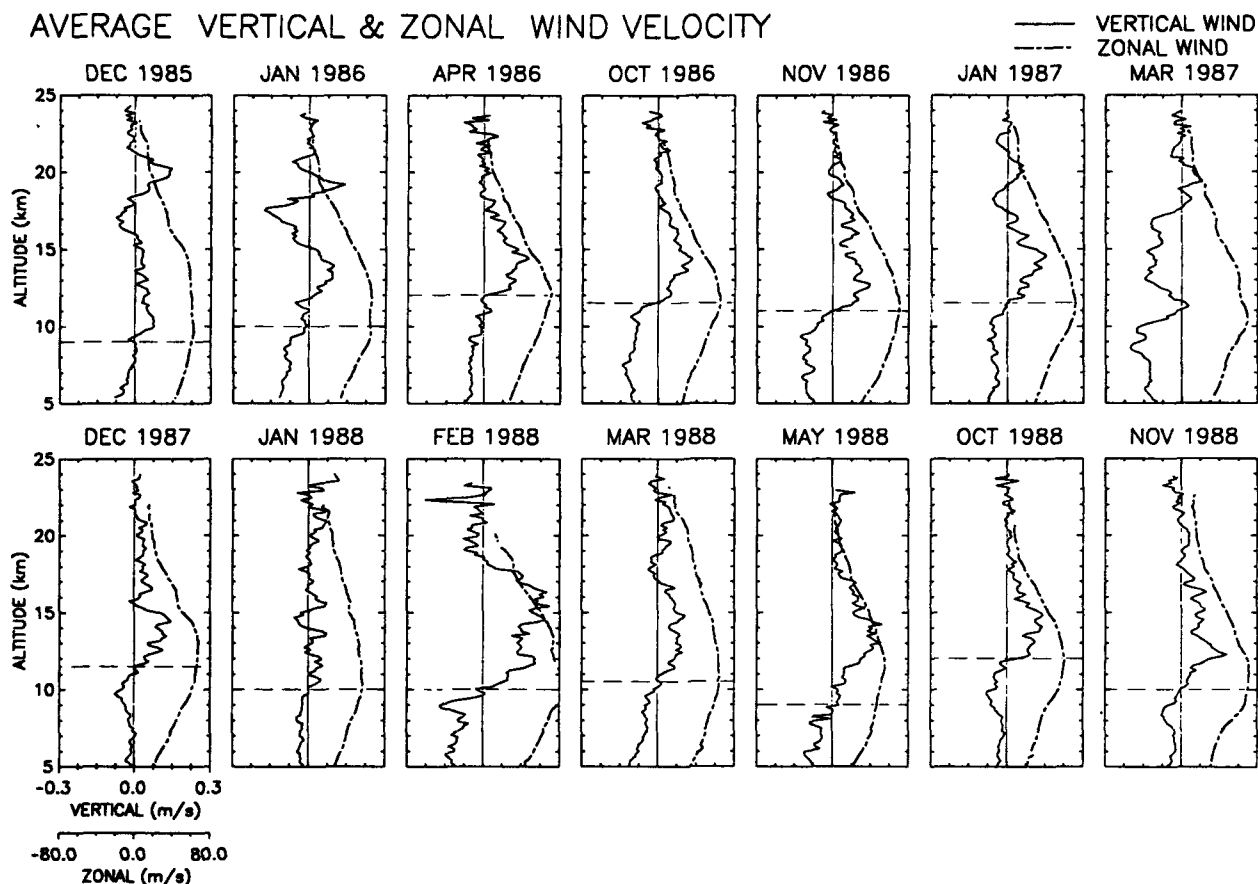


FIG. 3. Four-day average vertical and zonal velocities only for the cases showing the vertical circulation feature.

measurements. The radial velocities were then combined in order to carry out a VAD (velocity–azimuth display) analysis (see, e.g., Wilson and Miller 1972; or Browning and Wexler 1972) to yield the horizontal wind components.

3. Average vertical velocity profiles

a. Yearly averages

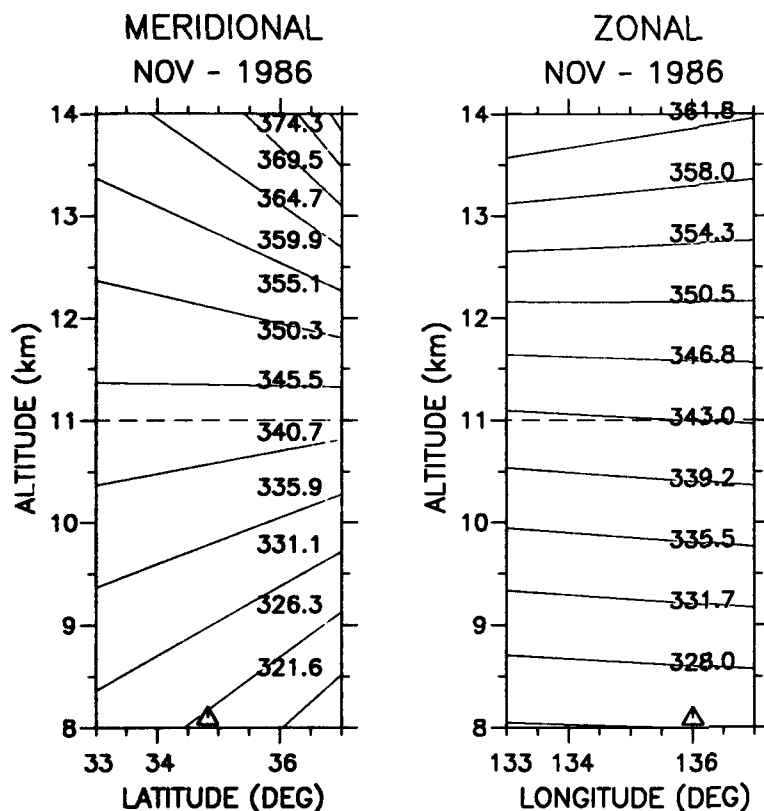
The averaged profiles of the horizontal and vertical velocities derived from the 4-day observation periods each month are shown for January–November 1986 in the top panel of Fig. 1, for January–December 1987 in the center panel, and for January–November 1988 in the bottom panel. A list of the observation periods that contributed to the averages is given in Table 3. During all three years, the average horizontal wind is almost entirely zonal, and the peak wind speed occurs at ~ 11 km. The peak magnitudes are close to 40 m s^{-1} . The behavior of the average vertical velocity profile is also consistent from year to year. In all three years, ascent occurs in the upper altitude range and subsidence at the lower heights. The maximum vertical ve-

locities are around 5 cm s^{-1} . The reversal in direction is found just below the maximum in the horizontal wind speed.

The vertical velocity profiles shown in Fig. 1 raise a concern about possible instrumental effects or other biases somehow affecting the long-term averages. For example, a small off-vertical tilt in the mechanical steering of the radar beam could contaminate the radial velocities in the nominally vertical beam with a small component of the horizontal velocity. The relatively large magnitude of the horizontal velocity in comparison to the vertical velocity can produce large errors in the vertical velocity measurements even if the beam-pointing error is small. Effective off-vertical pointing directions can also be induced in a system that is pointed accurately when aspect sensitivity effects at longer wavelengths are important (Larsen and Röttger 1991; Palmer et al. 1990; Larsen et al. 1991). Specifically, the strongest signals will come from a direction perpendicular to the refractivity layers at wavelengths around 6 m. Layers tilted slightly out of the horizontal plane will then produce effective off-vertical beam-pointing directions. Such effects have been discussed in detail in the articles cited above.

POTENTIAL TEMPERATURE DISTRIBUTION

Δ MU RADAR



AVERAGE WIND VELOCITY

NOV 1986

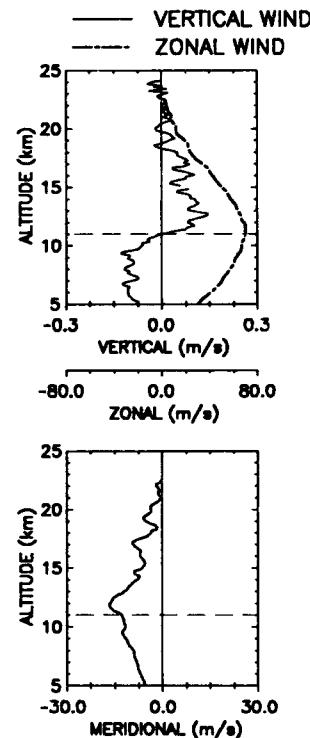


FIG. 4a. Potential temperature distribution along the south-north and west-east directions for the 4-day period in November 1986. The vertical, zonal, and meridional velocity profiles are shown to the right in the figure.

We have discounted effects due to inclined refractivity layers in the present study for two reasons. First, the study by Larsen and Röttger (1991) shows that the errors due to tilted layer effects can be large over periods shorter than one day, but the radial velocity in the vertical beam and the true vertical velocity become similar as the averaging interval increases. Second, we have compared direct vertical-beam vertical velocity measurements and vertical velocities calculated from VAD measurements in the earlier study by Larsen et al. (1991). Again, the differences were significant over shorter intervals of a few hours, but a 24-h average of the direct and calculated velocities produced essentially identical profiles. Since the latter study involved MU radar data, the results tend to vindicate not only the technique but also the particular instrument.

b. Monthly 4-day averages

The data were further divided into monthly 4-day averages, which are shown in Fig. 2 for the period from December 1985 to November 1988. The specific ob-

servation periods are listed in Table 3. The dramatic differences between the zonal wind speeds in summer and winter over the MU radar are evident. Winds during the period from June to September rarely exceed 20 m s^{-1} , while the winds during the period from October to May are often in excess of 60 m s^{-1} . The corresponding vertical velocity profiles show a similar dramatic change between the winter and summer periods. Generally, the vertical velocities are small during April to September, but the period from October to March often shows a feature similar to the long-term average feature evident in Fig. 1, although with larger magnitude. Specifically, a reversal in the vertical velocity direction occurs at a height close to the zonal wind speed maximum, with ascent above and subsidence below. The heights of the reversals are indicated by a thin horizontal dashed line in some of the profiles.

The reversal does not occur consistently in every month from October to May. For example, February and March 1986 show no effect, but the feature of interest is present in the profile for April 1986. An approximate discriminator between the cases showing

evidence of the vertical velocity feature and those showing no indication is that the maximum wind speeds exceed $\sim 60 \text{ m s}^{-1}$ when the feature is present; i.e., a well-developed jet stream/frontal zone system has to be in the vicinity of the radar for the feature to be evident.

The cases showing the effect have been isolated in Fig. 3. The discriminator used in choosing the cases shown in the figure was that the maximum horizontal wind speed exceeded 60 m s^{-1} . The February 1987 observation period showed some evidence of the vertical-velocity feature, but the maximum winds were less than the chosen cutoff. Therefore, that particular case was omitted, albeit somewhat arbitrarily. The profiles in Fig. 3 show the correspondence between the reversal in vertical velocity direction and the height of the wind maximum. The speeds associated with the vertical circulation are not constant from case to case but are in the range of $10\text{--}20 \text{ cm s}^{-1}$.

c. Vertical velocities and isentropic surface slopes

Figure 4a shows the 4-day average potential temperature surface heights along south–north and west–east cross sections derived from rawinsonde data for the period in November 1986. The rawinsonde stations used for the west–east cross section were Yonago (35.40°N , 133.35°E) and Hamamatsu (34.75°N , 137.70°E), and for the south–north cross section, Wajima (37.40°N , 136.90°E) and Shionomisaki (33.45°N , 135.75°E) were used. All are stations of the Japan Meteorological Agency, except Hamamatsu which belongs to the Japan Defense Agency. The location of the MU radar is indicated by the triangles along the two ordinates. The surfaces show only a small inclination in the zonal direction but a larger inclination in the meridional plane. The horizontal- and vertical-velocity profiles for the November 1986 period have been repeated at the right in the figure.

If the flow is isentropic, we have

$$\frac{\partial \theta}{\partial t} + \mathbf{V} \cdot \nabla \theta + w \frac{\partial \theta}{\partial z} = 0 \quad (1)$$

where θ is the potential temperature, \mathbf{V} is the horizontal wind vector, w is the vertical velocity, and t and z are the time and height coordinates, respectively. If the local time tendency is zero, Eq. (1) can be rewritten in finite difference form as

$$w = \left(u \frac{\Delta \theta}{\Delta x} + v \frac{\Delta \theta}{\Delta y} \right) \left(\frac{\Delta \theta}{\Delta z} \right)^{-1} \quad (2)$$

where u and v are the zonal and meridional velocity components, respectively, and x and y are the zonal and meridional coordinates. The combination of the horizontal velocities and the tilt angles of the isentropic surfaces should give vertical velocities in agreement with the measured velocities as long as the local time

SIMULATION OF VERTICAL WIND NOV - 1986

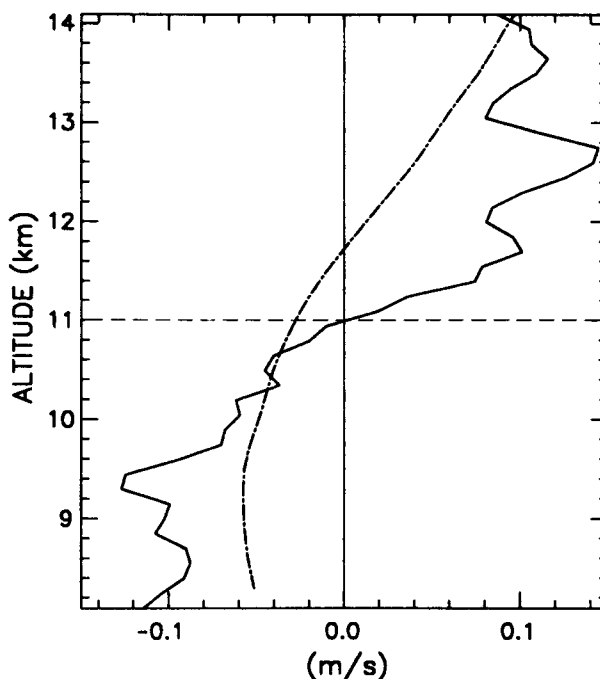
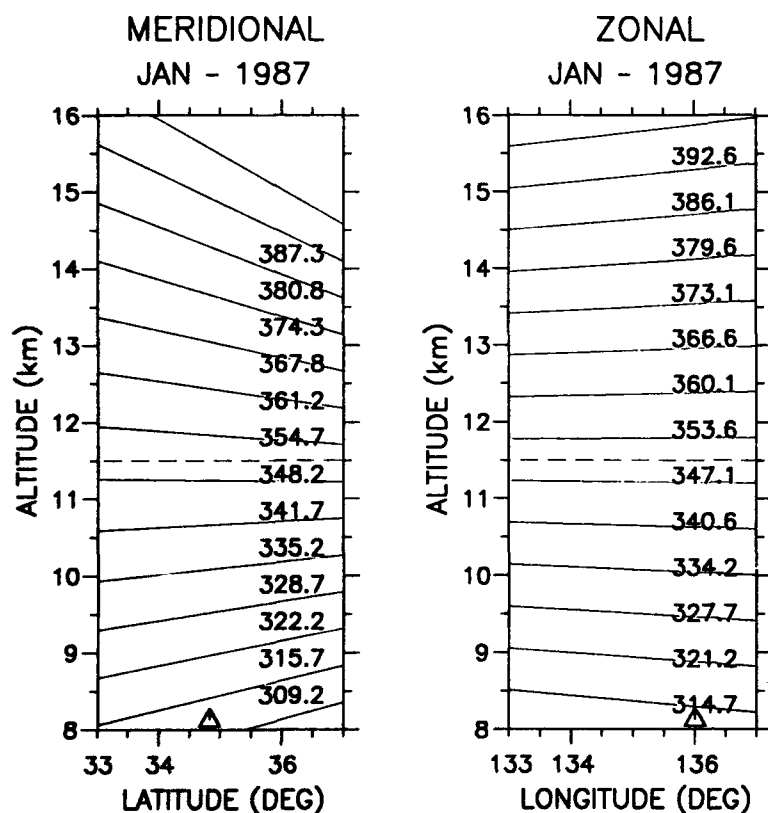


FIG. 4b. A comparison of the vertical velocities calculated by combining the measured horizontal winds and the slopes of the isentropic surfaces shown in Fig. 4a. The dashed-dotted line shows the calculated vertical velocity and the solid line represents the average measured profile.

derivative is zero, the flow is adiabatic, and the horizontal scale of the variations is larger than the rawinsonde station separation.

In November 1986, the zonal wind was large but the surface inclinations along the zonal direction were small. The meridional wind was smaller, although not negligible, and the meridional surface inclinations were large. Therefore, most of the contribution to the vertical-velocity profiles came from the combination of the meridional wind and the south–north isentropic surface tilt, although the contribution from the zonal wind was not negligible. The vertical velocities calculated as described above are compared to the average measured vertical velocities in Fig. 4b. The contributions from both the zonal and meridional wind components produced ascent above $\sim 12 \text{ km}$ and descent below. The agreement between the two profiles is not perfect but shows a reversal similar to the observations with ascent above $11.0\text{--}11.5 \text{ km}$ and subsidence below. The magnitude of the radar velocities is larger at almost all heights between 8 and 14 km , however. The agreement between the two curves, although not perfect, lends further credence to the idea that the averaged profiles are not artifacts of observational or instrumental effects.

POTENTIAL TEMPERATURE DISTRIBUTION

 Δ -MU RADAR

AVERAGE WIND VELOCITY

JAN 1987

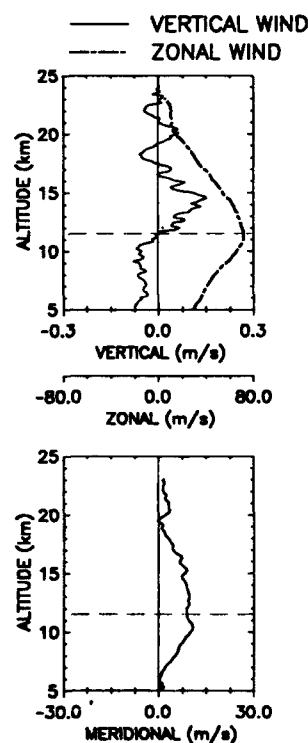


FIG. 5a. Similar to Fig. 4a but for January 1987.

The slopes of the isentropic surfaces for January 1987 are shown in Fig. 5a in a format similar to that used in Fig. 4a. Contrary to the November 1986 case, the meridional wind was northward during this period and produced descent above the jet stream maximum and ascent below. However, the zonal wind produced ascent above and descent below the maximum, so that the two contributions tended to offset, resulting in worse agreement than for the November 1986 case. Nonetheless, the reversal in direction was at nearly the same height in both profiles. Poor agreement will result if the adiabatic assumption is violated, if the average local time tendency of the potential temperature is not zero, or if the horizontal scale of the structure is less than the rawinsonde station separation.

d. Potential temperature cross sections

Cross sections of the equivalent potential temperature and horizontal wind speed are presented in Fig. 6 for all the cases shown in Fig. 3. The rawinsonde sta-

tions used in the analysis and the position of the cross sections were the same as those designated A-A' in the study by Fukao et al. (1988). The cases characterized by the presence of the vertical circulation feature have a distinct jet stream maximum near the location of the radar and show a divergence of the potential temperature contours toward the south. The patterns in the months that show no evidence of the vertical circulation feature (not shown) are not as well organized; i.e., there was no distinct wind speed maximum and the slopes of the isentropic surfaces were either small or highly variable.

e. Meridional winds

The meridional winds and vertical velocities for the cases showing the vertical velocity reversal are presented in Fig. 7. Of the total of 14 cases, 8 show a northward flow and 6 show a southward flow. The consistency in the isentropic surface patterns shown in Fig. 6 indicate that a southward flow is needed to ex-

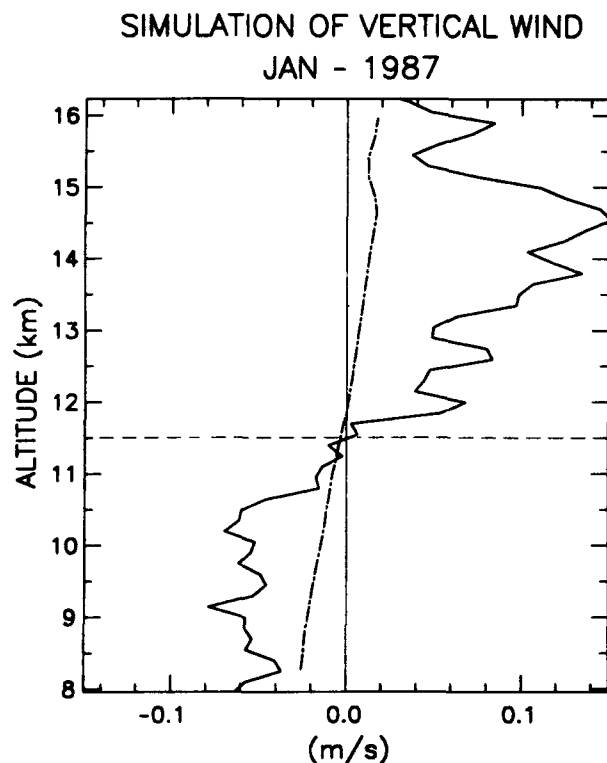


FIG. 5b. Similar to Fig. 4b but for January 1987.

plain the observed vertical circulation if the flow is diabatic and if the average local time tendency of the potential temperature is zero; this is so because a southward displacement along the isentropic surface will tend to produce ascent above the jet stream maximum and descent below. However, the conditions are only satisfied in 6 of the 14 cases. In the remaining 8 cases, Eq. (2) leads to a prediction of a vertical circulation in a direction opposite to the observations.

4. Discussion

The vertical circulation shown in the average 4-day vertical velocity profiles does not appear to be the result of instrumental effects or observational biases. The direction of the circulation is effectively upward and to the south above and downward and to the south below the wind speed maximum in 6 of 14 cases. The direction is upward and to the north above and downward and to the north below the wind speed maximum in the remaining 8 of 14 cases. In the 6 cases in which the observations were consistent with the vertical velocities predicted by time-stationary isentropic trajectory analysis, the ascent above would have produced adiabatic cooling south of the jet, while the subsidence below would have produced adiabatic heating to the

south. The thermal wind produced by the resulting horizontal temperature gradients would tend to strengthen the jet. In the remaining eight cases, the average local time tendency of the potential temperature, diabatic effects, or small-scale structure must have been significant.

A vertical-velocity feature similar to the one discussed here was also evident in a 4-day average vertical-velocity profile obtained with the SOUSY-VHF radar in West Germany in April 1984, although the dataset used by Larsen and Röttger (1991) in that study was much more limited in extent than the MU radar dataset. Their measurements showed subsidence above the jet stream and ascent below, i.e., a flow directed oppositely to that found in the MU radar data.

The details of the dynamics responsible for the observed circulation are not clear, but the directions appear to be in general agreement with the model described by Uccellini and Johnson (1979) and summarized by Mattocks and Bleck (1986). Figure 1 in the latter article shows the transverse circulation expected around a jet streak. A thermally indirect circulation is found in the exit region and a thermally direct circulation in the entrance region. The observed upward velocities above the wind maximum and downward velocities below would be expected either in the exit region south of the jet streak or in the entrance region north of the jet streak. The cross sections in Fig. 6 indicate that the jet was located either slightly north of, above, or slightly south of the radar site in all the cases showing evidence of the vertical circulation feature.

Our observations show that the vertical circulation feature appears when the maximum wind speeds exceed $\sim 60 \text{ m s}^{-1}$ and disappears when the peak wind speeds are less. There is no indication that the vertical-velocity magnitudes are proportional to the horizontal wind speeds, for example.

In a future study, the relationship between the observed circulation and proposed mechanisms such as that suggested by Eliassen (1962), for example, should be examined. He showed theoretically that a secondary ageostrophic, adiabatic circulation is generated in connection with frontogenesis by variations in the geostrophic wind and temperature fields. The transverse circulation, shown schematically in his Fig. 4, is accompanied by upward flow above the jet stream maximum and downward flow below. A weaker, oppositely directed vertical circulation is found south of the jet stream. A detailed investigation of the relevance of the theoretical model to the observed features is beyond the scope of the present study since the vertical velocities over a wide area would be needed, whereas only the velocities above the MU radar are available to us. However, the area over Japan is known to be an active cyclogenetic region, so we expect that Eliassen's (1962) theory will explain the observations, at least in part.

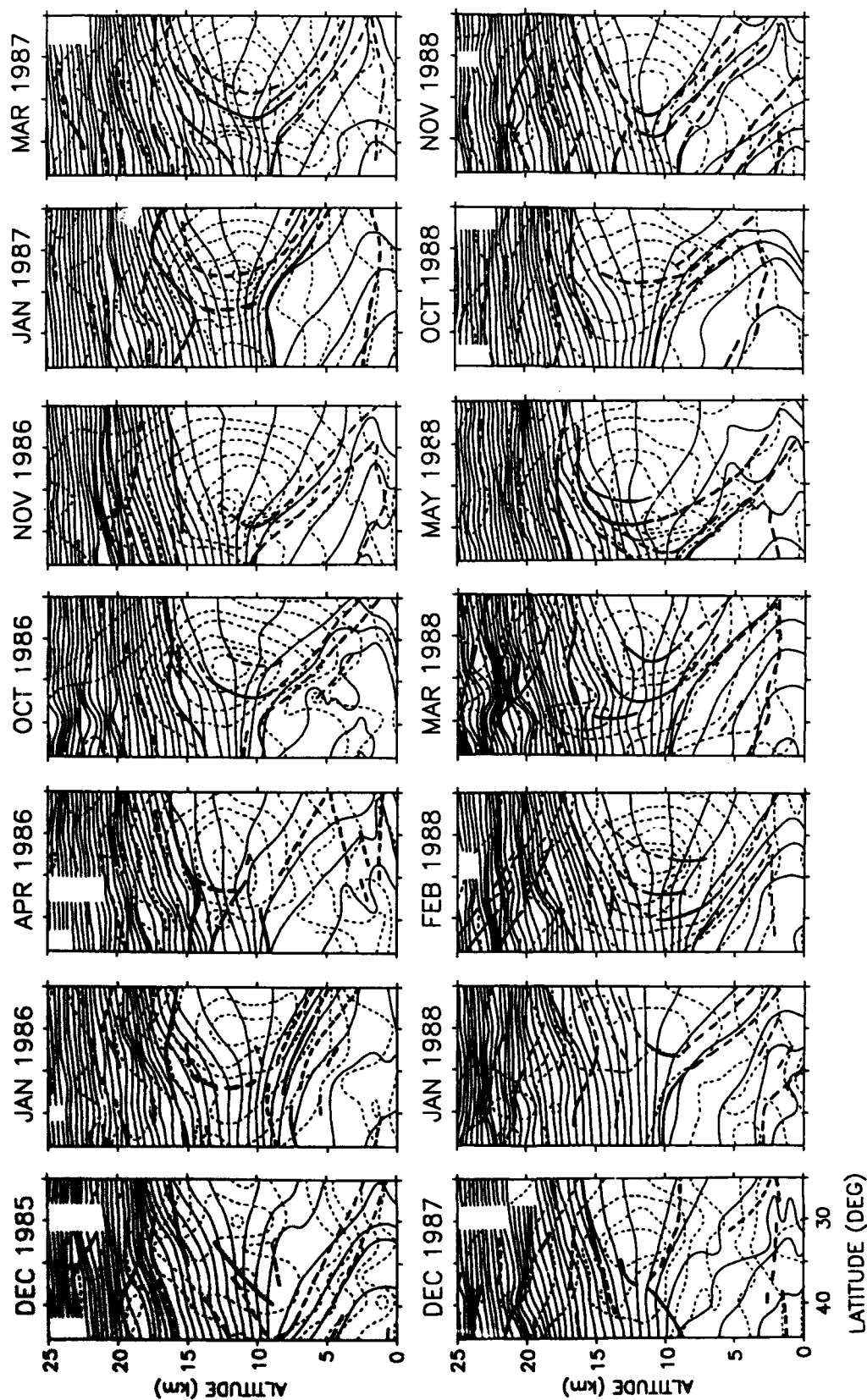


FIG. 6. Vertical cross sections of the equivalent potential temperature (thin solid lines) and the westerly winds (thin broken lines) for all the months showing evidence of the vertical velocity feature described in the text. The equivalent potential temperature contour interval is 10 K, and the contour interval for the winds is 10 m s^{-1} . Tropopause heights and frontal boundaries are shown by thick solid lines and thick broken lines, respectively.

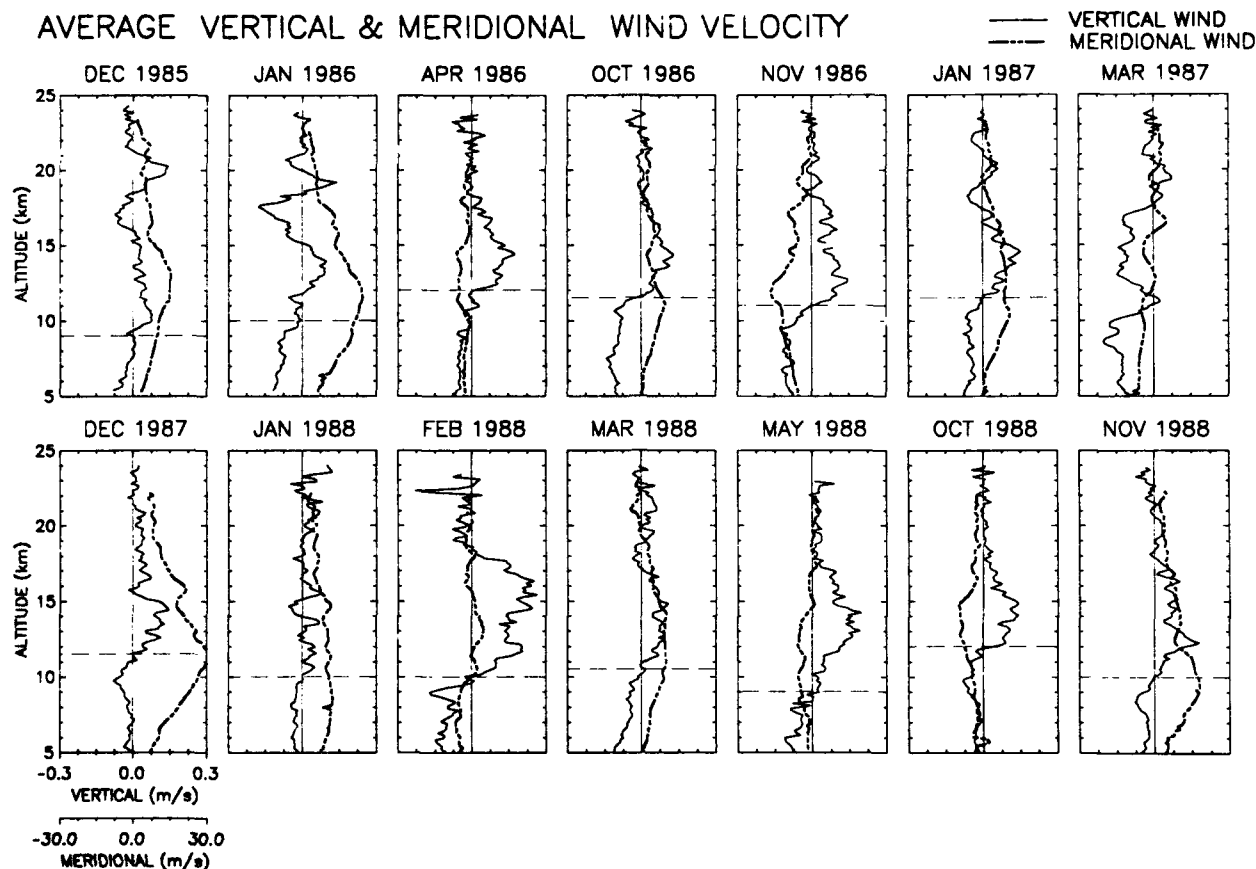


FIG. 7. Profiles of the vertical velocities and meridional winds for the months showing evidence of the vertical velocity reversal described in the text.

Acknowledgments. We thank Dr. I. Takayabu, Dr. Louis Uccellini, and an anonymous reviewer for helpful comments. MFL received support from the Ministry of Education, Research, and Culture of Japan and from AFOSR Contract F49620-88-C-0121 during the course of the study. The MU radar belongs to and is operated by the Radio Atmospheric Science Center of Kyoto University.

REFERENCES

- Acknowledgments.* We thank Dr. I. Takayabu, Dr. Louis Uccellini, and an anonymous reviewer for helpful comments. MFL received support from the Ministry of Education, Research, and Culture of Japan and from AFOSR Contract F49620-88-C-0121 during the course of the study. The MU radar belongs to and is operated by the Radio Atmospheric Science Center of Kyoto University.
- ### REFERENCES
- Browning, K. A., and R. Wexler, 1972: A determination of kinematic properties of a wind field using Doppler radar. *J. Appl. Meteor.*, **7**, 105-113.
- Eliassen, A., 1962: On the vertical circulation in frontal zones. *Geophys. Publ.*, **24**, 147-160.
- Fukao, S., T. Sato, T. Tsuda, S. Kato, K. Wakasugi and T. Makihiro, 1985a: The MU radar with an active phased array system, 1: Antenna power amplifiers. *Radio Sci.*, **20**, 1155-1168.
- , —, —, —, —, and —, 1985b: The MU radar with an active phased array system, 2: In-house equipment. *Radio Sci.*, **20**, 1169-1176.
- , M. D. Yamanaka, T. Sato, T. Tsuda and S. Kato, 1988: Three-dimensional air motions over the Baiu front observed by a VHF-band Doppler radar: A case study. *Mon. Wea. Rev.*, **116**, 281-292.
- Larsen, M. G., and J. Röttger, 1991: VHF radar measurements of refractivity layer tilt angles and associated vertical-beam radial velocity corrections. *J. Atmos. Oceanic Technol.*, in press.
- , S. Fukao, O. Aruga, M. D. Yamanaka, T. Tsuda and S. Kato, 1991: A comparison of VHF radar vertical measurements by a direct vertical beam method and by a VAD technique. *J. Atmos. Oceanic Technol.*, in press.
- Mattocks, C., and R. Bleck, 1986: Jet streak dynamics and geostrophic adjustment processes during the initial stages of lee cyclogenesis. *Mon. Wea. Rev.*, **114**, 2033-2056.
- Palmer, R. D., M. F. Larsen, R. F. Woodman, S. Fukao, M. Yamamoto, T. Tsuda and S. Kato, 1990: VHF radar interferometry measurements of vertical velocity and the effects of tilted refractivity surfaces on standard Doppler measurements. *Radio Sci.*, in press.
- Sechrist, F. S., R. A. Petersen, K. F. Brill, A. J. Kruger and L. W. Uccellini, 1986: Ozone, jet streaks, and severe weather. Preprint Volume, *Second Conf. on Satellite Meteorology-Remote Sensing and Applications*, Williamsburg, VA, Amer. Meteor. Soc., 388-392.
- Uccellini, L. W., and D. R. Johnson, 1979: The coupling of upper and lower tropospheric jet streaks and implications for the development of severe convective storms. *Mon. Wea. Rev.*, **107**, 682-703.
- Wilson, D. A., and L. J. Miller, 1972: Atmospheric motion by Doppler radar. *Remote Sensing of the Troposphere*, V. E. Derr, Ed.

Agg. 1000 1000 1000 1000

Reprinted from JOURNAL OF ATMOSPHERIC AND OCEANIC TECHNOLOGY, Vol. 8, No. 6, December 1991
American Meteorological Society

**A Comparison of VHF Radar Vertical-Velocity Measurements by a Direct
Vertical-Beam Method and by a VAD Technique**

M. F. LARSEN, S. FUKAO, O. ARUGA, M. D. YAMANAKA, T. TSUDA AND S. KATO

A Comparison of VHF Radar Vertical-Velocity Measurements by a Direct Vertical-Beam Method and by a VAD Technique

M. F. LARSEN,* S. FUKAO, O. ARUGA, M. D. YAMANAKA, T. TSUDA AND S. KATO

Radio Atmospheric Science Center, Kyoto University, Kyoto, Japan

(Manuscript received 30 April 1990, in final form 8 April 1991)

ABSTRACT

Vertical-velocity measurements made by a direct vertical-beam method are compared to vertical velocities derived from VAD (velocity–azimuth display) measurements over a 27-h period. The results indicate that the two types of measurements in regions where the scatter is isotropic agree well. The largest discrepancies occur in the regions characterized by strong stratification and anisotropic or aspect-sensitive scatter. Although there are various assumptions inherent in the VAD calculations of the vertical velocities, indications are that the source of error is the aspect sensitivity, which produces effective off-vertical pointing angles in the vertical beam when the refractivity layers are tilted out of the horizontal plane. However, other additional sources of bias or error cannot be excluded.

1. Introduction

In the past, horizontal wind measurements provided by radar wind profilers have been studied in some detail in order to gain confidence in the measurement technique and to understand potential sources of bias or error. Röttger and Larsen (1989) have reviewed much of the literature and the conclusions of the various studies. Assessments of the horizontal wind-profiling capabilities have been possible in large part because other independent measurements of the same parameters are available from balloons, for example. Some investigations have also relied on tests of internal consistency in the measurements. The work of Strauch et al. (1987) is an example.

Radar measurements of vertical velocities have already been shown to have an important potential role for research applications, both in diagnostic studies and for verification, but the difficulty has been in testing the technique. There are no other techniques for measuring vertical winds over temporal and spatial scales comparable to those sampled by the radars. Comparisons between radar vertical velocities and the vertical velocities derived from objective analysis show similarities in the overall features, but the two types of data are not well enough correlated, so that the objective analysis velocities, for example, can be used to assess

bias or error in the radar data (see, e.g., Nastrom et al. 1985; Larsen et al. 1988).

It is clear, of course, that the radar measures the radial velocity of the refractivity structures in the beam, but errors in the vertical-velocity measurements will result if the structures are moving with a velocity that is different from the air motion. Biases can also occur if the scatterers are not distributed uniformly throughout the sampled volume. May et al. (1988), for example, have discussed biases in the horizontal wind estimates that can be produced by the effect of thin scattering layers within the range volume, and Röttger and Larsen (1989) have reviewed the known biases and errors that can be introduced in the measurements. Recently Röttger and Ierkic (1985) and Larsen and Röttger (1990) have shown that tilted refractivity layers can cause errors in the vertical-velocity measurements made with longer-wavelength radars, which are subject to aspect-sensitivity effects. Since the strongest scatter will come from the direction perpendicular to the aspect-sensitive refractivity layers, the largest contribution to the received signals will come from an off-vertical angle within the beamwidth, when the refractivity layers are inclined with respect to the horizontal plane. The result is that a component of the horizontal wind is measured along with the projection of the vertical component along the effective beam direction. Although the tilt angles are small and have magnitudes of only $\sim 1^\circ$ – 2° (Larsen and Röttger 1991), the errors can still be large because of the small magnitude of the vertical velocities in comparison to the horizontal winds. Higher-frequency radars do not suffer from aspect sensitivity effects and, therefore, may avoid some

* On leave from the Department of Physics and Astronomy, Clemson University, Clemson, South Carolina.

Corresponding author address: Dr. Miguel F. Larsen, Dept. of Physics and Astronomy, Clemson University, Clemson, SC 29631.

of the problems associated with VHF vertical-velocity measurements. However, the higher-frequency signals are dominated by precipitation scatter even when the rainfall rates are light (see, e.g., Larsen and Röttger 1986). Therefore, the higher-frequency radar systems cannot be used to measure the vertical air motions directly in many of the more interesting situations.

In this article, we present the results of a study of the internal consistency in VHF radar measurements of vertical velocities made over a period of almost 27 h when an active frontal system passed the radar site. The MU radar is a phased array system similar in many respects to the Doppler radar wind profilers that are expected to be used operationally, although with considerably more flexibility in beam-steering capability and receiving antenna diversity. We have tested the internal consistency of the vertical-velocity data by comparing the vertical winds inferred from a 15-beam-direction VAD with the radial velocity measured directly with a vertical beam. Since the off-vertical measurements at 15° zenith angle do not exhibit aspect sensitivity effects, the errors or biases introduced by the latter should be evident when the two types of measurements are compared, as long as the errors in the measurements are smaller than the velocity differences introduced by the aspect-sensitivity effects. The uncertainties in the measurements will be discussed in more detail in section 5.

In the next section, we describe the details of the experimental setup. Section 3 deals with the meteorological conditions for the period of observation. The vertical-velocity data are presented in section 4, and the implications of the results are discussed in section 5.

2. Details of the experiment

a. Description of the MU radar system

The MU radar is located at Shigaraki near Kyoto, Japan (34.85°N , 136.10°E), as shown in Fig. 1, and is operated by the Radio Atmospheric Science Center of Kyoto University as a dedicated facility for atmospheric observations. The radar is a 46.5-MHz system using an active phased array (Fukao et al. 1980). The antenna is composed of 475 yagis and an equivalent number of solid-state power amplifiers or transmitter-receiver (TR) modules (Fukao et al. 1985a,b). Each yagi antenna is driven by a TR module with peak output power of 2.4 kW. All the yagi antennas and TR modules are grouped into 25 subarrays in such a way that each group of 19 yagis and associated electronics constitutes one subarray. The nominal peak and average radiated power are 1000 and 50 kW, respectively. The beam can be steered in steps of 5° in azimuth and 1° in zenith angle anywhere within 30° of zenith from pulse to pulse. The basic parameters of the system are given in Table 1.

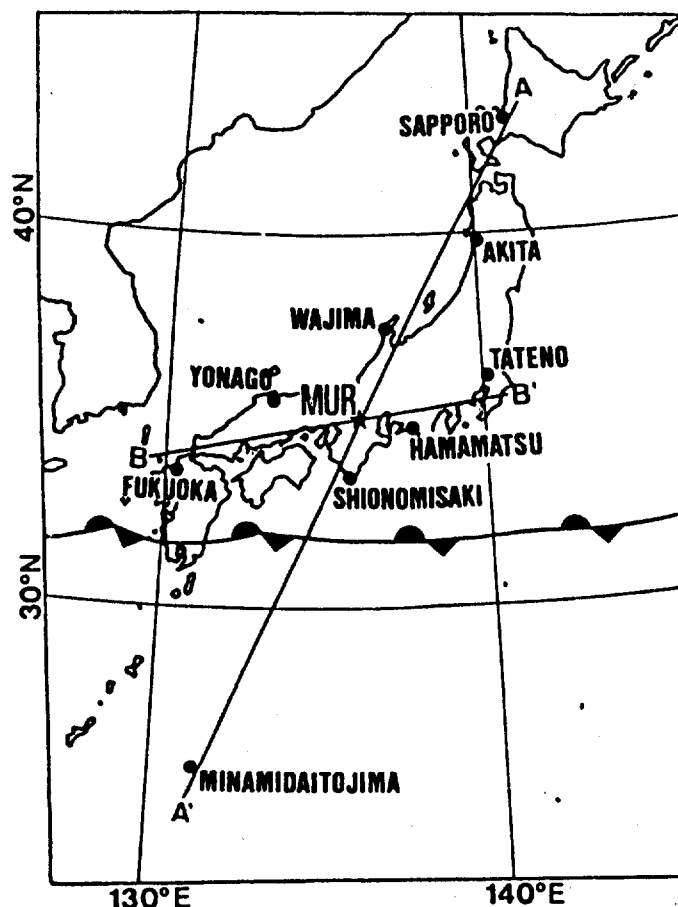


FIG. 1. Location of the MU radar (MUR) and the rawinsonde stations surrounding the radar site.

b. Methods for measuring vertical velocities

The radar was operated in a cycle that consisted of measurements along a vertical beam direction followed by measurements at a zenith angle of 15° at 15 positions spaced around the azimuth circle. The beam-steering in azimuth is limited to integral increments of 5° so that the separation between adjacent beam positions was either 20° or 25° rather than the 24° increment, which would have produced evenly spaced positions. The specific beam-pointing directions are listed in Table 2, along with other specific radar parameters used in the experiment. The Doppler spectra corresponding to a 65-s sample for the vertical-beam measurements were calculated with a spectral resolution corresponding to 12.3 cm s^{-1} , and the frequency offset of a Gaussian curve fitted nonlinearly in the least-squares sense to each spectrum was taken to be the mean Doppler shift in the radial direction, which was interpreted as being due to the vertical air velocity. The Doppler spectra corresponding to 65-s samples were also calculated for each of the 15 off-vertical beams, and Gaussian curves were fitted in the same way as was done for the vertical-beam measurements. The radial velocities were then combined in order to

TABLE 1. Basic parameters of the MU radar (Fukao et al. 1985a).

Radar system:	Monostatic pulse radar; active phased array system
Operational frequency:	46.5 MHz
Antenna:	Circular array of 475 crossed yagi antennas
Aperture:	8330 m ² (103-m diameter)
Beamwidth:	3.6° (half power for full array)
Steerability:	Steering is completed in each IPP
Beam directions:	1657; 0°–30° off-zenith angle
Transmitter:	475 solid-state amplifiers (TR modules) each with output power of 2.4 kW peak and 120 W average
Peak power:	1000 kW (max)
Average power:	50 kW (duty ratio 5%) maximum
Bandwidth:	1.65 MHz (max) (pulse width: 1–512 μ s variable)
IPP:	400 μ s to 65 ms (variable)
Receiver:	
Dynamic range:	70 dB
A/D converter:	12 bits \times 8 channels
Pulse compression:	Binary phase coding up to 32 elements (Barker and complementary codes presently in use)

carry out a VAD (velocity–azimuth display) analysis (see, e.g., Wilson and Miller 1972; or Browning and Wexler 1972). Note that the beam was being moved from pulse to pulse, so that the 65-s spectra for all 16 different beam directions correspond to the same 65-s period.

The VAD sampling scheme is shown schematically in Fig. 2. The horizontal wind vector is U , and the vertical-velocity component is w . The azimuth angle ϕ is measured clockwise from north. In the ideal case, the radial velocities measured around the azimuth circle will lie on a sine curve as shown in the lower part of the figure. The amplitude of the sine function is equal to the horizontal wind speed, and the phase is related directly to the wind direction. The offset of the sine curve from zero on the vertical axis is designated C_0 . If the winds are uniform across the sampled area,

$$C_0 = w \cos \theta \quad (1)$$

where θ is the zenith angle. If the vertical velocity is nonzero and varies with height, as is generally the case, the divergence of the horizontal wind will also be nonzero, at least in some range of heights. Assuming a linear variation in the wind field then gives the expression

$$C_0 = \left[w + \frac{z}{2} \tan^2 \theta (\nabla_h \cdot U) \right] \cos \theta \quad (2)$$

for the offset. Here z is the height along the vertical axis, and $\nabla_h \cdot U$ is the divergence of the horizontal wind in the horizontal plane. The vertical velocity has been assumed to be uniform over the sampling area. Equation (2) has been derived by various authors, among them Wilson and Miller (1972) and Doviak and Zrnić (1984, p 284). In this experiment, the diameter of the VAD circle was ~ 5.4 km at the 10-km altitude.

The contributions of the vertical velocity and the divergence to the measured offset cannot be separated without further assumptions. The simplest assumption is to ignore the variation in the horizontal wind and attribute all of the offset to the vertical velocity. However, the divergence term can be large, and its effect increases with height as shown by the proportionality of the second term in the parentheses to z in Eq. (2). The contribution from the horizontal flow gradients increases with height because the horizontal separation between the beams increases. The divergence and vertical-velocity parameters can be calculated directly if VAD measurements are made at two or more different zenith angles θ since we then end up with two equations and two unknowns for each height sampled. The latter method has become known as the EVAD (extended velocity–azimuth display) technique.

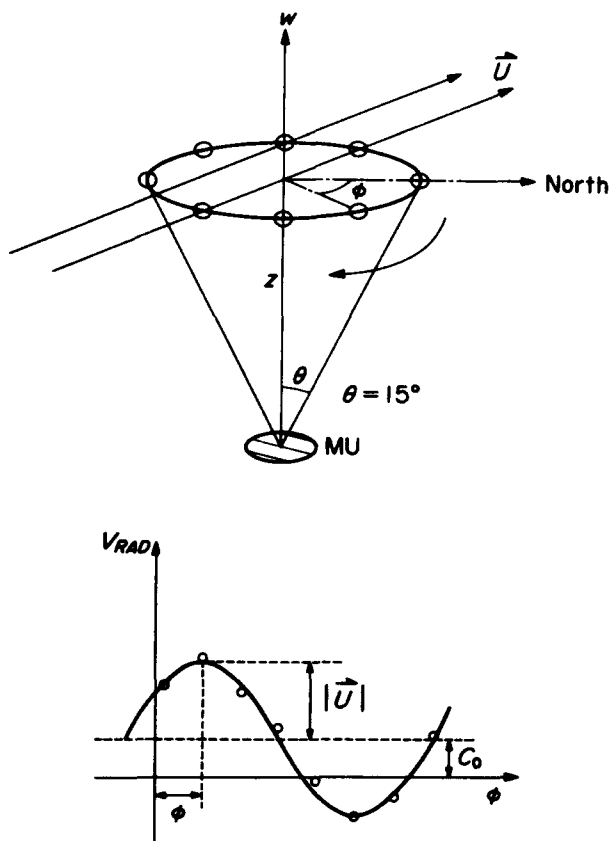
The two contributions cannot be separated unambiguously in our case, but a good approximation can be used to solve the equations. Specifically, we use the mass continuity equation and assume that the density is stationary in time locally and that the medium is horizontally stratified. Then, the mass continuity equation becomes

$$\nabla_h \cdot \rho U = \rho \nabla_h \cdot U = - \frac{\partial}{\partial z} (\rho w) \quad (3)$$

where ρ is the atmospheric density. We can substitute in Eq. (2) to get

TABLE 2. Observational parameters for VAD observations.

Altitude range:	5–15 km		
Height resolution:	150 m		
Pulse coding:	16-bit complementary code		
IPP:	400 μ s		
Coherent integrations:	8		
Incoherent integrations:	10		
Beam directions:	16		
(zenith angle, azimuth)	(0, 0)		
	(15, 0)	(15, 25)	(15, 50)
	(15, 70)	(15, 95)	(15, 120)
	(15, 145)	(15, 170)	(15, 190)
	(15, 215)	(15, 240)	(15, 265)
	(15, 290)	(15, 310)	(15, 335)



$$C_0 = [w + \frac{z}{2} \tan^2 \theta (\vec{v} \cdot \vec{U})] \cos \theta$$

FIG. 2. Schematic diagram showing the sampling scheme for the VAD analysis and the curve of radial velocity as a function of azimuth angle ϕ . The zenith angle is θ , and ϕ is measured from the north. The offset of the sine curve from the horizontal axis is designated C_0 , which can be shown to depend on both the vertical velocity and the divergence.

$$\frac{\partial}{\partial z}(\rho w) - \frac{2}{z} \cot^2 \theta (\rho w) = -\frac{2}{z} \frac{\cot^2 \theta}{\cos \theta} (\rho C_0) \quad (4)$$

where C_0 , ρ , and w are all functions of the height z . At each height where the measurements are made, the VAD analysis yields a C_0 value. Using a profile of the density ρ derived either from radiosonde data or a model, the equation can be solved numerically for the vertical velocity w at each height. Test integrations based on radiosonde data from Hamamatsu and Shinomizaki were carried out. The locations of the stations relative to the MU radar are shown in Fig. 1. The results indicated that the calculated velocities are not very sensitive to the changes in density that can be expected realistically. Therefore, the final calculations were made with a simple density profile based on an isothermal atmosphere with a scale height of 8 km. The latter provided a sufficiently accurate approximation for these

purposes, and the complications associated with interpolating the radiosonde measurements to provide profiles representative of the specific conditions at the radar site were avoided.

In this case, it is assumed that as a boundary condition the vertical velocity is zero at an upper height of 14 km, which is close to the upper limit where reliable measurements exist. The chosen boundary condition is not necessarily realistic but is preferable to the alternatives that would include setting the vertical velocity to zero at the lower boundary, that is, at the 5-km altitude, or at some arbitrary height within the sampled range. Another option would be to impose a nonzero vertical velocity somewhere. The assumed boundary condition is somewhat arbitrary, but test integrations show that its impact extends only to within approximately 1 km of the height where the condition is imposed. The point is discussed further in section 4. The solution to Eq. (4) is then known to have the integral form

$$(\rho w)_{z'} = \frac{\mu z'^{\mu}}{\cos \theta} \int_{z'}^1 (\rho C_0) z'^{-(\mu+1)} dz' \quad (5)$$

where z' is the height normalized to be unity at the altitude where w is zero. The parameter μ is defined as $\mu = 2 \cot^2 \theta$ where θ is the zenith angle.

3. Meteorological conditions

The meteorological conditions for the period from 2100 LST 22 April until 2100 LST 23 April 1988, which covers most of the period when the observations were carried out, are summarized by the 500-mb and surface charts shown in Fig. 3. The islands of Japan are shown as the heavily shaded regions on the maps. At 2100 LST 22 April, a cold front was aligned parallel to the Pacific coast of Japan from southwest to northeast. The frontal boundary's intersection with the surface was estimated to be approximately 100 km off the coast. As time progressed through the period, the front continued to move toward the southeast. The surface maps at 2100 LST 22 April and at 0900 LST 23 April both show that there is little rainfall at the center of the front along its southwest to northeast extent, presumably because of a lack of moisture during the passage across the mountainous terrain of the islands. The upper-level 500-mb maps for the period show the trough associated with the surface feature. The center of the trough is almost due west of the island of Hokkaido at 2100 LST 22 April. The front at the leading edge of that trough is more or less parallel to and located above the Japanese islands at the latter time. The system then moves across Japan and past the MU radar in the course of the observation interval.

More details are shown in Fig. 4, which represents a vertical cross section at 0900 LST 23 April along the line indicated as AA' in Fig. 1. The height-range cov-

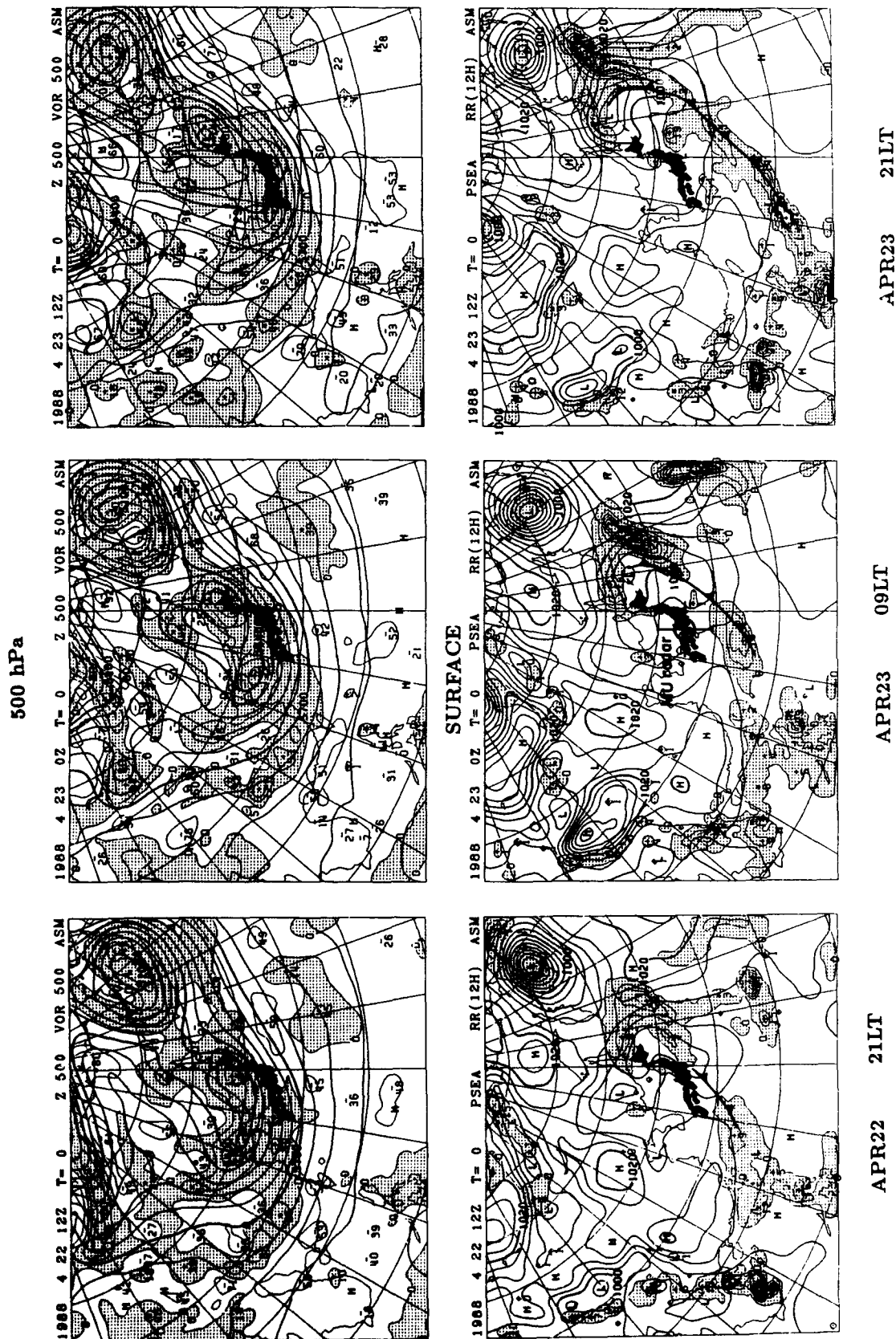


FIG. 3. Surface and 500-mb charts for the period from 1200 UTC 22 April to 1200 UTC 23 April 1988. The surface charts show contours of sea level pressure and rainfall rate for 12 h in millimeters (shaded). The upper-level charts show geopotential heights and vorticity. Regions of cyclonic vorticity have been shaded. The Japanese islands are indicated by the heavy shading.

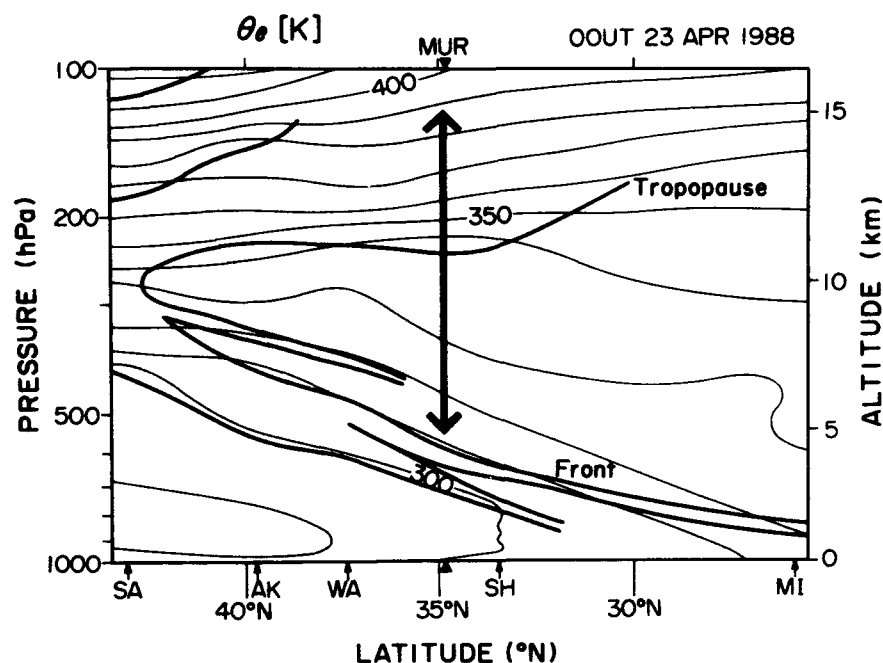


FIG. 4. Vertical cross section of equivalent potential temperature in a plane perpendicular to the front. The height range covered by the MU radar observations is shown by the heavy arrows.

erage of the MU radar is shown by the heavy vertical arrows that also serve to indicate the location of the MU radar relative to the radiosonde stations, which are Minamidaitojima (MI), Shionomisaki (SH), Wajima (WA), Akita (AK), and Sapporo (SA). The contours of equivalent potential temperature clearly show the location of the tropopause. The front is also evident as contours that slope from the tropopause to the surface. A more detailed analysis of the radiosonde data has allowed us to estimate the location of the frontal boundary and the tropopause more exactly than is possible with the equivalent potential temperature contours alone based on the vertical variations in the temperature, humidity, and wind shear. The inferred positions of the features are indicated by the heavy lines. There is an indication that the frontal boundary splits, as shown by the separation in the heavy lines. The data shown here do not represent conclusive evidence of tropopause folding since analysis of the potential vorticity for the period would be necessary to establish that the latter had occurred. However, Nastrom et al. (1989) have shown, based on data obtained with the Flatland radar and radiosonde data from the surrounding region, that tropopause folding occurred in every case observed with the radar for synoptic conditions similar to those shown here and for reflectivity patterns similar to those that are discussed next.

The reflectivities measured in the vertical beam for the period are shown in Fig. 5. Again, the tropopause location is evident as an enhancement in the reflectivities located just above 12 km at the beginning of the

period. Later, the tropopause descends in a pattern similar to that shown in Fig. 4.

The ratio of the reflectivity in the vertical beam to the reflectivity in the off-vertical beams is shown in the contour plot in Fig. 6. Darker shading indicates higher ratios, and no shading indicates a ratio close to one. The ratio is high at all times in the stratosphere, showing the large degree of anisotropy or aspect sensitivity in the scatter. The region in the warm sector above the frontal boundary is characterized by ratios close to one, indicating that there is little aspect sensitivity. There is also a region below 7 km between 0000 and 1200 LST 23 April that has high ratios or large aspect sensitivity and is most likely associated with the frontal inversion.

4. Vertical-velocity measurements

As described in section 2, the vertical velocities were derived in two different ways. One measurement was directly from the Doppler shift in the vertical beam. The other method involved calculating the offset parameter C_0 for each range gate, using a density profile for an isothermal atmosphere as a representative profile, and integrating Eq. (5) numerically. Sixty consecutive values were averaged to produce the hourly profiles, actually 65-min profiles, shown in Fig. 7. The dashed lines show the vertical velocities measured directly (W_D), while the solid lines show the values derived from the VAD measurements below 14 km (W_V). The lowest altitude is near 6 km and the upper height

ECHO POWER $(A_z, Z_e) = (0, 0)$
22-23 APR 1988

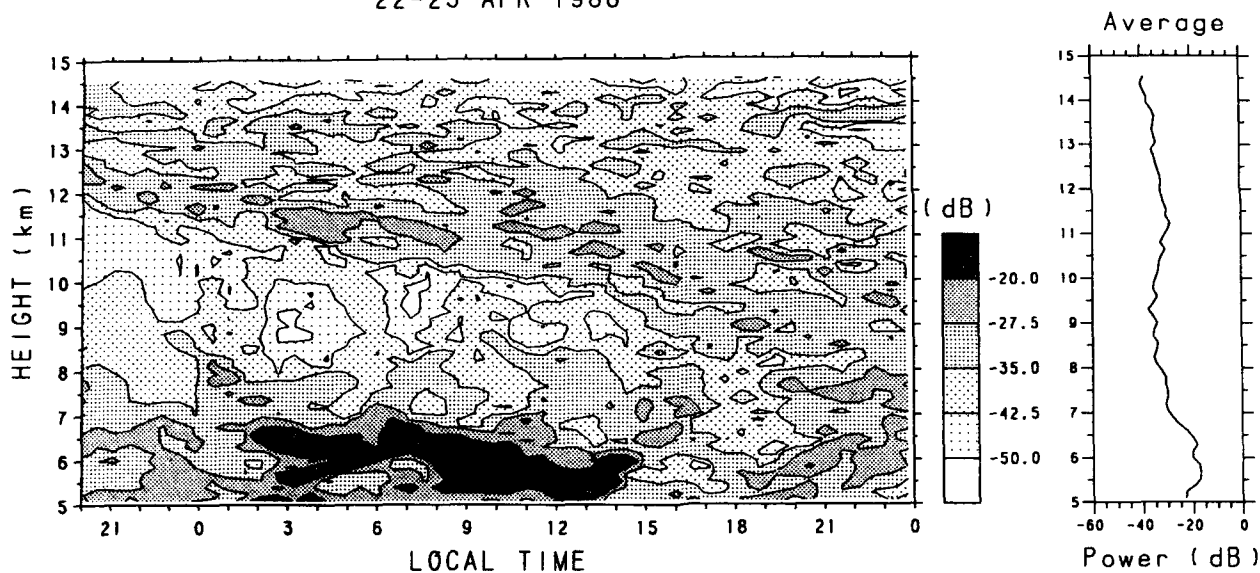


FIG. 5. Contours of reflectivity measured in the vertical beam with the MU radar for the period from 2100 LST 22 April to 2100 LST on 23 April 1988.

where reliable data was obtained was near 14 km. The integration of the VAD data effectively results in some filtering of the vertical-velocity curves since the value at any given height will depend on the C_0 values over

a range of heights above. A zero-phase-shift low-pass filter with a 1-km cutoff was therefore applied to the vertical-beam data to provide a more direct comparison.

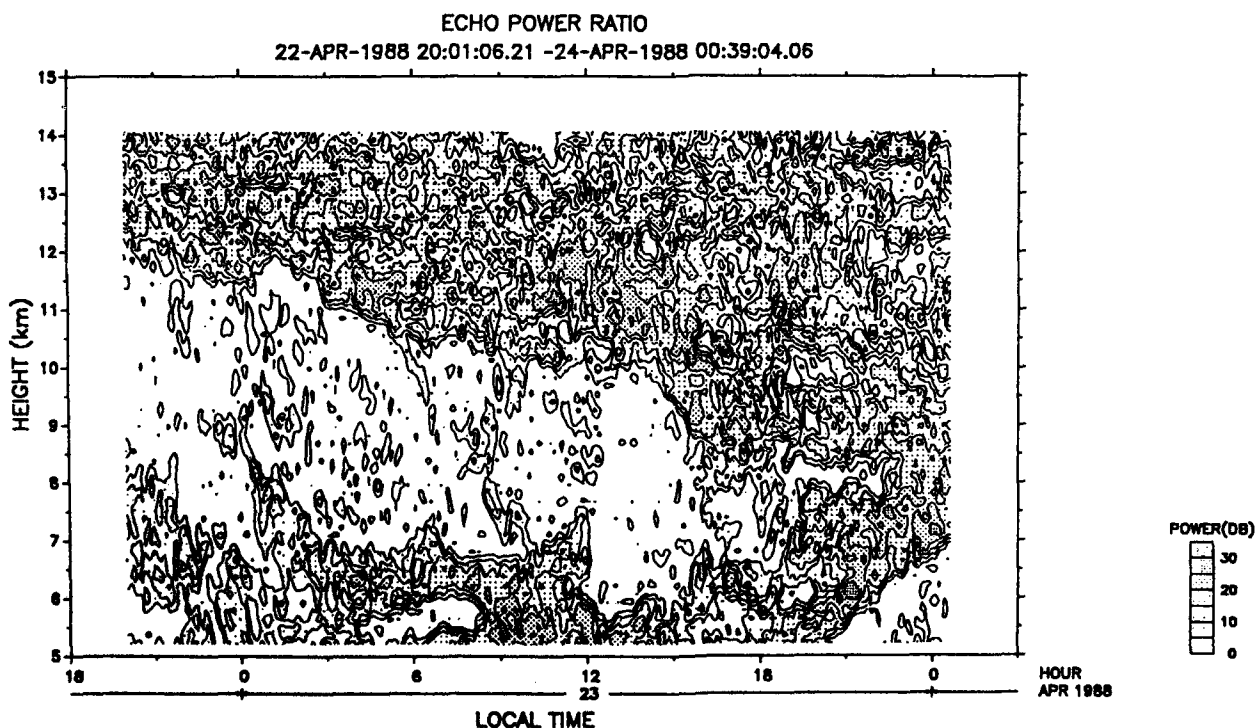


FIG. 6. Contours of the ratio of vertical to off-vertical reflectivity as a function of height and time. The higher ratio values have been shaded.

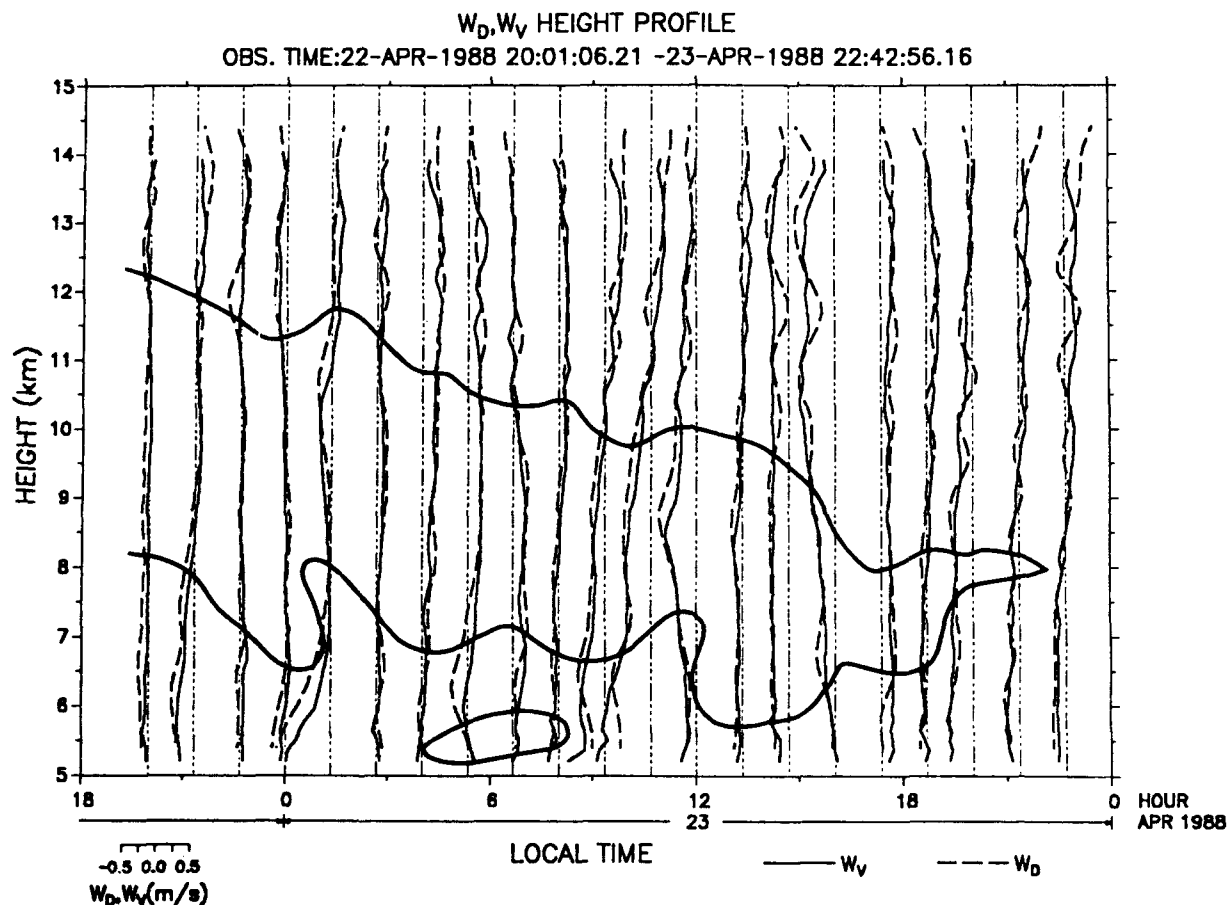


FIG. 7. Profiles of the vertical velocities derived from the vertical-beam measurements (dashed lines) and from the VAD analysis (solid lines). The boundary between high and low values of vertical to off-vertical reflectivity ratios has been indicated by the heavy line, which corresponds to the transition between shaded and unshaded values in Fig. 6.

There is no consistent pattern in the vertical velocities of the type that might be expected. For example, periods of ascent and subsidence alternate in the warm sector of the front, and, although the largest vertical velocities generally occur in the troposphere, there is no significant change in the characteristics of the vertical-velocity profiles across the transition from the troposphere to the stratosphere. Similar characteristics of the vertical circulations near frontal zones have been noted earlier by Larsen et al. (1988) and Fukao et al. (1988).

An obvious feature of the curves is that the two measurements agree well during some periods and in some height ranges, but disagree substantially at other times and in other height ranges. Closer examination of the transition heights from good to poor agreement shows that there is a correlation between the regions where the two measurements agree and the regions in which the scattering is more isotropic, as inferred from the contours in Fig. 6. With the exception of the profiles between 0900 and 1200 LST 23 April, the agreement is good at all heights in the isotropic scattering region.

The discrepancies in the lower stratosphere are over 100% of the magnitude of the vertical velocity at some heights.

Figure 8 shows a scatterplot of the direct versus the VAD vertical velocity for all heights between 6 and 14 km. The points lie close to a 45° line as expected, but there is spread in the data. The standard error S for the two measurements, defined by the equation

$$S^2 = \frac{1}{N-2} \sum (W_D - W_V)^2 \quad (6)$$

is 6.9 cm s^{-1} . Here N is the total number of vertical velocity values, and only those values from heights below 13 km were included in order to exclude the velocities affected significantly by the imposed boundary condition.

The data were further divided into two height ranges. The first covers the lower altitudes that correspond roughly to the tropospheric heights, and the second covers the upper altitudes that correspond to heights near the tropopause region and in the lower strato-

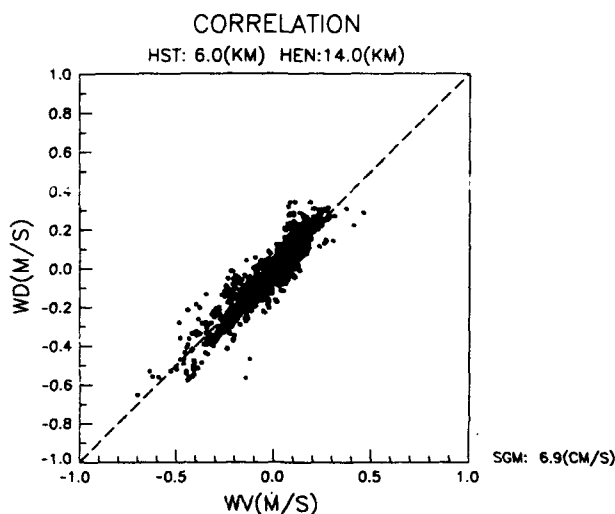


FIG. 8. Scatter diagram of the direct versus the VAD vertical velocities.

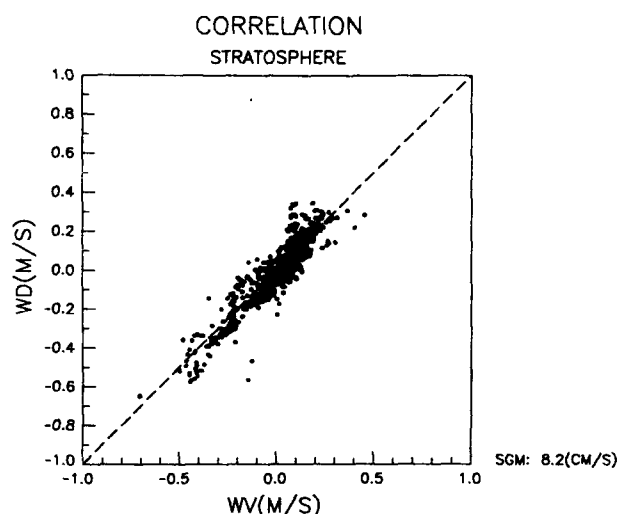


FIG. 10. Similar to Fig. 7, but only for the stratospheric data.

sphere. The boundary between the two height ranges was chosen as a line sloping downward from 12 km at 2000 LST 22 April to 8 km at 0000 LST 24 April. Figure 6 shows that the chosen cutoff heights give a good approximation to the boundary between high and low aspect-sensitivity regions, although the lower height range still includes some areas with high ratios of vertical to off-vertical reflectivities.

Figure 9 represents the scatterplot for the tropospheric velocities. In the troposphere, the spread is smaller than in the overall dataset and corresponds to an error of 5.3 cm s^{-1} . The stratospheric data shown in Fig. 10 have a larger spread corresponding to an error of 8.2 cm s^{-1} . Another measure of the agreement between the measurements is the correlation coefficient,

which was found to be 0.96 for the tropospheric data and 0.88 for the stratospheric data.

The average tropospheric velocity for the period was -5.0 cm s^{-1} for the VAD vertical velocity and -6.3 cm s^{-1} for the direct velocity. The corresponding stratospheric velocity averages were $+0.8$ and $+1.4 \text{ cm s}^{-1}$, respectively. The averages for the entire dataset were -2.5 and -2.1 cm s^{-1} for the direct and VAD vertical velocities, respectively.

The differences between the measurements will only be meaningful if the measurement errors are sufficiently small. The expected accuracy of a 1-h average radial velocity is approximately 1 cm s^{-1} , as discussed by Fukao et al. (1988). The standard errors, correlations, and averages are based on approximately 27 h of data, so that the uncertainties in those values will be approximately 20% of the uncertainty in the individual 1-h values.

Another concern is associated with the upper boundary condition imposed in the VAD analysis. There is no particular reason to expect that the vertical velocity will be zero at 14 km. Therefore, constraining the vertical velocity to vanish at that height is unrealistic. However, the effect of the boundary condition diminishes rapidly with height. Test integrations carried out in connection with the data analysis have shown that the calculated vertical velocities attain 90% of their true magnitudes within 1 km of the upper boundary.

5. Discussion

The fact that the regions of largest discrepancies between the direct and VAD measurements of the vertical velocities correspond to the regions of greatest anisotropy in the scatter, namely, strongest aspect sensitivity effects, indicates that the source of the differences is associated with the layered refractivity structure. When

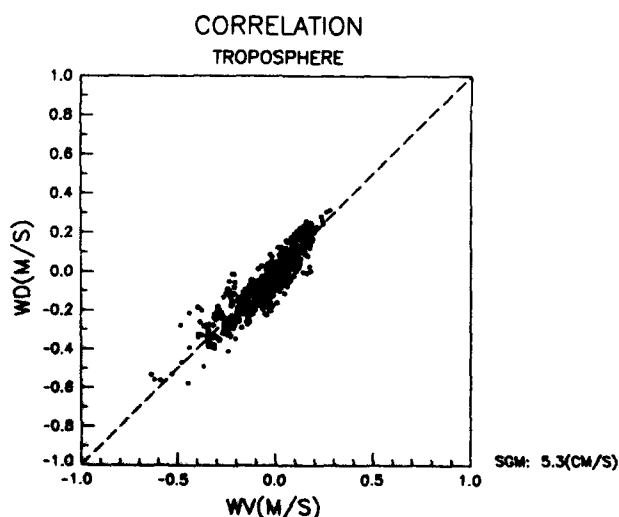


FIG. 9. Similar to Fig. 7, but only for the tropospheric data.

aspect-sensitivity effects are important, the largest contribution to the received signals will come from a direction perpendicular to the layers. Therefore, if the layers are tilted, the strongest signals in the vertical beam will come from a slightly off-vertical direction, so that the radial velocity measurement has a contribution from both the true vertical velocity and the horizontal velocity. The situation is shown schematically in Fig. 11. Röttger and Ierkic (1985) first suggested that such effects could contaminate the direct vertical-velocity measurements, and they analyzed a short dataset to show that the magnitude of the errors could be comparable to the magnitude of the vertical velocity. Larsen and Röttger (1990) have also shown that there is a strong correlation between the layer tilt angles and the vertical-beam radial velocities that they measured. Since the VAD measurements are made at an off-zenith angle large enough, so that the direction perpendicular to the layers is outside the beam, aspect sensitivity does not affect those measurements.

Horizontal gradients in the flow can produce errors in the VAD analysis, particularly if the gradients persist for extended periods. The terrain around the MU radar is mountainous, and the winds aloft varied from $\sim 20 \text{ m s}^{-1}$ at the 5-km altitude to a peak value of $\sim 40 \text{ m s}^{-1}$ at the 12-km altitude, suggesting that orographic waves were likely to be generated above the MU radar during the observation interval. Indeed, some of the oscillations in the vertical-velocity profiles shown in Fig. 7 may be due to orographic effects. The question then is whether the differences between the direct and VAD vertical velocities can be accounted for by horizontal gradients associated with the wave structure.

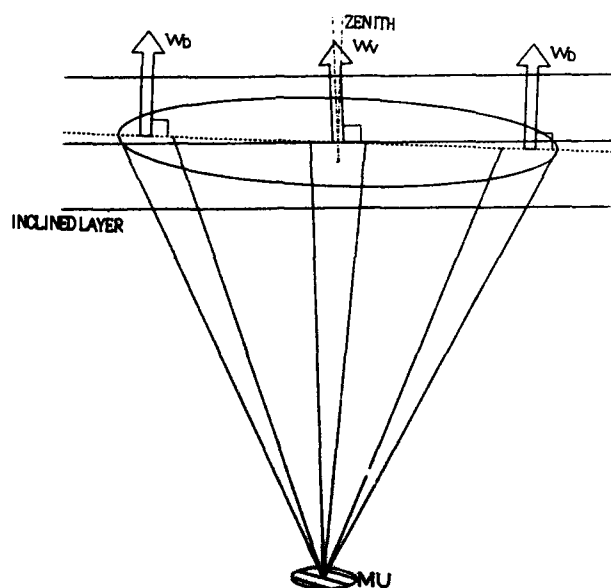


FIG. 11. Schematic diagram showing the effect of a tilted refractivity layer on the vertical-beam vertical-velocity measurements.

Fukao et al. (1988) have given a more detailed discussion about the VAD fitting procedure and associated errors. Their Fig. 2 shows examples of the radial velocities obtained from the VAD measurements, and those curves are also representative of the data presented here. The degree to which the radial velocities obtained from the VAD deviate from a sinusoid is an indication of the presence of smaller-scale structure. The horizontal wind fluctuations were found to be less than a few meters per second, indicating that the primary scale sizes were larger than the VAD circles. Also, the fact that the discrepancies are smaller in those regions where the scatter is isotropic and larger in those regions where aspect sensitivity effects are important, suggests that the scattering mechanism is responsible for the differences rather than wave-induced horizontal flow gradients.

There are other potential sources of error, although it is believed that these are smaller in magnitude. The VAD measurement is subject to several assumptions; namely, that the local time derivative of the density is zero, and that there are no significant temporal variations in the winds during the sampling period. Unfortunately, a quantitative analysis of the effect of these errors cannot be carried out with the data available.

In addition to the inclined refractivity layer effect, another potential source of error in the direct vertical-beam vertical-velocity measurements is due to the possibility that the refractivity layers are moving with a velocity other than the air velocity. The latter could occur if the refractivity structures are generated at a particular phase of a wave propagating through the medium, for example. There is no direct test for such an effect with the data that are available in this study.

The differences between the radial velocities measured with the vertical beam (dashed lines) and the vertical velocities derived from the VAD analysis (solid lines) in Fig. 7 are for the most part associated with fluctuations in the vertical-beam velocities characterized by vertical wavelengths of a few kilometers. Waves propagating through the lower stratosphere will likely produce vertical displacements of the nearly horizontal refractivity surfaces. The effective radar beam position is then expected to oscillate as the direction perpendicular to the layers moves back and forth within the beam, as discussed by Gage et al. (1981). Röttger et al. (1990) have seen evidence of such an effect in observations of layer tilt angles made with the Chung-Li VHF radar located in Taiwan.

Our analysis indicates that there may be biases or errors in direct vertical-beam vertical-velocity measurements and that there may be advantages to VAD vertical-velocity measurements. Peterson and Balsley (1979) analyzed a short dataset obtained with the Poker Flat radar in which the vertical velocities were measured with the direct method, the VAD technique, and the elevation scan method. They concluded that the direct method was preferable, in seeming contradiction

to our conclusions. However, the total observation period for each of the different techniques was only 20–30 min and the time between each of the observations was 30–50 min. Thus, the observation period was short, and the techniques were not applied simultaneously. Furthermore, the divergence term was not incorporated in the VAD analysis so that the derived velocities were based on Eq. (1) rather than the more general Eq. (2). The primary reason for preferring the direct measurements was the qualitative one that there were fewer oscillations in the vertical profiles.

6. Conclusion

The flexible beam-steering capabilities of the MU radar have made it possible to compare direct vertical-beam vertical-velocity measurements with the vertical velocities inferred from a VAD analysis. The agreement has been found to be excellent in regions of the atmosphere where the scattering is isotropic, but large differences have been found in height ranges where aspect sensitivity or strongly anisotropic scatter dominates. The results of this study, as well as those from the studies by Röttger et al. (1990) and Larsen and Röttger (1991), indicate that care has to be taken in using and interpreting longer-wavelength wind profiler vertical-velocity data. Application of the VAD technique is one means for circumventing the aspect sensitivity problems, but measurements in a number of directions are needed and at least two different zenith angles are necessary to avoid the assumptions and computational complexity inherent in using Eqs. (4) or (5). Operational wind profilers, and even most phased array research radar-profiler systems, are not likely to have the flexibility required to implement VAD measurements of vertical velocities. Larsen and Röttger (1991) have shown how to apply a method for correcting the vertical-beam velocities by using simultaneous measurements of layer tilt angles and horizontal velocities. The technique is fairly simple in principle, but requires at least three spaced receiving antennas and the appropriate electronic hardware to sample each. Most of the systems built specifically as Doppler systems cannot be readily adapted to spaced antenna measurements.

Our study, as well as the other recent studies previously cited, indicate that there are inherent difficulties in making vertical-velocity measurements, but such measurements are, nonetheless, possible. Clearly, the vertical-beam vertical velocities bear a strong resemblance to the VAD velocities, as shown by the curves in Fig. 7. However, the likelihood that there are biases and significant errors in certain height ranges has to be kept in mind in applying or interpreting the data in specific cases. Also, methods for either correcting the data or assessing its reliability have now been suggested. For example, the spaced antenna capability can be incorporated in future systems to make vertical velocity corrections possible. Those Doppler systems already

in operation will generally have two or more off-vertical beams along with a zenith-pointing beam. Our results suggest that the ratio of the vertical to the off-vertical reflectivity can be used as an indicator of the reliability of the data.

Acknowledgments. MFL received support from the Ministry of Education, Research, and Culture of Japan and from AFOSR Contract F49620-88-C-0121 during the course of the study.

REFERENCES

- Browning, K. A., and R. Wexler, 1972: A determination of kinematic properties of a wind field using Doppler radar. *J. Appl. Meteor.*, **7**, 105–113.
- Doviak, R. J., and D. S. Zrnić, 1984: *Doppler Radar and Weather Observations*. Academic Press, 458 pp.
- Fukao, S., S. Kato, T. Aso, M. Sasada and T. Makihiro, 1980: Middle and upper atmosphere radar (MUR) under design in Japan. *Radio Sci.*, **15**, 225–231.
- , T. Sato, T. Tsuda, S. Kato, K. Wakasugi and T. Makihiro, 1985a: The MU radar with an active phased array system. 1: Antenna power amplifiers. *Radio Sci.*, **20**, 1155–1168.
- , T. Tsuda, T. Sato, S. Kato, K. Wakasugi and T. Makihiro, 1985b: The MU radar with an active phased array system. 2: In-house equipment. *Radio Sci.*, **20**, 1169–1176.
- , M. D. Yamanaka, T. Sato, T. Tsuda and S. Kato, 1988: Three-dimensional air motions over the Baiu front observed by a VHF-band Doppler radar: A case study. *Mon. Wea. Rev.*, **116**, 281–292.
- Gage, K. S., D. A. Carter and W. L. Ecklund, 1981: The effect of gravity waves on specular echoes observed by the Poker Flat MST radar. *Geophys. Res. Lett.*, **8**, 599–602.
- Larsen, M. F., and J. Röttger, 1986: A comparison of thunderstorm reflectivities measured at VHF and UHF. *J. Atmos. Oceanic Technol.*, **4**, 151–159.
- , and —, 1991: VHF radar measurements of in-beam incidence angles and associated vertical-beam radial velocity corrections. *J. Atmos. Oceanic Technol.*, **8**, 477–490.
- , —, and T. S. Dennis, 1988: A comparison of operational analysis and VHF wind profiler vertical velocities. *Mon. Wea. Rev.*, **116**, 48–59.
- May, P. T., S. Fukao, T. Tsuda, T. Sato and S. Kato, 1988: The effect of thin scattering layers on the determination of wind by Doppler radars. *Radio Sci.*, **23**, 83–94.
- Nastrom, G. D., W. L. Ecklund and K. S. Gage, 1985: Direct measurement of large-scale vertical velocities using clear-air Doppler radars. *Mon. Wea. Rev.*, **113**, 708–718.
- , J. L. Green, M. R. Peterson and K. S. Gage, 1989: Tropopause folding and the variability of the tropopause height as seen by the Flatland VHF radar. *J. Appl. Meteor.*, **28**, 1271–1281.
- Peterson, V. L., and B. B. Balsley, 1979: Clear air Doppler radar measurements of the vertical component of wind velocity in the troposphere and stratosphere. *Geophys. Res. Lett.*, **6**, 933–936.
- Röttger, J., and M. F. Larsen, 1989: UHF/VHF radar techniques for atmospheric research and wind profiler applications. *Radar in Meteorology*, D. Atlas, Ed., Amer. Meteor. Soc., 235–281.
- , C. H. Liu, C. J. Pan and I.-J. Fu, 1990: Spatial interferometer measurements with the Chung-Li VHF radar. *Radio Sci.*, **25**, 503–515.
- Strauch, R. G., B. L. Weber, A. S. Frisch, C. G. Little, D. A. Merritt, K. P. Moran and D. C. Welsh, 1987: The precision and relative accuracy of profiler wind measurements. *J. Atmos. Oceanic Technol.*, **4**, 563–571.
- Wilson, D. A., and L. J. Miller, 1972: Atmospheric motion by Doppler radar. Chapter 13, *Remote Sensing of the Troposphere*, V. E. Derr, Ed., U.S. Department of Commerce, NOAA, (13)1–(13)34.

An Analysis Technique for Deriving Vector Winds and In-Beam Incidence Angles from Radar Interferometer Measurements

M. F. LARSEN,* R. D. PALMER, S. FUKAO, R. F. WOODMAN,** M. YAMAMOTO, T. TSUDA, AND S. KATO

Radio Atmospheric Science Center, Kyoto University, Uji, Japan

(Manuscript received 29 October 1990, in final form 8 April 1991)

ABSTRACT

We present a method for deriving horizontal velocities, vertical velocities, and in-beam incidence angles from radar interferometer data. All parameters are calculated from the slope and intercept of straight lines fitted in a least-squares sense to the variation of the signal phase as a function of radial velocity for each pair of receiving antennas. Advantages of the method are that the calculations are computationally fast and simple, and the analysis leads to relatively simple expressions for the uncertainty in the velocity measurements.

1. Introduction

The radar interferometer technique has not seen widespread use in the field of radar meteorology, but the results of a number of studies have been described in the literature (e.g., Farley et al. 1981; Röttger and Ierkic 1985; Adams et al. 1986; Kudeki 1988; Kudeki et al. 1989; Röttger et al. 1990; Palmer et al. 1990). Most applications of the method have focused on locating localized scatterers within a larger volume sampled by the radar. A by-product of the analysis is usually the velocity of either a single scatterer or a number of scatterers. A minimum requirement for interferometry is that there must be at least two spatially separated receiving antennas, although three antennas are preferable so that two nonparallel baselines can be formed. The imaging Doppler interferometer technique developed by Adams et al. (1986) uses many receiving antennas along each of two baseline directions. The phase progression in the signals across the array is used to create a map of the location of the scatterers in each range resolution cell. The radial velocities of at least three scatterers are then combined to give the three-dimensional velocity for a given height. Such a system may have potential as an operational wind-profiling system, but the complexity of the hardware, software, and the interpretation of the results are hurdles.

The spaced antenna method for deriving winds has been applied to measurements made with a number

of different research radars (e.g., see Larsen and Röttger 1989; and the references therein). The setup used in the spaced antenna method is for all practical purposes identical to the interferometer setup; that is, one transmitting array and a minimum of three receiving antennas deployed along two nonparallel baselines. As a result, there has been considerable confusion about the differences between the two methods. Early spaced antenna measurements utilized only the correlation between the received power, but later systems use the correlations between the complex time series so that the use of the signal phase cannot be applied as a clear discriminator between the two techniques. A possible distinction between interferometry and spaced antenna analysis may be that the latter deals with the macroscopic velocity appropriate to the sampling volume as a whole, whereas the former deals with the microscopic velocities associated with structure within the sampling volume. Nonetheless, confusion is warranted.

There has been ongoing discussion in the literature (e.g., see Larsen and Röttger 1989) about the relationships between the so-called Doppler wind measurement technique, in which the radial velocities from three or more beam directions are combined to yield the vector velocity, and the spaced antenna method, in which the winds are determined from measurements of the velocity with which the turbulent structure drifts across the array of receiving antennas, as indicated by the times when the peaks in the cross correlation of the received signals occur. Briggs (1980) first showed that there is a certain equivalence between the Doppler and spaced antenna techniques. More recently, Liu et al. (1990) and Van Baelen (1990) have shown that there is an exact equivalence between the spaced antenna and interferometer techniques, although the former is carried out in the time domain while the latter deals with Doppler velocities and is carried out in the fre-

* On leave from the Department of Physics and Astronomy, Clemson University.

** On leave from Instituto Geofísico del Perú, Lima, Perú.

Corresponding author address: Dr. Miguel F. Larsen, Dept. of Physics and Astronomy, Clemson University, Clemson, SC 29631.

quency domain. The result is perhaps not surprising when the similarity in the instrumental setup for the two methods is considered.

One result of the analyses by Liu et al. (1990) and Van Baelen (1990) was that they found the horizontal velocity is related to the slope of the linear variation of the difference in phase as a function of the radial Doppler velocity of the signals in two adjacent receiving antennas. The results suggested that the slope of a line fitted to the measured phase would give an alternative measure of the velocity, as opposed to determining maxima in the cross-correlation functions. The original idea, however, is not entirely attributable to either Liu et al. (1990) or Van Baelen (1990). Similar or related methods for determining the velocities have been discussed by other authors in connection with interferometry studies (Farley et al. 1981; Röttger and Ierkic 1985; Adams et al. 1986; Kudeki 1988; Kudeki et al. 1989; Röttger et al. 1990), although usually in the context of single scatterers. A further limitation of the equations presented by Liu et al. (1990) was that they applied only to a two-dimensional case, and some other effects related to aspect sensitivity were omitted from the analysis. Our purpose is to present a practical method for carrying out the interferometer analysis that leads to the vector horizontal winds, true vertical velocities, in-beam incidence angles, and error bar estimates. Off-vertical in-beam incidence angles can be introduced in the measurements when aspect sensitivity is important and, in particular, when the aspect sensitive layers are inclined with respect to the horizontal. Larsen and Röttger (1991) have dealt extensively with the latter effect. The essence of the method is to determine the arrival angle of signals within the beam from the phase difference between signals received in spatially separated receiving antennas. The change in the phase difference as a function of the radial Doppler velocity can be used to determine the horizontal winds. The value of the phase difference when the radial Doppler velocity is zero will depend on both the off-vertical incidence angle and the true vertical velocity. All the parameters can be derived from the phase of the coherence function as we will show. Our assumptions and approximations will be suitable for conditions characteristic of tropospheric and to some extent lower stratospheric flows.

Van Baelen (1990) and Van Baelen and Richmond (1990) have addressed some of the same questions that we address here. Our work has progressed in parallel with theirs and, although there is general agreement between the two sets of results, the approaches are somewhat different.

In the next section, the basic equations are derived. Section 3 uses sample data obtained with the MU radar located in Japan to illustrate the application of the method. Section 4 discusses the practical aspects of applying the method. Section 5 contains the conclusion.

2. Derivation of the equations

a. The case without aspect sensitivity

Given two spatially separated receiving antennas, the angle of arrival of the received signals in the plane defined by the antenna baseline and the vertical direction can be determined from the phase difference between the signals in the two antennas. Specifically, the phase difference ϕ_{ij} between the signals in the i th and j th receiving antennas will be given by

$$\phi_{ij} = kd_{ij} \sin \delta', \quad (1)$$

where d_{ij} is the distance separating the antennas, and $k = 2\pi/\lambda$ is the wavenumber, with λ being the radar wavelength. The angle δ' is measured with respect to zenith and defines the incidence angle in the vertical plane along the antenna baseline. Figure 1, taken from Larsen and Röttger (1991), illustrates the geometry. The relationship given in Eq. (1) is used in all interferometer analyses and has been presented or derived in a number of articles (e.g., Adams et al. 1986).

The horizontal area illuminated by the transmitted beam can be represented as in the schematic shown in Fig. 2. The x' axis is parallel to the receiving antenna baseline with positive x' along the azimuth α . The y' axis is perpendicular to the antenna baseline. The horizontal wind is in the direction defined by the azimuth angle θ shown by the heavy arrow. We define a rotated coordinate system such that x is parallel to the wind direction, and y is perpendicular to the wind direction. All azimuths are measured with respect to north, although the northward direction is not shown in the diagram in Fig. 2. The radial velocity V_r measured at any point within the beam will be given by

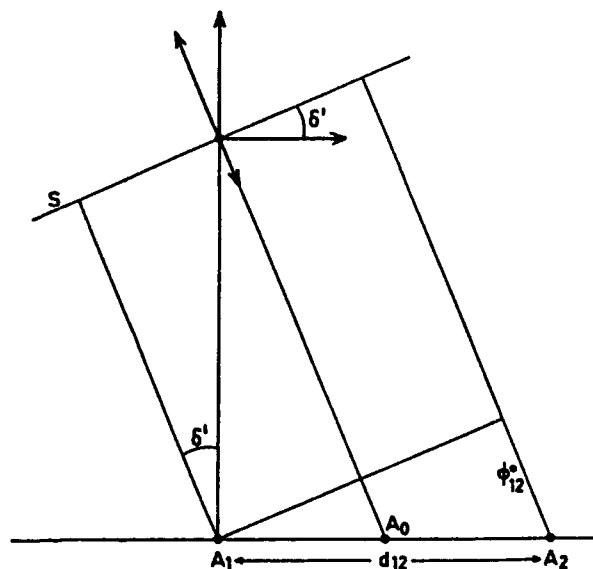


FIG. 1. Diagram showing how a phase difference is produced in two adjacent receiving antennas by asymmetric scattering within the beam.

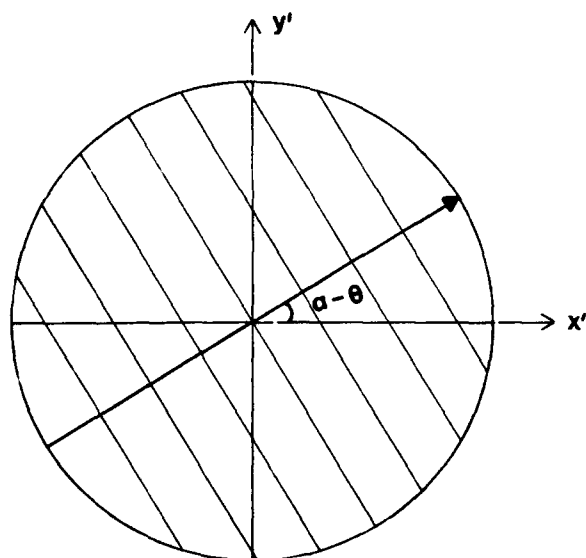


FIG. 2. Diagram showing contours of constant radial velocity (light solid lines) within the horizontal plane illuminated by the transmitted beam. The receiving antennas are located along the x axis, which corresponds to an azimuth measured from north of α . The wind direction is indicated by the heavy arrow that points in the azimuth direction θ .

$$V_r = V_h \cos \mu \sin \zeta + w \cos \zeta, \quad (2)$$

where μ is the angle between the x axis and the position vector of the point in the horizontal plane. Here V_h is the magnitude of the horizontal wind, ζ the zenith angle, and w the vertical velocity component. Equation (2) is valid for any point within the illuminated volume; that is, any point within the outer circle in Fig. 2, so that μ will vary from 0° to 180° , and ζ will vary from 0° to the beamwidth value for the range of points within the beam. We will assume that the horizontal and vertical velocities are uniform throughout the illuminated volume. The zenith angles considered throughout the paper are small since the measurements are all within the width of the vertically pointing beam. Therefore,

$$\cos \zeta \sim 1. \quad (3)$$

We can replace $\cos \mu$ and $\sin \zeta$ with functions of x and y to get

$$\begin{aligned} V_r &= V_h \frac{x}{(x^2 + y^2)^{1/2}} \frac{(x^2 + y^2)^{1/2}}{z} + w \\ &= V_h \left(\frac{x}{z} \right) + w \end{aligned} \quad (4)$$

where z is the altitude of the scattering volume. Since z , V_h , and w are constant for a given range resolution cell, lines of constant x are also lines of constant radial velocity. The latter are indicated in Fig. 2 by the light solid lines perpendicular to the heavy arrow representing the wind direction.

The Fourier transform of the time series of voltages measured with each of the receiving antennas leads to a representation of the signals as an amplitude and phase for each Doppler frequency ω . Details can be found in any number of basic texts, including Doviak and Zrnić (1984). We can represent the result of the Fourier transformation as

$$F(\omega) = A(\omega) \exp[i\phi(\omega)] \quad (5)$$

where $A(\omega)$ is the amplitude and $\phi(\omega)$ is the phase. The squared magnitude of $F(\omega)$ is the standard Doppler spectrum. With two receiving antennas, we have

$$F_1(\omega) = A_1(\omega) \exp[i\phi_1(\omega)] \quad (6a)$$

$$F_2(\omega) = A_2(\omega) \exp[i\phi_2(\omega)]. \quad (6b)$$

The cross spectrum is then defined as

$$\begin{aligned} C_{12} &= F_1(\omega) F_2^*(\omega) \\ &= A_1(\omega) A_2^*(\omega) \exp\{i[\phi_1(\omega) - \phi_2(\omega)]\} \end{aligned} \quad (7)$$

where $*$ represents the complex conjugate. The amplitude of C_{12} as a function of frequency is effectively the same as the amplitude of the Doppler spectrum, since F_1 and F_2 both represent the Fourier transforms of the signals received with vertically pointing transmitting and receiving beams. The phase of the cross spectrum represents the phase difference between the signals received in adjacent receiving antennas as a function of Doppler shift or radial velocity.

The cross spectrum produces a Doppler sorting of the contributions from the various scatterers within the scattering volume, and the contributions to a specific frequency component in the cross spectrum will come from all points along a line of constant radial velocity; that is, one of the light solid lines perpendicular to the wind direction shown in Fig. 2. The phase difference is related to the zenith angle measured in the vertical plane parallel to the antenna baseline; that is, in the x' - z plane in Fig. 2. The average phase for a given frequency component will correspond to the position at the center of the contour line of constant radial velocity; that is, along the heavy arrow representing the wind direction, if the reflectivities are symmetrically distributed or uniform. If the zenith angle measured in the vertical plane parallel to the wind direction is δ , then we can write

$$V_r = V_h \sin \delta + w. \quad (8)$$

Since

$$\sin \delta' = \sin \delta \cos(\alpha - \theta) \quad (9)$$

we get

$$V_r = V_h \frac{\sin \delta'}{\cos(\alpha - \theta)} + w. \quad (10)$$

Figure 3 illustrates the relationship between δ and δ' described by Eq. (9), and Fig. 4 of the article by Palmer

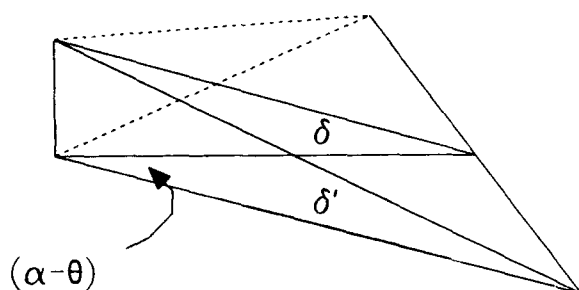


FIG. 3. Diagram showing the relationship between the inclination angles of a layer along two different vertical planes. The respective inclination angles are δ and δ' . The horizontal angle between the two vertical planes is $(\alpha - \theta)$.

et al. (1991) illustrates the relationships represented in Eqs. (8)–(10). Equation (10) has been proven more rigorously by Van Baelen (1990) by integration of the radial velocity contribution across the beam. Our derivation is not a mathematical proof, but is based on the geometry and is intended only as an illustration of the underlying principles.

The contribution to the radial velocity in Eq. (10) from the horizontal velocity component is actually the trace velocity multiplied by the sine of the zenith angle. Van Baelen (1990) was the first to point out this relationship. A number of previous studies have applied interferometer analysis to measurements made with only two receiving antennas. The assumption in those studies was that the measured radial velocity component was the projection of the horizontal velocity along the baseline; that is, $V_h \cos(\alpha - \theta)$, rather than the trace velocity along the baseline; that is, $V_h / \cos(\alpha - \theta)$. As stated in the Introduction, our own derivation proceeded in parallel with the work of Van Baelen (1990) and Van Baelen and Richmond (1990), and our original formulation was based on equations that used the velocity component rather than the trace-velocity component, similar to what was used by Kudski (1988), for example. The fact that the trace velocity rather than the velocity component appears in Eq. (10) is satisfying since it leads to a direct equivalence between the spaced antenna and interferometer analysis. The latter must be the case since the two methods merely provide alternative procedures for deriving the horizontal winds from the same set of measurements.

Substituting Eq. (1) in Eq. (10) and rearranging, we get

$$\phi_{ij} = \frac{kd_{ij} \cos(\alpha_{ij} - \theta)}{V_h} (V_r - w). \quad (11)$$

The phase ϕ_{ij} can be seen to vary linearly as a function of the radial Doppler velocity V_r . The line has slope m given by

$$m_{ij} = \frac{kd_{ij} \cos(\alpha_{ij} - \theta)}{V_h} \quad (12)$$

and intercept b given by

$$b_{ij} = -m_{ij}w. \quad (13)$$

Three receiving antennas yield three slopes and three intercepts. Any combination of two of the measured slopes can be used to calculate the horizontal wind components. Only the intercept from a single baseline is needed to calculate the vertical velocity component in the special case when there are no aspect sensitivity effects.

In spaced antenna analysis, the trace velocity along a given antenna baseline is calculated by dividing the antenna separation by the temporal lag at which the maximum in the cross-correlation function occurs. Trace velocities from two nonparallel antenna baselines can then be combined to yield the so-called apparent velocity. The velocities derived from the phase-difference slopes given in Eq. (12) correspond to the spaced antenna trace velocities. Indeed, Fourier transform theory predicts that a shift in the cross-correlation function will be equivalent to a phase slope in the frequency domain. Thus, the horizontal velocity vector derived by combining the various slope estimates from the interferometer analysis will be the apparent velocity. Equation (12) shows that the trace-velocity estimate will be ambiguous if the wind is perpendicular to the antenna baseline since the phase slope will be zero. In such a case, the slopes from two other baselines can be used in the analysis since the wind can only be perpendicular to one of the baselines. The same situation arises when the spaced antenna analysis is used.

From spaced antenna analysis, we know that the apparent velocity is a good estimate of the flow velocity, as long as turbulent fading within the medium is not significant. When turbulent fading is important, the apparent velocity will be an overestimate of the true velocity (e.g., see Larsen and Röttger 1989). We have not considered the effects of turbulent fading on the velocity estimates in our derivation. Such effects are known to be important in the mesosphere and stratosphere in certain height ranges (e.g., Kudski et al. 1989), but a number of studies have shown that the apparent velocity derived from spaced antenna measurements in the troposphere often gives a good estimate of the true flow velocity below the tropopause (e.g., Röttger and Vincent 1978; Vincent et al. 1987; and various studies summarized by Larsen and Röttger 1991). An indication of whether fading has to be considered in estimating the velocity is whether the Doppler spectra are dominated by beam broadening; that is, the spectral broadening produced by a range of radial velocity components over the finite beamwidth, or by comparable contributions from turbulent broadening and beam broadening. Simple calculations can be used to show that beam broadening will dominate in the troposphere for almost any reasonable combination of instrumental parameters. Hocking (1986) has shown the latter to be true.

If estimates of the true velocity are required, the parameters derived from the interferometer technique described here can easily be used as input for the full correlation analysis formulated by Meek (1980), for example. The parameters used in Meek's method are the lags corresponding to the maxima in the cross-correlation functions and an estimate of the characteristic fading time of the autocorrelation function. The antenna separations divided by the lags are equivalent to the trace velocities, which are also a product of the interferometer analysis. The fading time is directly related to the width of the autocorrelation function which, in turn, is related to the width of the power spectrum since the power spectrum and autocorrelation function are Fourier transform pairs. However, for the remainder of the article we will assume that the apparent velocity gives a good estimate of the true flow velocity for the reasons cited in the previous paragraph.

Using two of the measured slopes for the baselines between antennas 1 and 2 and antennas 1 and 3, for example, Eq. (12) yields

$$kd_{12}(\cos\theta \cos\alpha_{12} + \sin\theta \sin\alpha_{12}) = m_{12}V_h \quad (14a)$$

$$kd_{13}(\cos\theta \cos\alpha_{13} + \sin\theta \sin\alpha_{13}) = m_{13}V_h \quad (14b)$$

which can be rewritten as

$$X \sin\alpha_{12} + Y \cos\alpha_{12} = \frac{m_{12}}{kd_{12}} \quad (15a)$$

$$X \sin\alpha_{13} + Y \cos\alpha_{13} = \frac{m_{13}}{kd_{13}}, \quad (15b)$$

where $X = \sin\theta/V_h$ and $Y = \cos\theta/V_h$ are the inverse trace-velocity components. We can solve for X and Y to get

$$X = \frac{d_{13}m_{12} \cos\alpha_{13} - d_{12}m_{13} \cos\alpha_{12}}{kd_{12}d_{13} \sin(\alpha_{12} - \alpha_{13})} \quad (16a)$$

$$Y = \frac{d_{13}m_{12} \sin\alpha_{13} - d_{12}m_{13} \sin\alpha_{12}}{kd_{12}d_{13} \sin(\alpha_{13} - \alpha_{12})}. \quad (16b)$$

The ratio of X/Y gives the solution for θ

$$\tan\theta = -\frac{m_{12}d_{13} \cos\alpha_{13} - m_{13}d_{12} \cos\alpha_{12}}{m_{12}d_{13} \sin\alpha_{13} - m_{13}d_{12} \sin\alpha_{12}}. \quad (17)$$

The corresponding expression for V_h becomes

$$V_h = kd_{12}d_{13}[\sin(\alpha_{12} - \alpha_{13})\{[(m_{12}d_{13} \cos\alpha_{13} - m_{13}d_{12} \cos\alpha_{12})^2 + (m_{12}d_{13} \sin\alpha_{13} - m_{13}d_{12} \sin\alpha_{12})^2]\}^{-1/2}]. \quad (18)$$

Equation (13) gives the vertical velocity directly

$$w = -\frac{b_{ij}}{m_{ij}}. \quad (19)$$

Equation (19) comes directly from the expression for

the intercept in the linear relationship represented by Eq. (13), and the term results from setting $\phi_{ij} = 0$ in Eq. (13), which corresponds to obtaining the spectra component from the portion of the beam that point exactly in the vertical direction when there are no aspect sensitivity effects. The uncertainties in the slope estimates σ_m can be calculated by standard formulas, such as those given by Bevington (1969). We obtain

$$\sigma_m^2 = N \left[\frac{1}{N-2} \sum (\phi_n - b - mV_{r_n})^2 \right] \times [N \sum V_{r_n}^2 - (\sum V_{r_n})^2]^{-1} \quad (20)$$

where N is the total number of discrete values from the cross spectrum used in the line-fitting procedure and n ranges from 1 to N . The error in the intercept σ_b can be calculated from the formula (Bevington 1969)

$$\sigma_b^2 = N \left[\frac{1}{N-2} \sum (\phi_n - b - mV_{r_n})^2 \right] \times [\sum V_{r_n}^2][N \sum V_{r_n}^2 - (\sum V_{r_n})^2]^{-1}. \quad (21)$$

The uncertainty in the vertical velocity estimate becomes

$$\sigma_w = (b\sigma_m + m\sigma_b)m^{-2}. \quad (22)$$

Corresponding expressions for the velocity magnitude and direction error bars can be found in a straightforward way from Eqs. (17) and (18). Equation (22) shows that the error bars for w will become infinite if the slope m becomes zero. The latter can happen if the antenna baseline is perpendicular to the flow direction. The solution is to use a different pair of receiving antennas for the calculation. The method described here yields the uncertainties in a straightforward manner and with a minimum of calculations. We will discuss various aspects of implementing the scheme in practice in section 3.

b. The case with aspect sensitivity

Radar reflectivities at longer wavelengths, such as those around 6 m, are known to show aspect-sensitivity effects (e.g., Tsuda et al. 1986). The backscatter power decreases rapidly as the beam is moved away from zenith. The aspect sensitivity is not a problem in itself as long as the refractivity layers are horizontal; however, the layers are generally tilted a few degrees out of the horizontal plane. The effective beam-pointing direction then becomes essentially perpendicular to the layers since the strongest echoes come from that direction. Larsen and Röttger (1991) have discussed these problems in detail and have provided measurements of the in-beam incidence angles measured over a 4-day period. Palmer et al. (1991) have shown, based on an analysis of interferometer data, that the radial velocity measured with a nominally vertical beam

effectively the velocity perpendicular to the refractivity layers. The recent articles discuss the effects in detail, but the problems and effects associated with inclined refractivity layers have been known for a number of years (e.g., see Röttger and Ierkic 1985).

The configuration resulting from the aspect sensitivity effects is illustrated in Fig. 4, which shows the area in the horizontal plane illuminated by the transmitted beam as the large circle. Contours of constant radial velocity are shown as the light solid lines again, and the heavy arrow that forms the diameter of the outer circle indicates both the wind direction and the mean position for the constant-radial-velocity contours when aspect sensitivity effects are unimportant. Aspect sensitivity produces enhanced backscatter for a direction perpendicular to the refractivity layers. Typically, the aspect-sensitivity pattern is much narrower than the beamwidth so that the contribution to the backscatter comes from a small area within the illuminated volume. The smaller circle represents the area within the illuminated volume that produces the largest contribution to the received signal, due to aspect sensitivity effects. If the layers are horizontal, the smaller circle will be centered at the origin, and the only effect is to make the effective beamwidth narrower than the instrumental beamwidth. However, if the layers are inclined with respect to the horizontal, the smaller circle becomes displaced from the origin, as shown in Fig. 4.

The contours of constant radial velocity enclosed within the smaller circle in Fig. 4 will be the ones that contribute to the phase measurements, and the mean position will be along the arrow that forms the diameter

of the small circle. For the particular configuration shown in Fig. 4, the phase difference corresponding to a particular value of the radial velocity will be shifted to the right; that is, along the positive x' axis as a result of the aspect-sensitivity effects. As we will show in more detail below, the slope of the phase variation as a function of the radial velocity remains the same, but the intercept of the line describing the phase variation becomes shifted. Note also that a shift in the scattering area parallel to the wind direction produces no change in the measured value; that is, displacing the center of the small circle along the direction indicated by the large arrow produces the same mean phase or location for a given value of the radial velocity as would have been measured if there were equal contributions from all points within the instrumental beamwidth. Inspection of Fig. 4 will show the latter to be true. Therefore, we can limit our derivation to consideration of the effect of the component of the off-vertical incidence angle perpendicular to the wind direction.

The radial velocity measured at any point within the scattering volume will be

$$V_r = V_h \sin \delta + w \quad (23)$$

where δ is the zenith angle measured from the center of the scattering volume along the plane defined by the horizontal wind direction and the vertical. If x'_0 and y'_0 are the coordinates of the scattering center; that is, the center of the small circle in Fig. 4, then we can write

$$\begin{aligned} \sin \delta &= \frac{[(x' - x'_0)^2 + (y' - y'_0)^2]^{1/2}}{[(x' - x'_0)^2 + (y' - y'_0)^2 + z^2]^{1/2}} \\ &\approx \frac{x' - x'_0}{z \cos(\alpha - \theta)}. \end{aligned} \quad (24)$$

The approximate form of Eq. (24) was derived by using the fact that $(y' - y'_0) = (x' - x'_0) \tan(\alpha - \theta)$ and by noting that the height z is much greater than the horizontal displacements in either the x' or y' directions. Since

$$\frac{\phi}{kd} = \sin \delta' = \frac{x'}{(x'^2 + z^2)^{1/2}} \approx \frac{x'}{z} \quad (25)$$

and

$$\tan \psi_{\perp} = -\frac{x'_0}{z \sin(\alpha - \theta)} \quad (26)$$

where ψ_{\perp} is the component of the incidence angle perpendicular to the wind direction, we get

$$V_r = V_h \left[\frac{\phi}{kd \cos(\alpha - \theta)} + \tan \psi_{\perp} \tan(\alpha - \theta) \right] + w. \quad (27)$$

Rewriting Eq. (27) in the form of the phase difference as a function of the radial velocity gives

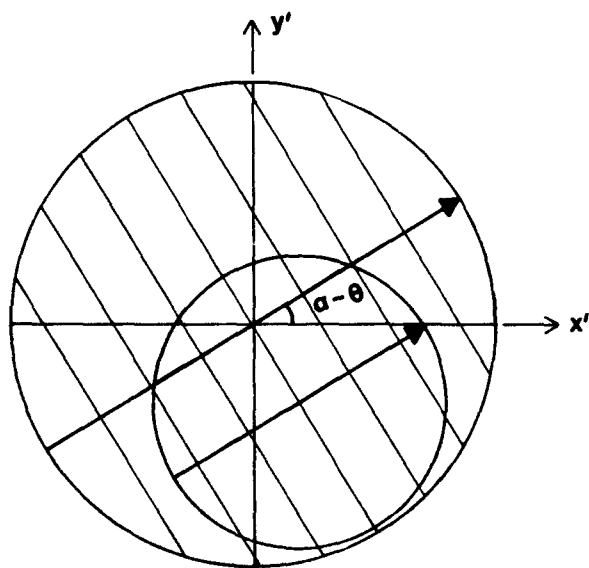


FIG. 4. Diagram showing the contours of constant radial velocity (light solid lines) in a format similar to that shown in Fig. 2. Aspect-sensitivity effects localize the scatter within a small area of the larger beam, however, as shown by the circle of smaller diameter. The center of the scattering region is located at coordinates x_0 and y_0 .

$$\phi = \frac{kd \cos(\alpha - \theta)}{V_h} V_r - kd \tan\psi \sin(\alpha - \theta) - \frac{wkd \cos(\alpha - \theta)}{V_h}. \quad (28)$$

The relationship is still linear, and the slope of the line is the same as we found before without aspect-sensitivity effects. However, the intercept, given by the sum of the last two terms in Eq. (28) now depends on both the vertical velocity and the component of the off-vertical incidence angle perpendicular to the wind direction.

For a layer tilted at the angle ψ from the vertical, the tilt component along another vertical plane will be related to ψ by

$$\tan\psi' = \tan\psi \cos\beta \quad (29)$$

where ψ' is the tilt angle in the vertical plane rotated by angle β in azimuth with respect to the vertical plane in which ψ is measured. We can then express $\tan\psi_{\perp}$ as

$$\tan\psi_{\perp} = \tan\psi \cos\left(\frac{\pi}{2} + \theta - \chi\right) \quad (30)$$

where χ is the azimuth along which the layer is tilted. Finally, we end up with

$$\phi = \frac{kd \cos(\alpha - \theta)}{V_h} V_r + kd \tan\psi \sin(\theta - \chi) \times \sin(\alpha - \theta) - \frac{wkd \cos(\alpha - \theta)}{V_h}. \quad (31)$$

For each baseline, there are two fitted parameters. The slope of the fitted line is given by

$$m_{ij} = \frac{kd_{ij} \cos(\alpha_{ij} - \theta)}{V_h}. \quad (32)$$

The intercept is given by

$$b_{ij} = kd_{ij} \tan\psi \sin(\theta - \chi) \sin(\alpha_{ij} - \theta) - m_{ij}w. \quad (33)$$

A more useful form of Eq. (33) is

$$b_{ij} = kd_{ij}(\tan\psi_x \cos\theta + \tan\psi_y \sin\theta) \times \sin(\alpha_{ij} - \theta) - m_{ij}w. \quad (34)$$

Any pair of the slope estimates can be used to calculate the horizontal wind components from Eq. (19). The slopes and intercepts can then be used to calculate ψ_x , ψ_y , and w from Eq. (34). The error estimation can be carried out as described in section 2b.

Palmer et al. (1991) presented some examples of the tilt-angle values derived by this technique. The half-

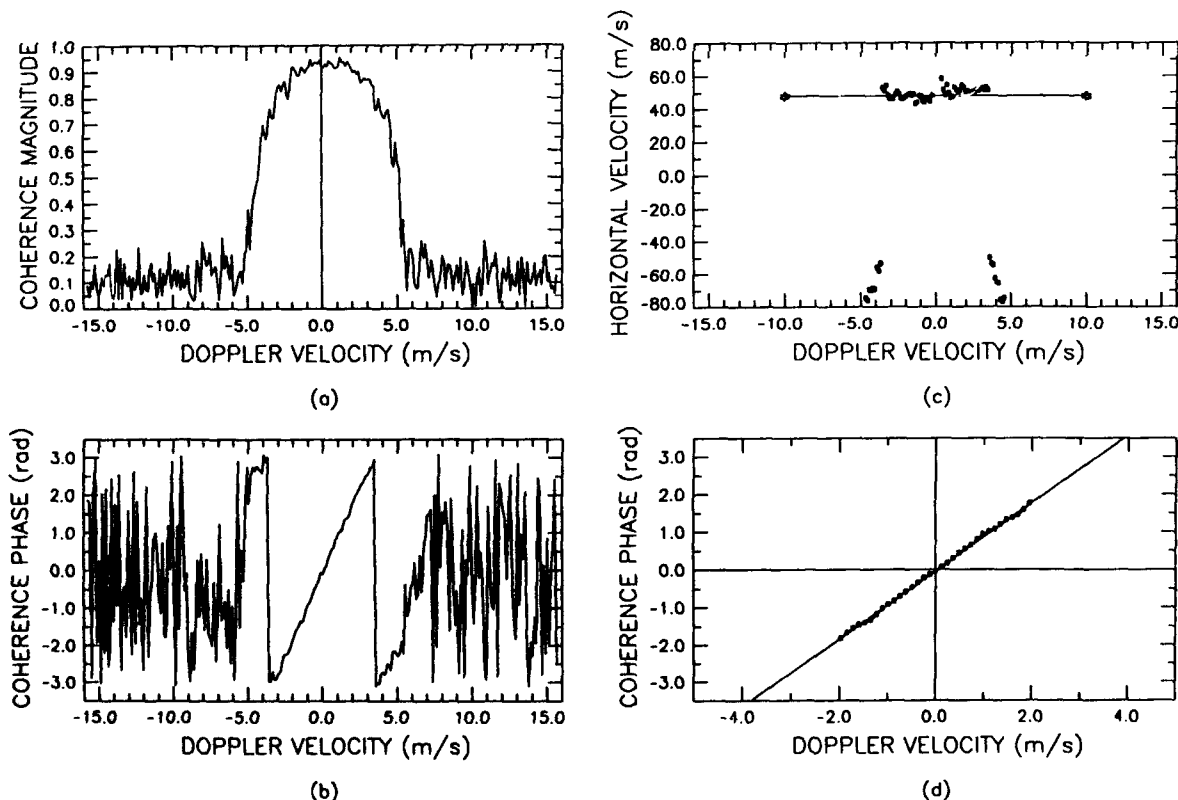


FIG. 5. (a) Coherence function amplitude for a height with a broad spectrum. (b) Phase of the coherence function. (c) Determination of the window for fitting the phase based on the implied horizontal velocity determined from the phase of the coherence function. (d) Fitted line and actual phase values.

hour average values were found to have magnitudes of $\sim 0.5^\circ$, which agrees, in general, with the results of Röttger et al. (1990) and Larsen and Röttger (1991), who derived the tilt angles by a different method. Röttger et al. (1990) have also presented results of tilt angle measurements based on data from the Chung-Li radar in Taiwan, which agreed with the other measurements as far as overall average magnitude is concerned.

An advantage of the analysis technique presented here over those that use Doppler measurements of the vertical velocity is that it leads to estimates of the true vertical velocity. Off-vertical in-beam incidence angles result in measured radial velocities that have a component that is the projection of the horizontal velocity along the line of sight. Although, the angles are typically small, the difference between the true vertical velocity and the radial velocity in a nominally vertical beam can be significant, as shown by Röttger and Ierkic (1985), Larsen and Röttger (1991), and Palmer et al. (1991).

3. An example of the application of the method

Our goal is not to make an exhaustive test of the technique or to compare results provided by different types of analysis. The purpose of the paper is merely

to provide a framework for carrying out the analysis of interferometer data, including the complexities imposed by aspect-sensitivity effects; however, the easiest way to illustrate the method is to apply it to a small sample of data. The observations were made on 24 October 1989 from 2100 to 2400 LST with the MU radar located in Shigaraki, Japan. The great flexibility of the radar system makes it possible to operate the radar in a number of different modes. In this case, the central portion of the array was used for transmission, and three spatially separated receiving antennas were used. The dataset has been described in more detail by Palmer et al. (1990, 1991).

The interferometer analysis, as described in the previous section, was carried out, including the calculation of the complex coherence function. Examples of the calculated functions from two heights are shown in Figs. 5a–d and Figs. 6a–d. Figure 5 corresponds to the case of a broad Doppler spectrum. Figure 5a shows that the spectral peak can be discerned between the approximate limits of $\pm 5.0 \text{ m s}^{-1}$. Over the same velocity or frequency interval, the phase in Fig. 5b can be seen to be varying linearly, as expected for small zenith angles. Actually, the phase changes by more than 2π rad, which produces the two discontinuous jumps near $\pm 3.5 \text{ m s}^{-1}$. As illustrated in Fig. 5a, the phase

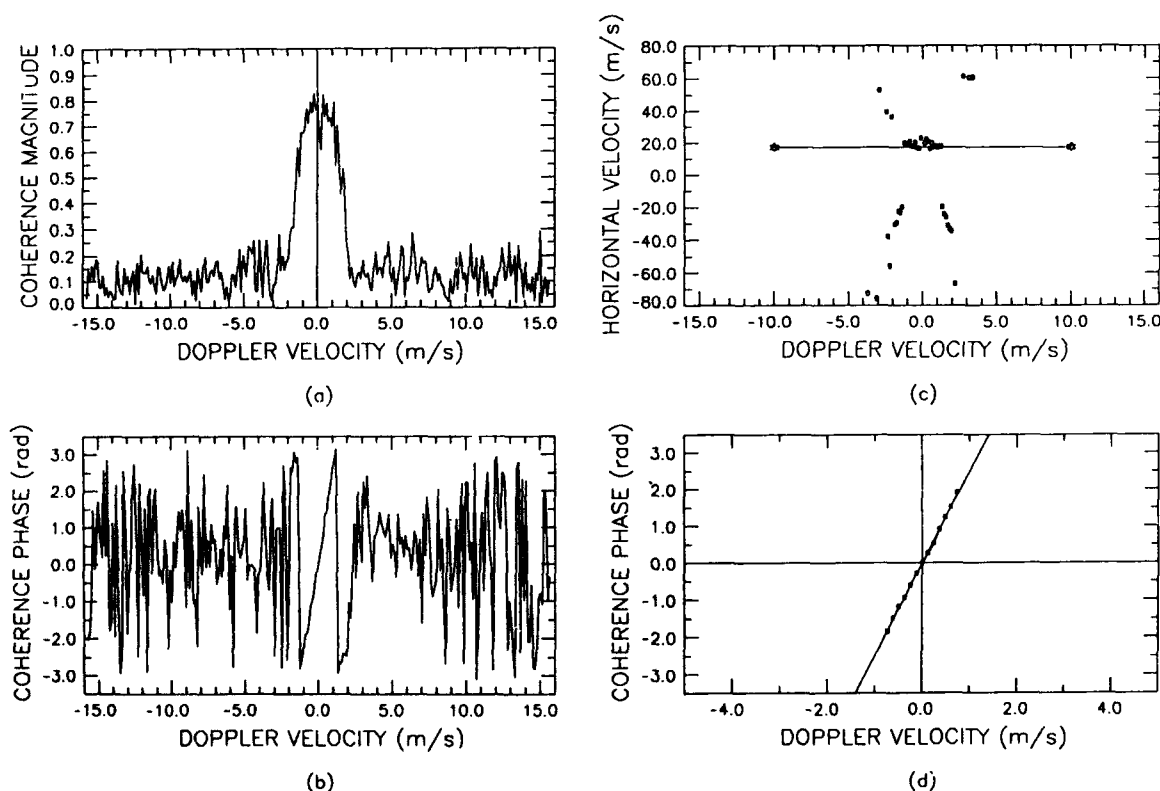


FIG. 6. (a) Coherence function amplitude for a height with a narrow spectrum. (b) Corresponding phase for the coherence function. (c) Window for the fitting determined from the beam broadening effects due to the approximate horizontal velocity. (d) Actual phase values and fitted line.

of the coherence function varies linearly only in the part of the Nyquist spectral interval that contains signal. Therefore, a window based on the beam broadening caused by the horizontal wind was chosen. Since the phase information defines a pointing direction, the velocities in the Doppler spectrum can be interpreted as the projection of the horizontal velocity along those pointing directions. Figure 5c shows the radial velocities converted to approximate horizontal velocities. The velocities should lie along a horizontal line if the winds are uniform. The median of the approximate horizontal velocity estimates was calculated and used to find the beam-broadened spectral width, which was used to define the window for the linear fitting procedure. The line fitted to the phase variation is shown in Fig. 5d superimposed on the actual phase values. Note that the horizontal axis in Fig. 5d has a different scale than the axis in Figs. 5a–c. More work is needed to refine the procedure for estimating the spectral window for fitting the line, although this procedure produced ad-

equated results for the case described here, in which the wind was almost entirely parallel to one of the antenna baselines.

Figure 6 shows an example involving a narrow spectral peak. The window for fitting is again determined by the beam broadening due to the approximate horizontal velocity as shown in Fig. 6c. The fitted line and the phase values are shown in Fig. 6d.

The winds were calculated for heights between 6 and 16 km based on 30-min-average spectra such as those shown in Figs. 5 and 6. The results are presented in Fig. 7a. The true vertical velocity was also calculated as indicated. The Doppler velocity measured with a vertical beam is effectively the radial velocity perpendicular to the tilted refractivity layers, as discussed by Röttger and Ierkic (1985), Larsen and Röttger (1991), and Palmer et al. (1991). The resulting velocity estimates are then contaminated by a component of the horizontal wind. However, the interferometer analysis described here yields the true vertical velocity, in ad-

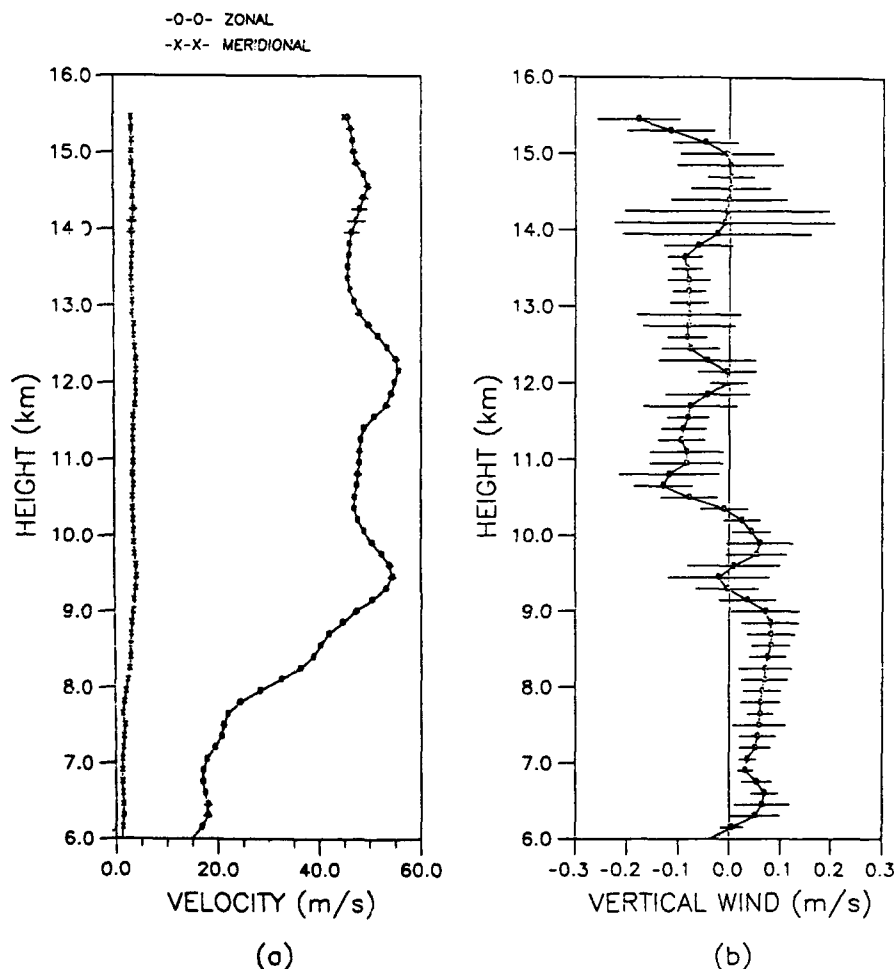


FIG. 7. On the left, profiles of the zonal and meridional wind determined by the interferometer method for the data from 2145 to 2215 LST. The true vertical velocity derived by the interferometer method is shown on the right.

dition to the layer tilt angles. The latter are not shown here but were presented by Palmer et al. (1991).

The curves for both the horizontal and vertical velocities in Figs. 7a and 7b have error bars plotted, although they are more obvious in the panel on the right. The uncertainty in the horizontal velocity determination is $\sim 0.5 \text{ m s}^{-1}$ at most heights. The uncertainties in the vertical velocity estimates are larger in comparison to the magnitude of the velocities than is the case for the horizontal winds. Typical magnitudes of the uncertainties of the vertical velocities at most heights are in the range from 5 to 10 cm s^{-1} .

For comparison, the horizontal winds deduced by a Doppler method are shown in Fig. 8a. The Doppler estimates lie outside the error bars derived from the interferometer analysis at many heights, indicating that the differences are attributable to more than statistical uncertainty, although there is no way to determine

which profile is a better estimate of the true winds with the data available here. The data that produced the curves in Fig. 7 were obtained between 2145 and 2215 LST, and the data in Fig. 8 were obtained between 2110 and 2120 LST, since the sampling scheme was different. Therefore, the differences in the profiles may be due to temporal evolution of the flow. However, the differences in the vertical velocity estimates obtained during the two observation intervals can be explained in large part by the effect of the off-vertical incidence angles that affected the Doppler measurements, as shown by the detailed analysis carried out in the study by Palmer et al. (1991), indicating that the temporal evolution, at least in the vertical velocities, was small during the gap in the observations.

The vertical velocities deduced by the Doppler method are shown in Fig. 8b. There are significant differences between the profiles in Figs. 7b and 8b for the

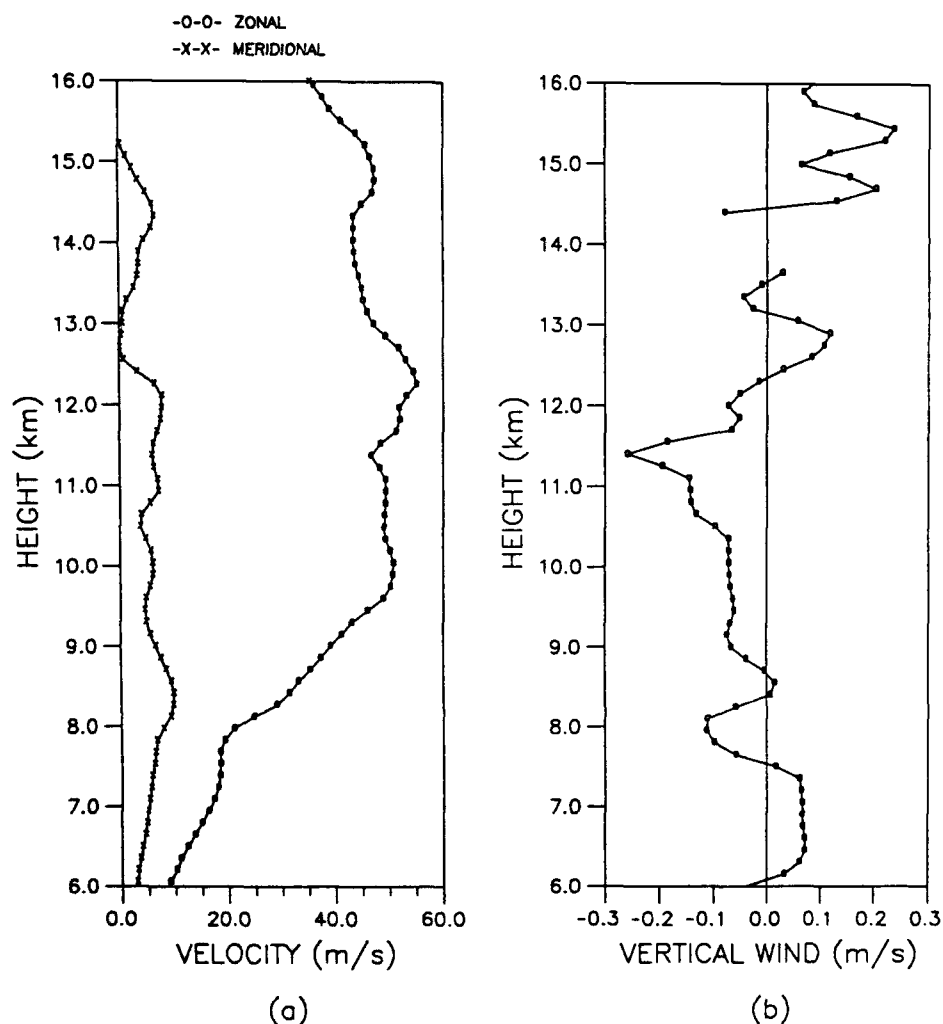


FIG. 8. On the left, profiles of the zonal and meridional velocity derived by the Doppler method for the data from 2110 to 2120 LST. The vertical velocity profile derived by the Doppler method is shown on the right.

reasons related to tilted refractivity layers already cited. Although the uncertainties in the vertical velocity estimates are relatively large in comparison to the velocity magnitudes, the differences between the vertical velocities derived by the interferometer and Doppler methods are larger than the uncertainties over a large part of the height range.

Figure 8 shows a gap in the vertical-velocity profile determined from the Doppler method. The received power in the vertical and off-vertical beams for the Doppler data near 14 km was comparable. However, the vertical spectra did not have well-defined peaks, and the spectral fitting procedure did not converge. The peaks in the off-vertical spectra were better defined, and horizontal wind estimates were possible. The interferometer profiles in the same height range show an increase in the size of the error bars, although both the horizontal and vertical velocities could be determined.

4. Discussion

An advantage of the analysis method described here is that the number of computations required to implement it are reduced in comparison to the spaced antenna analysis, for example. The spaced antenna analysis can provide the same parameters as the interferometer method, namely, the horizontal and true vertical velocities, and the layer tilt angles (Larsen and Röttger 1989, 1991); however, more calculations are required. The horizontal winds are calculated from the temporal lags of the peaks in the auto- and cross-correlation analysis. The tilt angle is calculated from the phase of the cross correlation at zero lag. The radial velocity in the vertical beam is derived from the variation of the phase of the autocorrelation function, and the corrected true vertical velocity is calculated by combining the vertical-beam radial velocity, tilt angles, and horizontal wind information. Error-bar estimation requires an iterative procedure. The interferometer method as outlined here only requires that the coherence function be calculated for each antenna pair and that a line be fitted to the phase variation. The slope and intercept parameters then yield all the same physical quantities as the spaced antenna analysis. There is a minimum of computational complexity, and simple expressions for the uncertainties in the calculated quantities emerge from the derivation.

Not only do the calculations appear to be simple enough to carry out in real time, but the implementation of the hardware is also straightforward since all beams point vertically. The Doppler method requires beam pointing in a number of directions, which adds some complexity to the hardware and leads to assumptions about uniformity of the wind field over the sometimes large horizontal separations between beam positions. The vertically pointing beam setup used for the interferometer measurements requires no beam steering. However, three receivers are necessary. Many

of the same advantages and disadvantages of interferometry apply to spaced antenna systems, which have the same hardware requirements (Larsen and Röttger 1989).

Ideally, the coherence values from all antenna pairs will be usable for the analysis, but in practice, the wind may be parallel to one of the baselines so that the coherence is low along the other two baselines. However, since the wind magnitude and direction are calculated as a first step by using the fitted slopes, such special situations should be evident before the second step of finding the in-beam incidence angles and true vertical velocities is implemented using the fitted intercept values. Clearly, more study of such potential practical problems is needed.

5. Conclusion

Although the basic idea of using the linear variation of the phase in interferometer measurements to infer the horizontal winds has been discussed by a number of authors, no complete analysis method has been proposed. Also, the additional complexity introduced by aspect-sensitivity effects has not been considered fully in the past in connection with the interferometer analysis. The analysis method introduced here involves only simple calculations but yields all the parameters that are typically of interest for operational or research wind profiler applications. Clearly, more detailed studies are needed in the future to determine how the interferometer method compares to the spaced antenna or Doppler beam swinging method in terms of both ease of implementation and accuracy and precision of the results.

Acknowledgments. We want to thank Dr. Joel Van Baelen who pointed out an important error in the original version of our manuscript. We also thank him for his input during many useful and interesting discussions about interferometry in general and our parallel efforts in particular over the last few months. We also thank Dr. Erhan Kudeki and Dr. Steve Franke who had many good insights about the work and the interferometry technique. MFL received support from the Ministry of Education, Research, and Culture of Japan and from AFOSR Contract F49620-88-C-0121 during the course of the study. RDP was supported as a Japan Society for the Promotion of Science (JSPS) postdoctoral fellow. The MU Radar is owned and operated by the Radio Atmospheric Science Center of Kyoto University.

REFERENCES

- Adams, G. W., J. W. Brosnahan, D. C. Walden, and S. F. Nerney, 1986: Mesospheric observations using a 2.66-MHz radar as an imaging Doppler interferometer: Description and first results. *J. Geophys. Res.*, **91**, 1671-1683.

- Bevington, P. R., 1969: *Data Reduction and Error Analysis for the Physical Sciences*. McGraw-Hill, 336 pp.
- Briggs, B. H., 1980: Radar observations of atmospheric winds and turbulence: A comparison of techniques. *J. Atmos. Terr. Phys.*, **42**, 823-833.
- Doviak, R. J., and D. S. Zrnić, 1984: *Doppler Radar and Weather Observations*. Academic Press, 458 pp.
- Farley, D. T., H. M. Ierick, and B. G. Fejer, 1981: A new technique for studying plasma turbulence in the ionosphere. *J. Geophys. Res.*, **86**, 1467-1472.
- Hocking, W. K., 1986: Observation and measurement of turbulence in the middle atmosphere with a VHF radar. *J. Atmos. Terr. Phys.*, **48**, 655-670.
- Kudeki, E., 1988: Radar interferometer observations of mesospheric echoing layers at Jicamarca. *J. Geophys. Res.*, **93**, 5413-5421.
- , F. Surucu, and R. F. Woodman, 1990: Mesospheric wind and aspect sensitivity measurements at Jicamarca using radar interferometry and post-statistics steering techniques. *Radio Sci.*, **25**, 595-612.
- Larsen, M. F., and J. Röttger, 1989: The spaced antenna technique for radar wind profiling. *J. Atmos. Oceanic Technol.*, **6**, 920-938.
- , and —, 1991: VHF radar measurements of in-beam incidence angles and associated vertical-beam radial velocity corrections. *J. Atmos. Oceanic Technol.*, **8**, 477-490.
- Liu, C.-H., J. Röttger, C. J. Pan, and S. J. Franke, 1990: A model for spaced antenna observational mode for MST radars. *Radio Sci.*, **25**, 551-563.
- Meek, C. E., 1989: An efficient method for analysing ionospheric drifts data. *J. Atmos. Terr. Phys.*, **42**, 835-839.
- Palmer, R. D., R. F. Woodman, S. Fukao, T. Tsuda, and S. Kato, 1990: Three-antenna post-statistic beam steering using the MU radar. *Radio Sci.*, **25**, 1105-1110.
- , M. F. Larsen, R. F. Woodman, S. Fukao, M. Yamamoto, T. Tsuda, and S. Kato, 1991: VHF radar interferometry measurements of vertical velocity and the effect of tilted refractivity surfaces on standard Doppler measurements. *Radio Sci.*, **26**, 417-427.
- Röttger, J., and R. A. Vincent, 1978: VHF radar studies of tropospheric velocities and irregularities using spaced antenna techniques. *Geophys. Res. Lett.*, **5**, 917-920.
- , and H. M. Ierick, 1985: Postset beam steering and interferometer applications of VHF radars to study winds, waves, and turbulence in the lower and middle atmosphere. *Radio Sci.*, **20**, 1461-1480.
- , C.-H. Liu, J. K. Chao, A. J. Chen, C. J. Pan, and I.-J. Fu, 1990: Spatial interferometer measurements with the Chung-Li VHF radar. *Radio Sci.*, **25**, 503-515.
- Tsuda, T., T. Sato, K. Hirose, S. Fukao, and S. Kato, 1986: MU radar observations of the aspect sensitivity of backscattered VHF echo power in the troposphere and lower stratosphere. *Radio Sci.*, **21**, 971-980.
- Van Baelen, J. S., 1990: Comparison of clear air atmospheric radar techniques for the study of atmospheric dynamics in the troposphere and the stratosphere. NCAR Cooperative Thesis No. 128, 191 pp. [Available from NCAR, Boulder, CO.]
- , and A. D. Richmond, 1990: Radar interferometry technique: 3-D wind measurement theory. *Radio Sci.*, (submitted.)
- Vincent, R. A., P. T. May, W. K. Hocking, W. G. Elford, B. H. Candy, and B. H. Briggs, 1987: First results with the Adelaide VHF radar: Spaced antenna studies of tropospheric winds. *J. Atmos. Terr. Phys.*, **49**, 353-366.

VHF Radar Measurements of In-Beam Incidence Angles and Associated Vertical-Beam Radial Velocity Corrections

M. F. LARSEN*

Radio Atmospheric Science Center, Kyoto University, Uji, Kyoto, Japan

J. RÖTTGER†

EISCAT Scientific Association, Kiruna, Sweden

(Manuscript received 12 April 1991, in final form 17 December 1990)

ABSTRACT

Atmospheric backscatter or partial reflections observed with VHF radars are strongly enhanced for angles within a few degrees of the vertical, although the strongest echoes are not necessarily exactly from the vertical direction. Consequently, a nominally vertical beam can actually receive the strongest echoes from a direction slightly off-vertical. The radial velocities measured in the vertical beam, then, are not true vertical velocities but have contributions from both the projection of the vertical and the horizontal velocity along the effective beam direction. We present measurements of the tropospheric and lower stratospheric incidence angles obtained over a period of four days with a spaced antenna radar system and calculate the true vertical velocities by means of a correction derived by combining the incidence-angle measurements, the radial velocities in the vertical beam, and the horizontal winds obtained by the standard spaced antenna method. Typical values for the incidence angles are less than 2° when averaged over 8 min or more. The vertical velocity corrections are typically 5%–200% of the magnitude of the vertical-beam radial velocity. The corrected vertical velocities are found to be in better qualitative agreement with expectations based on the meteorological conditions for the period.

1. Introduction

Even the early measurements made with VHF radars indicated that the atmosphere is strongly anisotropic, i.e., aspect sensitive, when observed with longer wavelengths, e.g., 6 m or greater. Examples are the studies by Green and Gage (1980) and Röttger (1980). Observations typically indicate 1) an enhancement of ~ 10 – 14 dB in the reflectivity when the beam is pointed vertically, i.e., as compared to 10° off-vertical, and 2) a rapid drop-off within a few degrees of vertical. More recently, Tsuda et al. (1986) used the flexible beam-steering capabilities of the MU (middle and upper atmosphere) radar located at Shigaraki, Japan, to study the problem and found that the enhanced reflectivities only occurred within $\sim 5^\circ$ of the vertical direction. The dynamics responsible for the layers are still poorly understood. Anisotropic turbulence has been suggested (Doviak and Zrnić 1984a), as well as sharp disconti-

nities in the vertical temperature gradient that would lead to Fresnel reflection or Fresnel scatter (e.g., Gage et al. 1981). Röttger and Larsen (1990) have reviewed the observations and cite much of the relevant literature.

Aspect sensitivity has been used to full advantage in spaced antenna VHF radar wind measurements (see e.g., Röttger and Larsen 1983; Larsen and Röttger 1989). Since all the beams are pointed vertically when using the technique, the signal-to-noise ratio improves. Radars using the Doppler technique to measure winds typically have one beam pointing vertically and two or more beams pointing in off-vertical directions. The signal-to-noise ratio then is greater in the vertical beam. These considerations apply only to longer wavelengths such as those around 6 m or greater. Studies have already shown that the aspect sensitivity effect is unimportant, except in unusual dynamical conditions, at UHF frequencies with wavelengths such as 70 cm. Little is known about the transition range between the two wavelengths since virtually all the radars being used for radar wind-profiling studies operate at wavelengths close to either 70 cm or 6 cm. Röttger and Larsen (1990) list most of the MST (mesosphere/stratosphere/troposphere) research radars presently in operation, along with the instrumental parameters.

Only a few measurements of the layer tilt angles have been carried out. Green and Gage (1980) and Tsuda

* On leave from: Department of Physics and Astronomy, Clemson University, Clemson, SC 29631.

† On leave from: Max-Planck-Institut für Aeronomie, Katlenburg-Lindau, West Germany.

Corresponding author address: Dr. Miguel F. Larsen, Dept. of Physics and Astronomy, Clemson University, Clemson, SC 29631.

et al. (1985) both used radar systems with flexible beam-steering capabilities to locate the pointing direction with maximum reflectivity. The latter direction was assumed to be the direction perpendicular to the tilted refractivity layers. Neither study examined an extended dataset. The method requires a fairly sophisticated instrument that is either built specifically for the purpose, such as the Sunset radar used in the earlier study, or a radar built with sufficient flexibility in beam-pointing and beam-steering capabilities to make the measurements possible, such as the MU radar used in the later study. Röttger (1981) first pointed out the possibility that tilted layers may bias vertical velocity measurements. Röttger and Ierkic (1985) first proposed an alternative method for determining the incidence angles from within the beam of the received signals based on measurements of the phase differences between the signals in two spatially separated, vertically pointing receiving antennas. Since the antenna beams are vertically pointing, no sophisticated beam steering is required. They also presented small samples of data, and Röttger et al. (1990) provided a more detailed analysis of data from the Chung-Li VHF radar showing the existence of tilted layers. However, no extensive measurements of the incidence or tilt angles over longer periods and no detailed studies of the vertical velocity corrections have been carried out previously.

In this paper, we present results from four days of observation carried out in April 1984 with the SOUSY-VHF radar (sounding system) located in the Harz Mountains in West Germany. In addition, we used the measured incidence angles, in combination with the radial velocities from the vertical beam and the horizontal winds measured with the radar, to produce a set of vertical velocities corrected for the effective off-vertical pointing angle of the nominally vertically pointing beam. We will show that the resulting velocities appear to be in better qualitative agreement with the expectations based on meteorological conditions for the period.

The experimental setup and a description of the technique are presented in section 2. A description of the measured incidence angle values is presented in the following section. Section 4 deals with the observed radial velocities in the vertical beam and the corrected values deduced from a combination of the incidence angles and the velocity measurements. Section 5 gives an assessment of the various potential errors in the measurements. The last section is a discussion of the results and the conclusions.

2. Details of the experiment

a. Description of the SOUSY-VHF radar system

The observations described here were obtained with the SOUSY-VHF radar operating in the spaced antenna mode. We will not describe the details of the standard spaced antenna technique for measuring

winds since detailed descriptions have been given by a number of authors including the recent review by Larsen and Röttger (1989). Basically, a single antenna is used for transmission, and a minimum of three spatially separated antennas are used for reception. The received signals are cross correlated in order to deduce the time required for the refractivity pattern aloft to traverse the array of receiving antennas. The resulting temporal lags, in combination with the known antenna separations, are used to calculate the horizontal velocities. The vertical velocity can be derived directly from the Doppler shift measured in any of the vertical beams, similar to the technique used in what has become known as the Doppler method. All indications are that the Doppler technique and the spaced antenna technique yield wind estimates of comparable accuracy and reliability (see e.g., Larsen and Röttger 1989), although there are additional advantages associated with the spaced antenna method (e.g., Röttger 1989), among them the possibility of applying the techniques described here.

The SOUSY-VHF radar is located in the Harz Mountains in West Germany near the town of Bad Lauterberg. The system radiates at 53.8 MHz with a single large transmitting antenna, as shown schematically in Fig. 1. The diameter of the large antenna is ~ 60 m. The radar can either receive with the same antenna used for transmission or with three smaller receiving antennas located adjacent to the large array, also shown in Fig. 1. The receiving arrays are each ~ 20 m in diameter. Two of the receiving arrays are located along a west-east line and will be designated as the west and east antennas, respectively. The third antenna is located south of the other two and will be designated the south antenna. The peak radiated power was 200 kW with an average power of ~ 10 kW. The particular combination of parameters used in the experiment produced acceptable signal-to-noise ratios of 3 dB or greater up to heights of ~ 16 – 18 km with 300-m height resolution.

During April 1984, the radar was operated continuously for four days from 1000 MET (middle European time) 9 April until 1500 MET 13 April. During the experiment, only the spaced antenna method was used for measuring the winds, so that the large array was used only for transmission and the three smaller antenna arrays were used for reception. The height resolution above 3 km was 300 m obtained with a coded pulse scheme. Data were also available for heights below 3 km but were not used in this study.

b. Method for measuring in-beam incidence angles

The method for measuring in-beam incidence angles with a spaced antenna system was first proposed by Röttger and Ierkic (1985). Figure 2 shows the method schematically. As an example, consider a tilted refractivity layer in the far field of the antenna, indicated as

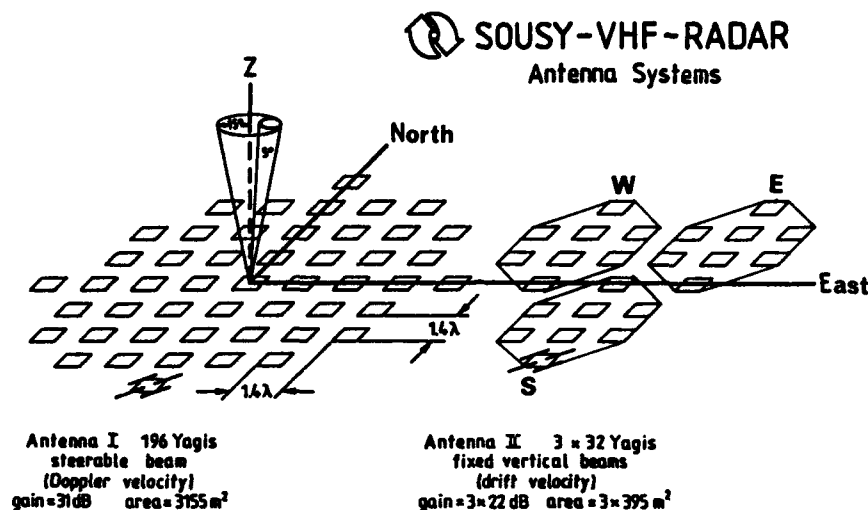


FIG. 1. Schematic diagram showing the layout of the SOUSY-VHF radar in the configuration used for spaced antenna wind measurements.

the line that is the cross section of the surface S , which will create a difference in the path length for the signals received in two spatially separated antennas. Thus, the phase difference between the two signals or, equivalently, the phase at zero lag of the cross correlation ρ_{ij} between the two complex signals is related to the incidence angle δ_{ij} , as shown schematically in Fig. 2b. Simple geometry shows that if d_{ij} is the distance between the i th and j th receiving antennas, ϕ_{ij} is the phase angle difference, and λ is the radar wavelength, then the incidence angle in the plane defined by the vertical direction and the baseline between the two antennas is given by

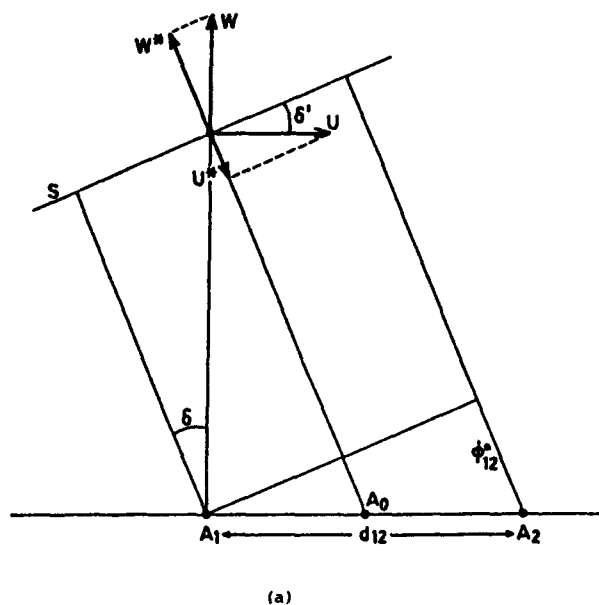
$$\delta_{ij} = \sin^{-1} \left(\frac{\lambda \phi_{ij}}{2\pi d_{ij}} \right). \quad (1)$$

A spaced antenna wind measurement requires at least three receiving antennas, which constitutes a typical setup (see, e.g., Röttger and Larsen 1990). Thus, there is redundancy in the measurement since there are three antenna combinations that can be used to full advantage to reduce the uncertainty in the measurement or to check on the internal consistency in the data. The parameters d_{ij} and λ are fixed for a given pair of receiving antennas and a given radar system. Equation (1) then implies that there is a limited range of incidence angles that can be determined unambiguously. The effect, as well as the antenna pattern weighting, was discussed by Röttger and Ierkic (1985).

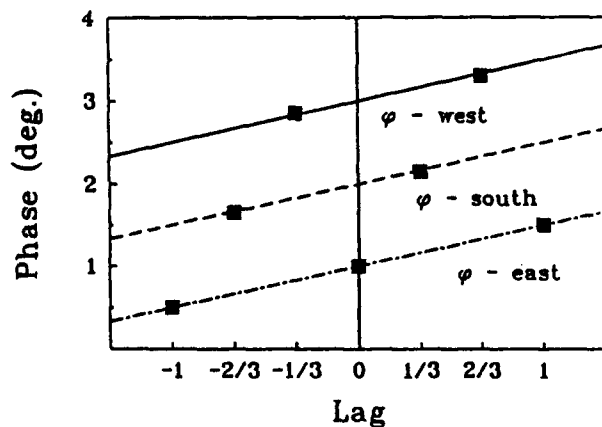
Off-vertical incidence angles can be produced by aspect sensitive refractive index layers if they are tilted out of the horizontal plane, as discussed in section 1. The scattering due to such layers is strongest in a direction perpendicular to the layers and decreases rapidly as the incidence angle moves away from perpendicularity. The result is illustrated schematically in Fig.

3, which represents the relatively broad beam pattern as a Gaussian with horizontal hatching. The aspect sensitivity pattern associated with the inclined layer is shown as the narrower Gaussian with vertical hatching. The effective beam pattern is the convolution of the other two patterns and is shown as the narrow Gaussian with diagonal hatching. Typically, the beamwidth is greater than the aspect sensitivity pattern width, so that the measured incidence angle is nearly the same as the tilt angle of the layers, as illustrated in Fig. 3. Therefore, when the off-vertical incidence angles are produced by layered structure and when the beamwidth is broader than the aspect sensitivity pattern, the measured incidence angles can be interpreted as layer tilt angles. Off-vertical incidence angles can also be produced by asymmetric distributions of localized scatterers across the beam. For example, if the strongest scatterers are located in the eastern quadrant of the beam, the incidence angles will be biased toward the east. The latter effect cannot be excluded, and there is no direct way to distinguish between the layer scattering and the asymmetric scattering distribution effect based solely on the vertical beam measurements described here. Therefore, there is no ambiguity about the incidence-angle measurements, but we have to be careful when interpreting the measured incidence angles as layer tilt angles.

At the time of the experiment, the preprocessing possible with the available computing equipment was limited. Therefore, in order to reduce the number of data tape changes required, a data-taking scheme was implemented in which measurements were taken for 8 min during each 20-min period. Another characteristic of the data-taking scheme was that the signals from the three receiving antennas had to be multiplexed in time rather than being sampled simultaneously, thus,



Phase Sampling Scheme



introducing a delay of one coherent integration period between the samples in adjacent antennas. The effective sampling period after coherent integration of 370 ms was thus three times the coherent integration period for one antenna. The sampling scheme is shown schematically in Fig. 2c, which represents the variation of the phase ϕ in the east, south, and west antennas. The slope of the phase curve is, of course, related to the radial velocity of the scattering-reflecting medium. The times when each of the curves was sampled are shown by the filled squares in the figure so that the cycle involved sampling the east antenna first, followed by the south and west antennas. The incidence angle measurements ideally require simultaneous samples, and even a delay of only one-third of the effective sampling period can produce unacceptable errors. Therefore, a linear interpolation had to be introduced in the analysis, as we will describe in the next section.

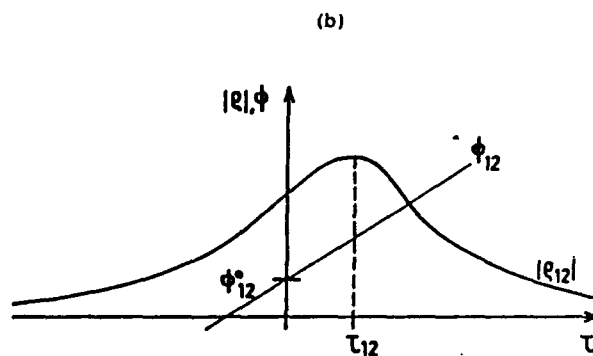


FIG. 2. Schematic showing the phase difference between the signals in two spatially separated receiving antennas, A_1 and A_2 , when the refractivity layer S is tilted at an angle δ . The measured radial velocity due to the off-vertical beam is w^* rather than the true vertical velocity w . (b) Representation of an ideal cross-correlation function for the signals in two spatially separated receiving antennas. The magnitude is shown by the Gaussian curve labeled ρ_{12} . The phase-angle variation is shown by the straight line labeled ϕ_{12} . The lag between the signals in the two receiving antennas is τ_{12} , which is related to the horizontal wind. (c) The variation of the phase angle with time for the three receiving antennas is shown in an idealized form. The time at which each of the antennas was sampled is shown by the filled squares.

3. Incidence-angle measurements

The observation period was characterized by weak convection with variable cloudiness and occasional light rain during the first two days, followed by the passage of a warm front that first reached the radar site aloft at the beginning of the third day and passed the site at the surface at the end of the same day. The fourth and final day of observations was characterized by mostly stable conditions and clear skies. Larsen and Röttger (1985) have described the meteorological conditions in more detail.

The radar reflectivities from the combined measurements of the three receiving antennas during the period are shown in Fig. 4, which represents contours of reflectivity at 4-dB intervals for the period beginning at 1200 LST 9 April and ending at 1200 LST 13 April. Higher values are indicated by darker shading. The

reflectivities generally decrease with height, even after the range-squared correction has been applied, due to the decreasing mean atmospheric density. The enhancement due to the sharp temperature variation near the tropopause is evident at heights between 9 and 12 km. The other notable feature is the band of enhanced reflectivities associated with the front, which stretches from the tropopause near 0000 LST 12 April to approximately 3 km at 0000 LST 13 April. The tropopause height rises after the front has passed.

Potential temperatures calculated from the Hannover rawinsonde profiles are shown in Fig. 5 in a similar format for the same period. The location of the radar and rawinsonde tropopause height agree well, as do the location of the frontal boundary inferred from the rawinsonde data and from the radar reflectivity data. Larsen and Röttger (1983, 1985) have discussed a number of such cases and have shown that the radar and rawinsonde observations generally agree well.

For the period corresponding to the reflectivity measurements shown in Fig. 4, the phase angle of the cross correlation at zero lag was calculated for each antenna pair. In addition, the phase angles for the previous and subsequent lags were also calculated. The

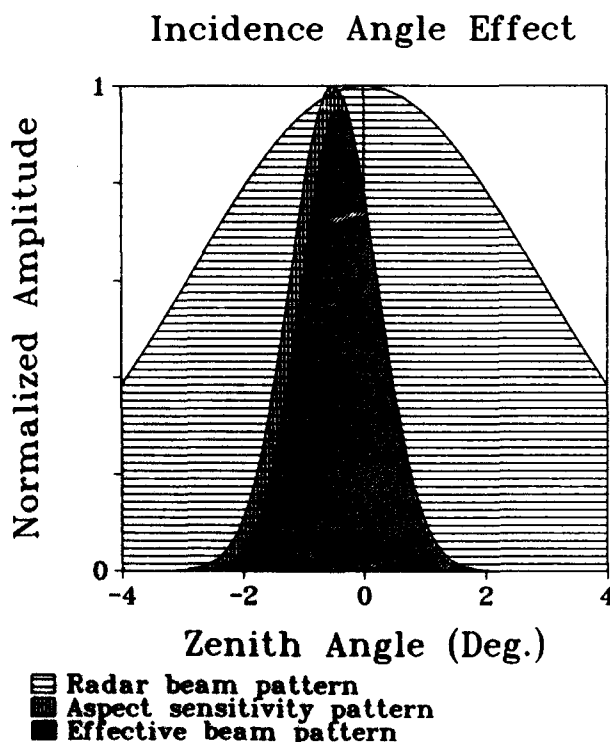


FIG. 3. Schematic showing the off-vertical incidence-angle effect for a nominally vertically pointing beam. The wide Gaussian represents the antenna beam pattern. The narrow Gaussian indicated by vertical hatching represents the backscatter pattern produced by a combination of the aspect sensitivity effect and a refractive index layer inclined with respect to the horizontal. The effective beam pattern is a convolution of the other two patterns and is shown as the narrow Gaussian with diagonal hatching.

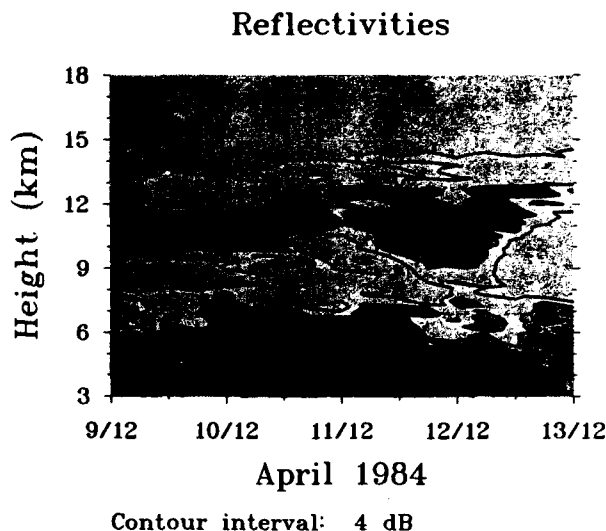


FIG. 4. Six-hour-average reflectivity measured with the SOUSY-VHF radar over the 4-day period. The contour interval is 4 dB, and the reflectivities are given in arbitrary units since the radar was not calibrated. The notation 9/12 refers to 1200 MET 9 April.

latter would not have been necessary if the three receiving antennas had been sampled simultaneously, but the offset in the sampling scheme illustrated in Fig. 2c had to be taken into account. The adopted correction scheme was a simple linear interpolation between the two values closest to the zero lag. We will return to an assessment of the validity of this approach in section 5.

As mentioned earlier, data were recorded for 8 min beginning at 0, 20, and 40 min after the hour. Each 1 min of data was analyzed separately to produce the cross-correlation phase angles, along with the standard horizontal winds, vertical velocities, and power pa-

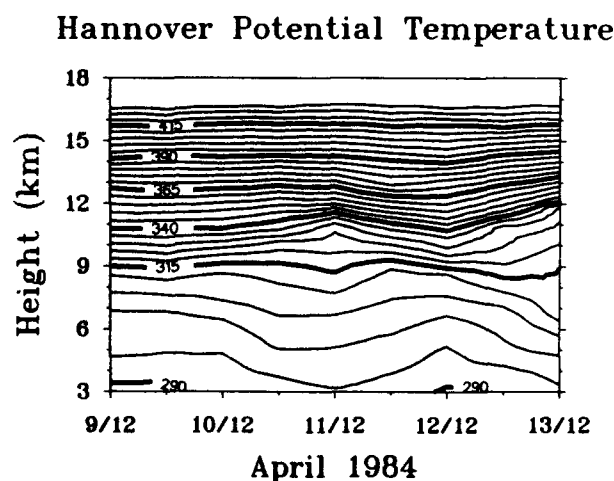


FIG. 5. Contours of potential temperature for the period corresponding to the data in Fig. 4. The values were calculated from the Hannover rawinsonde data. The Hannover station is located approximately 90 km northwest of the radar site.

rameters. The 8 min of data were averaged to produce a single value assumed to be representative of a given 20-min period. Since the sampling was not continuous, errors or biases may be introduced by assuming that the 8 min of data are representative of the true average for the entire 20-min period, but we have no means to test for such biases and will assume that any errors that are introduced are small and random.

The radar wavelength is 5.58 m. The separation between the centers of the west and south receiving antennas or the east and south antennas was 35.54 m, and the separation between the centers of the west and east antennas was 39.30 m. Substituting these values into Eq. (1) shows that incidence-angle measurements become ambiguous if the angles are outside the range $\pm 4.5^\circ$ for the smaller antenna separation or $\pm 4.0^\circ$ for the larger separation when the phase difference ϕ varies from -180° to $+180^\circ$. The ambiguity is eliminated, however, by the beam pattern weighting of the transmitting antenna, which has a half-power beamwidth of $\pm 2.5^\circ$. Nearly all of the 8-min-average angles for the entire dataset had magnitudes less than 2° , indicating that angular aliasing of the incidence-angle measurements was not a problem. Averaging over longer intervals further reduced the mean magnitudes of the angles, as might be expected.

Contours of the measured incidence angles are shown in Fig. 6. The upper portion of the figure shows the component along the west-east direction, derived from the west and east antenna measurements alone, while the lower portion shows the component along the south-north direction, derived from the combined west-south and east-south antenna pair measure-

ments. The contour interval is 0.2° , and larger positive values are indicated by darker shading. The contours corresponding to $+0.1^\circ$ are indicated by thicker lines. A positive angle corresponds to an effective incidence angle toward east or north, and negative angles correspond to incidence angles toward west or south. A northward incidence angle indicates, for example, that the refractivity layer is sloped from higher altitudes in the south to lower altitudes in the north if a layer is responsible for the off-vertical incidence angle. Figure 2a illustrates the geometry.

There is an uncertainty about the incidence-angle direction, but not about the magnitude, since instrumental phase calibrations are not available for the experiment period. In general, phase calibrations can be obtained easily but the application of the data described here was not anticipated at the time. The uncertainty was resolved by comparing the sign of the 4-day-average measured angles at the lower heights with the 4-day-average east-west and north-south slopes of isentropic surfaces calculated from the standard rawinsonde data for the area. A more detailed comparison is needed to determine if there is a correlation between the layer tilt angles inferred from the incidence angles measured with the radar and the orientation of the isentropic surfaces over scales of several hundred kilometers, but such a study is beyond the scope of the present work.

The contour plot in Fig. 6a shows that negative incidence angles dominate in the west-east plane, and that the maximum magnitudes of the angles are larger in the troposphere than in the stratosphere. At higher altitudes, the pattern becomes more erratic as regions with low signal-to-noise ratio begin to dominate.

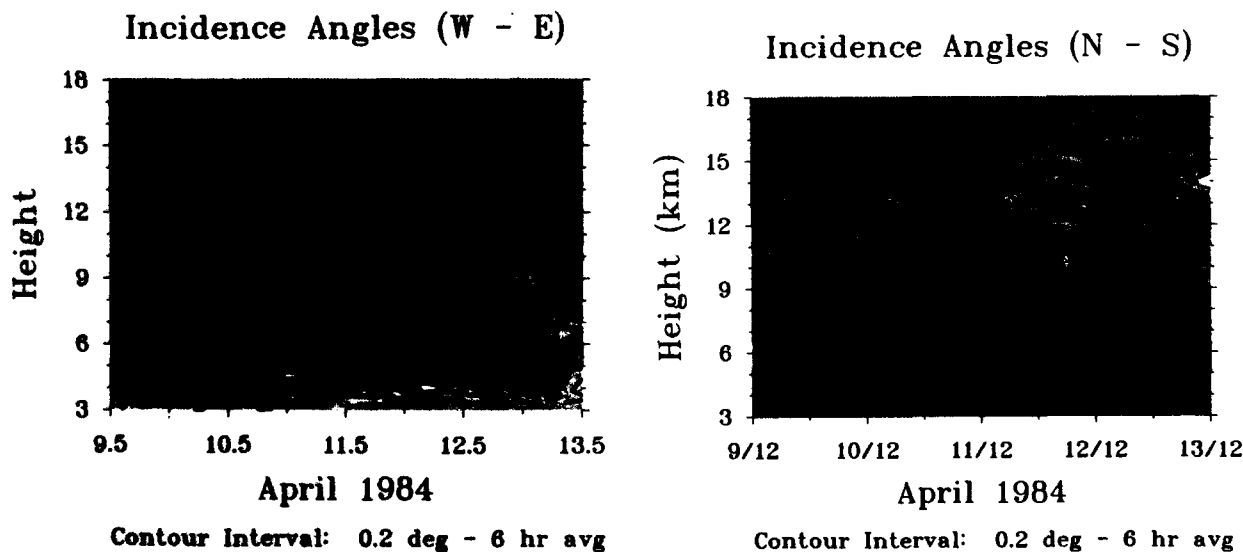


FIG. 6. (a) Incidence angles along the west-east direction calculated from the measured phase-angle differences. The contour interval is 0.2° . The contour lines corresponding to $+0.1^\circ$ are indicated by heavier lines, and larger positive values have darker shading. (b) Tilt angles along the south-north direction shown in a format similar to (a). The data from the west-south and east-south antenna pairs were combined to produce the values.

Figure 6b shows that positive incidence angles dominate in the troposphere in the north-south plane, whereas negative angles dominate in the stratosphere. The sloping frontal boundary is also evident in the figure and can be seen to stretch into the tropopause-lower stratosphere region. Both Figs. 6a and 6b show 6-h-average values of the incidence angles, which generally do not exceed magnitudes of 1° . Decreasing the averaging interval increases the small-scale structure evident in the figures and increases the maximum magnitudes, as mentioned earlier.

4. Vertical velocity corrections

a. Velocity correction formulas

A nominally vertical radar beam receiving signals primarily from an off-vertical angle δ , as shown in Fig. 2a, measures a radial velocity w' that is different from the vertical velocity w . The two are then related by the equation

$$w = (w' + V_h \sin \delta) / \cos \delta \quad (2)$$

where V_h is the horizontal wind component. More generally, both components of the inclination have to be taken into account, together with both wind components, and the expression for the true vertical velocity becomes

$$w = w' / \cos \delta + u \tan \delta_{ew} + v \tan \delta_{ns} \quad (3)$$

where δ is the total incidence angle, δ_{ew} is the east-west component, and δ_{ns} is the north-south component. The zonal velocity component u is positive toward the east, and the meridional component v is positive toward the north. Since the incidence angles are small, usually less than 2° , a good approximation to Eq. (3) is

$$w \approx w' + u \sin \delta_{ew} + v \sin \delta_{ns} \quad (4)$$

and is used in the remaining calculations.

b. Observed horizontal winds

The winds measured with the radar during the observation period are shown in Figs. 7a,b for the zonal and meridional velocities, respectively. The positive values, corresponding to eastward and northward wind components, have darker shading. The strongest winds are in the meridional direction with the largest northward velocities occurring in the first half of the period and the largest southward velocities in the second half. The circulation around the front is evident, as the two smaller areas of alternately southward and northward flow near the tropopause on 11 April and during the first half of the day on 12 April. The two sets of wind components have been combined to yield the total wind speed, which is represented in Fig. 7c. The 20 m s^{-1} contours are indicated by heavier lines.

c. Vertical-beam radial velocities

The radial velocities observed in the vertical beam are shown in Fig. 8a. Again, a 6-h averaging interval was used. The contour interval is 5 cm s^{-1} , and positive (i.e., upward) values are indicated by darker shading. The zero line is shown as a heavier contour. The dominant features are the larger radial velocities that generally occur in the troposphere rather than in the stratosphere. There is a period of predominantly positive radial velocities in the troposphere from the beginning of the observations until approximately 1200 LST 11 April. Positive velocities would be upward if the reflectivity layers are exactly horizontal, so that the tilt angles are zero or if the isolated scatterers are symmetrically distributed within the beam. There is also a band of positive velocities associated with the front that begins on 12 April and stretches into the early hours of 13 April. Finally, there are strong negative velocities between 9 and 12 km during the first half of the day on 13 April.

Radial velocity corrections were calculated according to Eq. (3) using the incidence-angle values shown in Figs. 6a,b and the horizontal wind data shown in Figs. 7a,b. The resulting radial velocity corrections are presented in Fig. 8b in the same format and with the same contour spacing as the radial velocities in Fig. 8a. The corrections are small except for the region below $\sim 9 \text{ km}$ from 1200 MET 9 April until 1200 MET 11 April. During this period, the corrections are comparable in magnitude to the measured radial velocities. The corrections in the region of the frontal zone are small in spite of the large incidence angles, because the velocities are either perpendicular to the incidence-angle azimuth or because the largest velocities do not coincide exactly with the regions in which the largest off-vertical angles occur.

The radial velocity corrections shown in Fig. 8b were applied to the radial velocities in Fig. 8a to produce a corrected vertical velocity, i.e., the best estimate of the real vertical velocity. The results are shown in Fig. 8c in the same format as the two previous figures. The most notable characteristics are that the region of apparent steady upward motion below 9 km during the first 48 h of observation is either weaker or has largely disappeared. In fact, subsidence can be seen during a portion of the period. The strongest region of ascent is now just below the tropopause and is centered at a time near 2200 MET 10 April. The strong apparent subsidence that was present between approximately 8 and 12 km after 1800 MET 13 April also has largely vanished. The ascent connected with the frontal band remains, although stronger upward motion is now evident below the frontal boundary in the troposphere, i.e., from about 0000 MET 12 April until 1200 MET 13 April. The periods with vertical velocity magnitudes greater than 10 cm s^{-1} are essentially limited to the region close to the tropopause near the jet and the re-

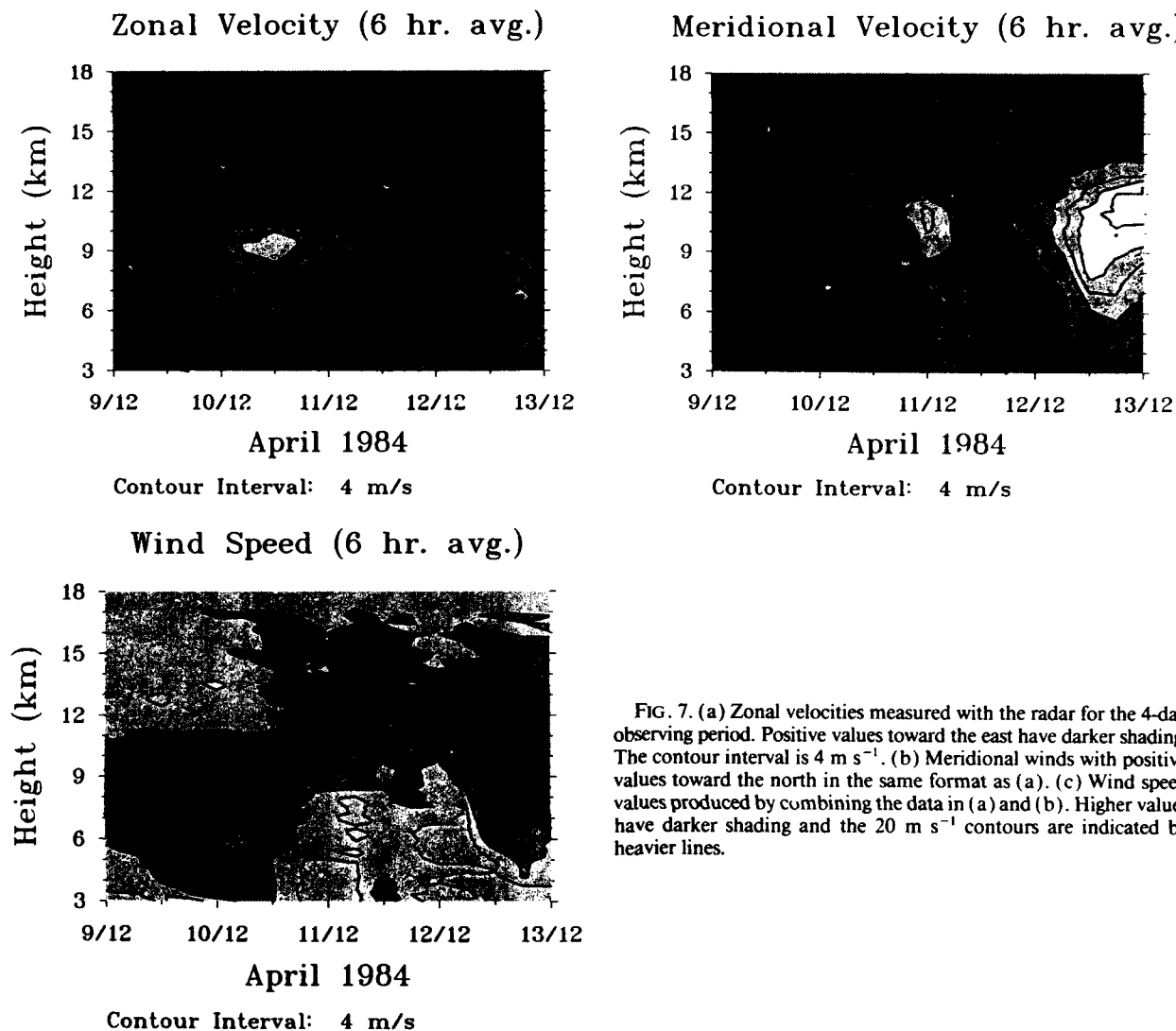


FIG. 7. (a) Zonal velocities measured with the radar for the 4-day observing period. Positive values toward the east have darker shading. The contour interval is 4 m s^{-1} . (b) Meridional winds with positive values toward the north in the same format as (a). (c) Wind speed values produced by combining the data in (a) and (b). Higher values have darker shading and the 20 m s^{-1} contours are indicated by heavier lines.

gion in the unstable air ahead of the front. Superimposing the corrected vertical velocity contours and the contours of potential temperature shown in Fig. 5 also gives an indication of better qualitative agreement. The strong vertical circulation evident near the tropopause during the latter half of the day on 10 April coincides with the region in which the potential temperature contours diverge, and the vertical velocities change direction where the slopes of the contours change sign. Also, the positive velocities are associated with the front end at the height where the potential temperature contours become horizontal in the stratosphere. A better correspondence between changes in slope of the potential temperature contours and the sign of the corrected vertical velocity was found at other times in the troposphere.

Figure 9a shows the 4-day-average profile of the radial velocity in the vertical beam and the corrected vertical velocity for heights between 3.0 and 17.1 km.

The largest corrections are found in the troposphere below the height of the jet stream. In fact, the effect of the corrections is to reduce the average to values close to zero for heights below $\sim 7 \text{ km}$. The large average velocities between 7 and 10 km are the result of the jet stream feature evident during the latter half of 10 April. The corrections are small above 13 km. Figure 9b shows the corresponding rms differences between the radial and corrected vertical velocities. The 6-h-average data were used for the calculation. The largest differences are $10\text{--}13 \text{ cm s}^{-1}$ and occur just below the tropopause. The differences decrease at the upper levels to values near 5 cm s^{-1} .

Examples of the 6-h-average profiles of the vertical-beam radial velocity and the corrected vertical velocity are shown in Figs. 10a–c. The curves represent the individual 6-h-average profiles that correspond to the data shown in the contour plots in Figs. 8a,c. The first example in Fig. 10a depicts the vertical-beam radial

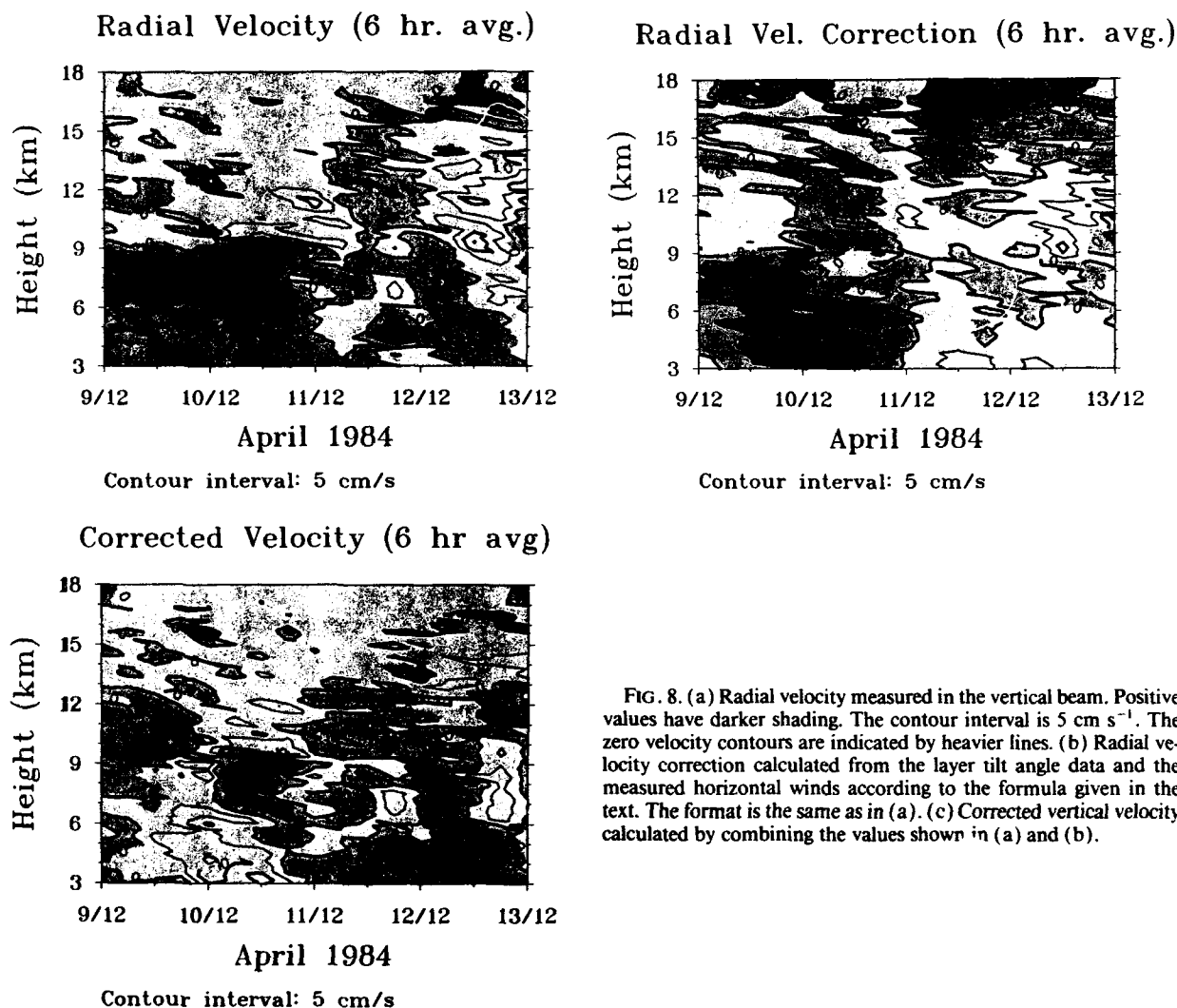


FIG. 8. (a) Radial velocity measured in the vertical beam. Positive values have darker shading. The contour interval is 5 cm s^{-1} . The zero velocity contours are indicated by heavier lines. (b) Radial velocity correction calculated from the layer tilt angle data and the measured horizontal winds according to the formula given in the text. The format is the same as in (a). (c) Corrected vertical velocity calculated by combining the values shown in (a) and (b).

velocity as the dashed curve and the corrected vertical velocity as the solid line. The time of the profile was 1800 MET 9 April during the period when the heights below the tropopause were characterized by steady positive velocities. The largest radial velocities were found between 5 and 9 km with peak values of $10\text{--}17 \text{ cm s}^{-1}$. The corrected velocities still show a residual upward velocity in that height range, but the largest magnitudes are reduced to $5\text{--}6 \text{ cm s}^{-1}$.

The second example shown in Fig. 10b corresponds to a time of 0600 MET 12 April and represents a profile through the frontal circulation. At that time, the corrections to the radial velocities are small, and the raw radial velocity and corrected vertical velocity profiles look similar.

The third example for 0000 MET 13 April when the radial velocities showed negative values of as much as 15 cm s^{-1} between 8 and 12 km is shown in Fig. 10c. At that time, the corrected vertical velocities showed negative velocities as well but with maximum magni-

tudes that were generally 5 cm s^{-1} or less. The profiles above 12 and below 7 km are relatively unaffected by the correction.

5. Assessment of possible errors

As mentioned earlier, the experimental setup was not ideal for incidence-angle measurements due to constraints imposed by the equipment, such as the need for time multiplexing. In particular, the sequential sampling scheme for the three antennas introduced a temporal lag of either one-third or two-thirds of the total cycle time of 370 ms, as illustrated in Fig. 2c. Since linear interpolation was used to produce phase-angle values at the same delay, errors can arise if the phase angle is varying nonlinearly. The phase-angle variation is produced by a radial velocity of the scatterers or reflectivity structures in the beam, and the variation will be linear for small temporal lags, as shown for the ideal case in Fig. 2c if the velocity is constant

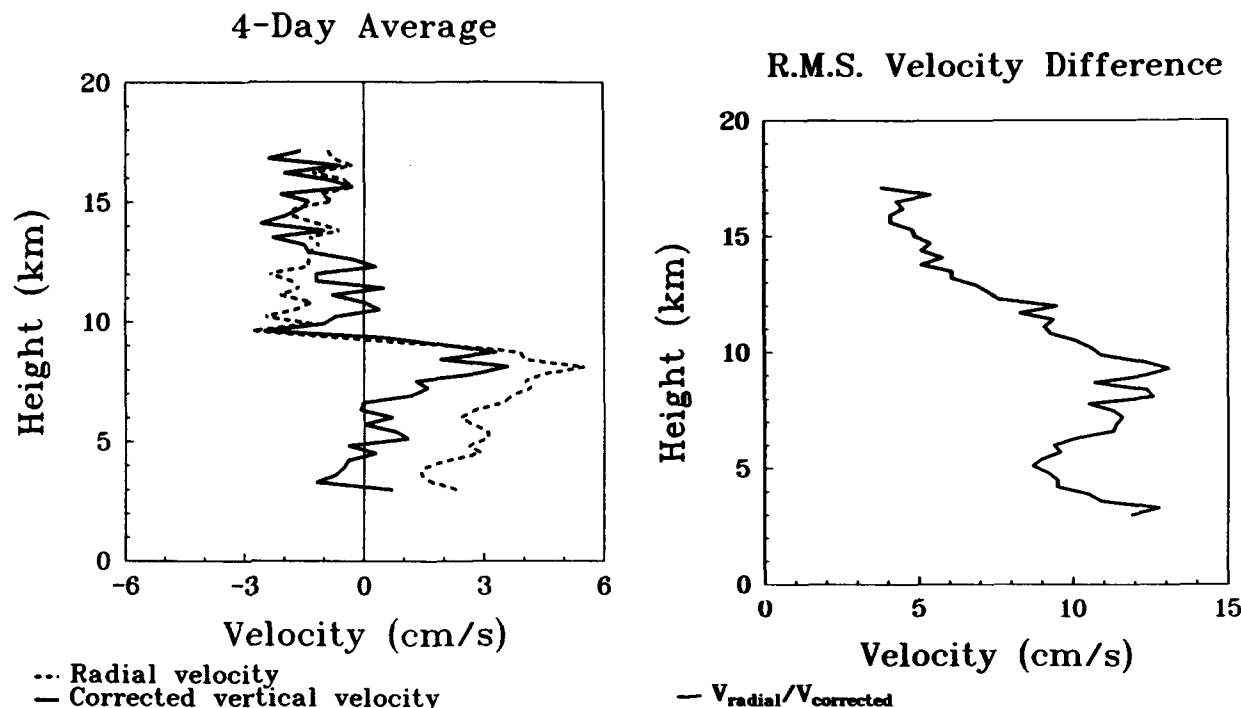


FIG. 9. (a) Four-day-average profiles of the radial velocity in the vertical beam and the corrected vertical velocities. (b) Root-mean-square difference between the radial velocity in the vertical beam and the corrected vertical velocity as a function of height for the 4-day observation period.

during the cycle time. Therefore, a deviation from a linear phase variation corresponds to variations in the velocity over the cycle period. One way to determine if such potential errors are indeed a problem is to compare the deviation of the zero-lag phase angle from the value predicted by a straight-line fit between the values at lags of -1 and $+1$. The deviation defined in this way is thus an angle measured in degrees, which is in the range between -180° and $+180^\circ$.

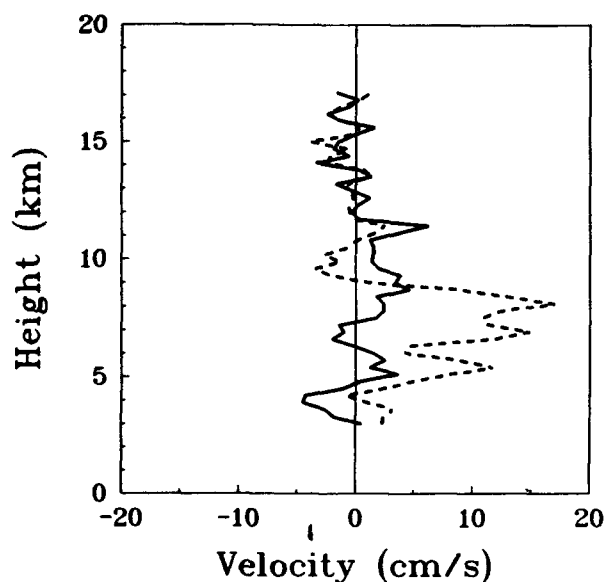
The calculated values of the phase deviation are shown as contours in Fig. 11. The contour spacing is 2° and the positive values have been shaded. Note again that the incidence angles δ_{ij} are limited to the range between -4° and $+4^\circ$ as described earlier, but the phase deviations shown in Fig. 11 are related to the ϕ_{ij} in Eq. (9) and can vary between -180° and $+180^\circ$. The calculated values, however, are generally less than 4° in magnitude on the average, indicating that the linear interpolation is valid. Figure 11 also shows that the deviations are randomly distributed without any bias toward particular periods in the observation interval, which is expected since there should not be significant velocity changes over the cycle time of 370 ms.

The average of the linear deviations for all four days is shown in Fig. 12, in which the deviations for the west-south antenna pair (ANT 1-3) are depicted as circles, the deviations for the west-east pair (ANT 2-1) are depicted as triangles, and the deviations for the east-south pair (ANT 2-3) are depicted as squares.

The average values are less than 1° at most heights. There is an indication of a small bias toward negative values for the west-east and west-south pairs below 10 km, but the magnitudes of the values are so small as to be insignificant in the present context.

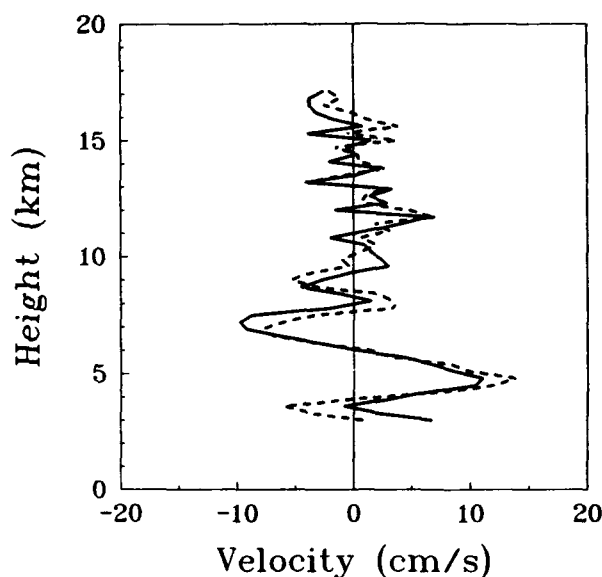
The small phase deviations shown in Fig. 11 indicate that the variations in the measured phases are systematic rather than noisy or random. However, the analysis presented so far does not give a direct indication of how accurately the phase differences between antennas can be measured with the technique that we have used. Estimating error bars directly from the measurements is difficult (see e.g., May 1988; or Hocking et al. 1989), but we can use the known radar and data analysis parameters in combination with the theoretical results presented by Hocking et al. (1989) to estimate the uncertainties in the measurements. Figure 11 in the Hocking et al. article shows curves of the phase-angle uncertainty as a function of the signal-to-noise ratio and the magnitude of the cross-correlation function at zero lag. The signal-to-noise ratio cutoff used in our data analysis procedure was 3 dB, and typical values of the cross correlation at zero lag was 0.7 or greater, giving an uncertainty in the phase of $\sim 10^\circ$. The corresponding uncertainty in the measured incidence angles will be 0.25° for a 1-min measurement. The uncertainty will be less when the measured values are averaged over longer periods, as was done for the data presented earlier.

9 April 1800 MET



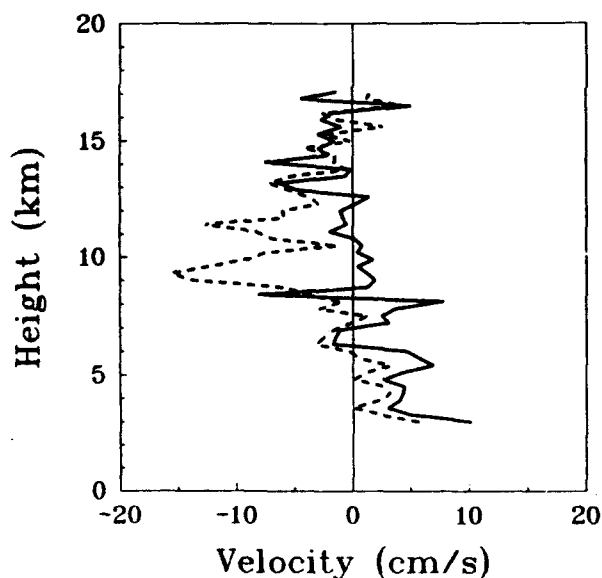
-- Radial velocity
— Corrected vertical velocity

12 April 0600 MET



-- Radial velocity
— Corrected vertical velocity

13 April 0000 MET



-- Radial velocity
— Corrected vertical velocity

FIG. 10. (a) Vertical beam radial velocity (dashed line) and corrected vertical velocity (solid line) at 1800 MET 9 April 1984. (b) Same as (a) but for 0600 MET 12 April 1984. (c) Same as (a) but for 0000 MET 13 April 1984.

A major uncertainty in the experiment is that there is no independent standard for comparison that can be used to corroborate the corrected vertical velocities. Thus, the data and the analysis indicate the potential importance of considering corrections of the type applied here, but the evidence that the corrected velocities give a better estimate of the true vertical velocity is circumstantial at best. Also, the incidence-angle mag-

nitudes are correct, but there is uncertainty about the sign for this particular dataset. Test signals could have been used to determine the direction unambiguously, but the application of the method described here to the April 1984 dataset was not anticipated at the time. The incidence-angle directions were ultimately chosen so that layer tilt angles corresponding to measured incidence angles agreed with the directions of the 4-day-

average slopes of the isentropic surfaces calculated from rawinsonde data from surrounding stations. However, an open question is whether the refractivity layers are also isentropic surfaces and, if so, whether the slopes are correlated over distances comparable to the separation between rawinsonde stations.

Uncertainties in the estimation of the radial velocities from the Doppler spectra are also of concern. Again, direct estimates of the errors based on the data alone are difficult (see e.g., May et al. 1989), but we can use Eq. (6.22a) from the text by Doviak and Zrnić (1984b), which was also used by May et al. (1989). The expression gives the variance in the velocity estimate as a function of sampling intervals, correlation magnitudes, and signal-to-noise ratios. Using the parameters already described earlier, the uncertainty in the radial velocity estimate based on the vertical beam data becomes $\sim 1.5 \text{ cm s}^{-1}$. Based on simulated data, May et al. (1989) found that the theoretical equation in some cases underestimated the uncertainty by as much as a factor of 2. However, the error bars will still be small in comparison to the typical magnitudes of the vertical-beam radial velocities even if the uncertainty is doubled.

Finally, scatterplots and correlation coefficients between the various parameters give some indication that the corrections that have been applied are sensible. Figure 13 shows a correlation matrix plot, which represents scatter diagrams for all combinations of the velocity and incidence-angle parameters. The radial velocity in the vertical beam is indicated by w , and the corrected radial velocity by w_{pri} . The highest corre-

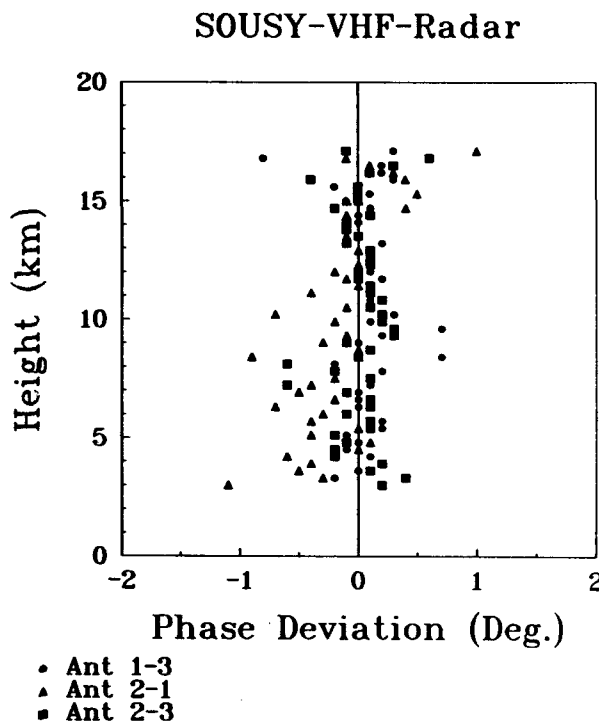


FIG. 12. Mean phase deviation for the three antenna pairs.

lation is between the radial velocity and the meridional wind component with a value of 0.57. However, the correlation is reduced to 0.01 after the correction is applied to the radial velocities. The correlations between the radial velocities and the east-west and north-south incidence angles are 0.29 and 0.25, respectively. The correlations are reduced to 0.08 and 0.06 after the corrections are applied. Röttger et al. (1990) also found correlation coefficients of ~ 0.3 between the vertical-beam radial velocities and the incidence angles.

6. Conclusion

To our knowledge, applying the incidence-angle correction to the radial velocity measurements from a vertical beam has not been attempted previously. Yet, the magnitude of the correction that we have calculated is comparable to the measured radial velocities for most of the 4-day period of our experiment. The correction is, of course, potentially important for VHF radar measurements of the vertical velocity. Shorter wavelength radars do not show aspect sensitivity effects and are unlikely to require the application of the correction discussed here, but the shorter wavelength instruments are also more sensitive to precipitation so that they cannot measure vertical air motions in all conditions as the VHF systems can (e.g., Larsen and Röttger 1986).

Since we have no independent vertical velocity measurements for comparison, we can only assess the

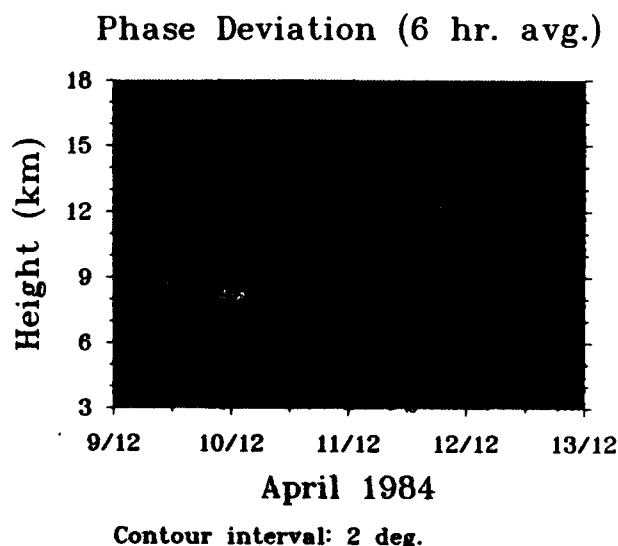


FIG. 11. Deviation of the measured phase at zero lag from the phase angle inferred by linearly interpolating between the phase-angle values at the -1 and $+1$ lags. The values are in degrees. Positive values have darker shading. The deviations for the west-south antenna pairs are shown, but the other antenna combinations give similar results.

Correlation Matrix

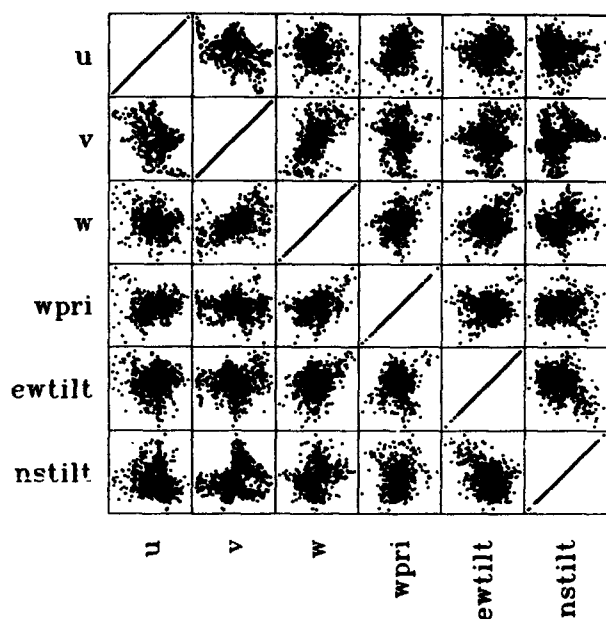


FIG. 13. Correlation matrix scatterplot for all combinations of the velocity and incidence-angle parameters. The radial velocities are indicated by *w*. The corrected vertical velocities are indicated by *wpri*.

qualitative improvement in the vertical velocities produced by application of the correction. Specifically, a period of steadily upward velocities stretching over 48 h and covering the entire sampled tropospheric height range was shown by the uncorrected vertical velocities. The period of steady ascent was inconsistent, however, with the meteorological conditions during the period that was characterized by varying cloudiness and occasional brief rain showers. The correction to the radial velocities produced a final set of corrected velocities that indicated interspersed subsidence and a more localized strong vertical circulation confined to the height range close to a wind speed maximum near the tropopause. In addition, the raw vertical velocity data indicated that the region of ascent was confined to the region around the frontal boundary with little ascent in the unstable air ahead of the front. The corrections left the ascent near the frontal boundary largely unaffected but showed that ascent was also present in the region ahead of the front. The conclusion is that the corrected velocities are in better agreement with expectations based on the meteorological conditions, at least in the qualitative sense. Also, the correlation between the radial velocities and the incidence angles and the radial velocities and the horizontal winds decrease after application of the corrections.

Only a few comparisons of radar vertical velocity data and vertical velocity values derived from rawin-

sonde data have appeared in the literature, notably the studies by Nastrom et al. (1985) and Larsen et al. (1988). The comparisons indicate some overall agreement, but there were also significant differences. The discrepancies were conjectured to be due in part to inherent differences in the way that the two datasets were sampled, since the radar provides a point measurement averaged over an extended period, while the rawinsonde data is a more-or-less instantaneous measurement over an extended area. It is likely that sampling differences are responsible for some of the discrepancies, but the magnitude of the corrections that we have calculated for the April 1984 dataset are sufficiently large to be taken into account for further comparisons.

The procedures for calculating the corrected vertical velocities are clear, as outlined here, but many questions remain about the basic properties of the layers that create the need for the correction terms. Röttger et al. (1990) found periodicities in the measured incidence angles, both in time and along the vertical direction, that suggested that the layers are associated with low-frequency gravity waves. Even so, it is not clear if the layers are being displaced by the flow velocities associated with the waves, in which case they may represent an isentropic surface, or if the layers are occurring at certain phases of breaking waves, for example, in which case the layers will not represent isentropic surfaces. Röttger et al. (1990) discuss various aspects of these points, although new types of measurements or analysis and comparisons between simple wave models and the observations will likely be needed to resolve some of the issues.

Our observations only cover a 4-day period but show that the uncorrected vertical-beam radial velocities can potentially lead to biases in the data. In our observations, the predominantly upward velocities during the first 48 h would lead to a bias in the average profile for the 4-day period. The off-vertical incidence angles may also produce biases in even longer term vertical-beam radial velocity measurements if the average layer tilt angles are nonzero and there is a steady wind component along the tilt direction. The latter cannot be excluded, even when the averaging interval is long. Shorter wavelength radars would not require the application of the correction, but great care would have to be taken to ensure that data dominated by precipitation scatter is eliminated before producing an average vertical velocity profile, since the latter would produce biases of a different kind.

More experiments are clearly needed to make a more quantitative assessment of the tilted layer corrections that we have calculated here. In particular, a combination of the spaced antenna measurements with vertical beams and simultaneous or near-simultaneous off-vertical beam measurements can be used to calculate the vertical beam radial velocity, the vertical velocity corrections, and the divergence as a function of height.

The integrated divergence can be used for comparison with the corrected vertical velocity, since the two should agree within an additive constant. The latter, however, was not possible with the SOUSY-VHF radar setup.

Acknowledgments. MFL received support from the Air Force Office of Scientific Research under Contract F49620-88-C-0121 and from the Ministry of Education, Research, and Culture of Japan during the course of the study. MFL and JR both thank the staff of the Max-Planck-Institut für Aeronomie for their invaluable help in the data-taking portion of the research.

REFERENCES

- Doviak, R. J., and D. S. Zrnić, 1984a: Reflection and scatter formula for anisotropically turbulent air. *Radio Sci.*, **19**, 325-336.
- , and —, 1984b: *Doppler Radar and Weather Observations*. Academic Press, 400 pp.
- Gage, K. S., B. B. Balsley and J. L. Green, 1981: Fresnel scattering model for the specular echoes observed by VHF radar. *Radio Sci.*, **16**, 1447-1453.
- Green, J. L., and K. S. Gage, 1980: Observations of stable layers in the tropopause and stratosphere using VHF radar. *Radio Sci.*, **15**, 395-405.
- Hocking, W. K., P. May and J. Röttger, 1989: Interpretation, reliability, and accuracies of parameters deduced by the spaced antenna method in middle atmosphere applications. *Pure Appl. Geophys.*, **130**, 571-604.
- Larsen, M. F., and J. Röttger, 1983: Comparison to tropopause height and frontal boundary locations based on radar and radiosonde data. *Geophys. Res. Lett.*, **10**, 325-328.
- , and —, 1985: Observations on frontal zone and tropopause structures with a VHF Doppler radar and radiosondes. *Radio Sci.*, **20**, 1223-1232.
- , and —, 1986: A comparison of thunderstorm reflectivities measured at VHF and UHF. *J. Atmos. Oceanic Technol.*, **4**, 151-159.
- , and —, 1989: The spaced antenna technique for radar wind profiling. *J. Atmos. Oceanic Technol.*, **6**, 920-938.
- , —, and T. S. Dennis, 1988: A comparison of operational analysis and VHF wind profiler vertical velocities. *Mon. Wea. Rev.*, **116**, 48-59.
- May, P. T., 1988: Statistical errors in the determination of wind velocities by the spaced antenna technique. *J. Atmos. Terr. Phys.*, **50**, 21-32.
- , T. Sato, M. Yamamoto, S. Kato, T. Tsuda and S. Fukao, 1989: Errors in the determination of wind speed by Doppler radar. *J. Atmos. Oceanic Technol.*, **6**, 235-242.
- Nastrom, G. D., W. L. Ecklund and K. S. Gage, 1985: Direct measurement of large-scale vertical velocities using clear-air Doppler radars. *Mon. Wea. Rev.*, **113**, 708-718.
- Röttger, J., 1980: Reflection and scattering of VHF radar signals from atmospheric refractivity structures. *Radio Sci.*, **15**, 259-276.
- , 1981: Wind variability in the stratosphere deduced from spaced antenna VHF radar measurements. *20th Conf. on Radar Meteorology*, Boston, Amer. Meteor. Soc., 22-29.
- , 1989: The interpretation of MST radar echoes: The present knowledge of scattering-reflection and the irregularity generation mechanisms. *Handb. MAP*, **28**, 68-82.
- , and M. F. Larsen, 1983: Potential advantages of the spaced antenna method for operational wind profiling. *Papers Presented at the Workshop on Very Short-Range Forecasting: Systems Research Aspects*, Boulder, WMO, 97-102.
- , and H. M. Ierke, 1985: Postset beam steering and interferometer applications of VHF radars to study winds, waves, and turbulence in the lower and middle atmosphere. *Radio Sci.*, **20**, 1461-1480.
- , and M. F. Larsen, 1990: UHF/VHF radar techniques for atmospheric research and wind profiler applications. *Radar in Meteorology*, D. Atlas, Ed., Amer. Meteor. Soc., 235-281.
- , C.-H. Liu, J. K. Chao, A. J. Chen, C. J. Pan and I.-J. Fu, 1990: Spatial interferometer measurements with the Chung-Li VHF radar. *Radio Sci.*, **25**, 503-515.
- Tsuda, T., T. Sato, K. Hirose, S. Fukao and S. Kato, 1986: MU radar observations of the aspect sensitivity of backscattered VHF echo power in the troposphere and lower stratosphere. *Radio Sci.*, **21**, 971-980.

Oblique frequency domain interferometry measurements using the middle and upper atmosphere radar

R. D. Palmer,¹ S. Fukao,² M. F. Larsen,¹ M. Yamamoto,² T. Tsuda,² and S. Kato²

(Received October 21, 1991; revised May 11, 1992; accepted May 17, 1992.)

First results are presented from oblique frequency domain interferometry (FDI) measurements conducted using the middle and upper atmosphere radar in Japan in October 1990. Using the idea of Doppler sorting, an equation is derived which shows a parabolic variation of the oblique FDI cross-spectral phase as a function of Doppler velocity. However, because of the small range of Doppler velocities observed with the measured cross spectra, the phase has an approximate linear variation; that is, the cross spectra sample only a small portion of the parabolic structure and are therefore approximately linear and are shown to follow the model closely. Using the oblique FDI configuration, a comparison is drawn between simultaneous measurements of signal-to-noise ratio, coherence, three-dimensional wind, and profiles of FDI cross spectra. We find that the regions that exhibit a well-defined scattering layer correspond to those regions of high aspect sensitivity. An explanation is suggested based on the anisotropy of the turbulence.

1. INTRODUCTION

Frequency domain interferometry (FDI) is a technique for improving the range resolution of Doppler radars, as has been described in previous works [Kudeki and Stitt, 1987; Franke, 1990; Kudeki and Stitt, 1990; Palmer et al., 1990; Stitt and Kudeki, 1991; Chu and Franke, 1991]. High-reflectivity layers, which are often observed in the troposphere and stratosphere, typically have a vertical extent ranging from a few tens of meters to several hundred meters [Woodman, 1980]. The location of the layers cannot be resolved by conventional mesosphere-stratosphere-troposphere (MST) radars which have a typical resolution no better than 150 m. By transmitting two closely spaced frequencies, usually on successive pulses, the phase difference between these signals can be used to determine the location of the mean center and the range extent of a localized scattering region which may exist within the resolution volume. If the scattering layer is larger than the resolution volume, the coherence of the signal is small, and the phase difference holds no information. On the other hand, if a well-defined, thin scattering layer exists within

the resolution volume, the coherence will be large and the phase difference will provide an estimate of the relative location of the layer. However, the location that is determined is not absolute. Any phase shift introduced by the radar hardware will create a systematic shift in the estimated mean location so that the phase difference can only be used for obtaining the relative location of the scattering layer, that is, relative to the location given by the phase bias in the system. In addition, because of the curvature of constant range surfaces, a large radar beam width can cause the coherence to be diminished, even when a localized scattering layer is present [Franke, 1990]. Nevertheless, the FDI technique is a promising method for studies of the fluctuations of scattering layers which are smaller than the resolution volume.

The technique described herein is simply the use of FDI measurements for a predetermined set of oblique pointing directions, such as in a Doppler beam-swinging (DBS) experiment. With this capability we will be able to have simultaneous comparisons between the wind profiles and the results obtained from FDI, such as the location of thin scattering layers. Simultaneous comparisons are needed if one hopes to determine the link between thin scattering layers and gravity wave activity, which can be seen in wind profiles.

We will present the initial results obtained from the oblique FDI experiment and the modeling of the cross-spectral phase in section 2. Section 3 shows the relationship between FDI-observed scattering

¹ Department of Physics and Astronomy, Clemson University, Clemson, South Carolina.

² Radio Atmospheric Science Center, Kyoto University, Kyoto, Japan.

layers, wind profiles, and aspect sensitivity. The conclusions are given in section 4.

2. EXPERIMENTAL CONFIGURATION AND CROSS-SPECTRAL RESULTS

The data presented were obtained with the middle and upper (MU) atmosphere radar located in Shigaraki, Japan (34.85°N, 136.10°E) [Fukao *et al.*, 1985a, b], on October 26, 1990. In 1989 the MU radar was modified to allow switching of the transmitter frequency between consecutive pulses, thus providing the capability for FDI measurements [Palmer *et al.*, 1990]. The present study is an extension of the initial vertically pointing FDI measurements to the case of multiple pointing directions. The MU radar can change beam directions electronically in one interpulse period (IPP), and therefore almost simultaneous measurements can be obtained from different regions of the atmosphere.

A pulse length of 2 μ s was chosen, providing a range resolution of 300 m, which is large compared to typical scattering layers observed in the stratosphere [Woodman, 1980]. Instrumental limitations on the resolution of most MST radars is the main reason for the advent of FDI. Thirty-two range gates were sampled with a 300-m spacing starting at 6.0 km, providing height coverage up to 15.3 km for the vertical beam. Figure 1 shows the four beam directions in a Cartesian coordinate system with the transmitter frequency switching scheme displayed at the bottom of the figure. Since the resolution volume is 300 m in range, a 2π -phase difference over the extent of the volume is obtained if the difference in transmitter frequencies is chosen to be 500 kHz. The MU radar center frequency is typically 46.5 MHz, so the two frequencies were chosen to be $f_h = 46.75$ MHz and $f_l = 46.25$ MHz. As shown in Figure 1, the whole antenna array was first phased to produce the pointing direction of beam 1. A 2- μ s pulse of frequency f_h was then transmitted, and subsequently f_l was transmitted. Then, the antenna was pointed in the direction of beam 2 and the same sequence was carried out. The procedure was repeated for all beam directions, and 32 coherent integrations were performed. An eight-bit complementary code was used with a flip of the code every 2-beam cycle. The IPP was set to the minimum for the MU radar, which is 400 μ s. Since it takes two pulses for each pointing direction and

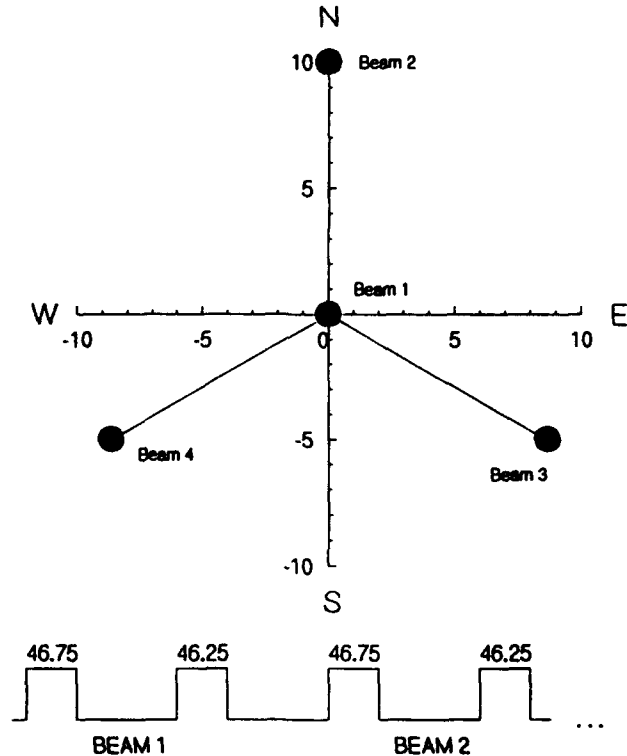


Fig. 1. Depiction of the four antenna pointing directions and the transmitter frequency switching scheme. Not shown is the complementary pulse coding, which was performed separately for each frequency.

with the number of coherent integrations set to 32 and an IPP of 400 μ s, the overall sampling time of the raw data stored on tape was 0.1024 s. The raw data were stored in blocks of 256 points approximately every 30 s for later processing.

In the postprocessing procedure the 256-point data sets from each frequency and each beam direction were Fourier transformed using a standard fast Fourier transform routine. The cross spectra were then estimated using the expression

$$S_{hl}(v_r) = \langle V_h(v_r) V_l^*(v_r) \rangle \quad (1)$$

where $V_h(v_r)$ and $V_l(v_r)$ are the Fourier transforms of the signals at f_h and f_l , respectively, angle brackets represent the ensemble average, and v_r is the Doppler radial velocity. For the data presented, the ensemble average was obtained by incoherently averaging over the 15-min time interval from 2117 to 2132 LT. The cross-correlation functions $R_{hl}(\tau)$ were obtained by calculating the inverse Fourier transform of (1). The cross-spectra and cross-correlations functions that we display were normal-

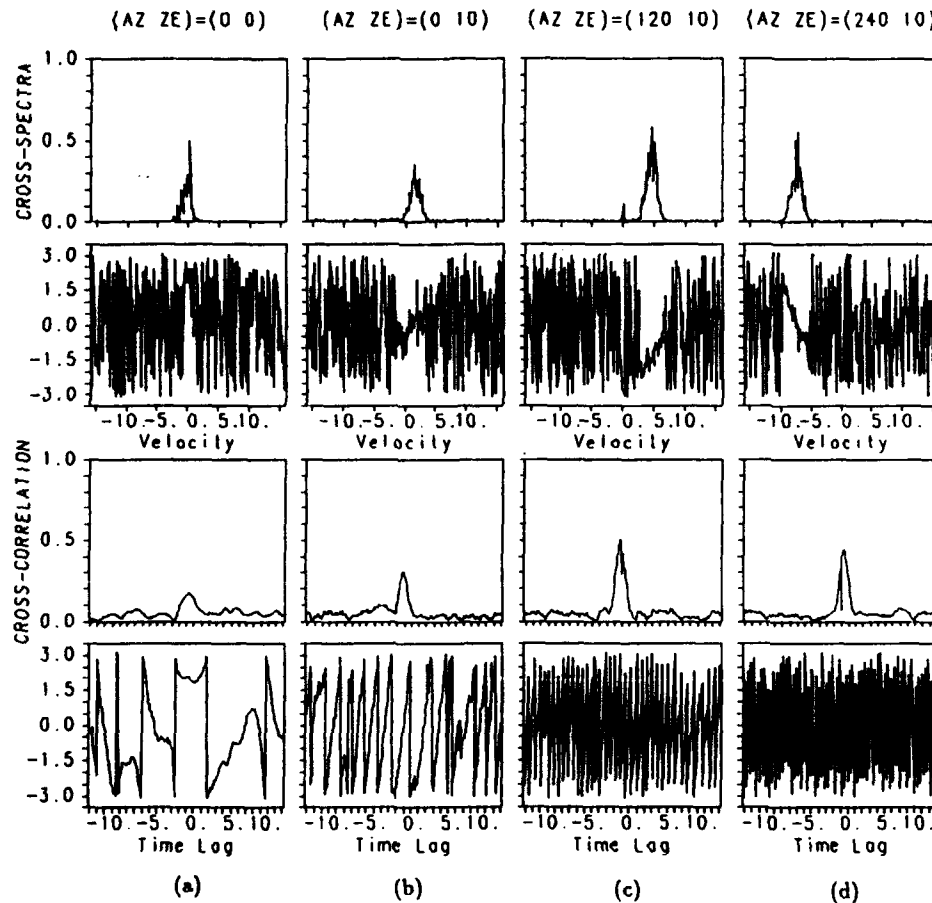


Fig. 2. Cross-spectra and cross-correlation functions at 11 km for a 15-min average of the FDI data taken on October 26, 1990, 2117–2132 LT using the MU radar. Azimuth and zenith angles are given by (a) Az = 0, Ze = 0, (b) Az = 0, Ze = 10, (c) Az = 120, Ze = 10, and (d) Az = 240, Ze = 10. The magnitudes of the cross-spectra and cross-correlation functions have been normalized to the peaks of the autospectra and autocorrelation functions, respectively.

ized by the peak in the autospectra and autocorrelation functions, respectively. Typical cross-spectra and cross-correlation functions are displayed in Figure 2 for an altitude of 11 km, with the azimuth and zenith angles displayed along the top of the figure. The first two rows of the figures are the magnitude and phase of the cross spectra and the last two rows are the magnitude and phase of the cross-correlation functions. A sampling time of 0.1024 s produces a Nyquist velocity of 15.8 m s^{-1} , and since there are 256 points in the data sequence, the inverse Fourier transform of the cross spectra produces a maximum lag time of 13.1 s.

The peaks in the spectra are shifted by the line-of-sight velocities along the various beam-pointing directions, as they would be in a non-FDI Doppler beam-swinging experiment. The Doppler

shifts indicate a predominantly zonal wind. The phase of the cross spectra $\phi(v_r)$, that is, the phase difference between the signals at the different frequencies, represents the relative location of the center of the scattering layer for a particular Doppler velocity:

$$\langle r(v_r) \rangle = \frac{\phi(v_r)}{2\Delta k} \quad (2)$$

where Δk is the wavenumber difference between the two transmitter frequencies. The so-called coherence function [Kudeki and Stitt, 1987] can give an estimate of the thickness of the scattering layer. If the coherence is small, the layer is diffuse or nonexistent. On the other hand, a large coherence can be used as an indication of a thin scattering

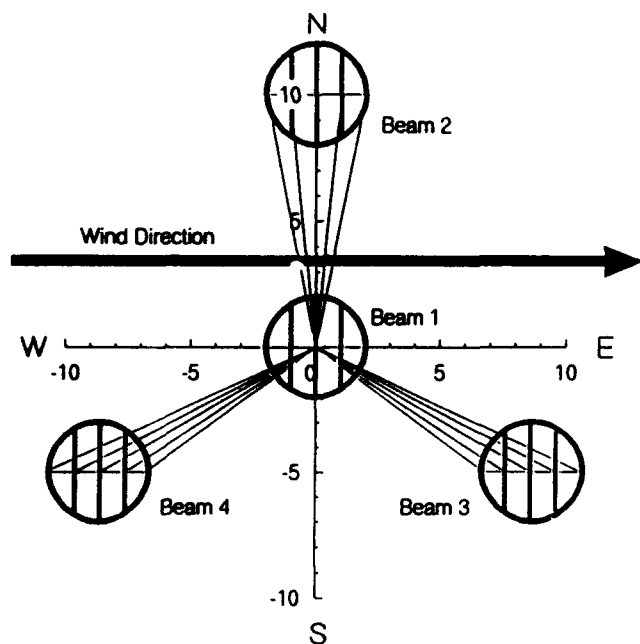


Fig. 3. Depiction of constant radial velocity contours (thick vertical lines within resolution volumes) for a hypothetical wind direction of 90° and the beam directions of Figure 1. When the cross spectra are calculated using the Fourier transform, these lines of constant radial velocity are integrated along to produce the corresponding phase in the cross spectra. The length of the lines emanating from the origin represent $\langle r(v_r) \rangle$ for each corresponding value of v_r .

layer if the beam width is relatively small [Franke, 1990]. It is interesting to recognize that the variance of the phase of the cross spectra also provides this information. Small variations, with much consistency in the phase, are produced by a well-defined, localized scattering layer.

It should be noted that in (2), $\langle r(v_r) \rangle$ and $\phi(v_r)$ have been given a dependence on radial velocity. When one calculates the cross spectra for a particular beam direction, the different angular regions of the resolution volume are Doppler sorted; that is, an integration takes place along lines of constant Doppler velocity. Figure 3 shows these lines of constant radial velocity as thick vertical lines in each of the different resolution volumes. The integration is weighted by the antenna pattern and any other weighting effects such as aspect sensitivity [Tsuda et al., 1986], producing a particular phase value for each Doppler velocity in the cross spectra. In Figure 3 the length of the lines, emanating from the origin and ending at the horizontal line in the middle of the resolution volume, represent the path

length traversed by the electromagnetic radiation $\langle r(v_r) \rangle$, for a corresponding Doppler velocity v_r .

To model $\phi(v_r)$, we begin by defining the unit vector, which is directed toward the center of radar beam pointing angle as

$$\mathbf{r} = [\sin \delta \sin \theta, \sin \delta \cos \theta, \cos \delta] \quad (3)$$

where θ and δ are the azimuth and zenith angle of the antenna beam, respectively. Let

$$\mathbf{r}' = [\sin \delta' \sin \theta', \sin \delta' \cos \theta', \cos \delta'] \quad (4)$$

define the variations of the pointing direction within the beam of the radar; that is, \mathbf{r}' is the unit vector in the direction of the position described by $\langle r(v_r) \rangle$ in (2). If the vector wind is constant throughout the beam and given as $\mathbf{v} = [u, v, w]$, then the radial velocity at any point in the radar beam can be described as

$$v_r = \mathbf{r}' \cdot \mathbf{v} = u \sin \delta' \sin \theta' + v \sin \delta' \cos \theta' + w \cos \delta' \quad (5)$$

Using the geometry of Figure 3, the various angles in (5) are found to be

$$\sin \delta' = \frac{(r'^2 - h^2)^{1/2}}{r'} \quad (6)$$

$$\cos \delta' = h/r' \quad (7)$$

$$\sin \theta' = \frac{[r'^2 - h^2(1 + \tan^2 \delta \cos^2 \theta)]^{1/2}}{(r'^2 - h^2)^{1/2}} \quad (8)$$

$$\cos \theta' = \frac{h \tan \delta \cos \theta}{(r'^2 - h^2)^{1/2}} \quad (9)$$

where $r' = |\mathbf{r}'|$ and h is the height to the center of the resolution volume. Assuming that w is small and substituting (6)–(9) into (5), an expression for r' is obtained, which is in terms of v_r . Using (2), the following model of the cross-spectral phase as a function of Doppler radial velocity is obtained:

$$\begin{aligned} \phi(v_r) &= 2\Delta k \langle r(v_r) \rangle = 2\Delta k r' \\ &= 2\Delta k h \left(\frac{1}{v_r^2 - u^2} \right) \{ v_r v \tan \delta \cos \theta \\ &\quad \pm u(u^2 - v_r^2 + \tan^2 \delta \cos^2 \theta [u^2 + v^2 - v_r^2])^{1/2} \} \end{aligned} \quad (10)$$

Figure 4 shows the expression for $h = 11$ km, $u = 40$ m s $^{-1}$, and $v = 9$ m s $^{-1}$ for the four beam positions.

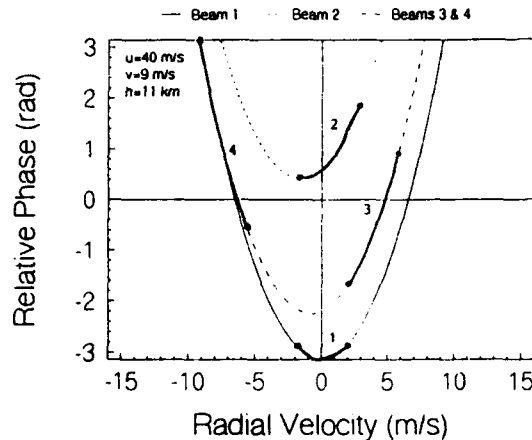


Fig. 4. Model of FDI cross-spectral phase as a function of Doppler radial velocity. The thick portions of the curves represent the ranges of Doppler velocities where the respective cross spectra have a nonrandom phase, that is, near the peak in the cross-spectral magnitude. It should be noted that these phase values are relative to the layer location, which has been assumed to be in the center of the resolution volume. Nevertheless, the shape of the curves shows the correspondence with the measured cross-spectral phase values of Figure 2.

The horizontal wind estimate was obtained from the Doppler velocities of the off-vertical beams and will be discussed in more detail in section 3. The above expression can be evaluated for all values of v_r , but the measured cross-spectral phases shown in Figure 2 are nonrandom only in the region centered at the mean Doppler velocity. These regions are emphasized in Figure 4 for the four beam positions. As one can readily see, the approximate linear variation is simply caused by the small range of Doppler velocities which the cross spectra can sample. As mentioned before, h in (10) has been set to 11 km which is the center of the resolution volume. Therefore all the phase values in Figure 4 are relative to the actual location of the scattering layer and should only be used to model the functionality of the phase and not the absolute values. Another possible problem is that the various beam positions could be observing different scattering layers, and therefore the relative positions would not be related by (10). Nevertheless, the measured cross-spectral phase values seem to indicate that this is not the case. In general, the height term in (10) could follow the relation $h = f(v_r, r', \theta, \delta, t)$ and therefore could be used to model the effects of tilted scattering layers [Larsen and Röttger, 1991; Palmer et al., 1991] or gravity wave activity on $\phi(v_r)$ from the ideal case

[Stitt and Kudeki, 1991]. Though not derived rigorously, turbulence will cause the contours of constant radial velocity in Figure 3 to change. In other words, the line integrals assumed in (10) will actually become surface integrals over all regions of the resolution volume, which possess the same radial velocity. Because of possible aspect sensitivity and beam pattern effects, the upward concavity of the parabolic structures of Figure 4 will be diminished. Therefore the slopes of the approximate linear variations in the measured cross-spectral phases will become smaller in the turbulent case.

3. COMPARISONS OF SIMULTANEOUS WIND FIELD AND CROSS-SPECTRAL ESTIMATES

One source of high-reflectivity layers in the troposphere and stratosphere is thought to be turbulent layers produced by Kelvin-Helmholtz instabilities (KHI). The criterion for such instabilities to occur is based on the Richardson number

$$Ri = \frac{N^2}{\nabla^2 v_h} = \frac{g}{\theta_p} \frac{\partial \theta_p}{\partial z} \left/ \left(\left(\frac{\partial u}{\partial z} \right)^2 + \left(\frac{\partial v}{\partial z} \right)^2 \right) \right. \quad (11)$$

where N^2 is the Brunt-Väisälä frequency, v_h is the horizontal velocity, g is the gravitational acceleration, θ_p is the potential temperature, u and v are the zonal and meridional components of the horizontal wind, respectively, and z is the height. When $Ri < 1/4$, the atmosphere becomes dynamically unstable and can produce turbulence. The shears that produce the instabilities may be associated with the large-scale flow field or with the perturbed wind field produced by gravity wave motions. The latter appears to be more likely, except in unusual, highly unstable regions of the atmosphere. Detailed studies of such instability processes are effectively impossible with the range resolution afforded by most radars. However, the oblique FDI technique provides a means for studying the relevant dynamical processes since the fluctuations in turbulent layers can be determined in combination with the large-scale wind profile measurements derived by applying a standard DBS analysis to the cross spectra measured in various directions.

By using a Gaussian least squares fitting routine [Yamamoto et al., 1988], the noise power, signal power, and Doppler velocity were obtained for the autospectra of the different beam directions. These were combined to produce the wind field, signal-to-

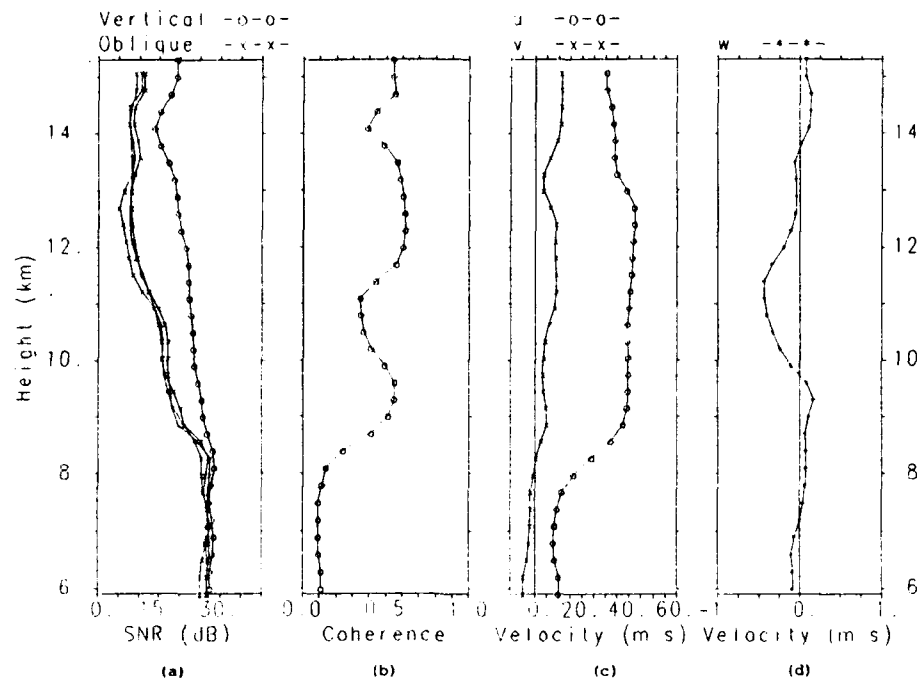


Fig. 5. Profiles of (a) signal-to-noise ratios (snr), (b) vertical beam coherence, (c) zonal and meridional wind, and (d) Doppler vertical velocity obtained from the exact same data used in Figure 2. A distinct transition from nonaspect sensitive to aspect sensitive regions can be seen at approximately 8 km, which is also the altitude of the largest vertical shear in the zonal wind and where the coherence increases dramatically. The profiles in the figure were obtained by fitting a Gaussian function to the autospectra and cross spectra from all beam directions.

noise ratio (snr), and vertical beam coherence profiles which are shown in Figure 5. The profiles of Figure 5 were then smoothed with a three-point running average with height. The profile of snr from the vertical beam shows larger values above 8 km than those of the oblique beams, which have similar magnitudes and height variations. The aspect sensitivity effects are only seen above approximately 8 km, that is, near the height of the largest vertical shear in the zonal wind. The altitude of 8 km also corresponds to the point where the coherence begins to show significant magnitude, that is, the existence of thin scattering layers. It should be noted that the coherence values were obtained from the cross-correlation function and are susceptible to a small bias due to the wave front curvature effect [Franke, 1990]. On the other hand, the MU radar has a two-way, half-power beam width of only 3.6° , and therefore this effect should be negligible. Doviak and Zrnić [1984], among others, have hypothesized that aspect sensitivity is caused by anisotropic turbulence, that is, turbulence which possesses different statistical characteristics along different directions within the medium. Such turbulence

could be caused by KHI or breaking gravity waves and would exist in high shear regions similar to that just above 8 km. Since Ri is also dependent on gravity wave activity, it is possible that regions of high coherence and large aspect sensitivity but low vertical shear could be caused by small-scale shear due to gravity wave instabilities, which cannot be observed with the range resolution of the wind profiles. For a review of other hypotheses of the origin of aspect sensitivity, see Gage [1990].

Direct comparisons can be drawn between the profiles of Figure 5 and the cross spectra. Figure 6 displays profiles of the magnitude and phase of the cross spectra from the four beam directions. As one would expect and as was evident in the curves shown in Figure 2, the coherent portions of $\phi(v_r)$ follow the peaks in the magnitude profiles. Also, the region of high coherence shown in Figure 5b corresponds to the region where nonrandom $\phi(v_r)$ exists, that is, above 8 km. The most interesting characteristic of these profiles is that coherence in $\phi(v_r)$, that is, when a well-defined layer exists, is observed only above approximately 8 km which is also the height range where aspect sensitivity effects are

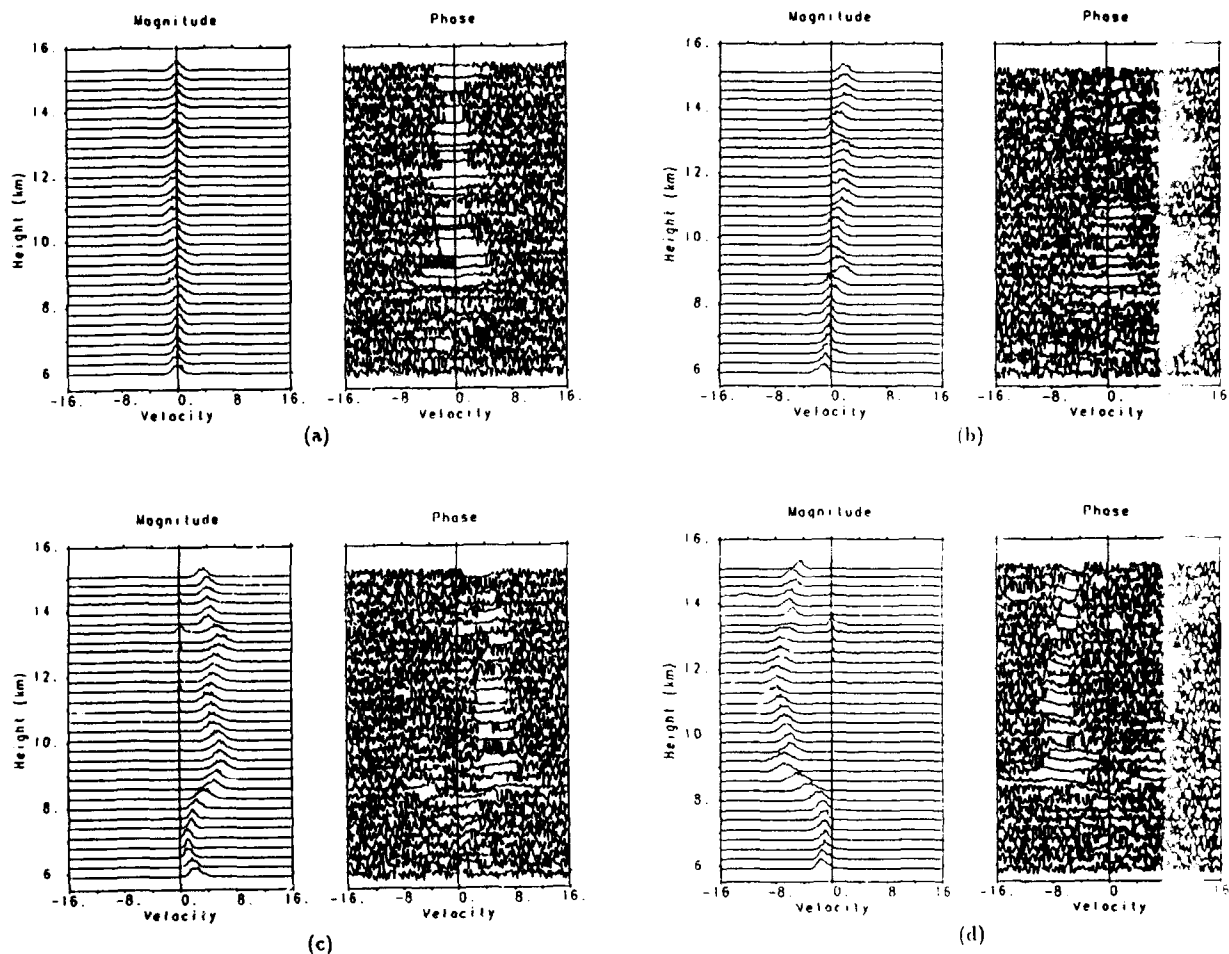


Fig. 6. Profiles of magnitude and phase of the cross spectra from the four beam directions: (a) $Az = 0$, $Ze = 0$, (b) $Az = 0$, $Ze = 10$, (c) $Az = 120$, $Ze = 10$, and (d) $Az = 240$, $Ze = 10$. Notice that the coherent portions of the cross-spectral phases follow the positions of the peaks in the Doppler spectra. It should also be observed that any coherence in the cross-spectral phase occurs above approximately 8 km, which is also the region of high aspect sensitivity.

evident in the curves shown in Figure 5a. The tropopause is located at approximately 8 km, so the well-defined scattering layers are found in the stratosphere, where the atmosphere is more stable. If turbulence was produced by large shear regions, such as during gravity wave activity, the stratospheric stability would restrict the vertical flow within the turbulent eddies, resulting in anisotropic turbulence.

4. CONCLUSIONS

A model of the cross-spectral phase $\phi(v_r)$ has been derived based on the idea that for each Dop-

pler velocity in the cross spectra, a corresponding value of $\phi(v_r)$ is obtained by integration along the lines of constant Doppler velocity, that is, Doppler sorting. These integrations produce values of $\phi(v_r)$, which can be thought of as weighted averages of the phase values along the lines of constant Doppler velocity. The weighting is given by the antenna pattern and other effects, such as aspect sensitivity. As one would expect, a parabolic structure is obtained for $\phi(v_r)$ as a function of v_r . The measured cross spectra obtained from near-simultaneous vertical and oblique FDI measurements have been shown to follow the model closely.

Another result of this work is the connection

between scattering layers observed by the FDI technique and regions of aspect sensitivity. Data from the various pointing angles showed that the regions of high aspect sensitivity correspond to the regions where scattering layers were evident in the FDI measurements, that is, regions of high coherence. Also, the aspect sensitivity effect had a distinct transition at approximately 8 km, where a large vertical shear was observed in the zonal wind, which could have produced gravity wave activity causing R_i to become less than 1/4 and producing KHI. These waves could propagate upward causing the distinct scattering layers seen above 8 km.

Acknowledgments. R.D.P. was supported under NSF grants ATM-9006846, ATM-9003448, and ATM-9121526. M.F.L. was supported by AFOSR contract AFOSR-91-0384 and NSF grant ATM-9006846. The MU radar belongs to and is operated by the Radio Atmospheric Science Center of Kyoto University.

REFERENCES

- Chu, Y.-H., and S. J. Franke, A study of frequency coherence of stratospheric and tropospheric radar echoes made with Chung-Li VHF radar, *Geophys. Res. Lett.*, 18(10), 1849–1852, 1991.
- Doviak, R., and D. Zrnić, Reflection and scatter formula for anisotropically turbulent air, *Radio Sci.*, 19(1), 325–336, 1984.
- Franke, S. J., Pulse compression and frequency domain interferometry with a frequency-hopped MST radar, *Radio Sci.*, 25(4), 565–574, 1990.
- Fukao, S., T. Sato, T. Tsuda, S. Kato, K. Wakasui, and T. Makihira, The MU radar with an active phased array, 1. Antenna and power amplifiers, *Radio Sci.*, 20(6), 1155–1168, 1985a.
- Fukao, S., T. Sato, T. Tsuda, S. Kato, K. Wakasui, and T. Makihira, The MU radar with an active phased array, 2. In-house equipment, *Radio Sci.*, 20(6), 1169–1176, 1985b.
- Gage, K. S., Radar observations of the free atmosphere: Structure and dynamics, in *Radar in Meteorology*, edited by D. Atlas, pp. 534–565, American Meteorological Society, Boston, Mass., 1990.
- Kudeki, E., and G. R. Stitt, Frequency domain interferometry: A high resolution radar technique for studies of atmospheric turbulence, *Geophys. Res. Lett.*, 14(3), 198–201, 1987.
- Kudeki, E., and G. R. Stitt, Frequency domain interferometry studies of mesospheric layers at Jicamarca, *Radio Sci.*, 25(4), 575–590, 1990.
- Larsen, M. F., and J. Röttger, VHF radar measurements of in-beam incidence angles and associated vertical-beam radial velocity corrections, *J. Atmos. Oceanic Technol.*, 8, 477–490, 1991.
- Palmer, R. D., R. F. Woodman, S. Fukao, M. F. Larsen, M. Yamamoto, T. Tsuda, and S. Kato, Frequency domain interferometry observations of tropo/stratospheric scattering layers using the MU radar: Description and first results, *Geophys. Res. Lett.*, 17(12), 2189–2192, 1990.
- Palmer, R., M. Larsen, R. Woodman, S. Fukao, M. Yamamoto, T. Tsuda, and S. Kato, VHF radar interferometry measurements of vertical velocities and the effect of tilted refractivity surfaces on standard Doppler measurements, *Radio Sci.*, 26(2), 417–427, 1991.
- Stitt, G. R., and E. Kudeki, Interferometric cross-spectral studies of mesospheric scattering layers, *Radio Sci.*, 26(3), 783–799, 1991.
- Tsuda, T., T. Sato, K. Hirose, S. Fukao, and S. Kato, MU radar observations of the aspect sensitivity of backscattered VHF echo power in the troposphere and lower stratosphere, *Radio Sci.*, 21(6), 971–980, 1986.
- Woodman, R. F., High-altitude-resolution stratospheric measurements with the Arecibo 2380-MHz radar, *Radio Sci.*, 15(2), 423–430, 1980.
- Yamamoto, M., T. Sato, P. T. May, T. Tsuda, S. Fukao, and S. Kato, Estimation error of spectral parameters of mesosphere-stratosphere-troposphere radars obtained by least squares fitting method and its lower bound, *Radio Sci.*, 23(6), 1013–1021, 1988.
- M. F. Larsen and R. D. Palmer, Kinard Laboratory of Physics, Department of Physics and Astronomy, Clemson University, Clemson, SC 29634-1911.
- S. Fukao, S. Kato, T. Tsuda, and M. Yamamoto, Radio Atmospheric Science Center, Kyoto University, Kyoto, Uji 611 Japan.

**FREQUENCY DOMAIN INTERFEROMETRY USING THE
1290 MHz SONDRESTROM RADAR: FIRST RESULTS**

R. D. Palmer,¹ M. F. Larsen,¹ C. Heinselman,² and S. I. Mikkelsen³

¹Department of Physics and Astronomy, Clemson University

²SRI International Inc., California

³Danish Meteorological Institute, Copenhagen, Denmark

Submitted to the
Journal of Atmospheric and Oceanic Technology
May 1992

Abstract

First results from the implementation of frequency domain interferometry (FDI) using an L-band frequency of 1290 MHz are presented. FDI has not previously been applied to such high-frequency measurements, to our knowledge. The experiment was conducted in September 1991 using the SRI radar located in Søndre Strømfjord, Greenland. The Sondrestrom radar is typically used for incoherent scatter measurements in the ionosphere but these are some of the first lower atmospheric results, viz., 8.6-13.4 km, since the data-taking system was revamped. At the time of the experiment, the steerability of the 32 m dish antenna was hampered because of a faulty elevation-scanning bearing. Therefore, the measurements were taken from an approximately vertical direction for the duration of the experiment. The spectra and correlation functions obtained from the FDI data are compared to previous results at other frequencies. The data show the Sondrestrom radar is giving reliable wind measurements in the lower atmosphere and that FDI can be implemented at L-band.

1 Introduction

The need for information about ever-smaller scales of motion in the atmosphere make instrument resolution a major concern. The mesosphere-stratosphere-troposphere (MST) radar technique has become increasingly important over the last decade as a tool for studying the winds, waves, and turbulent structure within the atmosphere. The signals received by these radars are produced by scattering and, in some cases, reflection from turbulent fluctuations in the refractive index. Often the structure manifests itself as well-defined layers with vertical scale sizes on the order of tens of meters (*Woodman, 1980*). Such small scales cannot be resolved by most MST radars, which typically have a minimum range resolution of 150-300 m.

The frequency domain interferometry (FDI) technique was developed by *Kudeki and Stitt (1987)* as a means for overcoming the range resolution limitation and was first implemented by them using a VHF radar. Subsequently, the technique has been given much attention in the literature (*Franke, 1990; Kudeki and Stitt, 1990; Palmer et al., 1990; Stitt and Kudeki, 1991; Chu and Franke, 1991*). By varying the transmitter frequency from one pulse to the next, the cross-correlation functions or cross-spectra between the two signals can be used to determine the location and thickness of a scattering layer within the resolution volume of the radar. If the layer is diffuse and relatively thick, in comparison to the resolution volume, the FDI measurements will provide results comparable to what can be achieved with the normal range resolution of the radar. On the other hand, if a thin scatter layer exists within the medium, the FDI technique can be used to determine the location and width of the layer, subject to certain acceptable assumptions inherent in the analysis procedure.

In this paper, the first results from FDI measurements at an L-band frequency of 1290

MHz are presented. The radar wavelengths used previously for such measurements have all been in a range that is strongly affected by aspect sensitivity in which there is an enhancement of the scatter for incidence angles near vertical. At 1290 MHz, there is no significant aspect sensitivity. The incoherent scatter radar located in Søndre Strømfjord, Greenland, was used for the experiment and observations were made in the troposphere and lower stratosphere. The next section summarizes the basic analysis techniques used for FDI observations. Following sections show the FDI cross-spectra and cross-correlation functions and analysis is provided to verify the operation of the FDI system. Conclusions are provided in the final section.

2 Frequency Domain Interferometry

Range resolution is inversely proportional to the bandwidth of the radar system, and proportional to the length τ of the transmitted pulse. By decreasing τ , the range resolution is increased, but a limit exists because of the limited bandwidth of the radar. Although, some observations have been made with an increased resolution (*Woodman, 1980*), typical MST radars are limited to a range resolution of 150 m.

FDI uses the phase difference of two signals separated in frequency by Δf to determine the position of a high-reflectivity layer within the resolution volume (*Kudeki and Stitt, 1987*). A vertically-pointing beam is typically used, although off-vertical beam directions can be used too, in principle. The frequency difference should be chosen such that $\Delta f = f_h - f_l \leq 1/\tau$, which assures that there is no 2π ambiguity in the phase difference. If $\Delta f = 1/\tau$, the range of possible phase differences between the two signals would range from 0 to 2π between the lower and upper boundaries of the resolution volume. Even though such a situation is desirable, it is by no means necessary for the successful

implementation of the technique. As the position of the scattering layer changes, the phase difference will change accordingly so that the phase difference can be used to produce an estimate of the *relative* layer position. The absolute position of the scattering layer cannot be determined unless the initial transmitted phase is known.

The FDI technique can be used to determine the location of a single scattering layer within the resolution volume. The technique fails if there is more than one layer within the range volume. Of course, the probability of having only a single layer can be improved by a smaller initial resolution. With only a single scattering layer, the accuracy of the estimated location is a function only of the statistical uncertainty of the phase estimate (*Kudeki and Stitt, 1987*).

Data from a standard FDI experiment is analyzed by calculating the normalized cross-spectrum between the signals at the different frequencies using

$$S_{hl}(v_r) = \frac{\langle V_h(v_r)V_l^*(v_r) \rangle}{(\langle |V_h(v_r)|^2 \rangle \langle |V_l(v_r)|^2 \rangle)^{1/2}} \quad (1)$$

where $V_h(v_r)$ and $V_l(v_r)$ are the Fourier transforms of the signals at the high and low frequencies, respectively, and $\langle \cdot \rangle$ represents the expected value operator. Finding the magnitude and phase of $S_{hl}(v_r)$, one obtains

$$|S_{hl}(v_r)| = e^{-2\Delta k^2 \sigma_r^2(v_r)} \quad (2)$$

$$\phi(v_r) = 2\Delta k \langle r(v_r) \rangle \quad (3)$$

where Δk is the difference in the wavenumbers between the two frequencies, i.e., $\Delta k = 2\pi/\Delta f$. The relative location and thickness of the scattering layer are given by $\langle r(v_r) \rangle$ and $2\sigma_r(v_r)$, respectively. It should also be noted that $|S_{hl}(v_r)|$ is the so-called coherence function. By finding the normalized cross-spectrum and using (2) and (3), the relative range and thickness can be estimated.

3 Experimental Configuration and Results

A FDI experiment was conducted on September 24, 1991, using the incoherent scatter radar (*Heinselman et al.*, 1992) located in Søndre Strømfjord, Greenland (67°N, 50°E). The Sondrestrom radar, which operates at an L-band frequency of 1290 MHz, is typically used for incoherent scatter radar measurements of ionospheric parameters, although the instrument is also well suited for MST radar studies of the lower atmosphere. To achieve the dual-frequency transmission needed for FDI, alternating pulses were transmitted with two frequencies of $f_l=1290$ MHz and $f_h=1290.45$ MHz. The pulse length τ was set to 2 μ s providing a range resolution of 300 m.

The inter-pulse period (IPP) was set to 1 ms, but alternate frequencies were transmitted on alternate pulses so that the effective IPP was 2 ms. Fourteen coherent integrations were used, providing an aliasing velocity of 2.07 ms^{-1} . At the time of the experiment, the elevation-scanning bearings of the dish were not functioning properly and all measurements were taken at elevation and azimuth angles of 89.6° and 0° , respectively. Within the accuracy of the beam-pointing direction of $\pm 0.2^\circ$ and a one-way, half-power beamwidth of approximately 0.5° , one can consider the results to be a system with a beam that is essentially vertically pointing. Future campaigns are planned where the full steerability of the dish will be utilized. Measurements with adequate signal-to-noise ratios were taken in the altitude range of 8.6-13.4 km, with a gate spacing and resolution of 300 m. Using the above sampling time, 512 points of raw data for each frequency were stored on magnetic tape approximately every 15 s. These 512-point data sets were used to produce spectra and correlation functions, which are shown in Figure 1 for a height of 11 km after 100 incoherent integrations. The data were obtained from 1432-1457 LT.

The first two rows of Figure 1 display the magnitude and phase of the auto- and cross-spectra, respectively. Auto-spectra are shown in the first two columns while the cross-spectrum is in the last column. As should be expected, the two auto-spectra from the combination of signals at frequencies hh and ll are very similar. A ground clutter signal can be seen at zero Doppler shift. A symmetric 60 Hz signal is also present at approximately $\pm 1.4 \text{ ms}^{-1}$. In the last column, the cross-spectrum has a smaller magnitude than the auto-spectra because of the decorrelation effects of the Δf frequency shift. The constant noise level, observed in the auto-spectra, is gone as a result of the independence of the two noise sequences from the frequency-separated signals.

The phase of the cross-spectrum is the quantity of primary interest for FDI measurements. In a recent article, *Palmer et al.* (1992) presented a model which showed the FDI cross-spectral phase to have a parabolic structure centered close to zero Doppler frequency. The concavity of the parabola can be upward or downward and slightly shifted from center depending on the beam position and the horizontal wind speed. The cross-spectral phase, shown in Figure 1, confirms the parabolic structure. For completeness, the last two rows of the figure show the auto- and cross-correlation functions obtained by the inverse Fourier transform. Of course, the information contained in the cross-spectrum can also be obtained from the cross-correlation function. If only the average location of the layer is desired, the phase at lag zero of the cross-correlation function is useful because of its small statistical fluctuations. On the other hand, wave front curvature can cause the coherence, obtained from the cross-correlation function, to be biased toward smaller values (*Franke*, 1990). In contrast, the cross-spectrum sorts the different regions of the layer by Doppler velocity. Therefore, a better understanding of the true layer structure is provided by using the cross-spectrum.

Figures 2a and 2b show the profiles of magnitude and phase of the cross-spectra for

the 17 useful gates. The horizontal lines in the cross-spectral phase plot represent the boundaries between the adjacent gates. As in Figure 1, the ground clutter and 60 Hz signals are readily seen. A Doppler shift is present in the profile, which could be due to a vertical wind or to a small component of the horizontal wind since the beam actually has a small but nonnegligible zenith angle of 0.4° . The outer wings of the phase curves show a noisy structure. The portions of the curves with signal follow the peak in the cross-spectral magnitude and have either an upward or downward concavity.

The first few gates show more randomness in the cross-spectral phase. Coherence, given by (2), provides a means of locating thin scattering layers. It is possible that thin scattering layers can exist when the echo power is low and that they may not exist in regions of high echo power. An example of the former can be seen in Figures 3a and 3b, where profiles of echo power and coherence are given, respectively. At approximately 9.5 km, relatively low echo power is observed but the coherence is rather large. In Figure 2b, this region has a non-random cross-spectral phase, and therefore a well-defined, thin, scattering layer is present. Comparing the coherence profile with the cross-spectral phase plots shows that the existence of the well-defined layer can be predicted by either a large coherence or a non-random, cross-spectral phase.

4 Conclusions

The new data-taking system which has been implemented at the Sondrestrom radar has been verified for wind measurements in the troposphere and lower stratosphere, and the first results from frequency domain interferometry measurements using an L-band Doppler radar have been presented. The auto- and cross-spectra and correlation functions obtained from the FDI data are similar to previously reported results at longer

wavelengths which are typically affected by aspect sensitivity in the scatter. Our results show that the FDI method can be implemented successfully at higher frequencies and that the method is not dependent on aspect sensitive or anisotropic scatter. An advantage of the Sondrestrom radar is that the antenna is fully steerable to within a few degrees of the horizon in all azimuth directions so that the location of turbulent layer structure can be mapped out three-dimensionally over a broad region in a relatively short time. Future experiments will use the flexible beam steering of the Sondrestrom radar in conjunction with FDI analysis in order to study the spatial and temporal variations in the turbulent structure in more detail.

Acknowledgements. R.D.P. was supported under NSF grants ATM 90-06846, ATM 90-03448 and ATM 91-21526. M.F.L. was supported by AFOSR grant AFOSR-91-0384 and NSF grant ATM 90-06846. The Sondrestrom radar facility is funded by the NSF under Cooperative Agreement ATM 88-22560.

References

- Chu, Y. H., and S. J. Franke, 1991, A study of the frequency coherence of stratospheric and tropospheric radar echoes made with Chung-Li VHF radar, *Geophy. Res. Lett.*, *18*(10), 1849-1852.
- Franke, S. J., 1990, Pulse compression and frequency domain interferometry with a frequency-hopped MST radar, *Radio Sci.*, *25*(4), 565-574.
- Kudeki, E., and G. R. Stitt, 1987, Frequency Domain Interferometry: A High Resolution Radar Technique for Studies of Atmospheric Turbulence, *Geophy. Res. Lett.*, *14*(3), 198-201.

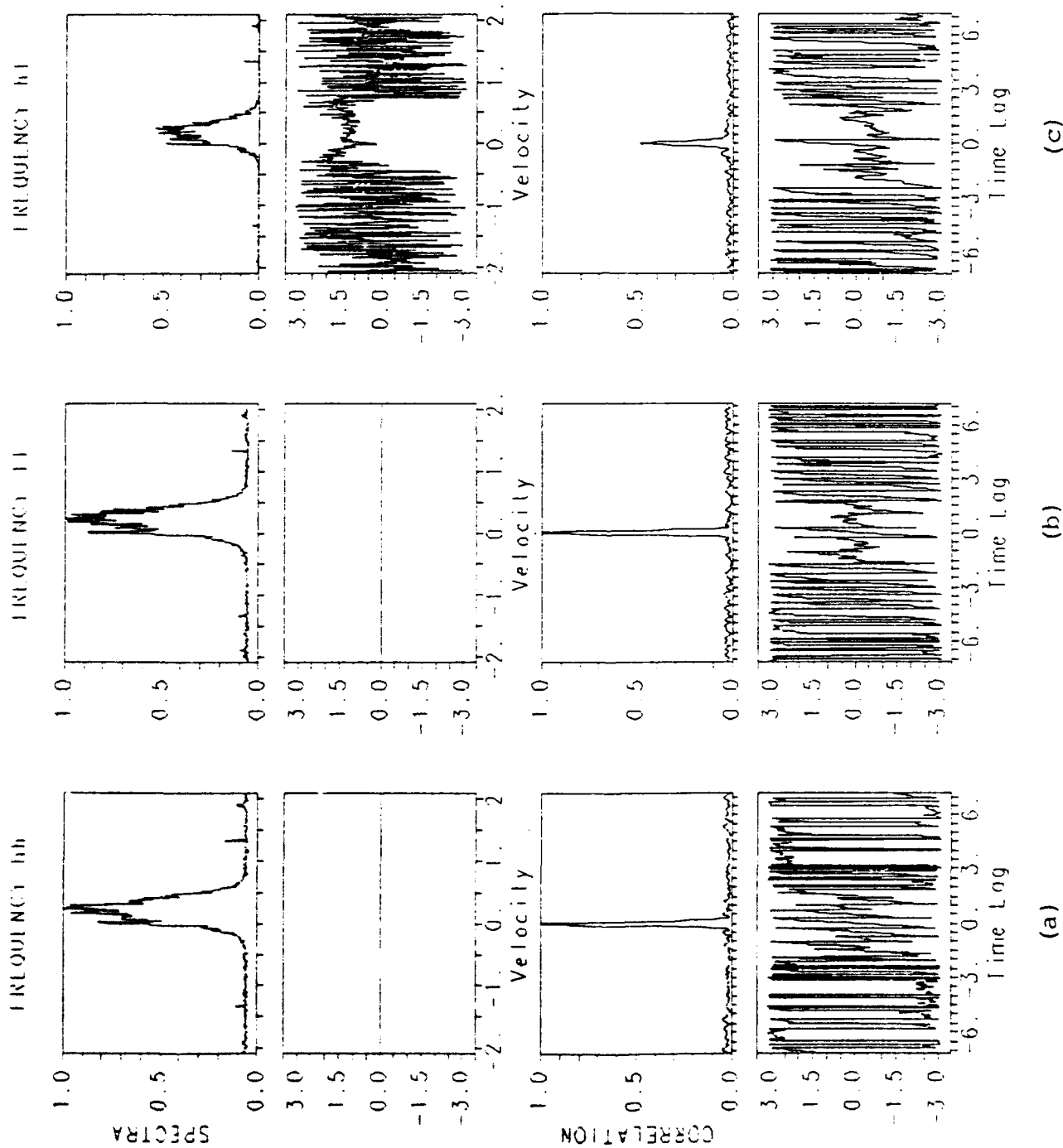
- Kudeki, E., and G. R. Stitt, 1990, Frequency domain interferometric studies of mesospheric layers at Jicamarca, *Radio Sci.*, 25(4), 575-590.
- Palmer, R. D., R. F. Woodman, S. Fukao, M. F. Larsen, M. Yamamoto, T. Tsuda, and S. Kato, 1990, Frequency domain interferometry observations of tropo/stratospheric scattering layers using the MU radar: Description and first results, *Geophys. Res. Lett.*, 17(12), 2189-2192.
- Palmer, R. D., S. Fukao, M. F. Larsen, M. Yamamoto, T. Tsuda, and S. Kato, 1992, Oblique frequency domain interferometry measurements using the MU radar, *Radio Sci.*, in press.
- Stitt, G. R., and E. Kudeki, 1991, Interferometric cross-spectral studies of mesospheric scattering layers, *Radio Sci.*, 26(3), 783-799.
- Woodman, R. F., 1980, High-altitude-resolution stratospheric measurements with the Arecibo 2380-MHz radar, *Radio Sci.*, 15(2), 423-430.

Figure Captions

Fig. 1. A typical 25-min average of (a-b) auto-spectra and auto-correlation functions, and (c) cross-spectrum and cross-correlation function at a height of 11 km. Notice the non-random cross-spectral phase in the region of high signal power, which is a typical phase characteristic for FDI measurements.

Fig. 2. Profiles of (a) magnitude and (b) phase of the cross-spectra in the region 8.6-13.4 km. The horizontal lines in the phase plot represent the boundaries between the neighboring gates. Cross-spectral phase in a FDI experiment represents the relative location of a scattering layer within the resolution volume.

Fig. 3. Profiles of (a) echo power and (b) coherence. Large coherence values represent a stable layer within the resolution volume and can also be used to estimate the layer thickness. The maximum of the coherence profile is approximately 0.75.



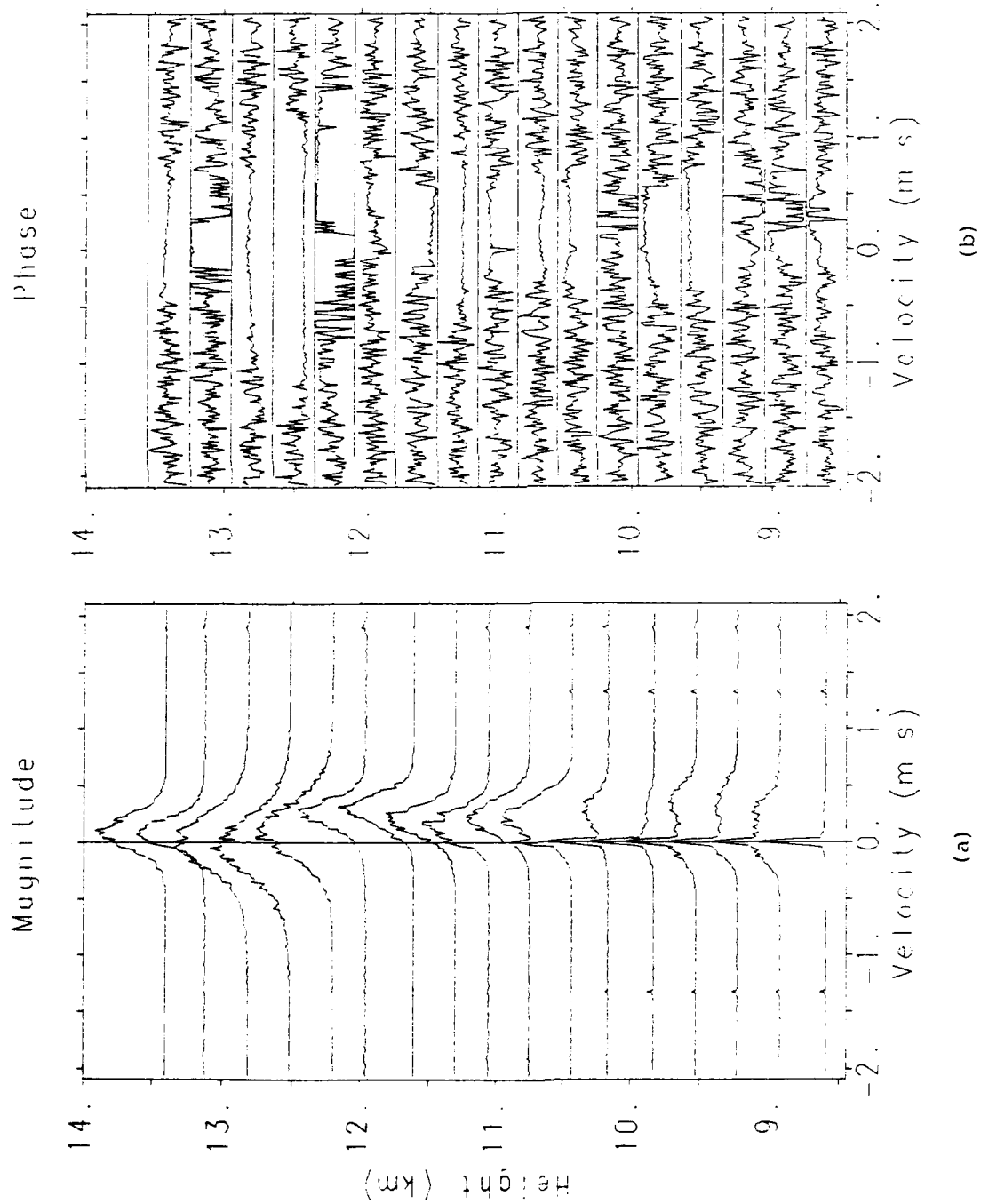


Fig 2

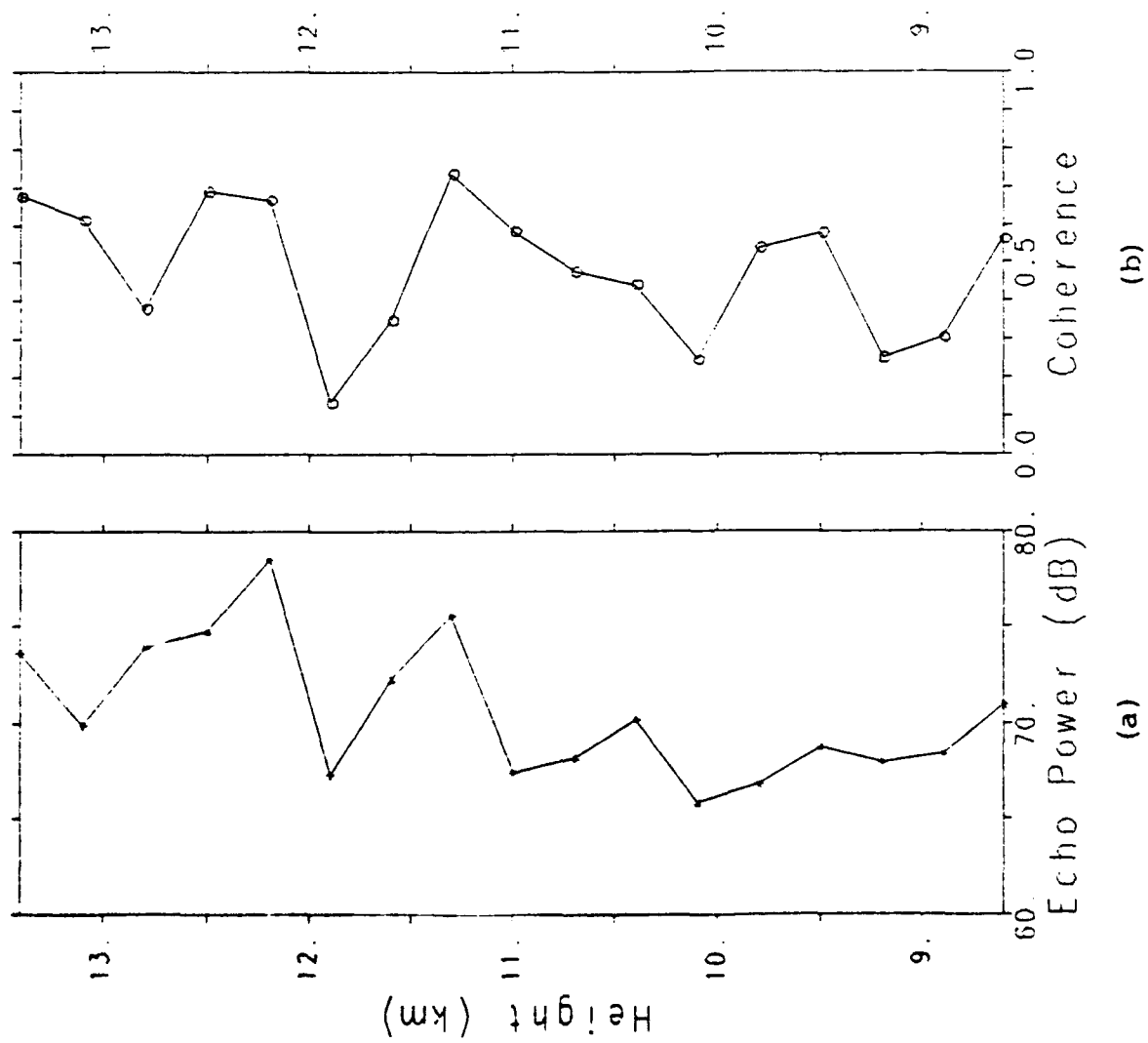


Fig 3

Poststatistic-Steering Wind Estimation in the Troposphere and Lower Stratosphere

Robert D. Palmer, Miguel F. Larsen, E. Lamar Sheppard

Department of Physics and Astronomy
Clemson University
Clemson, SC 29634-1911

Shoichiro Fukao, Mamoru Yamamoto, Toshitaka Tsuda, and Susumu Kato

Radio Atmospheric Science Center
Kyoto University
Uji, Kyoto 611 JAPAN

Submitted to *Radio Science*
January 1992

Abstract

Poststatistic steering (PSS) techniques are applied for estimating the wind vector. Since spatially separated receivers can be used to synthesize a radar beam in an arbitrary direction, Doppler beam swinging (DBS) techniques can be used in conjunction with PSS to obtain estimates of the vector wind. Data obtained with the MU radar in Japan are used to implement this technique in the troposphere and lower stratosphere at a VHF wavelength. To obtain an accurate estimate of the beam pointing direction, the synthesized antenna power pattern is calculated. Also, the effects of aspect sensitivity on this technique are explored. Results from the PSS method of obtaining the vector wind are compared to the spaced antenna (SA) technique, which shows that the PSS horizontal wind estimate is equivalent to the SA *true* velocity.

1 Introduction

The mesosphere-stratosphere-troposphere (MST) radar technique has been used extensively to study the atmosphere since the work of *Woodman and Guillen* [1974]. Typically, an MST Doppler radar uses a large phased array antenna for reception and transmission and steers the beam in at least three directions to obtain a profile of the wind vector in what has become known as the Doppler beam swinging (DBS) technique. The method has been used extensively in atmospheric studies [for a review, see *Röttger and Larsen*, 1990]. Even though DBS has proven to be a reliable means of obtaining the wind vector, other methods have also been developed which may prove to have advantages. Examples are the spaced antenna (SA) technique, interferometry, and imaging Doppler interferometry.

The SA method is an alternative to DBS and has been studied thoroughly in the literature [*Briggs*, 1980; *Hocking*, 1983; *Briggs*, 1984; *Larsen and Röttger*, 1989; *Liu et al.*, 1990]. Like the DBS technique, a standard SA experiment uses a large array for transmission but receives the returned signals on three spatially separated antennas with either multiplexed reception on a single receiver or, preferably, individual receivers, filters, amplifiers, and associated hardware. By calculating the cross-correlation functions between the signals received at the different receivers, the time lag between the signals can be used to estimate the horizontal wind. Unfortunately, this estimate is biased if the turbulent structure fades significantly with time and must be corrected using the so-called full correlation analysis (FCA) [*e.g.*, *Briggs*, 1984]. The hardware configuration may seem more complex but the SA technique does not require the steering of the antenna beam in the standard mode, although it has been implemented recently in off-vertical directions in an attempt to obtain estimates of vorticity and divergence [*Liu et al.*, 1991]. It should be noted that the DBS and SA techniques have been shown to be theoretically equivalent [*Briggs*, 1980] and experimental comparisons have

also been carried out [Van Baelen et al., 1990].

Probably, the most important advantage of the SA technique over DBS is its ability to calculate other important dynamical parameters. When these parameters are calculated from SA data, the term radar interferometry (RI), or spatial interferometry (SI), is used to describe the technique [Woodman, 1971; Röttger and Vincent, 1978; Vincent and Röttger, 1980; Farley et al., 1981; Royrvik, 1983; Meek and Manson, 1987; Kudeki, 1988; Röttger et al., 1990; Larsen and Röttger, 1991; Van Baelen et al., 1991; Palmer et al., 1992]. Recently, Palmer et al. [1991], Van Baelen and Richmond [1991], and Larsen et al. [1992] have shown that the SI technique can be used to obtain an estimate of the wind vector with particular advantages for estimating the vertical velocity. Also, Briggs and Vincent [1992] and Sheppard and Larsen [1992a] have shown that the parameters needed for FCA can be obtained from either the time or frequency domain. Another technique, which is closely related to SI-based methods, is the imaging Doppler interferometer (IDI) method [Adams et al., 1986; Adams et al., 1989]. A recent comparison of IDI and SA/FCA has shown that, if implemented properly, IDI can provide an almost unbiased estimate of the horizontal velocity [Franke et al., 1990].

The postset beam steering (PBS) technique [Röttger and Ierkic, 1985] has arisen out of the interferometric techniques. Since SI measurements typically involve reception on three spatially separated arrays, a systematic phase shift can be applied to the signals to produce a two-way beam pattern in any arbitrary direction within the volume illuminated by the transmitted beam. More recently, Kudeki and Woodman [1990] have shown that the systematic phase shift can be introduced in the spectra and correlation functions of the signals rather than just in the time series, thus reducing the computational load. The technique has become known as poststatistic steering (PSS) and further studies have been performed to test its usefulness [Kudeki et al., 1990; Palmer et al., 1990]. Recently, poststatistic steering

was applied to SI data from a MF radar to synthesize beams in various directions so that DBS could be performed and the vector wind estimated [Sürücü *et al.*, 1992]. Of course, the technique for estimating the wind is basically the DBS technique applied to SI data. The purpose of this paper is to implement the same PSS method for wind estimation in the troposphere and lower stratosphere using a VHF Doppler radar.

Section 2 describes the experimental configuration using the middle and upper (MU) atmosphere radar and also the signal processing techniques used. A review of PSS is given in Section 3 and the two-way synthesized beam patterns are described in Section 4. Wind vector estimation results are given in Section 5, and conclusions are provided in Section 6.

2 Experimental Configuration and Signal Processing

From June 29, 1990, 1910 LT through July 2, 1990, 0950 LT, an oblique spaced antenna (OSA) experiment was conducted using the MU radar located in Shigaraki, Japan (34.85° N, 136.10° E) [Fukao *et al.*, 1985a, 1985b]. The OSA experiment is basically a standard SA or SI experiment except that the beams are also directed in off-vertical directions [Liu *et al.*, 1991]. Azimuth and zenith angles of the beams used in this experiment are given by: $(Az, Ze) = (0^\circ, 0^\circ)$, $(0^\circ, 20^\circ)$, $(120^\circ, 20^\circ)$, and $(240^\circ, 20^\circ)$. In this paper, the data from only the vertical beam will be used. The MU radar is capable of segmenting the antenna array among the four possible receiving channels. Figure 1 shows the groups used for receivers 1, 2, and 3. The entire beam was used for transmission.

The pulse length was set at $2 \mu\text{s}$ and the height range from 6.0 to 15.3 km was sampled. An 8-bit complementary code was used with a flip of the code every interpulse period (IPP), which was set to $400 \mu\text{s}$. With 200 coherent integrations, the effective sampling time was 0.08 s. Five complex 256-point time series from the 32 gates were stored for each beam

direction in sequence and then the beam directions were cycled through repeatedly until the end of the experiment. Each 256-point time series has a length of approximately 24.26 s, which includes the time needed for data storage and beam switching.

As an initial preprocessing procedure, the gain for both the I and Q channels of the three receivers were equalized. This is accomplished by calculating the variance of each 256-point time series and then normalizing the time series so that the variances are equal in order to eliminate any gain imbalance in the different channels. After this process, any DC levels in the time series were removed and four additional coherent integrations were applied, producing an effective sampling time of 0.32 s, and a data length of 64 points. Since only the data from the vertical beam was used for this paper, the four additional coherent integrations did not produce any aliasing problems. Using the 64-point time series, the auto- and cross-spectra were calculated using a standard fast Fourier transform (FFT) routine with a rectangular window.

3 Poststatistic Steering

Consider a SI experimental configuration where the transmit array is phased so that a vertical beam is produced and three complex voltage time series are obtained, integrated, and received from vertically pointing, spatially separated antennas, i.e., $v_1(t)$, $v_2(t)$, and $v_3(t)$. If these signals are summed to produce a composite signal, the results will be equivalent to a standard Doppler experiment with a vertically pointing antenna beam. On the other hand, if a systematic phase shift is introduced in each of the signals before the summation process, the receiving elements' array factor will be steered off-vertical by an amount corresponding to the phase shift. The latter process is known as postset beam steering (PBS) [Röttger and Ierke, 1985]. It should be noted that the overall beam power pattern is produced by the

multiplication of the square of the above mentioned array factor with the receiver element power pattern and the transmitter power pattern, which are both pointing vertically.

Kudeki and Woodman [1990] used an analytical treatment to determine that the systematic phase shift can be introduced after the various spectra and correlation functions are calculated so that incoherent integration can be applied to the signals before the beam steering is implemented, thus saving large amounts of computer memory and processing time. *Kudeki and Woodman* [1990] termed the latter technique poststatistic steering (PSS). Subsequently, [Palmer *et al.*, 1990] generalized the PSS equations to the case of two-dimensional steering.

Consider the SI configuration in a standard xyz coordinate system, with x , y , and z pointing in the east, north and vertical directions, respectively. The position vectors of the antennas are denoted by \mathbf{D}_1 , \mathbf{D}_2 , and \mathbf{D}_3 and are three-dimensional vectors even though z will typically be zero. Define a unit vector \mathbf{n} which points in the direction of the desired array factor given by

$$\mathbf{n} = \begin{pmatrix} \sin\theta_s \sin\phi_s & \sin\theta_s \cos\phi_s & \cos\theta_s \end{pmatrix} \quad (1)$$

where θ_s is the zenith angle, with respect to the z axis, and ϕ_s is the azimuth angle, with respect to the y axis. The components of \mathbf{n} are found by simple projections onto the coordinate axes. The phase shift at each of the receivers that is needed to produce an array factor in the direction of \mathbf{n} is given by the dot-product of \mathbf{n} with the position vectors of the antennas. *Palmer et al.* [1990] showed that the synthesized spectra produced from the overall beam pattern is given by

$$\begin{aligned} \Phi_s(v_r; \theta_s, \phi_s) = & \Phi_{11}(v_r) + \Phi_{22}(v_r) + \Phi_{33}(v_r) \\ & + 2\text{Re}[\Phi_{12}(v_r)e^{-jk\mathbf{n} \cdot (\mathbf{D}_1 - \mathbf{D}_2)}] \\ & + 2\text{Re}[\Phi_{13}(v_r)e^{-jk\mathbf{n} \cdot (\mathbf{D}_1 - \mathbf{D}_3)}] \\ & + 2\text{Re}[\Phi_{23}(v_r)e^{-jk\mathbf{n} \cdot (\mathbf{D}_2 - \mathbf{D}_3)}] \end{aligned} \quad (2)$$

where $\Phi_{ij}(v_r)$ is the auto- or cross-spectra between $v_i(t)$ and $v_j(t)$, and k is the wavenumber of the radar.

The vectors, which represent the centers of the receiving antennas shown in Figure 1, are given by

$$\begin{aligned} \mathbf{D}_1 &= \begin{pmatrix} 3.33\lambda & 1.4\lambda & 0 \end{pmatrix} \\ \mathbf{D}_2 &= \begin{pmatrix} -0.303\lambda & -3.5\lambda & 0 \end{pmatrix} \\ \mathbf{D}_3 &= \begin{pmatrix} -2.727\lambda & 2.1\lambda & 0 \end{pmatrix} \end{aligned}$$

where λ is the wavelength of the radar. By using the auto- and cross-spectra, calculated from the experimental data described in the previous section, equation (2) can now be used to synthesize beams in various directions. Figures 2a and 2b show profiles of the spectra obtained by phasing the array factor with azimuth and zenith angles of $(90^\circ, 3^\circ)$ and $(270^\circ, 3^\circ)$, respectively. As expected, the spectra from the opposing azimuth angles are approximately mirror images of each other. Also shown in Figure 2 are the least-squares Gaussian fits to these spectra calculated using the routines developed by *Yamamoto et al.* [1988]. The frequency offset of the Gaussian fits will be used to estimate the wind vector.

As is the case in PBS and even hardware phased array systems, \mathbf{n} represents the pointing direction of only the receiver array factor and not the true pointing angle of $\Phi_s(v_r; \theta_s, \phi_s)$. To obtain the two-way antenna power pattern, and therefore the true pointing angle, the transmitter power pattern and the receiver element power pattern must be calculated. Section 4 deals with this calculation and also addresses biases that may arise because of the additional factor introduced by the aspect sensitivity function, which also contributes to the two-way power pattern seen by the radar.

4 Two-way Antenna Pattern Calculations

As described above, the angles in equation (1) do not represent the pointing angle of the two-way antenna pattern but only that of the receiving array factor. Therefore, to use the results obtained from equation (2) in a meaningful way, the two-way antenna pattern must be calculated. The two-way antenna power pattern is the product of the transmitter power pattern and the receiver power pattern. Since the MU radar has an approximately circular aperture, the transmitter power pattern is given by a formula involving a first order Bessel function [Oliver, 1982]. In order to simplify the computations, the pattern will be approximated by a sinc function with the same beamwidth and the following form

$$P(\theta) = \left(\frac{1}{n} \frac{\sin(n\psi/2)}{\sin(\psi/2)} \right)^2 \quad (3)$$

where n is the number of elements in the array, $\psi = kd\sin\theta$, d is the spacing between the elements, and θ is the independent variable of zenith angle. The approximation introduces very little bias in the calculation. It should be noted that (3) is the equation for a linear array. Nevertheless, the equivalent beamwidth for the array is equal to that of the MU radar if $n = 23$ and $d = 0.7\lambda$. Because we have a circular array, $P(\theta)$ is not a function of the independent variable, the azimuth angle ϕ . The above equation represents the array factor for the transmitter power pattern. To obtain the true transmitter power pattern, the above equation should be multiplied by the element pattern, which is the pattern for a single yagi antenna. Since the single element pattern is very wide compared to the array factor, it can be ignored.

For the receiver power pattern of the SI antenna configuration, the element pattern of antennas 1, 2, or 3 should be multiplied by the array factor squared of the synthesized beam,

which is obtained by

$$P_{ar}(\theta, \phi) = \frac{1}{9} | e^{-jk(\mathbf{n}-\tilde{\mathbf{n}})\cdot\mathbf{D}_1} + e^{-jk(\mathbf{n}-\tilde{\mathbf{n}})\cdot\mathbf{D}_2} + e^{-jk(\mathbf{n}-\tilde{\mathbf{n}})\cdot\mathbf{D}_3} |^2 \quad (4)$$

where

$$\tilde{\mathbf{n}} = \begin{pmatrix} \sin\theta\sin\phi & \sin\theta\cos\phi & \cos\theta \end{pmatrix} \quad (5)$$

The receiver element pattern for antennas 1, 2, or 3 is obtained from equation (3) with $n=8$ and $d = 0.7\lambda$. As in the transmitting power pattern the element pattern of the single yagi antenna has not been used in the calculation.

By multiplying the (i) transmitter power pattern, (ii) receiver element power pattern of antennas 1, 2, or 3, and (iii) the square of the synthesized array factor, the two-way antenna power pattern can be obtained for the synthesized beam. Figure 3 shows the resulting pattern for the 5 synthesized beam directions used in our experiment. The vertical dotted lines located at the peak in each pattern represent the true pointing angles of the synthesized beams. These angles will be used in the next section to estimate the wind vector.

At VHF and longer wavelengths, the returned echo power depends on the zenith angle. The effect is known as aspect sensitivity and has been described in numerous articles in the literature [Gage and Green, 1978; Röttger and Liu, 1978; Fukao et al., 1979; Tsuda et al., 1986]. Since the effect enhances the reflectivity at zenith angles near vertical, the two-way antenna power pattern becomes distorted. The aspect sensitivity function is known to be approximately Gaussian with a peak close to vertical which tends to narrow the effective beamwidth of the radar. Unfortunately, the exact width and location of the peak of the aspect sensitivity function cannot be determined. Therefore, the two-way power pattern, including aspect sensitivity, cannot be calculated without various assumptions which are subject to errors. Here, we use an analytical approach in which various aspect sensitivity functions are assumed and the resulting effects on the two-way antenna pattern are determined.

Table 1 shows the derived zenith angles for the 5 synthesized beam positions with and without the aspect sensitivity function with a beamwidth of approximately 10° . Without aspect sensitivity, i.e., for isotropic scatter, the zenith angles for the meridional and zonal beams are 0.63° and 0.64° , respectively. When an aspect sensitivity function is introduced, which is centered at zenith, the two-way pattern zenith angles are reduced as expected. The effect would produce an underestimate of the horizontal wind if the radial velocity given by the synthesized beams were divided by the zenith angles from the non-aspect sensitive case. When the aspect sensitivity function is centered at azimuth and zenith angles of 0° and 1° , respectively, the zenith angle of the north-pointing beam is increased while the south-pointing beam zenith angle is reduced. Because of the narrowing of the beam, the two zonal zenith angles are reduced by the same amount. The same effect is seen when the aspect sensitivity function is directed in the zonal direction. An example is also shown for azimuth and zenith angles of 45° and 1° , respectively. The results are consistent with what one would expect intuitively, but we have a limited number of cases with only a few aspect sensitivity pointing angles and only one width. Nevertheless, our results illustrate that small biases may exist in the horizontal wind estimates when the PSS technique is used.

5 Observations

As described in Section 2, the auto- and cross-spectra were obtained using the 64-point data sets, which have an effective sampling time of 0.32 s. The FFT of each of the time series was calculated with a rectangular window and then combined to obtain the auto- and cross-spectra using the following equation

$$\Phi_{ij}(v_r) = V_i(v_r)V_j^*(v_r) \quad (6)$$

where $V_i(v_r)$ is the Fourier transform of $v_i(t)$. Fifteen incoherent integrations were carried out, and the resulting spectra were used for the PSS procedure, i.e., equation (2).

The zonal, meridional, and vertical wind were derived by synthesizing spectra in the 5 beam positions shown in Figure 3. The zonal wind was calculated by averaging the velocities obtained by dividing the radial velocities at azimuth angles 270° and 90° by the respective two-way antenna pattern zenith angles. The same procedure was carried out to obtain the meridional wind estimate. Figure 4 shows profiles for the meridional and zonal wind estimates for the entire 62.67-hour data set, based on fifteen incoherent integrations. Because beam directions other than vertical were interspersed in the OSA experiment, the incoherently integrated spectra correspond to a time resolution between profiles of approximately 24.26 min. For display purposes, two of the profiles were averaged and then displayed as a time history of the wind profiles. The smaller plot in the lower righthand corner represents the average of the entire observation period with $\pm\sigma$ errors bars. In the upper righthand plot, the averages without error bars are again displayed but in comparison to the SA/FCA estimates of the *apparent* and *true* velocities [e.g., Larsen and Röttger, 1989]. The *true* velocity profile has a smaller magnitude than the *apparent*. These estimates were obtained from a separate study of the same data set [Sheppard et al., 1992b]. As is evident, the PSS estimates of the zonal and meridional wind are in good agreement with the *true* velocity estimate, but aspect sensitivity has not been taken. Nevertheless, the results indicate that the method works well in comparison to the SA/FCA technique. Of course, the placement and width of the aspect sensitivity function may have been favorable during the observation period. Further study is needed to fully elucidate the effect of aspect sensitivity on PSS estimation of the winds.

Profiles of the echo power and Doppler vertical velocity time histories are presented in Figure 5. The echo power profiles exhibit a typical tropo/stratospheric characteristic in that the tropopause can clearly be detected at approximately 14 km, where a peak is seen in the

profiles. The upper righthand figure again shows the average profile with $\pm\sigma$ error bars. Also shown is the profile of the number of failures, i.e., when the PSS procedure produced a wind estimate which was more than 2σ away from the mean indicating the relationship with echo power. As is expected, larger failure rates occur at the lower echo power regions and vice versa. The Doppler vertical velocity estimates were obtained by setting θ_s and ϕ_s equal to zero in (1). Of course, this estimate of the vertical velocity is affected by the aspect sensitivity function and therefore should not be taken to be the true vertical velocity [Larsen and Röttger, 1991; Palmer *et al.*, 1991]. It may be possible to correct the phase of the array factor in (1), to produce a truly vertical beam, but this is beyond the scope of this study.

6 Conclusions

Recently in the MST radar community, much emphasis has been placed on alternative methods for estimating the wind vectors. Many arguments have been made for one technique over others although no clearly superior method has emerged. Here, we have examined poststatistical steering (PSS) [Kudeki and Woodman, 1990; Palmer *et al.*, 1990] and have shown the method to be a viable alternative to other techniques for application in the troposphere and lower stratosphere. PSS has already been implemented for a MF radar making measurements in the mesosphere [Sürücü *et al.*, 1992].

The implementation of the technique in the troposphere/lower stratosphere region at VHF has shown that technique worked well for the particular data presented here, but our results suggest that biases can be introduced by aspect sensitivity effects in certain cases. An advantage of PSS wind estimation is the robust nature of the algorithm. By using equation (2), the synthesized beams are produced and can be used to find the radial velocity for a particular beam direction. In turn, these radial velocity estimates are used to calculate the

three components of the vector wind. The SA/FCA and RI/FCA techniques are plagued by a complicated procedure which can produce many different types of failures. These techniques estimate the *apparent* velocity and then correct it to produce the *true* velocity. The PSS method produces the *true* velocity directly since it is just a standard DBS experiment, except that the beam is steered after the data is stored. Therefore, wind vector estimation using PSS appears to hold promise if the aspect sensitivity problem can be handled adequately.

Acknowledgements. R.D.P. was supported under NSF grant #ATM9003448. M.F.L. and E.L.S. were supported by AFOSR contract #F49620-88-C-0121. The MU radar belongs to and is operated by the Radio Atmospheric Science Center of Kyoto University

References

- Adams, G., J. Brosnahan, D. Walden and S. Nerney, Mesospheric Observations Using a 2.66-MHz Radar as an Imaging Doppler Interferometer: Description and First Results, *J. Geophys. Res.*, 91(A2), 1671-1683, 1986.
- Adams, G., J. Brosnahan and R. Johnson, Aspect sensitivity of 2.66-MHz radar returns from the mesosphere, *Radio Sci.*, 24(2), 127-132, 1989.
- Briggs, B., Radar observations of atmospheric winds and turbulence: a comparison of techniques, *J. Atmos. Terr. Phys.*, 42, 823-833, 1980.
- Briggs, B., The analysis of spaced sensor records by correlation techniques, *Handbook for MAP, 19*, SCOSTEP Secretariat, University of Illinois, Urbana, 166-186, 1984.
- Briggs, B. and R. A. Vincent, Spaced-antenna analysis in the frequency domain, *Radio Sci.*, submitted for publication, 1992.

- Farley, D., H. Ierikic and B. Fejer, Radar Interferometry: A New Technique for Studying Plasma Turbulence in the Ionosphere, *J. Geophys. Res.*, **86**(A3), 1467-1472, 1981.
- Franke, P. M., D. Thorsen, M. Champion, S. J. Franke and E. Kudeki, Comparison of time- and frequency-domain techniques for wind velocity estimation using multiple-receiver MF radar data, *Geophys. Res. Lett.*, **17**(12), 2193-2196, 1990.
- Fukao, S., T. Sato, S. Kato, R. M. Harper, R. F. Woodman, and W. E. Gordon, Mesospheric winds and waves over Jicamarca on May 23-24, 1974, *J. Geophys. Res.*, **86**, 4379-4386, 1979.
- Fukao, S., T. Sato, T. Tsuda, S. Kato, K. Wakasugi and T. Makihira, The MU radar with an active phased array, 1, Antenna and power amplifiers, *Radio Sci.*, **20**(6), 1155-1168, 1985a.
- Fukao, S., T. Tsuda, T. Sato, S. Kato, K. Wakasugi and T. Makihira, The MU radar with an active phased array, 2, In-house equipment, *Radio Sci.*, **20**(6), 1169-1176, 1985b.
- Gage, K. S. and J. L. Green, Evidence for specular reflection from monostatic VHF radar observations of the stratosphere, *Radio Sci.*, **13**(6), 991-1001, 1978.
- Hocking, W., The spaced antenna drift method, in *Handbook for MAP*, **9**, 171-186, 1983.
- Kudeki, E., Radar interferometer observations of mesospheric echoing layers at Jicamarca, *J. Geophys. Res.*, **93**, 5413-5425, 1988.
- Kudeki, E., F. Sürücü, and R. Woodman, Mesospheric wind and aspect sensitivity measurements at Jicamarca using radar interferometry and poststatistic steering, *Radio Sci.*, **25**(4), 595-612, 1990.

- Kudeki, E. and R. Woodman, A post-statistic steering technique for MST radar applications, *Radio Sci.*, 25(4), 591-594, 1990.
- Larsen, M. F. and J. Röttger, The spaced antenna technique for radar wind profiling, *J. Atmos. Ocean Tech.*, 6, 920-938, 1989.
- Larsen, M. F. and J. Röttger, VHF radar measurements of refractivity layer tilt angles and associated vertical-beam radial velocity corrections, *J. Atmos. Ocean Tech.*, 8(4), 477-490, 1991.
- Larsen, M. F., R. D. Palmer, S. Fukao, R. F. Woodman, M. Yamamoto, T. Tsuda and S. Kato, An analysis technique for deriving vector winds and in-beam incidence angles from interferometer measurements, *J. Atmos. Ocean Tech.*, in press, 1992.
- Liu, C., J. Röttger, C. Pan and S. Franke, A model for spaced antenna observational mode for MST radars, *Radio Sci.*, 25(4), 551-563, 1990.
- Liu, C., J. Röttger, G. Dester, S. Franke and C. Pan, The oblique spaced antenna method for measuring atmospheric wind field, *J. Atmos. Ocean Tech.*, 8(2), 247-258, 1991.
- Meek, C. E. and A. H. Manson, Mesospheric motions observed by simultaneous medium-frequency interferometer and spaced antenna experiments, *J. Geophys. Res.*, 92D, 917-930, 1987.
- Olver, A. D., Basic properties of antennas, *The handbook of antenna design*, Vol. 1, A. W. Rudge, K. Milne, A. D. Olver and P. Knight, Eds., 708 pp., Peter Peregrinum Ltd., London, 1982.
- Palmer, R., R. Woodman, S. Fukao, T. Tsuda and S. Kato, Three-antenna post-statistic steering using the MU radar, *Radio Sci.*, 25(6), 1105-1110, 1990.

- Palmer, R., M. Larsen, R. Woodman, S. Fukao, M. Yamamoto, T. Tsuda and S. Kato, VHF Radar Interferometry measurements of vertical velocities and the effect of tilted refractivity surfaces on standard Doppler measurements, *Radio Sci.*, 26(2), 417-427, 1991.
- Palmer, R., M. Larsen, S. Fukao, M. Yamamoto, T. Tsuda and S. Kato, Comparison of spatial interferometry refractivity layer inclination angles with isentropic surface inclinations obtained from rawinsonde measurements, *J. Geophys. Res.*, submitted for publication, 1992.
- Röttger, J. and C. H. Liu, Partial reflection and scattering of VHF radar signals from the clear atmosphere, *Geophys. Res. Lett.*, 5, 357-360, 1978.
- Röttger, J. and R. A. Vincent, VHF radar studies of tropospheric velocities and irregularities using spaced antenna techniques, *Geophys. Res. Lett.*, 5(11), 917-920, 1978.
- Röttger, J. and H. Ierke, Postset beam steering and interferometer applications of VHF radars to study winds, waves, and turbulence in the lower and middle atmosphere, *Radio Sci.*, 20(6), 1461-1480, 1985.
- Röttger, J. and M. F. Larsen, UHF/VHF radar techniques for atmospheric research and wind profiler applications, *Radar in Meteorology*, D. Atlas, Ed., 806 pp., Amer. Meteor. Soc., 1990.
- Röttger, J., C. H. Liu, J. K. Chao, A. J. Chen, C. J. Pan and I-J. Fu, Spatial interferometer measurements with the Chung-Li VHF radar, *Radio Sci.*, 25(4), 503-515, 1990.
- Royrvik, O., VHF radar signals scattered from the equatorial mesosphere, *Radio Sci.*, 18(6), 1325-1335, 1983.

- Sheppard, E. L. and M. F. Larsen, Analysis of model simulations of spaced antenna/radar interferometer measurements, *Radio Sci.*, submitted for publication, 1992a.
- Sheppard, E. L., M. F. Larsen, R. D. Palmer, S. Fukao, M. Yamamoto, T. Tsuda and S. Kato, A statistical comparison of spaced antenna and radar interferometry wind estimation, *Radio Sci.*, to be submitted for publication, 1992b.
- Sürücü, F., P. M. Franke, E. Kudeki, G. W. Adams and J. Brosnahan, On the use of software beam synthesis in multiple-receiver MF radar wind estimation, *Radio Sci.*, submitted for publication, this issue, 1992.
- Tsuda, T., T. Sato, K. Hirose, S. Fukao and S. Kato, MU radar observations of the aspect sensitivity of backscattered VHF echo power in the troposphere and lower stratosphere, *Radio Sci.*, 21(6), 971-980, 1986.
- Van Baelen, J. S., T. Tsuda, A. D. Richmond, S. K. Avery, S. Kato, S. Fukao and M. Yamamoto, Comparison of VHF Doppler beam swinging and spaced antenna observations with the MU radar: First results, *Radio Sci.*, 25(4), 629-640, 1990.
- Van Baelen, J. S., A. D. Richmond, T. Tsuda, S. K. Avery, S. Kato, S. Fukao and M. Yamamoto, Radar interferometry technique and anisotropy of the echo power distribution: First results, *Radio Sci.*, 26(5), 1315-1326, 1991.
- Van Baelen, J. S. and A. D. Richmond, Radar interferometry technique: Three-dimensional wind measurement theory, *Radio Sci.*, 26(5), 1209-1218, 1991.
- Vincent, R. A. and J. Röttger, Spaced antenna VHF radar observations of tropospheric velocities and irregularities, *Radio Sci.*, 15(2), 319-335, 1980.

Woodman, R., Inclination of the geomagnetic field measured by an incoherent scatter radar technique, *J. Geophys. Res.*, **76**(1), 178-184, 1971.

Woodman, R. F. and A. Guillen, Radar observations of wind and turbulence in the stratosphere and mesosphere, *J. Atmos. Sci.*, **31**, 493-505, 1974.

Yamamoto M., T. Sato, P. T. May, T. Tsuda, S. Fukao and S. Kato, Estimation error of spectral parameters of mesosphere-stratosphere-troposphere radars obtained by least squares fitting method and its lower bound, *Radio Sci.*, **23**(6), 1013-1021, 1988.

Figure captions

- Fig. 1. Receiver antenna configuration used for the spatial interferometer experiment conducted on June 29, 1990 1910 LT to July 2, 1990 0950 LT.
- Fig. 2. Profiles of PSS synthesized spectra and Gaussian fits for (θ_s, ϕ_s) equal to (a) $(90^\circ, 3^\circ)$ and (b) $(270^\circ, 3^\circ)$.
- Fig. 3. Calculated two-way antenna power patterns for the five beams positions used in the DBS analysis, i.e., (θ_s, ϕ_s) equals $(0^\circ, 0^\circ)$, $(0^\circ, 3^\circ)$, $(90^\circ, 3^\circ)$, $(180^\circ, 3^\circ)$, and $(270^\circ, 3^\circ)$. In this figure, \hat{Z}_e represents the zenith angle of the two-way antenna power pattern.
- Fig. 4. Profiles of zonal and meridional wind for the entire observation period obtained from approximate 24-min averages. For display purposes, 2 of these profiles were averaged and then displayed in the figure. The lower right figure is the average of the zonal and meridional wind for the observation period, with $\pm\sigma$ error bars. The upper right figure again shows the zonal and meridional averages, but compared to the *true* and *apparent* winds obtained from the SA/FCA technique [Sheppard *et al.*, 1992].
- Fig. 5. Profiles of echo power and Doppler vertical velocity with the same averaging scheme used in Figure 4. As in Figure 4, the figures to the right are the averages over the entire observation period. In addition, the upper right figure shows the number of outliers in the 155 wind profiles. As one would expect, the failure count is inversely proportional to the echo power.

TABLE 1. Synthesized Two-way Antenna Pattern Zenith Angles

Beam		Aspect	Sensitivity	Pointing	Direction
ϕ, θ	Isotropic	0 0	0 1	45 1	90 1
0 0	8.3×10^{-5}	6.8×10^{-5}	6.8×10^{-5}	6.8×10^{-5}	6.8×10^{-5}
0 3	0.63	0.60	0.64	0.63	0.60
90 3	0.64	0.61	0.61	0.64	0.65
180 3	0.63	0.60	0.56	0.57	0.60
270 3	0.64	0.61	0.61	0.58	0.57

An aspect sensitivity function with a 10° width was assumed.

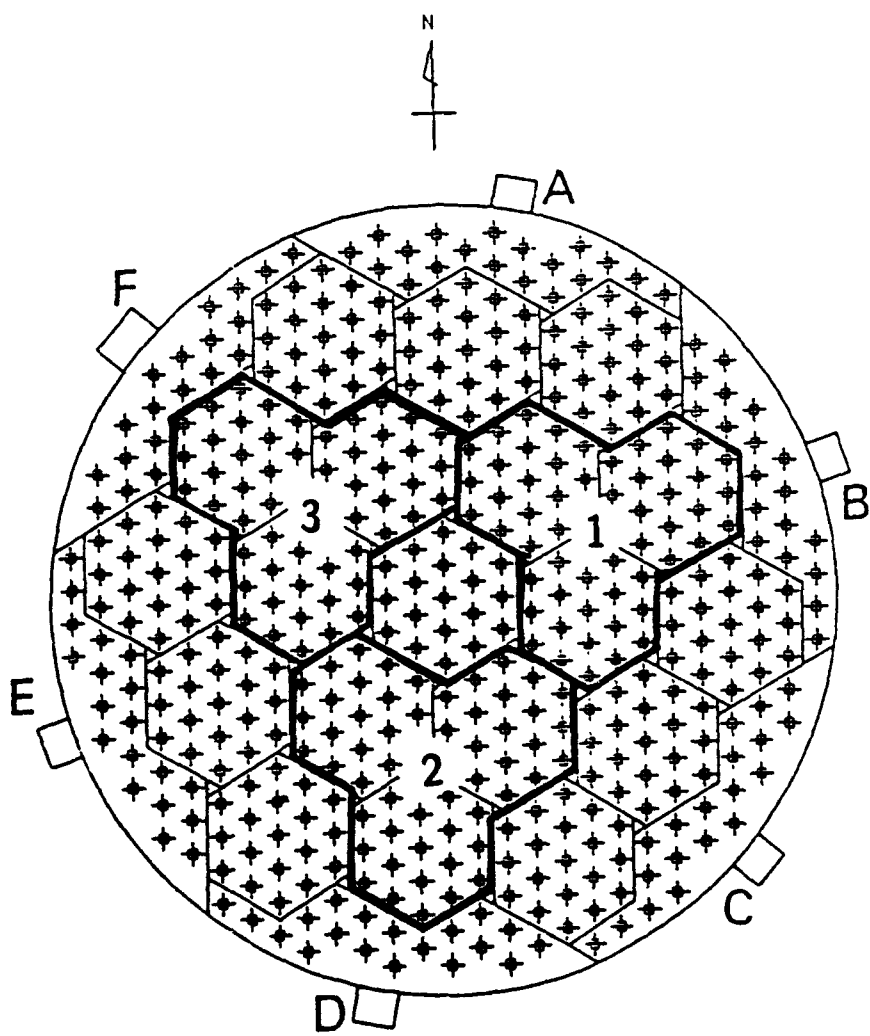


Fig. 1

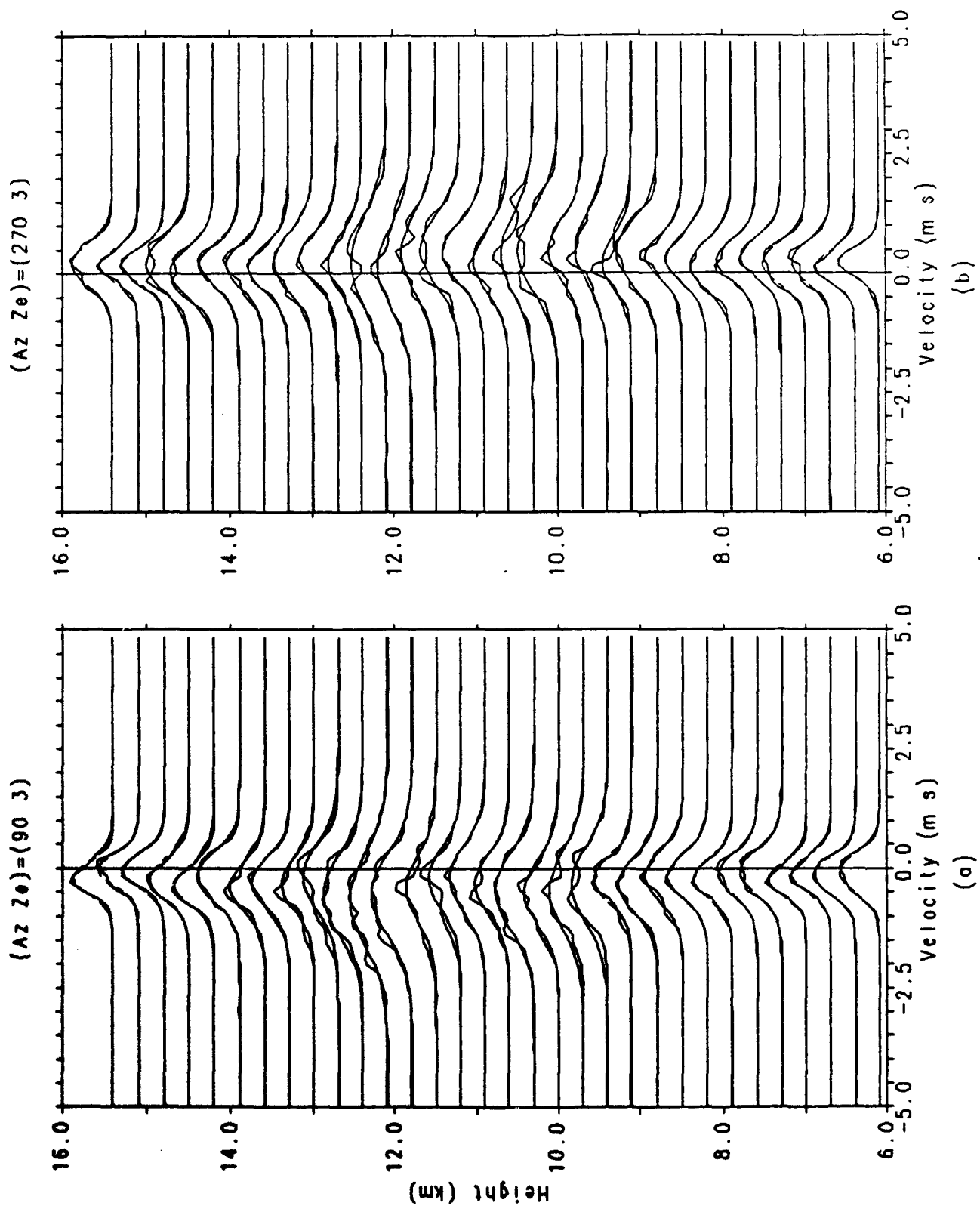


Fig. 2

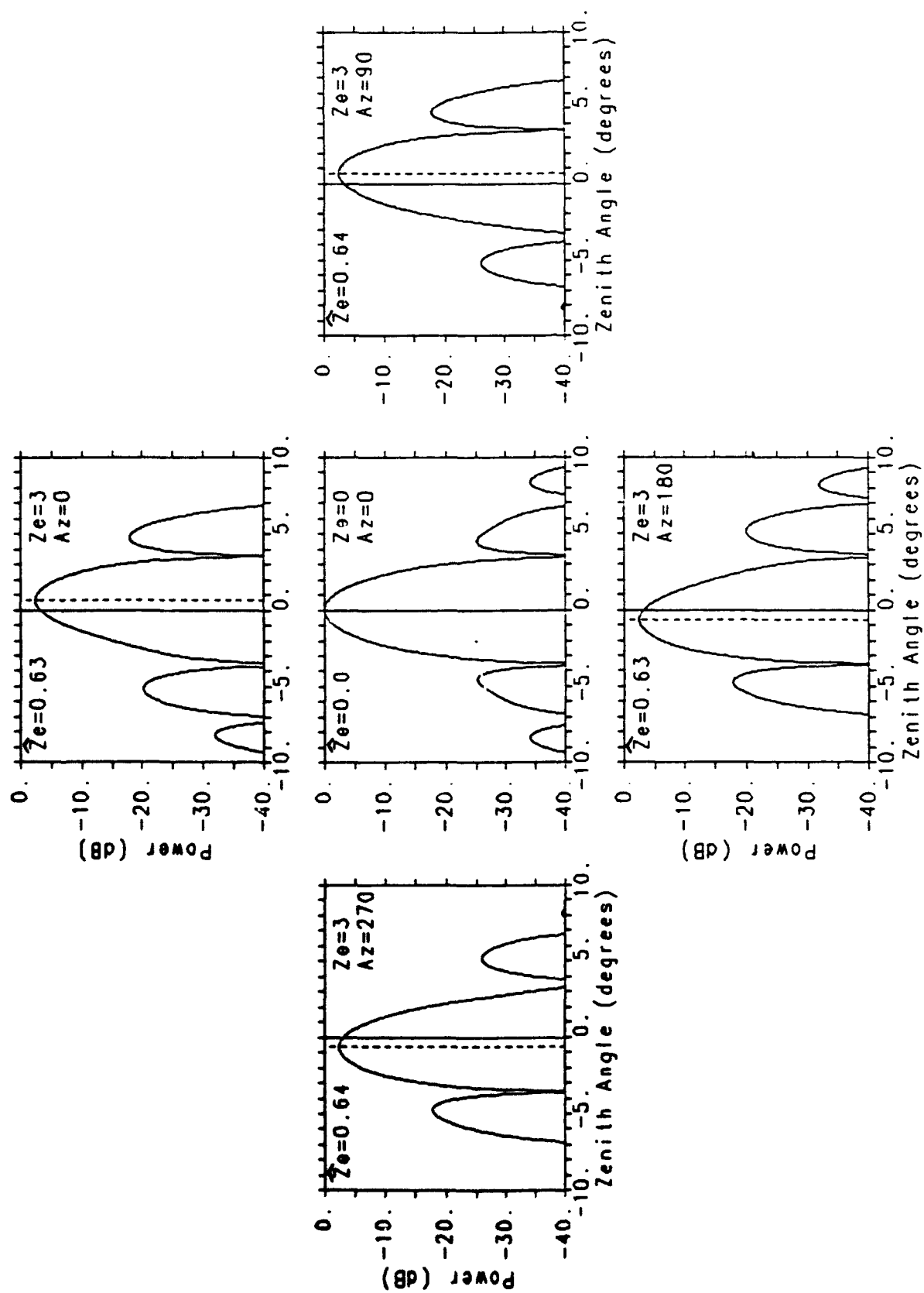


Fig. 3

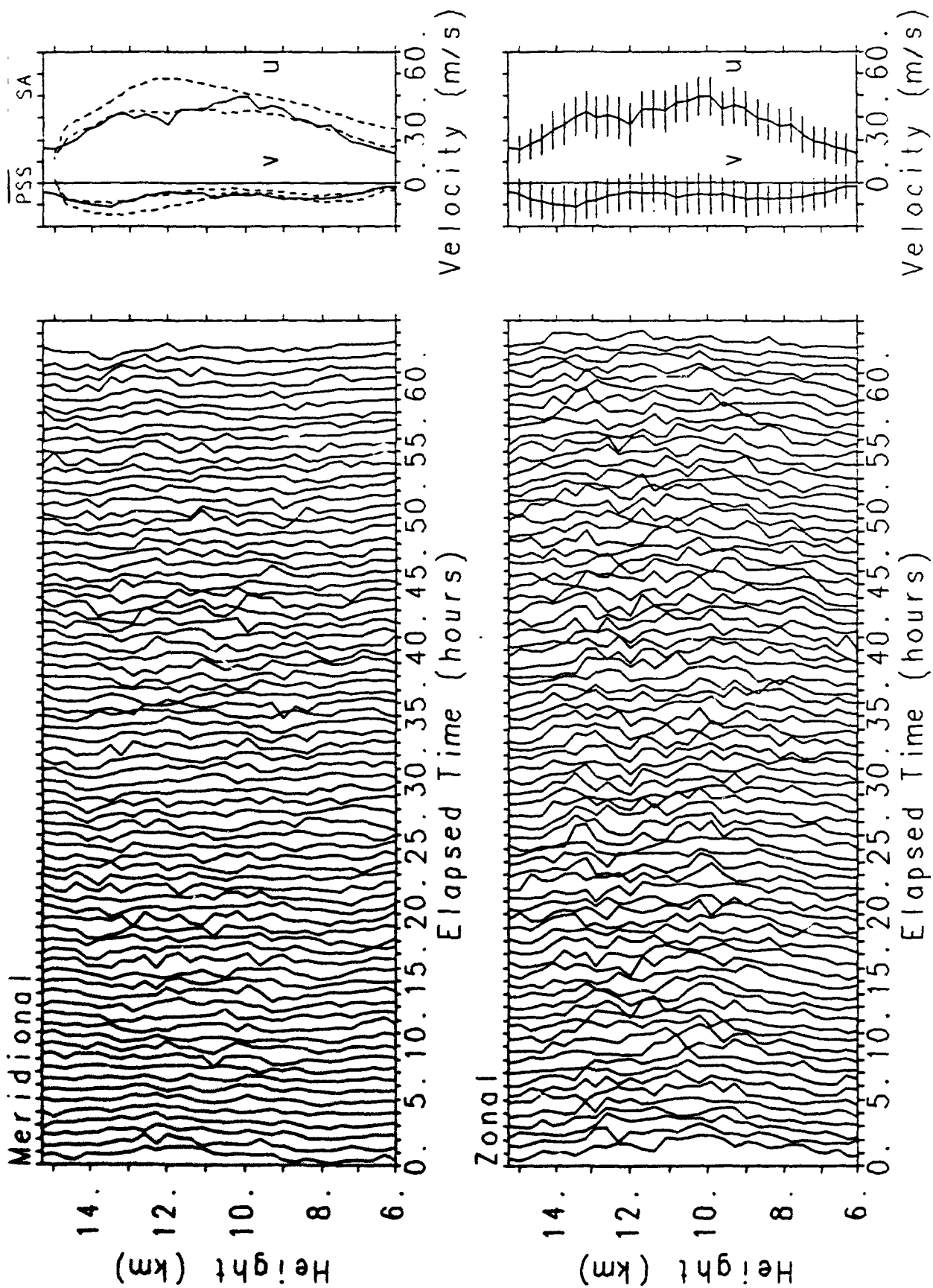


Fig. 4

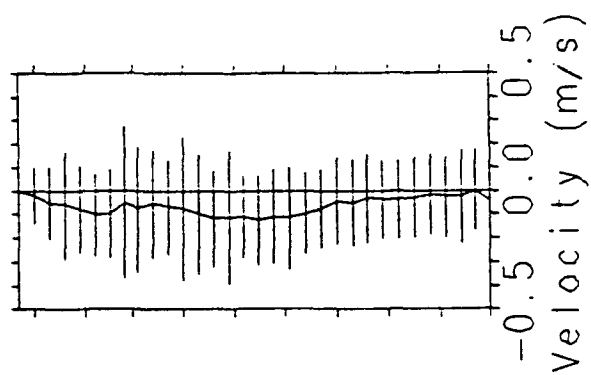
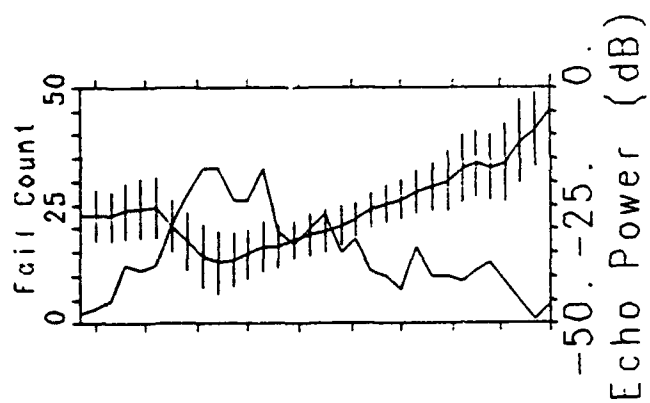
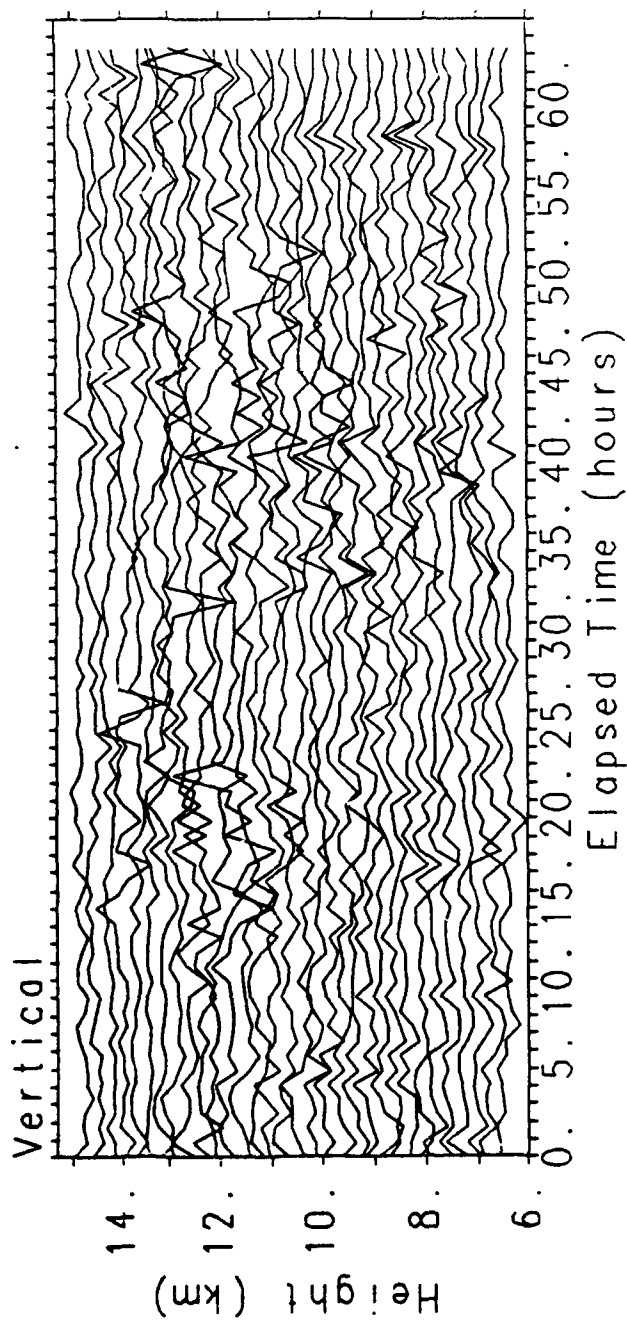
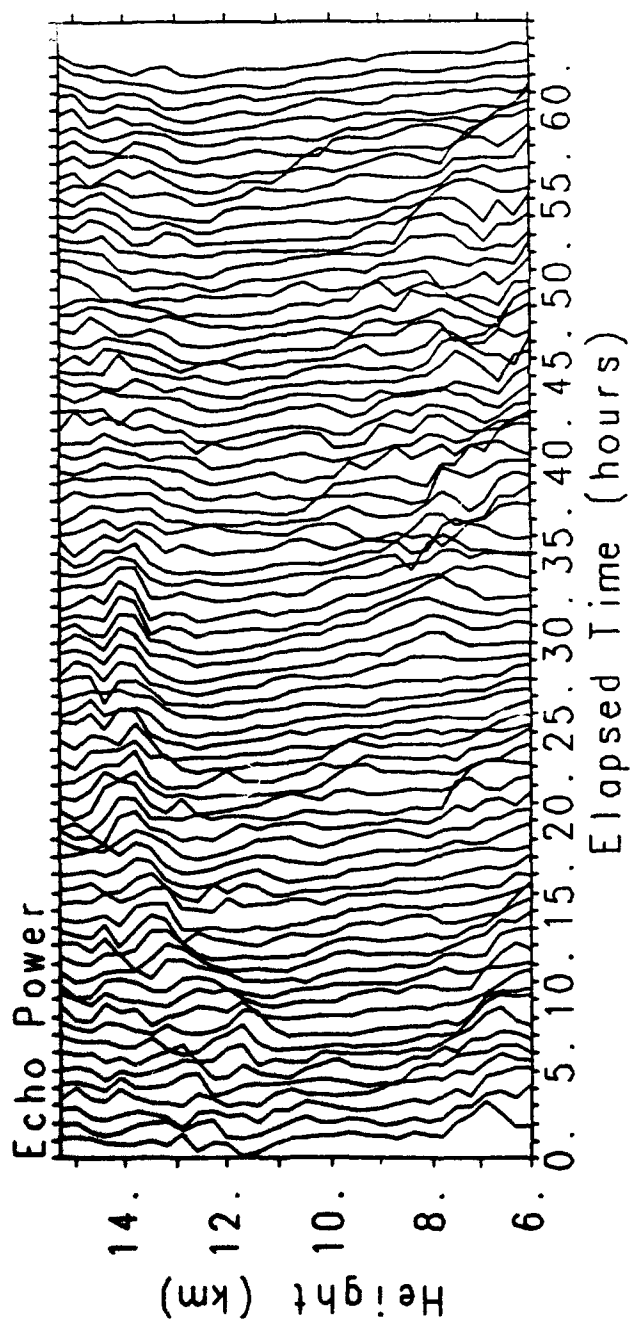


Fig. 5

VHF radar interferometry measurements of vertical velocity and the effect of tilted refractivity surfaces on standard Doppler measurements

Robert D. Palmer,¹ Miguel F. Larsen,² Ronald F. Woodman,³ Shoichiro Fukao, Mamoru Yamamoto, Toshitaka Tsuda, and Susumu Kato

Radio Atmospheric Science Center, Kyoto University, Uji, Kyoto, Japan

(Received April 16, 1990; revised October 19, 1990; accepted December 3, 1990.)

At VHF wavelengths, aspect sensitivity may result in an apparent beam direction that is off vertical even for a nominally vertically pointing beam direction if the refractivity surfaces responsible for the scatter are tilted with respect to the horizontal plane. Middle and upper atmosphere radar measurements obtained by using the system in a standard multireceiver configuration typical for radar interferometry (RI) and spaced antenna measurements have been analyzed for evidence of such effects. The analysis is based on the linear variation of the cross-spectral phase as a function of the radial velocity in the frequency domain for the RI cross spectra. True-vertical velocity estimates are obtained by using the fact that the phase difference between two antennas should be equal to zero when the echoes are being received from the vertical direction. The tilt angles of the refractivity surfaces were obtained from the phase of the cross-correlation function at zero lag, and the radial velocity in that direction was determined from the cross spectra. The results indicate that the vertical velocity derived from standard Doppler analyses is actually the velocity perpendicular to the refractivity surfaces and thus can be biased by the projection of the horizontal wind along the effective pointing direction.

1. INTRODUCTION

Understanding the vertical circulations in the atmosphere is of fundamental importance for a number of problems in the atmospheric sciences, ranging from long-term vertical transport of trace constituents to short-term weather forecasting. There have been few techniques for measuring vertical velocities directly, although the integration of the mass continuity equation and other indirect methods for estimating the velocities become useful for larger temporal and spatial scales. For smaller scale flows characteristic of the mesoscales and microscales, indirect methods are often not tractable either because many approximations are required in the calculations or dense measurement networks are needed. For these reasons, the potential capabilities of the wind profiling radars or mesosphere-stratosphere-troposphere (MST) ra-

dars for measuring vertical velocities over short time scales are of great interest.

In spite of the interest in the measurements, tests to establish the accuracy or potential biases in the measurements have been difficult to design or implement. A few studies have compared vertical velocities derived from standard radiosonde measurements with the vertical velocities measured by the Doppler technique with VHF radars [Nastrom *et al.*, 1985; Larsen *et al.*, 1988]. While some agreement was found, discrepancies were large enough that detailed quantitative comparisons were meaningless.

So far, the wavelengths used for wind profiling or MST radar studies have been primarily around 6 m in the VHF band or around 70 cm in the UHF band. The longer wavelength has the advantage that the turbulent scatter contribution to the signals is almost always dominant, even in precipitation, unless the rainfall rates become very large. The shorter wavelength signals are dominated by precipitation even for relatively light rainfall rates, and vertical velocity measurements by a direct Doppler method with a vertically pointing beam become impossible. Larsen and Röttger [1986] have discussed the relative reflectivities at the two wavelengths in more detail. Typically, vertical velocities are estimated by pointing the beam of a Doppler radar in the

¹ Now at Department of Physics and Astronomy, Clemson University, Clemson, South Carolina.

² On leave from the Department of Physics and Astronomy, Clemson University, Clemson, South Carolina.

³ On leave from the Jicamarca Radio Observatory, Instituto Geofísico del Perú, Lima.

vertical direction and processing the received signals, caused by fluctuations in the refractive index of the atmosphere, to obtain the Doppler shift. At VHF frequencies the received signals usually show aspect sensitivity effects, i.e., the reflectivity decreases as the beam is tilted off vertical [e.g., Tsuda *et al.*, 1986]. If the refractivity surfaces are tilted away from the horizontal plane, the aspect sensitivity may cause errors in the estimate of the vertical velocity since the largest contribution to the received signals will come from an off-vertical direction. By finding the center of the aspect sensitivity function, tilt angles estimates with VHF radar were made by Vincent and Röttger [1980]. Röttger and Ierkic [1985] estimated tilt angles using spatial interferometry. More recently, Larsen and Röttger [1991] analyzed the layer tilt angle measurements derived from a data set obtained over 4 days with the sounding system (SOUSY) VHF radar. Their results have provided qualitative evidence that biases in the vertical velocity measurements resulted from the tilted refractive structures.

In this paper we apply the radar interferometer technique to test the relationship between the tilted layers and biases in the velocity estimates. Radar interferometry (RI), also known as spatial interferometry (SI), is based on receiving signals in multiple receiving antennas and has been described in detail by Woodman [1971], Farley *et al.* [1981], and Adams *et al.* [1989]. In section 2 we describe the experimental procedure, which was previously used for an interferometer application [Palmer *et al.*, 1990]. The derivation of the method is presented in section 3. Section 4 shows a comparison of measurements with the Doppler and RI methods. Conclusions are given in section 5.

2. EXPERIMENTAL PROCEDURE

A radar interferometer experiment was conducted on October 24, 1989, 2100–2400 LT using the MU radar located in Shigaraki, Japan (34.85°N, 136.10°E) [Palmer *et al.*, 1990]. The transmitting and receiving antennas are shown in Figures 1a and 1b, respectively. The transmitting antenna can be seen to use only the middle portion of the radar. This was done so that the beam width of the radar could be increased to approximately 6.8° [Fukao *et al.*, 1988], giving a wider range of zenith angles that one could observe. This was accomplished at a loss of sensitivity, due to the decrease in transmitting

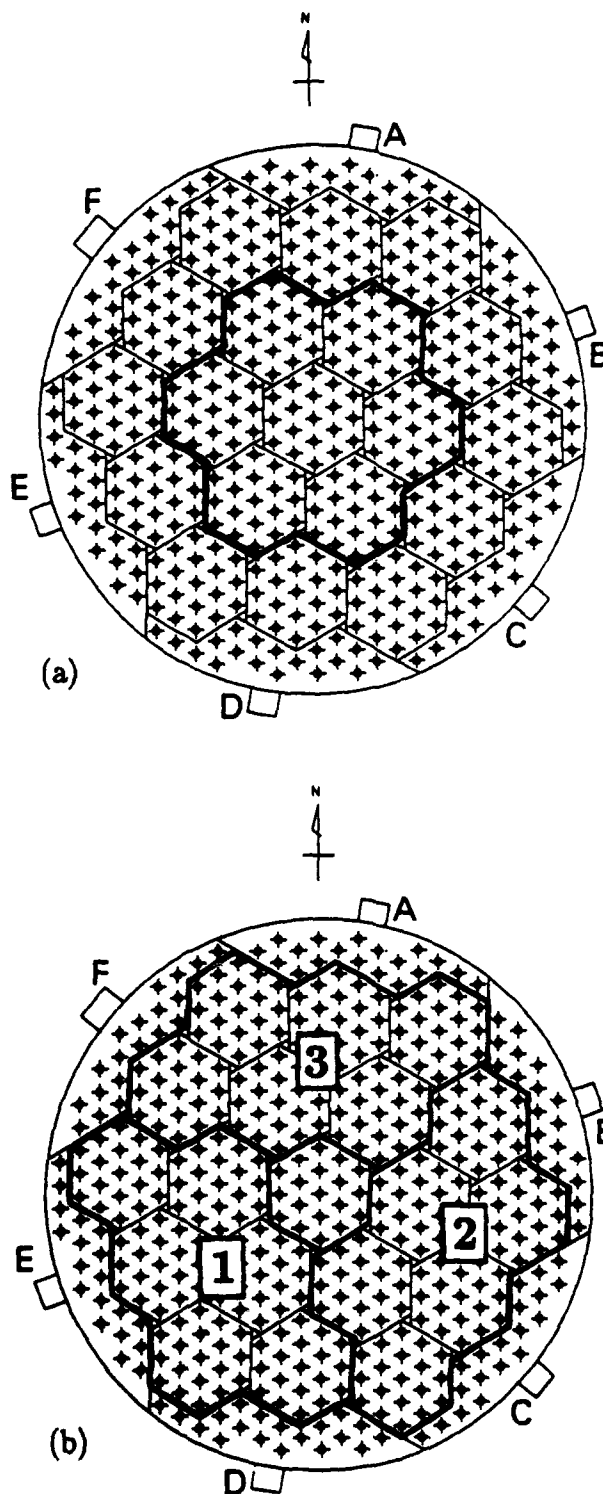


Fig. 1. Antenna configurations used for the interferometer experiment conducted on October 24, 1989, 2100–2400 LT using the MU radar. (a) transmitting antenna, (b) receiving antennas.

power, but was deemed sufficient for tropospheric/stratospheric observations. On reception the antenna was segmented into three equal-area antennas, which are denoted as antennas 1, 2, and 3.

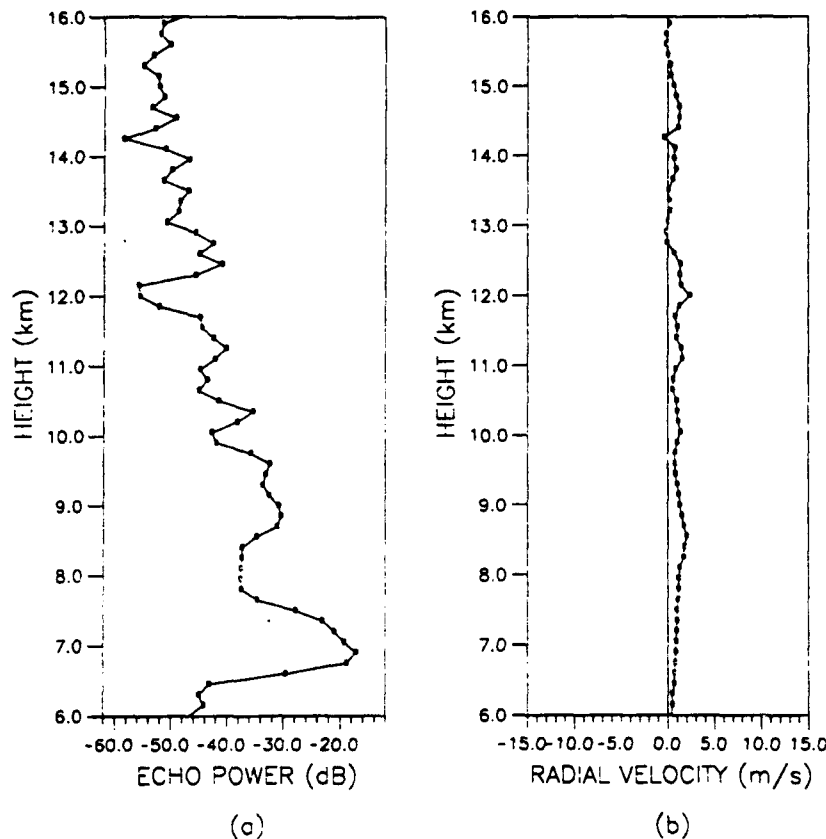


Fig. 2. Standard Doppler measurements at azimuth 0° and zenith angle of 10° , (a) echo power profile, and (b) radial velocity.

The height resolution of this experiment was 150 m, with observations taken from 6.0 to 15.45 km. Pulse compression was used with a flip of the code with every interpulse period (IPP), which in this experiment was set to 400 μ s. Coherent integration was performed with 256 points, giving a sampling interval of 0.1024 s. After this process, 256 points of raw data was stored on magnetic tape, with a small time gap for data processing. Therefore approximately every 30 s, another 256 point data set was stored. Two 30-min averages of autospectra and cross spectra, processed by a rectangular window periodogram, were obtained for all combinations of antennas. These will be used in later sections to illustrate the technique presented in this paper.

Before the RI experiment was conducted a standard Doppler experiment was performed and the radial velocity was estimated by a standard first moment estimate of the Doppler spectra. Figures 2 and 3 show the echo powers and radial velocities for a zenith angle of 10° and azimuth angles of 0° and 90° , respectively. The reflectivity profiles show a typical structure with a decrease of approximately 2

dB km^{-1} . A high reflectivity stratospheric layer is evident around 12.5 km, and the enhancement in the signal strength near the tropopause can be seen at a height just above 10 km. The largest contribution to the radial velocity measured at a zenith angle of 10° is expected to be from the horizontal components. Therefore Figures 2b and 3b imply that almost all of the contribution to the horizontal wind is from the zonal component and that the wind vector is essentially aligned with the baseline between antennas 1 and 2. The uniform wind direction will simplify the analysis discussed later, although the techniques can be applied equally well when the wind direction is not aligned with a baseline.

3. THREE-DIMENSIONAL WIND VECTOR MEASUREMENT USING RADAR INTERFEROMETRY

One way to test for biases in the vertical velocity measurements due to tilted refractivity layers would be to compare the direct vertical beam measurements with the vertical velocity calculated from

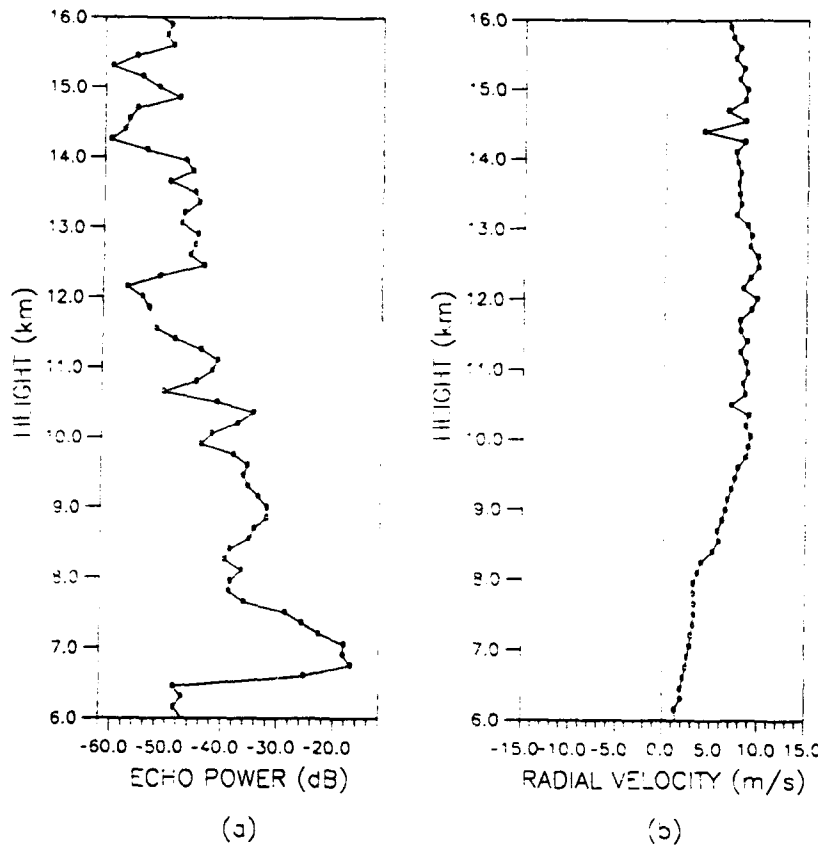


Fig. 3. Same as Figure 2, but with azimuth 90° .

two off vertical beams separated by 180° in azimuth. Differences in the two measurements could then be attributed to aspect sensitivity effects. However, the separation between beams quickly becomes large and can easily be 5–10 km near the tropopause for typical zenith angles of 10° to 20° . The large area over which the velocities are sampled suggests that the horizontal winds and vertical velocities may not be uniform in which case differences in the measurements may be due to either inhomogeneity in the wind field or biases produced by the characteristics of the scattering mechanism.

The RI technique is similar to a many beam-direction. Doppler experiment in that the radial velocity can be obtained as a continuous function of zenith angle, within the beam width of the radar. The RI method for obtaining the three-dimensional wind vector uses only a vertical beam, and the beam steering is accomplished in the data processing stage [Röttger and Ierkic, 1985; Kudeki and Woodman, 1990]. It should be pointed out that an analysis technique, which is similar but more general to the following, has been independently derived by Van Baelen [1990]. The derivation of the

equations relevant to our analysis begins with an equation for the radial velocity

$$v_r = v_H \sin \gamma' + w \cos \gamma' \quad (1)$$

where v_H and w are the horizontal and vertical wind components, respectively. Figure 4 displays the configuration used in this analysis. The angle γ' is the zenith angle in the direction of the wind vector, which would produce a radial velocity of v_r . We would like to find γ' in terms of the zenith angle, which is produced on the baseline, i.e., γ . From Figure 4 it can be seen that

$$\cos(\alpha - \theta) = \frac{\tan \gamma}{\tan \gamma'} \quad (2)$$

where θ and α are the azimuth angles of the wind vector and the baseline, respectively. But, since for an interferometer experiment, the zenith angles are usually very small, the above equation becomes

$$\cos(\alpha - \theta) \approx \frac{\sin \gamma}{\sin \gamma'} \quad (3)$$

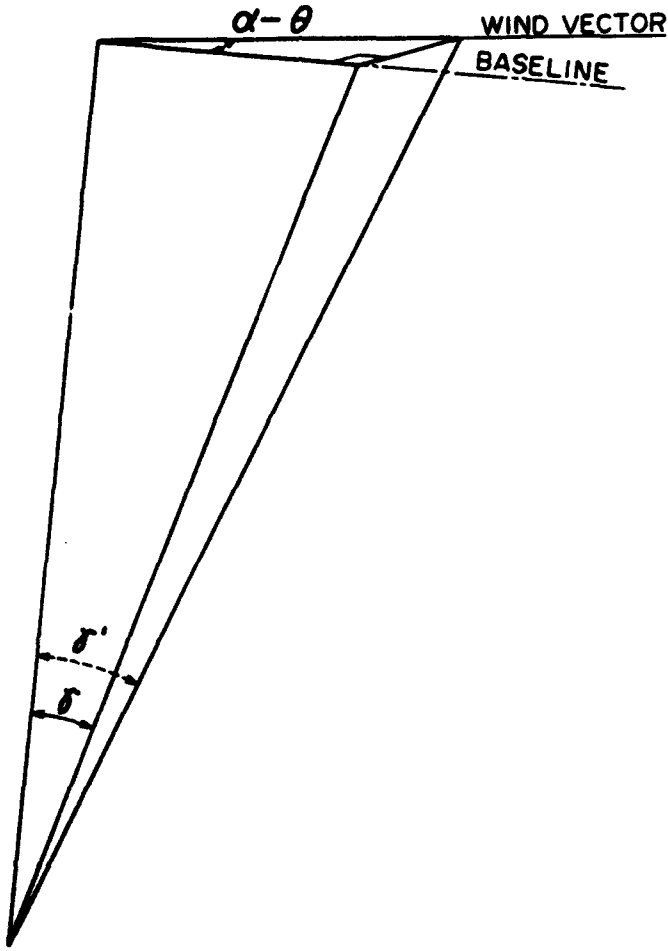


Fig. 4. Configuration of the baseline with respect to the wind vector used for the derivation of the equation of the phase in terms of the radial velocity. The wind vector and baseline have azimuth angles θ and α , respectively. The coefficients γ' and γ denote the zenith angles in the direction of the wind vector and the baseline, respectively.

Substituting for the $\sin \gamma'$ term in (1), and using the fact that $\cos \gamma' \approx 1$, the radial velocity becomes

$$v_r = \frac{v_H \sin \gamma}{\cos (\alpha - \theta)} + w \quad (4)$$

It is well known that the phase difference between two antennas is related to the zenith angle by

$$\phi = kD \sin \gamma \quad (5)$$

where k is the radar wave number and D is the distance between the two antennas, which form a baseline that defines a plane with the vertical in which γ is measured. Using this expression to

substitute the $\sin \gamma$ term in (4) and solving for the ϕ , the following relation is found

$$\phi = \left[\frac{kD \cos (\alpha - \theta)}{v_H} \right] v_r - \left[\frac{wkD \cos (\alpha - \theta)}{v_H} \right] \quad (6)$$

This equation is easily seen to have the form of a line with slope m and intersection b given by

$$m = \frac{kD \cos (\alpha - \theta)}{v_H} \quad (7)$$

$$b = \frac{-wkD \cos (\alpha - \theta)}{v_H} \quad (8)$$

The linear variation of the cross-spectral phase ϕ as a function of v_r has been seen in a number of earlier experiments [e.g., Farley *et al.*, 1981; Röttger *et al.*, 1990] and is expected on physical grounds. Since the phase of the signal is related to the angular position from which the echoes are received, the radial velocity should change linearly for small zenith angles, as the angle changes from positive to negative.

More details of the derivation of (6) have been given by Van Baelen [1990]. A more general equation for the phase of the cross spectra has recently been presented by Liu *et al.* [1990, equation (27)]. In this equation the contribution of the spectral width due to turbulence is assumed to be dominated by the beam-broadening effect, which has been shown to typically be the case [Hocking, 1985]. This is especially true in the troposphere/stratosphere but may not be the case in the mesosphere. The turbulent spectral width is related to the correlation length of the scatterers and is also one source of problems in the SA technique [Briggs, 1984]. As stated by Liu *et al.* [1990], one component of this phase equation can be ignored if sufficient incoherent averaging is performed to insure statistically homogeneous turbulence within the resolution volume. The remaining component of the phase can easily be shown to reduce to (6), and the equation given by Van Baelen [1990] with only the assumption that the magnitude of the horizontal wind is much greater than that of the vertical.

From (7) and (8) we would like to estimate the three components of the wind vector. We will start with a substitution of $v'_H = 1/v_H$, which gives a slope of the form

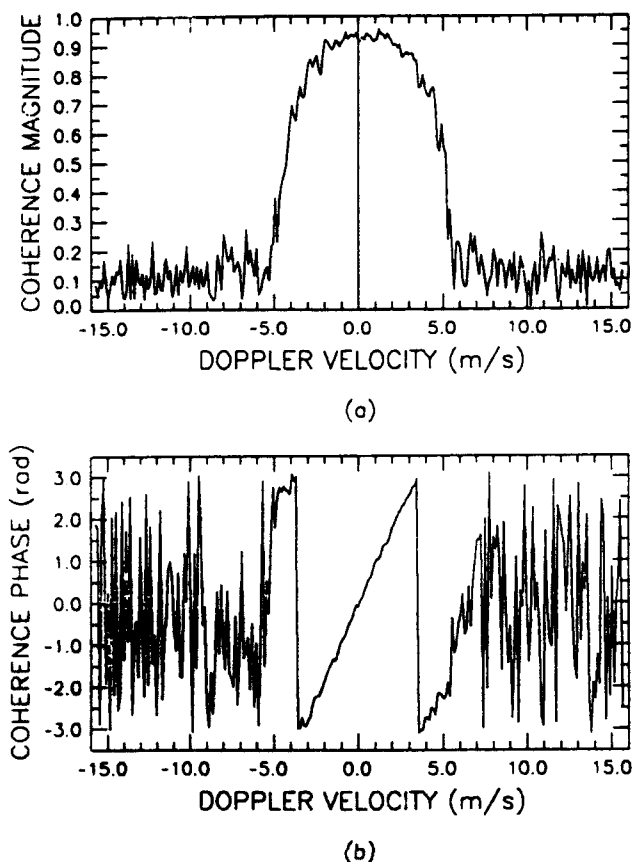


Fig. 5. Typical coherence function, obtained from spatial domain interferometry data, (a) magnitude, and (b) phase with an obvious linear variation.

$$m = kDv_H' \cos(\alpha - \theta) \\ = kD(u' \sin \alpha + v' \cos \alpha) \quad (9)$$

where u' and v' are the zonal and meridional components of v_H' .

From (9) it is evident that u' and v' can be estimated if two independent estimates of the slope m are available from two pairs of receiving antennas, for example. Three antennas are used in the usual interferometer configuration. Therefore three different cross spectra are available. Figure 5 displays the magnitude and phase of a typical normalized cross-spectra, i.e., coherence function. As one can see, there is a linear variation in the phase of the coherence function. In some cases the signals from an antenna pair with a baseline perpendicular to the wind will have low coherence and will be excluded from the calculation of the wind vector. The relationship between u' , v' , and the slopes is given by

the following equation for two independent slope measurements.

$$\begin{pmatrix} \sin \alpha_{12} & \cos \alpha_{12} \\ \sin \alpha_{13} & \cos \alpha_{13} \end{pmatrix} \begin{pmatrix} u' \\ v' \end{pmatrix} = \begin{pmatrix} \frac{m_{12}}{kD} \\ \frac{m_{13}}{kD} \end{pmatrix} \quad (10)$$

where ij denote the baseline formed between antennas i and j . Equation (10) could be extended to include three independent slope measurements, but if one of the cross spectra has low coherence, there is a deterioration in the estimate. Similar problems sometimes arise in SA measurements if one of the antenna pairs is oriented perpendicular to the wind direction. From (10) the u' and v' components of the wind are estimated by

$$u' = \frac{1}{kD\Delta} [m_{12} \cos \alpha_{13} - m_{13} \cos \alpha_{12}] \quad (11)$$

$$v' = \frac{1}{kD\Delta} [m_{13} \sin \alpha_{12} - m_{12} \sin \alpha_{13}] \quad (12)$$

where $\Delta = \sin \alpha_{12} \cos \alpha_{13} - \sin \alpha_{13} \cos \alpha_{12}$.

Once u' and v' have been estimated, the horizontal wind can be obtained by

$$v_H = \frac{1}{\sqrt{(u')^2 + (v')^2}} \quad (13)$$

and the azimuth angle of the wind vector is given by

$$\theta = \arctan \left(\frac{u'}{v'} \right) \quad (14)$$

The vertical velocity can be estimated using (8) once the horizontal component has been computed. However, another approach is to find the radial velocity when the beam is pointing exactly vertically, i.e., $\phi = 0$. Therefore a simple way to estimate the vertical velocity is obtained by letting $\phi = 0$ in (6).

$$w = v_r|_{\phi=0} = -\frac{b_{12}}{m_{12}} \quad (15)$$

When the phase difference between the signals in two adjacent receiving antennas is zero, the contribution must be from the true vertical direction within the accuracy of the mechanical layout of the radar system. The simplicity of (15) is somewhat

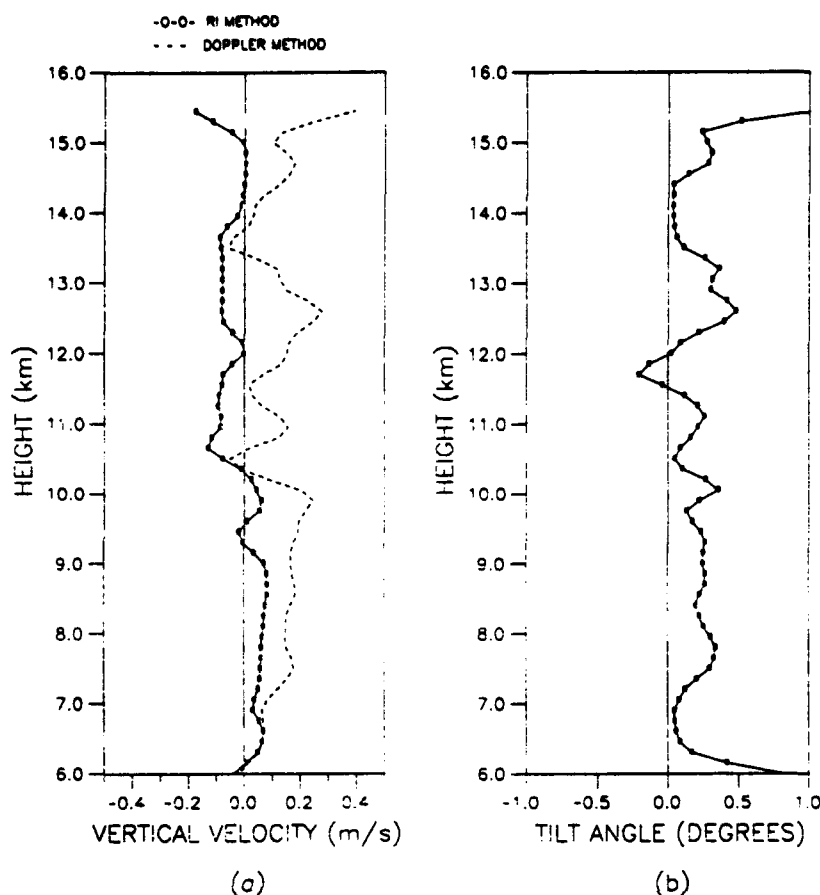


Fig. 6. Data taken from a 30-min average from 2145 to 2215 LT. (a) Comparison of RI and Doppler vertical velocity estimates and (b) estimates of tilt angles obtained from the phase of the cross-correlation function at zero lag.

deceptive. It appears that only one estimate of the slope and intercept are needed in which case one antenna pair is sufficient. However, the apparent beam direction can also be tilted in the direction transverse to the antenna pair baseline so that in the general case, information from at least two antenna pairs must be combined to yield the true vertical velocity. The uniformity of the wind direction with height during our observations has simplified the analysis so that the problem is essentially two dimensional. The general case of the wind vector determination method described in this paper, which includes aspect sensitivity and tilt in all directions, has been derived by *Larsen et al.* [1991].

4. COMPARISON OF THE RI AND DOPPLER TECHNIQUES

Figures 6a and 7a show the profiles of vertical velocity estimated from two independent 30-min averages. The RI estimate was obtained by using

(15), and the Doppler method estimate was obtained by calculating the first moment of the average of the three autospectra obtained from the RI experiment. The two estimates are thus derived from exactly the same data. Only the processing is different. The result is that most of the usual uncertainties associated with temporal or spatial beam separations or differences in sampling schemes are eliminated. The difference between the two curves is clearly significant and amounts to more than 30 cm s^{-1} at some heights. Figures 6b and 7b show the tilt angles inferred from the phase of the cross correlation at zero lag as a function of height [*Röttger and Ierkic*, 1985; *Larsen and Röttger*, 1991] from the antenna pair which was aligned along the east/west direction parallel to the wind. A general trend at all altitudes is that the large differences in the vertical velocity estimates occur at those heights where the tilt angles are large.

A further test that can be applied to the data is to

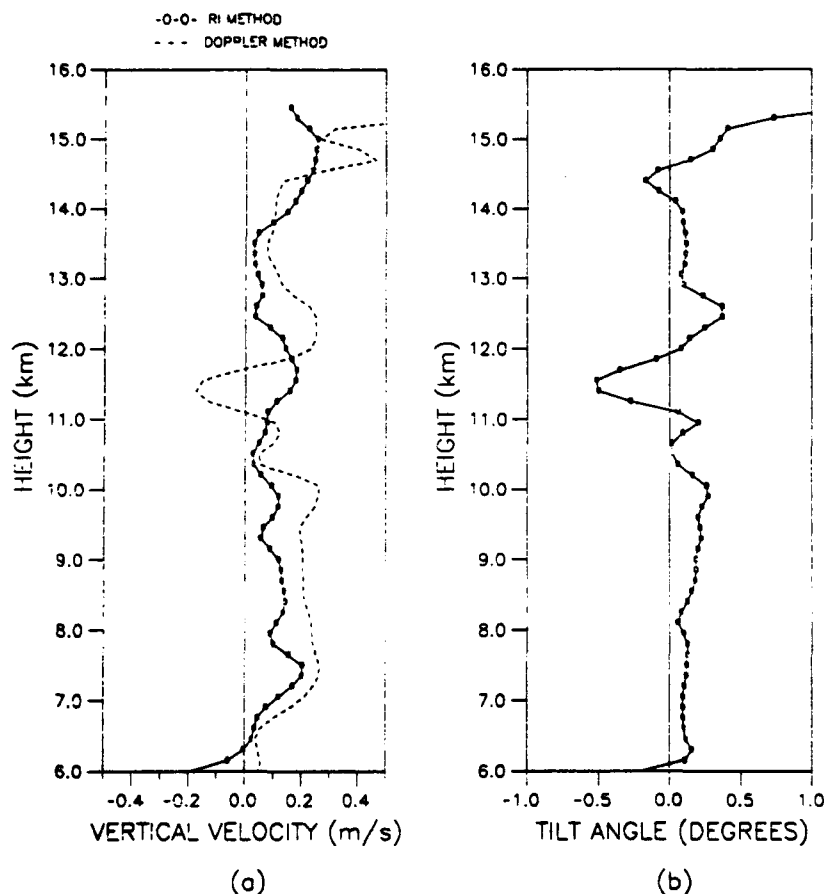


Fig. 7. Same as Figure 6, except for a 30-min average taken from 2215 to 2245 LT.

calculate a predicted difference between the two vertical velocity estimates, which should be equal to the projection of the horizontal velocity along the tilt direction. Figures 8a and 9a show this comparison. The two sets of curves follow each other very closely.

Finally, the velocity perpendicular to the refractivity layers v_{\perp} can be estimated by using the tilt angle information and the cross-spectral phase information together. Instead of isolating the contribution from the true-vertical direction as we did with the curves in Figures 6a and 7a, we now choose a specific off-vertical component along a direction that varies as a function of height. Specifically, the phase corresponding to the tilt angle, obtained from the cross-correlation function, was substituted into (6) and the corresponding value of v_r was calculated.

$$v_{\perp} = v_r \sin \delta_{12} = \frac{kD \sin \delta_{12} - b_{12}}{m_{12}} \quad (16)$$

where δ_{12} is the tilt angle in the baseline formed by antennas 1 and 2. Again, the alignment of the wind vector with the baseline between antennas 1 and 2 made the calculations simple. The perpendicular velocity estimate is compared to the standard Doppler method estimate in Figures 8b and 9b. The agreement between the curves indicates that the Doppler vertical velocities are actually velocity components along the apparent beam direction and are thus biased by the horizontal velocity.

5. CONCLUSIONS

Analysis of interferometer measurements has shown that a bias can exist in standard Doppler estimates of the vertical velocity caused by tilting of refractivity surfaces, at least at certain times and in certain height ranges. Since all the analysis has involved different processing procedures applied to the exact same data set, many, if not all, of the

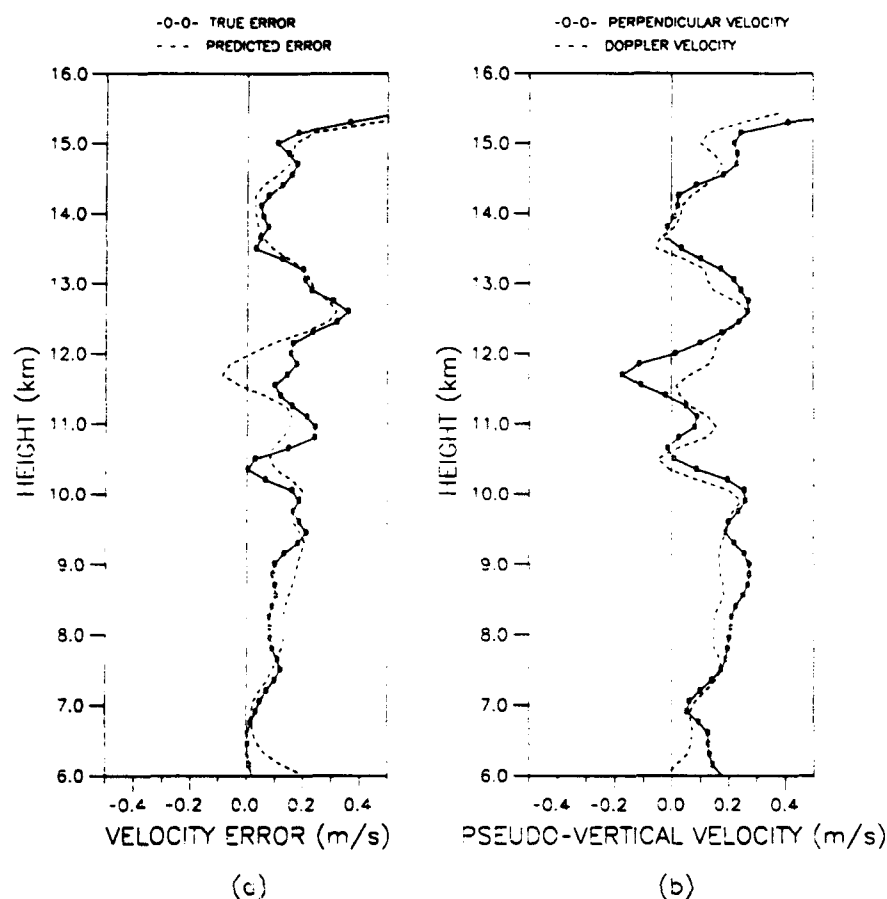


Fig. 8. Data taken from a 30-min average from 2145 to 2215 LT. (a) Comparison of observed error (difference between vertical velocities obtained from the RI and Doppler methods) and the predicted error (obtained from tilt angles and estimates of the horizontal velocity) and (b) Comparison of radial velocities perpendicular to the refractivity layers and the standard Doppler velocities obtained from a vertical beam.

usual uncertainties associated with unknown spatial or temporal variations in the atmospheric medium have been eliminated. The bias is a direct consequence of the aspect sensitivity of VHF echoes received from refractivity surfaces, which when tilted, cause the apparent beam to be tilted away from vertical as illustrated in Figure 10. VHF echoes are known to be aspect sensitive [Tsuda *et al.*, 1986], but the origin of this effect is still an open question. The aspect sensitivity causes the apparent antenna beam to be smaller than the antenna beam of the radar, since the echoes from off-vertical angles will be attenuated. This does not cause a problem with the vertical velocity measurements obtained from the Doppler method, if the refractivity surface which is causing the echo is not tilted. The tilting of the apparent beam toward the perpendicular of the refractivity surface will cause the vertical velocity estimate to be biased by the component of the horizontal wind in the direction of the

tilted beam [Larsen and Röttger, 1991]. If the tilt angle is denoted by δ_T , then the horizontal wind contribution to the vertical velocity is given by the magnitude of the horizontal wind component in the direction of the tilt multiplied by $\sin \delta_T$. Since the tilt angles are usually small, i.e., less than 2° , this contribution is small, but the vertical velocity is also small, and therefore the overall error is significant.

At present, no aspect sensitivity effect has been observed at UHF frequencies, but tilted refractivity layers could still cause a bias in the vertical velocity estimate. This bias could be caused if the wind flow is not horizontal, causing a wind shear within the resolution volume of the radar. But the results presented in the previous section seem to indicate that the flow is horizontal. If the flow was along the refractivity structure, then the perpendicular velocity, shown in Figures 8b and 9b, would be zero.

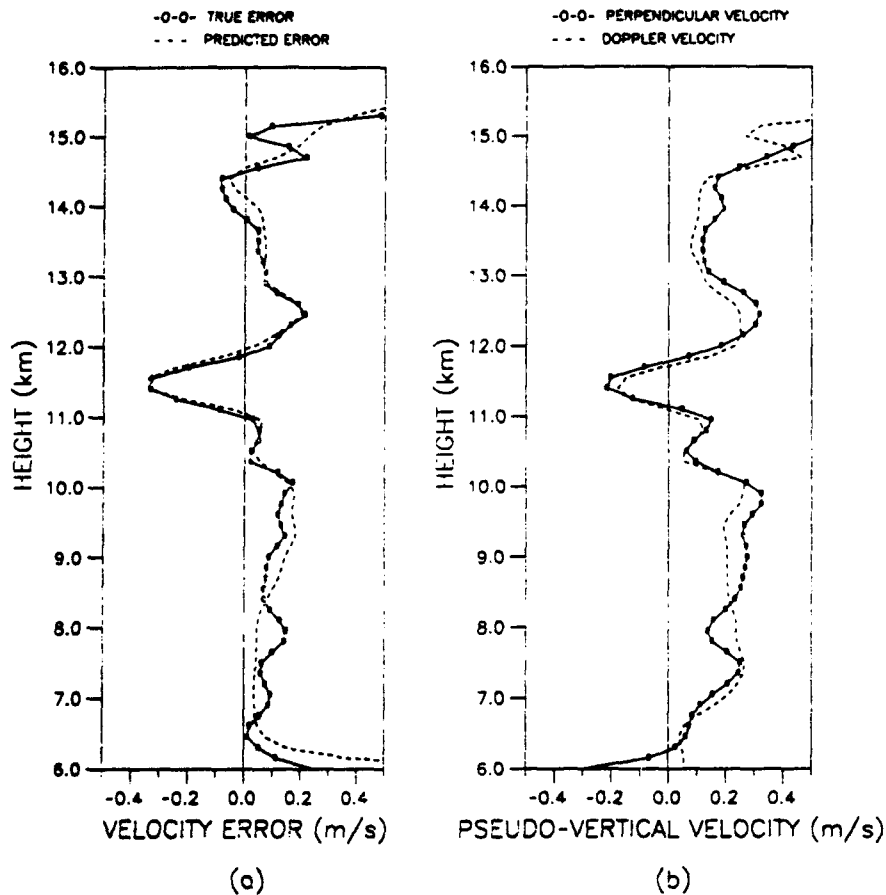


Fig. 9. Same as Figure 8, except for a 30-min average taken from 2215 to 2245 LT.

This is not the case, leading one to believe that the flow is close to horizontal.

The magnitude of the errors indicated both by the data presented here and by the earlier data pre-

sented by *Larsen and Röttger* [1991] can be 200% or more. However, the problems associated with such biases can be eliminated; however, by using multiple receiving antennas and applying the techniques presented in this paper.

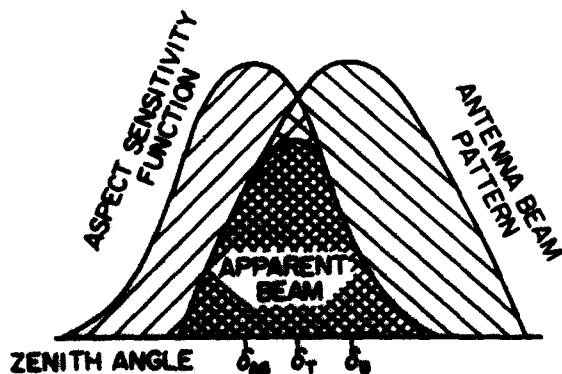


Fig. 10. Depiction of the apparent beam pattern of a VHF radar, when the strongest echoes are received from an off-vertical zenith angle. This effect is due to the aspect sensitivity observed at VHF wavelengths. The aspect sensitivity function has a tilt of δ_{AS} and the desired antenna beam pattern δ_B , which is in this case set to zenith. As a result, the apparent beam is tilted by the angle δ_T (reproduced from *Röttger* [1980]).

Acknowledgments. The research described here was carried out while one of the authors (R. D. P.) was a Japan Society for the Promotion of Science (JSPS) postdoctoral fellow at the Radio Atmospheric Science Center of Kyoto University. M. F. L. was supported by the Japan Ministry of Education, Culture, and Research and by AFOSR contract F49620-88-C-0121. The authors would like to thank J. S. Van Baelen, who pointed out an error in (6). The comments of the anonymous reviewers are gratefully acknowledged. The MU radar belongs to and is operated by the Radio Atmospheric Science Center of Kyoto University.

REFERENCES

- Adams, G., J. Brosnahan, and R. Johnson, Aspect sensitivity of 2.66-MHz radar returns from the mesosphere, *Radio Sci.*, 24(2), 127–132, 1989.
- Briggs, B., The analysis of spaced sensor records by correlation techniques, in *Handbook for MAP*, vol. 13, pp. 166–186,

- SCOSTEP Secretariat, University of Illinois, Urbana, 1984.
- Farley, D., H. Ierke, and B. Fejer, Radar interferometry: A new technique for studying plasma turbulence in the ionosphere, *J. Geophys. Res.*, **86**(A3), 1467–1472, 1981.
- Fukao, S., T. Sato, P. May, T. Tsuda, S. Kato, M. Inaba, and I. Kimura, A systematic error in MST/ST radar wind measurement induced by a finite range volume effect, 1, Observational results, *Radio Sci.*, **23**(1), 59–73, 1988.
- Hocking, W. K., Measurement of turbulent energy dissipation rates in the middle atmosphere by radar technique: A review, *Radio Sci.*, **20**, 1403–1422, 1985.
- Kudeki, E., and R. Woodman, A poststatistic steering technique for MST radar applications, *Radio Sci.*, **25**(4), 591–594, 1990.
- Larsen, M. F., and J. Röttger, A comparison of thunderstorm reflectivities measured at VHF and UHF, *J. Atmos. Oceanic Technol.*, **4**, 151–159, 1986.
- Larsen, M. F., and J. Röttger, VHF radar measurements of in-beam incidence angles and associated vertical-beam radial velocity corrections, *J. Atmos. Oceanic Technol.*, in press, 1991.
- Larsen, M. F., J. Röttger, and T. S. Dennis, A comparison of operational analysis and VHF wind profiler vertical velocities, *Mon. Weather Rev.*, **16**, 48–59, 1988.
- Larsen, M., R. Palmer, S. Fukao, R. Woodman, M. Yamamoto, T. Tsuda, and S. Kato, An analysis technique for deriving vector winds and in-beam incidence angles from interferometer measurements, *J. Atmos. Oceanic Technol.*, in press, 1991.
- Liu, C., J. Röttger, C. Pan, and S. Franke, A model for spaced antenna observational mode for MST radars, *Radio Sci.*, **25**(4), 551–563, 1990.
- Nastrom, G. D., W. L. Ecklund, and K. S. Gage, Direct measurement of large-scale vertical velocities using clear-air Doppler radars, *Mon. Weather Rev.*, **113**, 708–718, 1985.
- Palmer, R., R. Woodman, S. Fukao, T. Tsuda, and S. Kato, Three-antenna poststatistic steering using the MU radar, *Radio Sci.*, **25**(6), 1105–1110, 1990.
- Röttger, J., Reflection and scattering of VHF radar signals from atmospheric refractivity structures, *Radio Sci.*, **15**(2), 259–276, 1980.
- Röttger, J., and H. Ierke, Postset beam steering and interferometer applications of VHF radars to study winds, waves, and turbulence in the lower and middle atmosphere, *Radio Sci.*, **20**(6), 1461–1480, 1985.
- Röttger, J., C. Liu, C. Pan, and I. Fu, Spatial interferometry measurements with the Chung-Li VHF radar, *Radio Sci.*, **25**(4), 503–515, 1990.
- Tsuda, T., T. Sato, K. Hirose, S. Fukao, and S. Kato, MU radar observations of the aspect sensitivity of backscattered VHF echo power in the troposphere and lower stratosphere, *Radio Sci.*, **21**(6), 971–980, 1986.
- Van Baelen, J. S., Comparison of clear air atmospheric radar techniques for the study of atmospheric dynamics in the troposphere and the stratosphere, Ph.D. thesis, 191 pp., Univ. of Colo., Boulder, 1990.
- Vincent, R. A., and J. Röttger, Spaced antenna VHF radar observations of tropospheric velocities and irregularities, *Radio Sci.*, **15**(2), 319–335, 1980.
- Woodman, R., Inclination of the geomagnetic field measured by an incoherent scatter radar technique, *J. Geophys. Res.*, **76**, 178–184, 1971.
- S. Fukao, S. Kato, T. Tsuda, and M. Yamamoto, Radio Atmospheric Science Center, Kyoto University, Uji, Kyoto 611, Japan.
- M. F. Larsen and R. D. Palmer, Department of Physics and Astronomy, Clemson University, Clemson, SC 29631.
- R. F. Woodman, Jicamarca Radio Observatory, Instituto Geofísico del Perú, Apartado 3747, Lima, Peru.

Analysis of model simulations of spaced antenna/radar interferometer measurements

E. L. Sheppard and M. F. Larsen

Department of Physics and Astronomy, Clemson University, Clemson, South Carolina

(Received May 16, 1991; revised November 25, 1991; accepted March 3, 1992.)

A computer simulation of scattering from inhomogeneities in the refractive index is used to compare the spaced antenna and interferometer methods for measuring winds in clear air, both with and without turbulent fading. The results show that the spaced antenna analysis which is carried out in the time domain and the interferometer analysis which is carried out in the frequency domain are equivalent in terms of the information that the two methods yield. A data analysis method, equivalent to full correlation analysis, which can be carried out in the frequency domain is presented. The method is applied to model-generated, simulated data in order to extract the typical full correlation analysis output parameters such as the apparent and true velocity. The results obtained are consistent with the model input parameters.

1. INTRODUCTION

The Doppler technique for measuring horizontal winds has been used extensively for wind profiling with both experimental systems and prototype operational systems. Röttger and Larsen [1990] have reviewed many of the studies that have been carried out over the last decade. Recently, there has been increasing interest in the spaced antenna method for measuring winds because the instrumental setup provides the possibility of measuring a number of other parameters besides the wind velocity and allows some uncertainties in the vertical velocity measurements, for example, to be eliminated [Larsen and Röttger, 1989, 1992; Palmer *et al.*, 1991]. The interferometer technique has developed in parallel with the spaced antenna method, and many authors have discussed the relationships between cross-spectral phase and wind velocities. However, the primary focus has been on the problem of locating scatterers or other fine structure within the beam [e.g., Farley *et al.*, 1981; Adams *et al.*, 1986; Kudeki, 1988; Kudeki *et al.*, 1990; Franke *et al.*, 1990; Woodman, 1991]. In contrast, the spaced antenna method has focused mostly on measurements of the macroscopic properties of the atmospheric medium such as the bulk flow velocities. A number of recent articles have explored the similarities between the spaced antenna and inter-

ferometer techniques and especially possible advantages of using interferometer measurements as the basis for wind measurement systems [Liu *et al.*, 1990; Larsen *et al.*, 1992; Van Baelen and Richmond, 1991].

The fact that identical instrumentation is used in the interferometer and spaced antenna methods leads us to believe that the two methods must be frequency and time domain analogues; that is, the same information about the atmospheric medium can be obtained with either method. Larsen *et al.* [1992] have argued, however, that there may be advantages inherent in carrying out the analysis in the frequency domain since the required computations are simpler. Liu *et al.* [1990] have shown analytically that there is an equivalence between the spaced antenna and interferometer methods as long as turbulent fading is not important, but the effect of the latter, due to its analytical complexity, has not been explored in any detail in the studies that we are aware of. The goal of the present study is to investigate the effects of turbulent fading on the estimation of atmospheric parameters by using a numerical simulation of the scatter from turbulent structures. Analysis methods are sought which can be carried out in the frequency domain for the estimation of atmospheric parameters in the presence of turbulent fading.

Section 2 describes the features common to spaced antenna and radar interferometer measurements. In section 3, we will present the analytical formulation relevant to spaced antenna and inter-

Copyright 1992 by the American Geophysical Union.

Paper number 92RS00636.
0048-6604/92/92RS-00636\$06.00

ferometer methods, followed by the development of a method similar to full correlation analysis for parameter estimation in the frequency domain. Section 4 describes the computer simulation and the model output. Finally, section 5 will discuss the implications of the results for the analysis of real data.

2. SPACED ANTENNA AND INTERFEROMETER ANALYSIS

The instrumental setup used for spaced antenna and interferometer measurements is identical for all practical purposes. A single beam is transmitted vertically, and the backscattered signals are received on three or more separate receiving antennas. The quadrature components of the voltages in each of the receiving antennas are recorded for later analysis or, in some cases, for analysis on line. The spaced antenna analysis then proceeds by calculating the cross-correlation functions for each pair of receiving antennas. The delays at which the correlation functions peak are used to determine the drift velocity of the turbulent structure across the array of receiving antennas. The interferometer technique utilizes the measured phase differences between the signals in adjacent antennas and the frequency content information in the received signals to determine the location and velocities of scatterers illuminated by the transmitting beam. Clearly then, the differences between the two approaches are in the analysis step rather than in the instrumentation.

Spaced antenna or interferometer systems for wind measurements in the troposphere and stratosphere have generally operated in the VHF band at about 50 MHz, although there is no theoretical reason for believing that a higher frequency cannot be used. These systems obtain backscattered energy from turbulent variations in the refractive index, and at VHF frequencies, aspect sensitivity effects can enhance the signal power by as much as 10–15 dB. The spaced antenna method was first used to measure drift velocities in the ionosphere [e.g., *Phillips and Spencer*, 1955; *Fooks and Jones*, 1961] and later to measure winds and wave parameters in the mesosphere and lower thermosphere with MF and HF radars [e.g., *Manson et al.*, 1974]. A minimum of three receiving antennas is needed to measure the magnitude and direction of a horizontal drift velocity. If the drift velocity is parallel to the baseline between two receiving antennas and turbu-

lent fading is also absent, the magnitude of the velocity aloft is one-half the ratio of the antenna separation to the time delay, as discussed by *Briggs et al.* [1950].

Turbulent fading refers to variations in the diffraction pattern seen on the ground that result from turbulence in the medium aloft. These variations cause a decorrelation of voltage time histories which increases with time delay. The effect of turbulent fading is to cause a bias toward smaller cross-correlation lag times and therefore toward an overestimate of velocity [see *Larsen and Röttger*, 1989]. The method used to correct for errors due to turbulent fading when processing data in the time domain is known as full correlation analysis (FCA). Spatial decorrelation occurs because two receiving antennas not aligned with the horizontal velocity direction see different cuts of the diffraction pattern on the ground. Thus voltage time histories are further decorrelated by an amount which increases with the spatial separation perpendicular to the horizontal velocity. Nevertheless, spatial decorrelation does not produce a bias in the wind estimate.

The spaced antenna method and FCA signal processing techniques have been used extensively over a period of nearly 40 years [e.g., *Phillips and Spencer*, 1955; *Fooks and Jones*, 1961; *Röttger and Vincent*, 1978; *Vincent and Röttger*, 1980; *Meek et al.*, 1979]. It is apparent that the radar interferometer technique [*Larsen et al.*, 1992] obtains the same information as the spaced antenna system, although it is not clear what signal-processing techniques will be optimum. The FCA method has been presented in different forms by a number of authors [e.g., *Briggs et al.*, 1950; *Fooks*, 1965; *Fedor*, 1967]. One of the more recent algorithms is that described by *Meek* [1980]. In his method, the autocorrelations and cross correlations are assumed to be Gaussian functions of equal width. The analytical results presented in section 3 are also based on this assumption. Initially, spaced antenna systems were incoherent, and data analysis was based on amplitude only. Today these radars are usually fully coherent, and the processing of spaced antenna data can make use of phase information as well [*Larsen and Röttger*, 1989]. Including the phase information also makes it possible to determine the vertical velocity and refractivity layer tilt angles [*Larsen and Röttger*, 1992].

3. AN ANALYTICAL FORMULATION

The analytical results presented in this section are primarily to provide motivation for the interpretation of the model-generated results in section 4. Assuming a Gaussian form for the cross-correlation amplitude and including a phase term to account for a nonzero vertical velocity and an off-vertical angle of arrival [see *Larsen et al.*, 1992], the general cross-correlation function for the i th antenna pair can be written as

$$\rho_i(t) = \rho_{mi} e^{i(\omega_0 t - \phi_{0i})} e^{-[(t + t_{mi})/t_c]^2} \quad (1)$$

where ρ_{mi} is the peak cross-correlation amplitude relative to the peak autocorrelation amplitude, t_{mi} is the lag time, and t_c is the width factor. With an incoherent system the phase term which contains information about the vertical velocity and angle of arrival is not present. In this term, $\omega_0 = -2kw$ is the Doppler shift due to the vertical velocity, and $\phi_{0i} = kD_i \sin \delta_{0i}$ is the phase shift between antennas resulting from the mean off-vertical angle of arrival δ_{0i} . It should be noted that we have assumed the off-vertical angle of arrival in the plane parallel to the horizontal velocity to be zero. With this assumption the component of horizontal velocity in ω_0 is also zero. Clearly, this is not always true, but it greatly simplifies the following development of the relationship between radial velocity and phase, and the result is unchanged by the assumption. The off-vertical incidence angles may be the result of inclined aspect-sensitive refractivity layers or regions of concentrated reflectivity, as discussed by *Larsen and Röttger* [1992] and *Larsen et al.* [1992]. Now if we allow the antenna separation to approach zero, ρ_{mi} approaches one, t_{mi} and ϕ_{0i} approach zero, and the autocorrelation becomes

$$\rho(t) = e^{-[(t/t_c)^2]} e^{i\omega_0 t} \quad (2)$$

To perform a full correlation analysis with *Meek's* [1980] method, the seven parameters ρ_{mi} , t_{mi} , and t_c are obtained from the autocorrelation and cross-correlation functions. Taking the Fourier transform of (1) and (2), we see that these same parameters can be obtained from the frequency domain. The cross spectra are given by

$$C_i(\omega) = \rho_{mi} t_c \pi^{1/2} \exp \{ i[(\omega - \omega_0)t_{mi} - \phi_{0i}] \} \cdot \exp [-t_c^2(\omega - \omega_0)^2/4] \quad (3)$$

and the autospectrum is given by

$$P(\omega) = t_c \pi^{1/2} \exp [-t_c^2(\omega - \omega_0)^2/4] \quad (4)$$

As expected, the autospectrum amplitude is shifted in the positive ω direction by an amount equal to the Doppler shift resulting from the vertical velocity. Furthermore, the phase of the cross spectrum is seen to be a linear function of frequency given by

$$\phi = (\omega - \omega_0)t_{mi} - \phi_{0i} \quad (5)$$

and the phase at $\omega = \omega_0$ is just ϕ_{0i} , that is, the phase between antennas resulting from the off-vertical incidence angles. Recalling that the radial velocity is given by

$$v_r = \omega/2k \quad (6)$$

Equation (5) becomes

$$\phi = 2kt_{mi}(v_r - w) - \phi_{0i} \quad (7)$$

and solving for v_r , we get

$$v_r = w + (\phi + \phi_{0i})/2kt_{mi} \quad (8)$$

Now considering a horizontal velocity which is not parallel to the antenna baseline, we have

$$D_i/t_{mi} = 2v_h/\cos \theta_i \quad (9)$$

where D_i is the distance between antennas and θ_i is the azimuth of the horizontal velocity direction with respect to the antenna baseline. Substitution of (9) into (8) yields

$$v_r = w + (\phi + \phi_{0i})v_h/kD_i \cos \theta_i \quad (10)$$

This result is in agreement with that of *Larsen et al.* [1992]. It provides a convenient method for determining vertical velocity from the phase intercepts at $v_r = 0$ in two baselines and the layer tilt angles from the phase values corresponding to the maximum values of v_r .

The two special cases treated with the model in section 4 are presently considered. First, if we consider the special case without turbulent fading, without spatial decorrelation, with zero vertical velocity, and zero off-vertical angle of arrival, (3) reduces to

$$C_i(\omega) = e^{i\omega t_{mi}} P(\omega) \quad (11)$$

where $P(\omega)$ is the autospectrum. The cross-spectral phase is seen to be a linear function of frequency

with a slope of t_{mi} , the cross-spectral amplitude is identical to the autospectrum, and the cross-correlation amplitude is just the time-shifted autocorrelation. Since turbulent fading is not included, the spectrum width is due only to the beam-broadening effect. Thus the spectral width is determined by the projection of the horizontal velocity along the radial direction for zenith angles within the beam which are not vertical. Furthermore, the spatial correlation interval of the diffraction pattern on the ground is inversely related to the transmitting antenna beam width and likewise to the spectral width due to beam broadening. Now, for the second case with everything the same except for the inclusion of a nonzero vertical velocity, (11) becomes

$$C_i(\omega) = e^{i(\omega - \omega_0)t_{mi}} P(\omega - \omega_0) \quad (12)$$

Thus a vertical velocity produces a frequency shift in both the amplitude and phase of the cross spectrum.

4. NUMERICAL SIMULATION

Although analytical techniques for relating time domain and frequency domain parameters have been presented in section 3, it is not clear how the effects of turbulent fading will appear in the frequency domain. For this reason a numerical model which simulates the radar interferometer system will be valuable in evaluating the frequency domain analysis techniques. The simulation developed for this purpose uses a simplified model of the scattering mechanism which consists of N isotropic scatterers of random reflectivity, randomly distributed within a predetermined volume of xyz space. As seen in Figure 1, the volume is chosen so that the scatterers illuminated by the radar are always contained in a subset of the volume as the motion of the scatterers evolves. The actual scattering volume for each time increment is determined by the antenna beamwidth and the radar pulse length. The assumed antenna pattern has a Gaussian shape between the half power points but is zero elsewhere. This assumption is necessary to limit the scattering volume to a manageable size. The range-weighting function is assumed to be triangular. Although the true scattering process is an unknown combination of Bragg scatter, Fresnel reflection, and Fresnel scatter [Röttger and Larsen, 1990], the properties investigated here are believed to be independent of

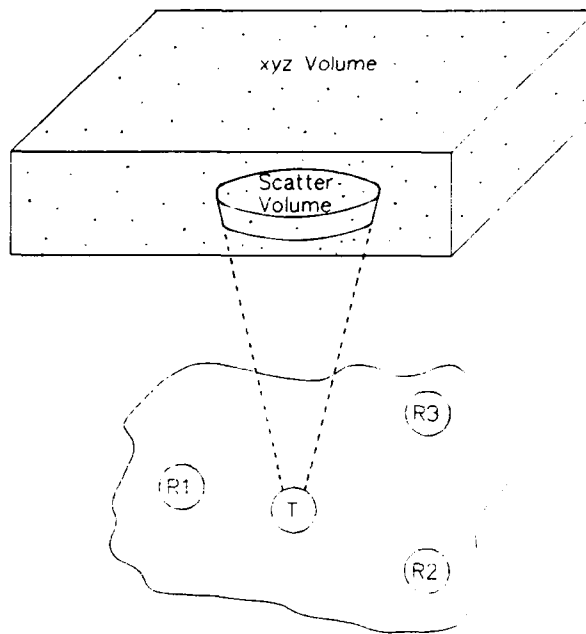


Fig. 1. Illustration of the radar scatter volume determined by the transmitting antenna beamwidth and the pulse width as a subset of the xyz volume of scatterers.

the exact scattering mechanism. In an earlier simulation of spaced antenna ionospheric drift measurements, Wright and Pitteway [1978] concluded that exact modeling of the scattering mechanism is not essential for determining spaced antenna parameters. In the present model, initial positions for the scatterers are selected randomly according to a uniform distribution in x , y , and z . For each time increment, positions are updated according to the x , y , and z components of velocity chosen from a Gaussian probability density. The mean value of this density is the average velocity, and the variance is a measure of the turbulence. After each update of position, a new set of randomly distributed reflectivities can be assigned. The simulation sums scattered voltages at successive time increments to calculate a complex time history of antenna voltage for each of the receiving antennas. A fast Fourier transform routine is used to calculate the autospectra, cross spectra, autocorrelations, and cross correlations.

The antenna arrangement and coordinate system used for the simulation are shown in Figure 2. Other parameters held at fixed values for the simulations are given in Table 1. The autospectra, cross spectra, autocorrelations, and cross correlations used in

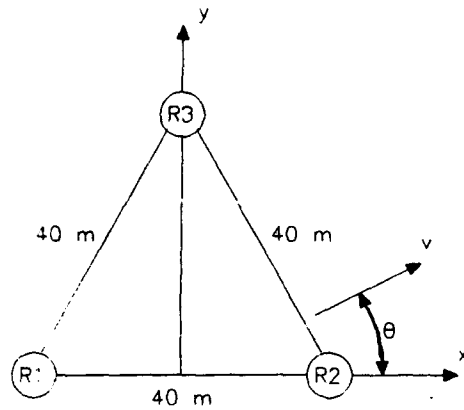


Fig. 2. Spaced antenna arrangement showing the locations of the receiving antennas used for the computer simulation. The transmitting antenna location is not shown.

the subsequent analysis are obtained by ensemble averaging the results for many samples. The actual length of a single time history is 32 s; however, a 32-s interval of zero signal is added to each time history to improve resolution in the spectrum and to prevent wrap-around errors in calculating the cross correlations. With 80 samples of 32 s each, the actual observation time is approximately 43 min. For the simulation results presented, the input parameters which were varied include the velocity and velocity variance in the x , y , and z directions.

As a simple test of the simulation program, all scatterers were given a 20 m/s horizontal velocity with zero variance parallel to the x axis. Also, scatter amplitudes, once assigned, were held constant thereafter. The mean autocorrelation and the mean autospectrum are shown in Figures 3a and 3b. The cross correlation and the cross spectrum between antennas 1 and 2 are given in Figures 3c and 3d. The autocorrelation and the cross correlation

have been normalized to the peak autocorrelation, and the autospectrum and cross spectrum have been normalized to the peak autospectrum. Except for the small amount of decorrelation which results from the movement of scatterers into and out of the scattering volume, these particular conditions correspond to the case of no turbulent fading or spatial decorrelation for which analytical results are given in (11). Referring to Figures 3c and 3d, it is seen that a t_{mi} of 1 s is obtained from both the peak in the cross correlation and the slope of the cross-spectral phase, as expected for a horizontal velocity aloft of 20 m/s. In Figure 3d the cross spectrum calculated by the simulation program for a vertical velocity of 0.24 m/s and a horizontal velocity of 20 m/s in the x direction is shown by the dashed curves. These conditions correspond to the case for which analytical results are given in (12). In Figure 3d, $\omega_0 = 0.5 \text{ rad s}^{-1}$ which is just $2k\omega$ when $\omega = 0.24 \text{ m/s}$. This result indicates that the frequency offset corresponding to zero phase determines the vertical velocity when the tilt angles are zero. Also, ω_0 corresponds to the peak amplitude of the cross spectrum. The above results indicate that the model is working correctly since they agree with the analytical results for the simple case of no turbulent fading or spatial decorrelation.

4.1. Effects of turbulent fading and spatial decorrelation

The effects of turbulent fading and spatial decorrelation in the cross spectrum were investigated separately. Referring to Figure 2, we see that spatial decorrelation must exist between antennas 1 and 3 since each antenna sees a different cut of the diffraction pattern on the ground when the horizontal velocity is in the x direction. Figures 4a and 4b

TABLE 1. Fixed Parameters Used to Obtain Simulation Results

Parameter	Value
Center height of scattering volume	10,075 m
Range extent of scattering volume	150 m (pulse width is $1 \mu\text{s}$)
Diameter of scattering volume	800 m (antenna beam width is 5°)
Wavelength	6 m (frequency is 50 MHz)
Density of scatterers	$3,000 \text{ k}^{-3}$
Number of samples averaged	80
Range of scatterer reflectivity	0.5 to 1.0
Number of points in Fast Fourier transform	256
Sample time	0.25 s

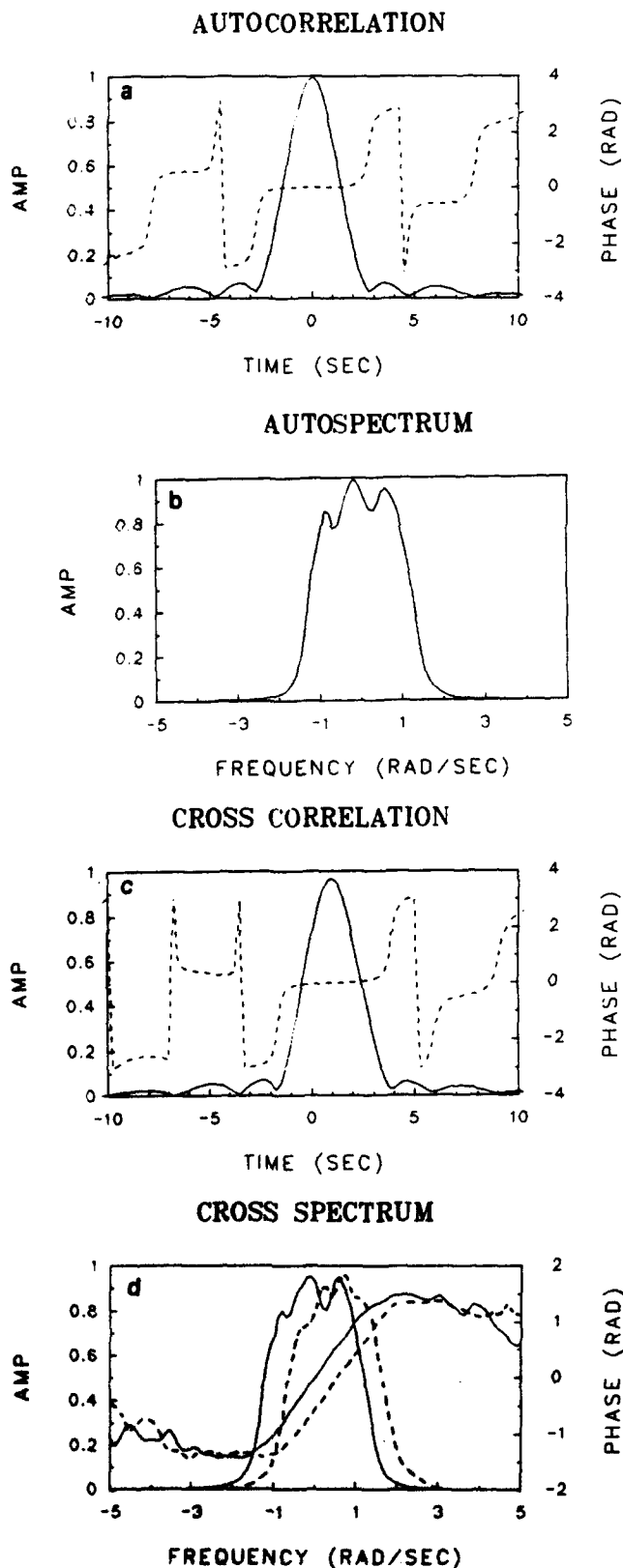


Fig. 3. (a) Normalized mean autocorrelation, (b) normalized mean autospectrum, (c) cross correlation $\rho_{12}(t)$, and (d) cross spectrum $C_{12}(\omega)$ for the case of no turbulent fading or spatial decorrelation and $v_x = 20$ m/s, $v_y = v_z = 0.0$, $\sigma_x = \sigma_y = \sigma_z = 0.0$. The frequency shift of the complex cross spectrum resulting from a vertical velocity is shown by the dashed curves in Figure 3d.

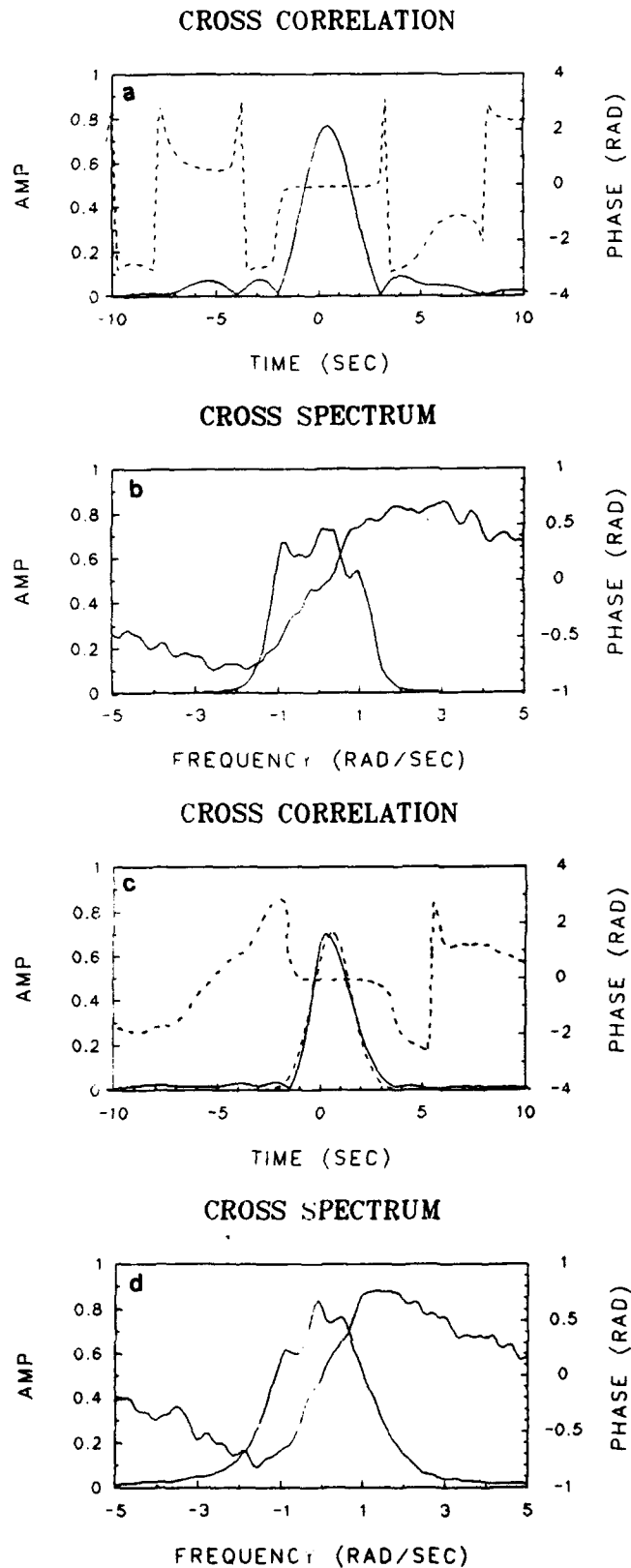


Fig. 4. (a) Cross correlation $\rho_{13}(t)$ and (b) cross spectrum $C_{13}(\omega)$ for the case including spatial decorrelation only and $v_x = 20$ m/s, $v_y = v_z = 0.0$, $\sigma_x = \sigma_y = \sigma_z = 0.0$; (c) Cross correlation $\rho_{12}(t)$ and (d) cross spectrum $C_{12}(\omega)$ for the case including turbulent fading only and $v_x = 20$ m/s, $v_y = v_z = 0.0$, $\sigma_x = \sigma_y = 8$ m/s, $\sigma_z = 0.88$ m/s. A Gaussian fit of cross-correlation amplitude in Figure 4c is shown by the dashed curve.

show the cross correlation and the cross spectrum between antennas 1 and 3 for a horizontal velocity of 20 m/s in the x direction and a zero velocity variance in all directions. Since the velocity variance is zero, the spectral width is due only to beam-broadening effects. The roughness in the cross-spectral amplitude and phase resulting from decorrelation is clearly seen, and the need for a least squares fit for both amplitude and phase is apparent. Here, a t_{mi} of approximately 0.5 s is observed from both the cross-correlation lag time and the slope of the cross-spectral phase. This value of t_{mi} corresponds to a trace velocity of 40 m/s as expected for the distance of 40 m at an angle of 60° . The trace velocity corresponds to the horizontal drift velocity divided by the cosine of the angle between the drift direction and the antenna baseline. When the horizontal drift velocity is perpendicular to the antenna baseline, t_{mi} is zero, and the trace velocity becomes infinite.

To observe the effects of turbulent fading, a nonzero variance was introduced in the x , y , and z components of the velocity, while the average velocity was maintained at 20 m/s in the x direction. For standard deviations in velocity of $\sigma_x = \sigma_y = 8$ m/s and $\sigma_z = 0.88$ m/s, the cross correlation and the cross spectrum between antennas 1 and 2 are shown in Figures 4c and 4d. Since the average velocity is parallel to the antenna baseline, turbulent fading is present, but spatial decorrelation is not. These values of velocity standard deviation are much larger than typically observed values; however, they are needed to emphasize the effects of turbulent broadening since beam broadening will generally be dominant at the altitude presently being considered. The broadening effects of turbulent fading are clearly seen in the cross spectrum with the spectral width broader than it is for the case without turbulence. Furthermore, the effects of turbulence are seen in the reduced peak amplitude and the noiselike addition to amplitude and phase in the cross spectrum. To estimate the lag time, a Gaussian curve was fitted in the least squares sense to the cross-correlation amplitude function. This fit is shown by the dashed curve superimposed on the cross correlation in Figure 4c. The value of t_{mi} estimated from the cross-correlation lag is approximately 0.65 s, while the estimate from the cross-spectrum phase slope is approximately 0.7 s. These values are consistent with the fact that temporal fading increases the apparent velocity.

As expected, turbulent fading causes a positive bias in apparent velocity, whereas spatial decorrelation does not. Nevertheless, both turbulent fading and spatial decorrelation reduce the peak amplitude and introduce roughness in the amplitude and phase of the cross spectrum.

4.2. Full spectral analysis

The FCA analysis by Meek [1980] requires as input a width factor from the mean autocorrelation plus the three lag times t_{mi} and the three cross-correlation amplitudes ρ_{mi} . As discussed in section 3, these parameters can be estimated from the mean autospectrum and the three cross spectra. Thus by analogy with FCA a full spectral analysis (FSA) can be implemented by determining these parameters via a least squares Gaussian fit for the autospectrum and cross-spectral amplitudes, and a least squares line fit for the cross-spectral phase. As a first step toward evaluating the performance of the FSA procedure, the model was used to generate time histories for the assumed velocities and velocity variances of the wind aloft, and the spectra and cross spectra were calculated for the assumed antenna configuration. FSA was then used to determine the parameters needed for Meek's analysis method which was subsequently used to calculate the apparent velocity, the true velocity, the spatial correlation ellipse parameters, and the characteristic time constant of the pattern.

For an average velocity aloft of 20 m/s in a direction of 30° with respect to the x axis and velocity standard deviations of $\sigma_x = \sigma_y = 8$ m s⁻¹ and $\sigma_z = 0.88$ m/s, the mean autospectrum and the three complex cross spectra calculated from the output of the simulation are shown in Figure 5. Also, in Figure 5, the least squares fits are shown by dashed lines. Corresponding velocity estimates and additional outputs are given in Table 2 for three simulation runs, each of which used a different initial seed number for the random number generator. Additional velocity estimates, for a wide range of turbulence parameters and different seed numbers, have resulted in values which are consistently within 10% of the expected horizontal velocity. Some of these estimates are given in Table 3.

5. DISCUSSION

The above results indicate that an unbiased estimate of true velocity can be obtained by the full

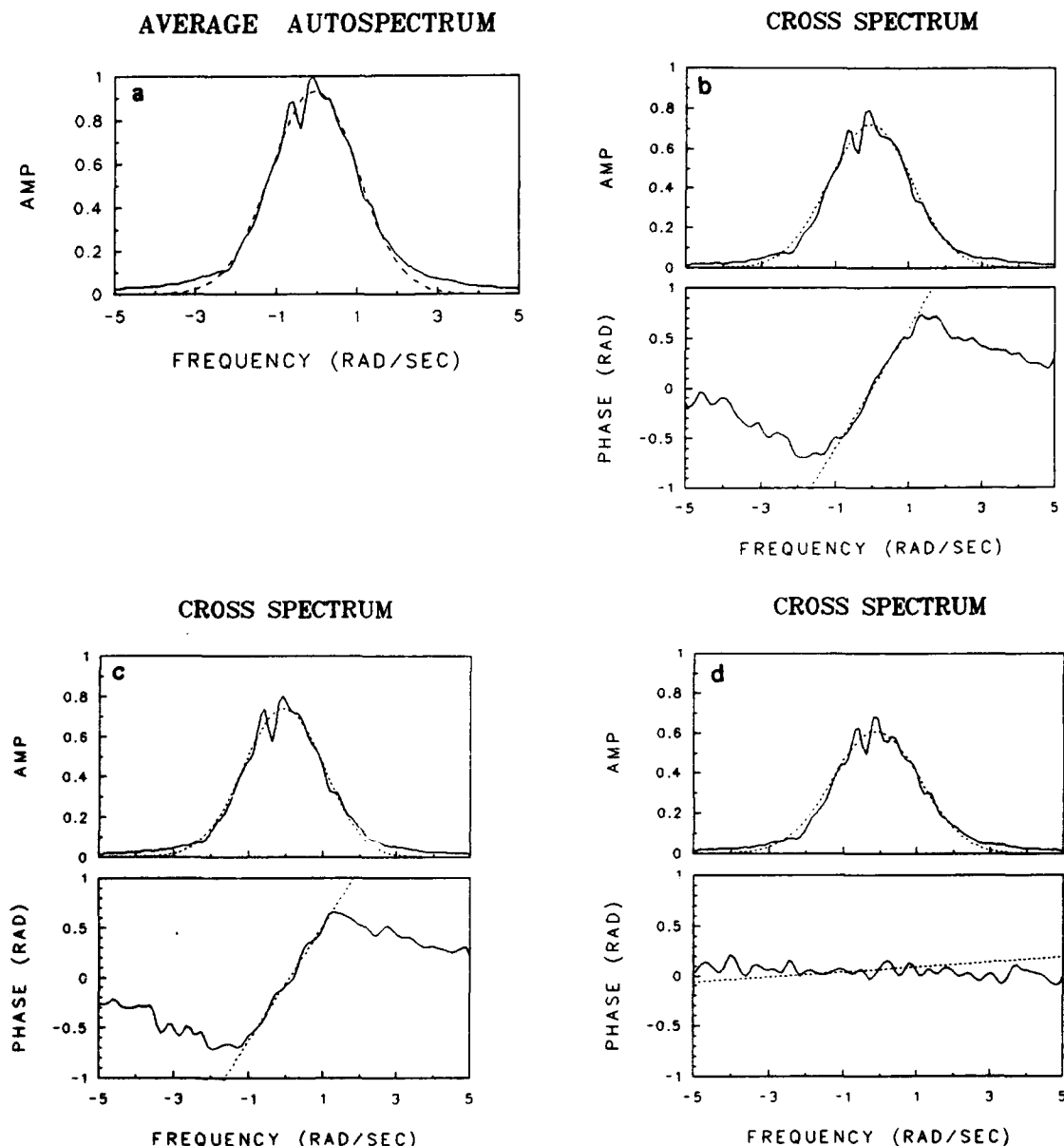


Fig. 5. (a) Normalized mean power spectrum, (b) cross spectrum $C_{13}(\omega)$, (c) cross spectrum $C_{12}(\omega)$, and (d) cross spectrum $C_{23}(\omega)$. The dashed lines show the least squares Gaussian fits of amplitude and the least squares linear fits of phase. The other parameters are $v_x = 17.32$ m/s, $v_y = 10$ m/s, $v_z = 0.0$, $\sigma_x = \sigma_y = 8$ m/s, $\sigma_z = 0.88$ m/s.

TABLE 2. FSA Results Obtained From Model-Generated Spectral Data for $\sigma_x = \sigma_y = 8$ m/s and $\sigma_z = 0.88$ m/s

	Run 1	Run 2	Run 3
Expected value of true velocity, m/s and deg	20.00, 30.00	20.00, 0.00	20.00, 0.00
Estimated value of true velocity, m/s and deg	18.01, 30.58	20.10, 1.55	21.90, 0.25
Apparent velocity, m/s and deg	31.13, 35.39	38.61, 0.49	41.97, -0.87
Major correlation ellipse axis, m	45.98	46.28	55.18
Minor correlation ellipse axis, m	42.27	43.61	39.50
Correlation ellipse tilt angle, deg	-13.85	-9.41	1.42
Characteristic time constant, s	1.43	1.20	1.32

TABLE 3. Comparisons of Expected and FSA Estimated Horizontal Velocity

Velocity Standard Deviation, for $\sigma_x, \sigma_y, \sigma_z$, m/s	Horizontal Velocity, m/s and deg	
	Expected	Estimated
4, 4, 0.44	20.00, 0.00	20.79, -1.77
2, 2, 0.24	20.00, 0.00	21.91, -4.19
4, 4, 0.44	16.97, 45.00	15.70, 50.81
8, 8, 0.88	20.00, 0.00	21.90, 0.25
8, 8, 0.88	20.00, 30.00	18.01, 30.58
8, 8, 0.88	20.00, 0.00	20.10, 1.55

spectral analysis method presented. Clearly, these results were obtained under ideal circumstances using model-generated data. No noise was introduced in the simulation, a sufficiently large number of spectra were averaged to produce a reasonably smooth average spectrum, and the turbulent motion of the scatterers was assumed to be Gaussian. Although the scattering mechanism is complex and not completely understood, it is reasonable to believe that the scattering model, which assumes randomly placed isotropic scatterers, will generate time histories which are physically realistic. The time-phase relationships for scatterer voltages on the ground are, in fact, the physical quantities which the model must accurately reproduce. Model-generated time histories, spectra, and correlations bear a close resemblance to those obtained from real spaced antenna systems. The assumed abrupt cutoff of the antenna pattern is seen in the shape of the spectrum when turbulence is not present, but it does not appear to be significant when turbulence is included. Since the radial component of average velocity can be as large as 0.8 m/s for the altitude, beamwidth, and horizontal drift velocity assumed, it is necessary that the values of σ_x , σ_y , and σ_z be chosen to give turbulent radial velocities in the range of 0.8 m/s or larger if the effects of turbulence are to be seen in the spectrum. These values of the variance due to turbulence are large; however, for the antenna beamwidth and altitude chosen for the simulation, beam-broadening effects would mask the effects of normal turbulence. Furthermore, these large values were only chosen to emphasize the effects of turbulent broadening and temporal decorrelation. Overall, it is likely that the assumptions made in formulating the model will not significantly detract from the validity of the results.

6. CONCLUSIONS

A method for estimating true velocities in the middle and lower atmosphere from the autospectrum and the cross spectra of a spaced antenna system has been presented. The numerical simulation described in section 4 has been used to provide a preliminary evaluation of the method, and the results are consistent with the assumed wind velocities in the simulation. It is apparent that the same quantities previously determined by FCA can in fact be determined from the mean autospectrum and the cross spectra in the coherent spaced antenna system. Since phase information is also available in a coherent system, additional useful quantities such as tilt angle and vertical velocity can also be determined. The frequency domain signal-processing techniques presented here may be faster and simpler to implement since it is not necessary to calculate the cross correlation as required for the FCA. However, a definitive judgment on the relative ease of the two methods is probably a long time away. The results presented in this paper have not included the effects of system noise since the primary objective has been the development of signal-processing techniques which compensate for fading. Future work will need to consider power requirements, system noise, and processing techniques which are optimum for estimating system parameters in the presence of noise.

Acknowledgments. E.L.S. and M.E.L. were supported by AFOSR contract F49620-88-C-0121 during the course of this study.

REFERENCES

- Adams, G. W., J. W. Brosnahan, D. C. Walden, and S. F. Nerney, Mesospheric observations using a 2.66-MHz radar as an imaging doppler interferometer: Description and first results, *J. Geophys. Res.*, **91**, 1671-1683, 1986.
- Briggs, B. H., G. J. Phillips, and D. H. Shinn, The analysis of observations on spaced receivers of the fading of radio signals, *Proc. Phys. Soc. London, Sect. B*, **B63**, 106-121, 1950.
- Farley, D. T., H. M. Ierke, and B. G. Fejer, Radar interferometry: A new technique for studying plasma turbulence in the ionosphere, *J. Geophys. Res.*, **86**, 1467-1472, 1981.
- Fedor, L. S., A statistical approach to the determination of three-dimensional ionospheric drifts, *J. Geophys. Res.*, **72**, 5401-5415, 1967.
- Fooks, G. F., Ionospheric drift measurements using correlation analysis: Methods of computation and interpretation of results, *J. Atmos. Terr. Phys.*, **27**, 979-989, 1965.
- Fooks, G. F., and I. L. Jones, Correlation analysis of the fading

- of radio waves reflected vertically from the ionosphere, *J. Atmos. Terr. Phys.*, 20, 229-242, 1961.
- Franke, P. M., D. Thorsen, M. Champion, S. J. Franke, and E. Kudeki, Comparison of time- and frequency-domain techniques for wind velocity estimation using multiple-receiver MF radar data, *Geophys. Res. Lett.*, 17, 2193-2196, 1990.
- Kudeki, E., Radar interferometer observations of mesospheric echoing layers at Jicamarca, *J. Geophys. Res.*, 93, 5413-5421, 1988.
- Kudeki, E., F. Surucu, and R. F. Woodman, Mesospheric wind and aspect sensitivity measurements at Jicamarca using radar interferometry and poststatistics steering techniques, *Radio Sci.*, 25, 595-612, 1990.
- Larsen, M. F., and J. Röttger, The spaced antenna technique for radar wind profiling, *J. Atmos. Oceanic Technol.*, 6, 920-938, 1989.
- Larsen, M. F., and J. Röttger, VHF radar measurements of in-beam incidence angles and associated vertical-beam radial velocity corrections, *J. Atmos. Oceanic Technol.*, 8, 477-490, 1992.
- Larsen, M. F., R. D. Palmer, S. Fukao, R. F. Woodman, M. Yamamoto, T. Tsuda, and S. Kato, An analysis technique for deriving vector winds and in-beam incidence angles from radar interferometer measurements, *J. Atmos. Oceanic Technol.*, 9, 3-14, 1992.
- Liu, C. H., J. Röttger, C. J. Pan, and S. J. Franke, A model for spaced antenna observational mode for MST radars, *Radio Sci.*, 25, 551-563, 1990.
- Manson, A. H., J. B. Gregory, and D. G. Stephenson, Winds and wave motions to 110 km at mid-latitudes, I, Partial reflection radiowave soundings, 1972-73, *J. Atmos. Sci.*, 31, 2207-2215, 1974.
- Meek, C. E., An efficient method for analysing ionospheric drifts data, *J. Atmos. Terr. Phys.*, 42, 835-839, 1980.
- Meek, C. E., A. H. Manson, and J. B. Gregory, Internal consistency analysis for partial and total reflection drifts data, *J. Atmos. Terr. Phys.*, 41, 251-258, 1979.
- Palmer, R. D., M. F. Larsen, R. F. Woodman, S. Fukao, M. Yamamoto, T. Tsuda, and S. Kato, VHF radar interferometry measurements of vertical velocity and the effect of tilted refractivity surfaces on standard Doppler measurements, *Radio Sci.*, 26, 417-427, 1991.
- Phillips, G. J., and M. Spencer, The effects of anisometric amplitude patterns in the measurement of ionospheric drifts, *Proc. Phys. Soc. London, Sect. B*, B68, 481-492, 1955.
- Röttger, J., and M. F. Larsen, UHF/VHF radar techniques for atmospheric research and wind profiler applications, in *Radar in Meteorology, Battan Memorial and 40th Radar Meteorological Conference Volume*, chap. 21a, pp. 235-281, American Meteorological Society, Boston, Mass., 1990.
- Röttger, J., and R. A. Vincent, VHF radar studies of tropospheric velocities and irregularities using spaced antenna techniques, *Geophys. Res. Lett.*, 5, 917-920, 1978.
- Van Baelen, J. S., and A. D. Richmond, Radar interferometry technique: Three-dimensional wind measurement theory, *Radio Sci.*, 26, 1209-1218, 1991.
- Vincent, R. A., and J. Röttger, Spaced antenna VHF radar observations of tropospheric velocities and irregularities, *Radio Sci.*, 15, 319-335, 1980.
- Woodman, R. F., A general statistical instrument theory of atmospheric and ionospheric radars, *J. Geophys. Res.*, 96, 7911-7928, 1991.
- Wright, J. W., and M. L. V. Pitteway, Computer simulation of ionospheric radio drift measurements, and their analysis by correlation methods, *Radio Sci.*, 13, 189-210, 1978.

M. F. Larsen and E. L. Sheppard, Department of Physics and Astronomy, Clemson University, Clemson, SC 29634.

**A STATISTICAL COMPARISON OF SPACED ANTENNA
AND SPATIAL INTERFEROMETRY WIND ESTIMATION**

E. Lamar Sheppard, M. F. Larsen, Robert D. Palmer

**Department of Physics and Astronomy
Clemson University
Clemson, SC 29634**

Shoichiro Fukao, Mamoru Yamamoto, Toshitaka Tsuda, and Susumu Kato

**Radio Atmospheric Science Center
Kyoto University
Uji, Kyoto 611 JAPAN**

**Revised
September 1992**

ABSTRACT

A statistical comparison of spaced antenna (SA) and spatial interferometry (SI) methods for estimating horizontal winds in the troposphere and lower stratosphere is presented. The data analyzed were obtained with the Middle and Upper (MU) atmosphere radar from 1910 LT on June 29, 1990, through 0950 LT on July 2, 1990. At all heights, velocity estimates based on frequency domain analysis are within 4% of those based on the time domain analysis. We conclude that frequency domain techniques provide an alternative method for estimating the so-called *true* velocity. It is not clear, however, that they offer a significant advantage over the time domain methods. Some analysis parameters are easier to extract in the frequency domain while others can be extracted more easily and efficiently in the time domain.

1. INTRODUCTION

The spaced antenna (SA) method has been employed for estimating horizontal winds at altitudes from the troposphere to the mesosphere (Manson et al., 1974; Vincent and Röttger, 1980; Vincent et al., 1987; Larsen and Röttger, 1989; Röttger and Larsen, 1990; Van Baelen et al., 1990) and plasma drifts in the ionosphere (e.g., Phillips and Spencer, 1955; Fooks and Jones, 1961), although the latter studies led to questionable results in many cases. A method known as full correlation analysis (FCA) is generally applied for estimating the so-called *true* horizontal velocity (e.g., Fooks, 1965; Fedor, 1967; Meek, 1980; Briggs, 1984). Initially spatial interferometry (SI) studies, also known as radar interferometry (RI), concentrated on the location of scatterers or fine structure within the radar beam whereas the SA method had concentrated on macroscopic properties of the atmospheric medium such as the bulk flow velocities (e.g. Röttger and Vincent, 1978; Farley et al., 1981; Adams et al., 1986; Kudeki, 1988; Kudeki et al., 1990; Röttger et al., 1990; Franke et al., 1990; Woodman, 1991). A number of recent articles have explored the possible advantages of using the SI method, which is closely related to the SA method, as the basis for bulk flow wind estimation (Liu et al., 1990; Larsen et al., 1992; Van Baelen and Richmond, 1991). Sheppard and Larsen (1992) and Briggs and Vincent (1992) have shown that the parameters needed for FCA can also be obtained from the frequency domain. The equivalence of these two methods, full spectral analysis (FSA) and full correlation analysis (FCA), is rather obvious from the Fourier transform relationships between the auto- and cross-correlations and the auto- and cross-spectra. In this paper a statistical comparison of the time domain and frequency domain methods for estimating the so-called *true*

velocity is presented. Data for the comparison were obtained with the MU radar during a sixty-three hour period from June 29, 1990, through July 2, 1990.

Apparent and *true* horizontal velocities are estimated with both frequency domain and time domain methods, and a statistical comparison of the results is presented. These methods are briefly discussed in Section 2. The experimental setup and signal processing is presented in Section 3. Observational results are presented in Section 4, a discussion of differences in the implementation of the SA and SI methods is given in Section 5, and conclusions are given in Section 6.

2. SI AND SA WIND ESTIMATION METHODS

Like the SA system, the SI system uses a minimum of three receiving antennas which are generally positioned so the baselines form a triangle. The SI method can estimate the *apparent* horizontal velocity with the data from any two baselines that have sufficient cross-spectral amplitude. The relevant equations have appeared in several recent papers (Liu et al., 1990; Palmer et al., 1991; Van Baelen and Richmond, 1991; Larsen et al., 1992) and are as follows:

$$\tan \theta = \frac{\frac{d_1}{m_1} \cos \alpha_1 - \frac{d_2}{m_2} \cos \alpha_2}{\frac{d_2}{m_2} \sin \alpha_2 - \frac{d_1}{m_1} \sin \alpha_1} \quad (1a)$$

$$V_h = \frac{d_1}{2 m_1} \cos (\alpha_1 - \theta) \quad (1b)$$

where d_i is the baseline length, α_i is the baseline azimuth angle, m_i is the cross-spectral phase slope in units of seconds, V_h is the velocity magnitude, and θ is the wind

direction. When estimating the *apparent* velocity with the SA method the slopes required in *Equation 1* are taken as the lag times corresponding to the maxima in the cross-correlation functions. If the data from all three baselines of the SI/SA system are used, the redundancy provided by the third baseline can be used to our advantage. A consistent set of *apparent* velocities is generally found by a least-squares fit of the three *apparent* velocity vectors to a straight (e.g., Fooks, 1965; Meek, 1980). When the data from only two baselines are used, the two baselines with the largest signal-to-noise ratio (SNR) are chosen for the calculation. Furthermore, if the horizontal wind happens to be parallel to one of the baselines, the other two baselines may have low cross-spectral amplitude. Under these conditions, the use of data from only one baseline is often sufficient (e.g., Palmer et al., 1991).

At altitudes where turbulence is low and beam broadening is much larger than turbulent broadening, the *apparent* velocity provides the most accurate estimate of the actual wind velocity. However, in cases where turbulence is large the *apparent* velocity overestimates the wind and the *true* velocity provides the most accurate estimate of the actual wind. Even in the absence of turbulence, *true* and *apparent* velocities may be different as the result of an anisometric spectrum for refractive index irregularities. Spaced antenna systems were first used in the early 1950's for measuring drifts in the ionosphere. The FCA method was developed at that time, and there is an abundance of literature on the subject (e.g., Fooks, 1965; Fedor, 1967; Meek, 1980; Briggs, 1984). Recently, Sheppard and Larsen (1992) and Briggs and Vincent (1992) have shown that the parameters needed for FCA can also be obtained from the frequency domain. In the comparison of FCA and FSA described here, the method of Meek (1980) is used to estimate the *apparent* and *true* velocities from both time domain and frequency domain data. The data required for this method are the auto-correlation width, the three cross-

correlation lag times, and the three cross-correlation amplitudes relative to the auto-correlation amplitude. Using time domain data all of these quantities are obtained directly from Gaussian fits of the auto- and cross-correlations. However, when using frequency domain data the auto-correlation width is calculated from the auto-spectrum width, the cross-spectral phase slopes are taken as three cross-correlation lag times, and the relative cross-spectral amplitudes are taken as the relative cross-correlation amplitudes. Therefore, in the frequency domain Gaussian fits of auto- and cross-spectral amplitude and linear fits of cross-spectral phase are required. Clearly, the FCA and FSA methods differ only in that the parameters needed for FCA are obtained from the auto- and cross-correlations whereas the parameters needed for FSA are obtained from the auto- and cross-spectra.

3. EXPERIMENTAL SETUP AND SIGNAL PROCESSING

An experiment suitable for SA and SI wind estimation was carried out between 1910 LT on June 29, 1990, and 0950 LT on July 2, 1990, using the MU radar located in Shigaraki, Japan (34.85° N, 136.10° E). The MU radar antenna array is shown in *Figure 1*. The transmitting antenna used the entire array while the receiving antennas, designated as antennas 1, 2, and 3, used smaller array segments of equal area. The altitude range from 6.0 to 15.3 km was divided into 32 range bins of 300 m each. An eight-bit complementary was used with a flip of the code every interpulse period (IPP), which was set at $400 \mu\text{s}$. Coherent integration was performed with 200 points, giving an effective sampling interval of 0.08 s. The data recorded on magnetic tape included 256 complex time series points for each of the 32 heights and each of the three receivers. Five records were recorded for each pointing direction which included zenith and three off-zenith directions. Adding the time for switching the beam direction and recording

the data, a total interval of 8.08 min exists between each consecutive five record group of vertically-pointing data. The spectra from fifteen records were incoherently averaged before each estimate of the wind vector giving a total time between estimates of 24.26 min. The total observation time was 62.67 hours which results in a total of 155 estimates of the wind velocity and echo power.

Data read from the magnetic tape was processed to obtain the auto- and cross-correlations and the auto- and cross-spectra. Before calculating the spectra, the number of coherent integrations was increased by a factor of two, giving a 3 dB increase in SNR, reducing the number of points in each record to 128, and increasing the effective sampling interval to 0.16 s. Also, mean values were removed from both the I and Q signals separately. Since each receiving antenna looks at identical scatterers with only a small angular separation, the receiver output powers would be nearly equal if it were not for unavoidable differences in the receiver channel gains. Calibrating the hardware to make these gains equal throughout the experiment would be very difficult. Thus, a software equalization of signal power was implemented. This method for equalizing the power is simply to adjust relative signal levels so that the signal variances are equal. Since peak cross-correlation amplitudes relative to the peak auto-correlation amplitude are needed for FCA, and peak cross-spectral amplitudes relative to the peak auto-spectral amplitude are needed for FSA, accurate power levels are needed for both methods. The relative amplitudes required by the FCA/FSA methods must be a measure of turbulence and spatial decorrelation and not the result of unequal receiver channel gains. Estimates of the *true* velocity have been made with and without signal power equalization, and the number of failures were significantly greater when power equalization was not used. A standard FFT with a rectangular window was used to calculate the mean auto- and cross-spectra, and fifteen spectra were then incoherently

averaged. Next, the mean auto- and cross-correlations were calculated by applying the inverse FFT. The noise spike at zero-lag was removed from the mean auto- and cross-correlations, and the average noise level was subtracted from the mean auto- and cross-spectra. Because of the variability in the spectral amplitude, a three-point running average was applied before attempting a fit. A Gaussian function was fitted to the correlation and spectral amplitudes while a line was fitted to the spectral phase. The fitting was carried out within a window defined by the half-power points of relative amplitude for both the correlations and the spectra. *Figure 2* shows a typical set of spectra and correlations with the fits superimposed and the frequency range of the fitting windows indicated by the range of frequencies between the small circles on the plots.

4. STATISTICAL ANALYSIS

Figures 3 and 4 show the time history of wind profiles with each profile representing the average of two 15-record averages. Missing data in the profiles represent a failure to fit or a failure to calculate a velocity within $\pm 40 \text{ m s}^{-1}$ of the mean velocity. A discussion of these failures and their relationship to the echo power is presented later in this section. There are a total of 155 wind profile estimates, each of which is obtained by incoherently averaging 15 records. The total elapsed time between estimates is 24.26 min and the elapsed time between plotted profiles is 48.52 min. A total of 77 profiles are plotted for a total elapsed time of nearly 63 hours. Also plotted in the figures are the average profiles obtained over the same time period with the standard deviations $\pm \sigma$ indicated by the horizontal bars. The standard deviation represents the combined effect of variance in the estimation method and temporal variance in the velocity over the 63 hour period.

Auto-correlation width, lag times, and relative amplitudes obtained from the auto- and cross-correlations were used to calculate profiles of the zonal and meridional components of the *apparent* and *true* velocity using Meek's (1980) method. These auto- and cross-correlations were obtained with an inverse FFT of a 15 record incoherent average of auto- and cross-spectra. The results for the zonal component are presented in *Figure 3a* and those for the meridional component in *Figure 3b*. Note that the average *apparent* velocity profile is repeated by the dashed curve in the plot of the average *true* velocity profile. These curves show the correction for *true* zonal velocity as a percentage of the *apparent* zonal velocity, to be approximately 27% , 31% , and 23% at heights of 8, 12, and 14 km, respectively. For the meridional component the correction is roughly 33% except in the region near 12 km where it is close to 50% . The standard deviations for the *true* zonal and *true* meridional components of velocity averaged for all heights over the 63 hour period are $\pm 7.1 \text{ m s}^{-1}$ and $\pm 7.5 \text{ m s}^{-1}$, respectively.

Auto-spectral width, phase slopes, and relative amplitudes obtained from the auto- and cross-spectra were also used to calculate profiles of the zonal and meridional components of the *apparent* and *true* velocity using Meek's method. These auto- and cross-spectra were obtained by a 15 record incoherent average of auto- and cross-spectra. Presently we are referring to this method as either the FSA or the SI method. Profiles of the zonal and meridional components of the horizontal velocity are shown in *Figures 4a* and *4b*, respectively. The zonal velocity correction as a percentage of zonal *apparent* velocity was found to be approximately 24% , 31% , and 15% at heights of 8, 12, and 14 km, respectively. For the meridional component the correction was found to be 2% or so less than that found from the time domain method. This trend toward a smaller correction with the SI method is consistent with the results presented by Briggs and

Vincent (1992) and may be due to the noise spike at zero lag in the auto-correlation function. If the spike is not removed properly, an overestimate of the effects of turbulent fading may result. For the SI method, the standard deviations for the *true* zonal and *true* meridional components of velocity averaged for all heights over the 63 hour period are $\pm 7.6 \text{ m s}^{-1}$ and $\pm 8.0 \text{ m s}^{-1}$, respectively. The larger average standard deviation obtained for the SI method is attributable primarily to the heights with lower echo power. Average *true* velocities calculated with the SA and SI methods are close with the maximum differences of 4.0 m s^{-1} and 1.5 m s^{-1} seen at a height of 12 km for the zonal and meridional components, respectively.

Scatter plots of FSA *true* velocities vs. FCA *true* velocities are shown in *Figures 5a* and *5b* for the zonal and meridional components respectively. Standard deviations between FSA and FCA velocities, defined as

$$\sigma_{\Delta v} = \sqrt{\frac{1}{N} \sum (V_{FCA} - V_{FSA})^2} \quad (2)$$

are calculated to be 4.8 m s^{-1} and 4.10 m s^{-1} for the zonal and meridional components, respectively.

Finally, *Figures 6a* and *6b* show the profiles of the average echo power and total failure count for both the SA and SI methods. The solid line represents SA (time domain) failures and the dashed line represents SI (frequency domain) failures. Failures attributable to the *true* velocity correction accounted for only 5% of the total failures while the rest could be attributed to failures in the fitting procedure. Except for the lower altitudes between 6 and 8 km, the larger failure counts are closely correlated with regions of lower echo power. Examination of the spectra in the 6 to 8 km range between 50 and 60 hours elapsed time, showed a larger than normal amount of

interference, which is the primary contributor to the failure counts seen at the lower heights. Interference often appears over a finite frequency band, and it may be possible to reduce interference by using frequency domain filtering. Since we calculated the auto- and cross-correlations needed for FCA velocity estimates via the inverse FFT of the auto- and cross-spectra, frequency domain filtering methods would also be applicable for our time domain method. Possibly, in some future work, it will be convenient for us to implement frequency domain interference filtering.

5. DISCUSSION

While time domain and frequency domain methods for estimating *true* horizontal velocity are analytically equivalent when Gaussian spectra are assumed, in practice there are significant differences in the two methods. When fitting the auto- and cross-correlation functions, regions outside of the primary peak, i.e., the oscillatory tails, are generally ignored. In the region of the primary peak, where the fitting procedure is applied, correlation functions are usually smooth and monotonically decreasing. Thus, in the time domain most fitting routines work with little difficulty. On the other hand, the oscillatory tails of the correlation functions, generally ignored in the time domain analysis, are transformed into a highly fluctuating structure in the primary lobes of the spectral functions where the fitting procedures are attempted in the frequency domain. One of the basic differences between time domain and frequency domain methods is that time domain fits are determined more by the high frequency portion of the spectrum while frequency domain fits are determined more by the low frequency portion. With higher signal power and/or longer time averages, the poor convergence properties of the spectra can be circumvented, and the frequency domain method also becomes easy to implement. However, in practice these conditions do not always exist

and fitting the spectra can be significantly more complex. For the fitting routines we investigated, smoothing of the spectra was necessary in order to prevent excessive fitting failures.

For estimates of the *apparent* velocity, only a linear fit to the phase of the cross-spectra is necessary, but *true* velocity estimates also require a determination of cross-spectral amplitudes relative to the auto-spectral amplitude which entails fitting of a Gaussian or parabola. Failure to accurately determine the relative amplitudes will result in failures of the FCA/FSA routine. Furthermore, even when only the *apparent* velocity is estimated, an appropriate width for the fitting window must still be determined. If care is not taken to make the fitting window sufficiently small, random phase values that occur at the lower amplitude portions of the cross-spectra will bias the phase slope estimate toward zero causing an overestimate of the *apparent* velocity. A window width equal to the half-power spectral width appeared to produce acceptable results in our study.

6. CONCLUSIONS

As seen in *Figure 6*, the failure rates for the SA and SI methods are very similar. With the exception of a small increase in the FSA *true* velocity standard deviation in the region of low SNR, neither method significantly outperforms the other with regard to the accuracy or quality of the results. Since the difference between the two techniques is simply the manner in which the parameters needed for the *true* velocity calculation are obtained, the computational load of the techniques must be the same after these parameters are obtained. The SI method requires that the auto- and cross-spectra be fitted with Gaussian functions, and this task presently appears to be more difficult than fitting the auto- and cross-correlations. In addition, the SI method

requires that the phase of the cross-spectra be fitted with a line. The SA method requires only Gaussian fitting to be performed on the auto- and cross-correlation functions, thus eliminating the need for the linear fit used in the SI technique. Therefore, the SA method is obviously more computationally efficient for the estimation of horizontal velocity. Presently, it is not clear which of the two methods will be the easier for estimating true vertical velocity and refractivity layer tilt angles.

Future work will include a detailed study of the statistical nature of estimates for true vertical velocity and refractivity layer tilt angles using both time and frequency domain methods. Most probably, a combination of these methods will provide the optimal wind estimation technique.

Acknowledgments. E.L.S. and M.F.L. were supported by AFOSR Grant #AFOSR-91-0384 during the course of the study. R.D.P. was supported under NSF grants #ATM9121526, #ATM9006846, and #ATM9003448. The MU radar belongs to and is operated by the Radio Atmospheric Science Center of Kyoto University.

REFERENCES

- Adams, G. W., J. W. Brosnahan, D. C. Walden, S. F. Nerney (1986), Mesospheric observations using a 2.66-MHz radar as an imaging Doppler interferometer: description and first results, *J. Geophys. Res.*, **91**, 1671-1683.
- Briggs, B. H., (1984), The analysis of spaced sensor records by correlation techniques, *Handbook for MAP*, **13**, 166-186.
- Briggs, B. H., and R. A. Vincent (1992), Spaced-antenna analysis in the frequency domain, *Radio Sci.*, **27**(2), 117-129.
- Farley, D. T., H. M. Ierikic, and B. G. Fejer (1981), Radar interferometry: A new technique for studying plasma turbulence in the ionosphere, *J. Geophys. Res.*, **86**, 1467-1472.
- Fedor, L. S. (1967), A statistical approach to the determination of three-dimensional ionospheric drifts, *J. Geophys. Res.*, **72**, 5401-5415.
- Fooks G. F., and I. L. Jones (1961), Correlation analysis of the fading of radio waves reflected vertically from the ionosphere, *J. Atmos. Terr. Phys.*, **20**, 229-242.
- Fooks, G. F. (1965), Ionospheric drift measurements using correlation analysis; methods of computation and interpretation of results, *J. Atmos. Terr. Phys.*, **27**, 979-989.

Franke, P. M., and D. Thorsen, M. Champion, S. J. Franke, E. Kudeki (1990), Comparison of time- and frequency-domain techniques for wind velocity estimation using multiple-receiver MF radar data, *Geophys. Res. Lett.*, **17**, 2193-2196.

Kudeki, E., (1988), Radar interferometer observations of mesospheric echoing layers at Jicamarca, *J. Geophys. Res.*, **93**, 5413-5421.

Kudeki, E., F. Surucu, and R. F. Woodman (1990), Mesospheric wind and aspect sensitivity measurements at Jicamarca using radar interferometry and post-statistics steering techniques, *Radio Sci.*, **25**, 595-612.

Larsen, M. F., and J. Röttger (1989), The spaced antenna technique for radar wind profiling, *J. Atmos. Ocean Tech.*, **6**, 920-938.

Larsen, M. F., R. D. Palmer, S. Fukao, R. F. Woodman, M. Yamamoto, T. Tsuda, and S. Kato (1992), An analysis technique for deriving vector winds and in-beam incidence angles from radar interferometer measurements, *J. Atmos. Ocean Tech.*, **9**(1), 3-14.

Liu, C. H., J. Röttger, C. J. Pan, and S. J. Franke (1990), A model for spaced antenna observational mode for MST radars, *Radio Sci.*, **25**, 551-563.

Manson, A. H., J. B. Gregory, and D. G. Stephenson (1974), Winds and wave motions to 110 km at mid-latitudes. I. Partial reflection radiowave soundings, 1972-73, *J. Atmos. Sci.*, **31**, 2207-2215.

Meek, C. E. (1980), An efficient method for analyzing ionospheric drifts data, *J. Atmos. Terr. Phys.*, **42**, 835-839.

Palmer, R. D., M. F. Larsen, R. F. Woodman, S. Fukao, M. Yamamoto, T. Tsuda, and S. Kato (1991), VHF radar interferometry measurements of vertical velocity and the effect of tilted refractivity surfaces on standard Doppler measurements, *Radio Sci.*, **26**, 417-427.

Phillips, G. J., and M. Spencer (1955), The effects of anisometric amplitude patterns in the measurement of ionospheric drifts, *Proc. Phys. Soc. London*, **B68**, 481-492.

Röttger, J., and R. A. Vincent (1978), VHF radar studies of tropospheric velocities and irregularities using spaced antenna techniques, *Geophys. Res. Lett.*, **5**, 917-920.

Röttger, J., and M. F. Larsen (1990), UHF/VHF radar techniques for atmospheric research and wind profiler applications, in *Radar in Meteorology, Battan Memorial and 40th Radar Meteorological Conference Volume*, American Meteorological Society, Boston, Massachusetts, Chapter 21a, 235-281.

Röttger, J., C. H. Liu, J. K. Chao, A. J. Chen, C. J. Pan, and I. J. Fu (1990), Spatial interferometer measurements with the Chung-Li VHF radar, *Radio Sci.* **25**, 503-515

Sheppard, E. L., and M. F. Larsen (1992), Analysis of model simulations of spaced antenna/radar interferometer measurements, *Radio Sci.*, in press.

Van Baelen, J. S., T. Tsuda, A. D. Richmond, S. K. Avery, S. Kato, S. Fukao, and M. Yamamoto (1990), Comparison of VHF Doppler beam swinging and spaced antenna observations with the MU radar: First results, *Radio Sci.*, 25, 629-640.

Van Baelen, J. S., and A. D. Richmond (1991), Radar interferometry technique: Three-dimensional wind measurement theory, *Radio Sci.*, 26(5), 1209-1218.

Vincent, R. A., and J. Röttger (1980), Spaced antenna VHF radar observations of tropospheric velocities and irregularities, *Radio Sci.*, 15, 319-335.

Vincent, R. A., P. T. May, W. K. Hocking, W. G. Elford, B. H. Candy and B. H. Briggs (1987), First results with the Adelaide VHF radar: Spaced antenna studies of tropospheric winds, *J. Atmos. Terr. Phys.*, 49, 353-366.

Woodman, R. F. (1991), A general statistical instrument theory of atmospheric and ionospheric radars, *J. Geophys. Res.*, 96(A5), 7911-7928.

FIGURE CAPTIONS

Figure 1. Receiver antenna configuration used for the SI experiment conducted from 1910 LT on June 29, 1990, through 0950 LT on July 2, 1990, using the MU radar.

Figure 2. Auto- and cross-spectra and the corresponding auto- and cross-correlations at 7.8 km for a 5.12 min average of vertical-pointing SI data taken on June 29, 1990, during the period 1910-1935 LT, using the MU radar. Superimposed are Gaussian fits of amplitude for spectra and correlations and linear fits of phase for cross-spectra. The small circles indicate the fitting windows used.

Figure 3. Profiles of *true* and *apparent* (a) zonal velocity and (b) meridional velocity calculated from time-domain parameters, shown at 48.52 min intervals for a total elapsed time of 62.67 hours, plus average profiles over the same period with $\pm\sigma$ standard deviation bars superimposed. The average *apparent* velocity is repeated by the dashed curve in the profile of average *true* velocity.

Figure 4. The same as Fig. 3 except using frequency domain data.

Figure 5. Scatter plots of FSA velocity vs. FCA velocity for (a) the zonal component and (b) the meridional component.

Figure 6. Profile of (a) average echo power and (b) total failures for both frequency domain and time domain methods. Time domain failures are shown by the solid line and frequency domain failures are shown by the dashed line.

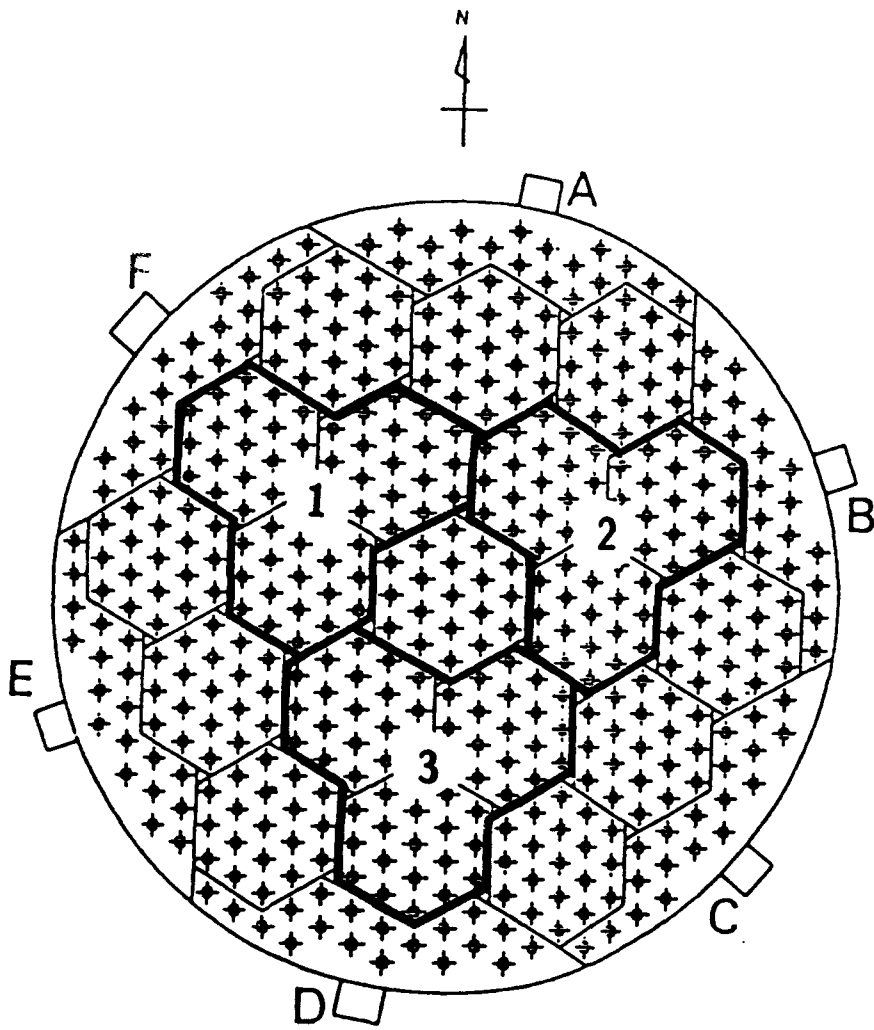


Fig 1

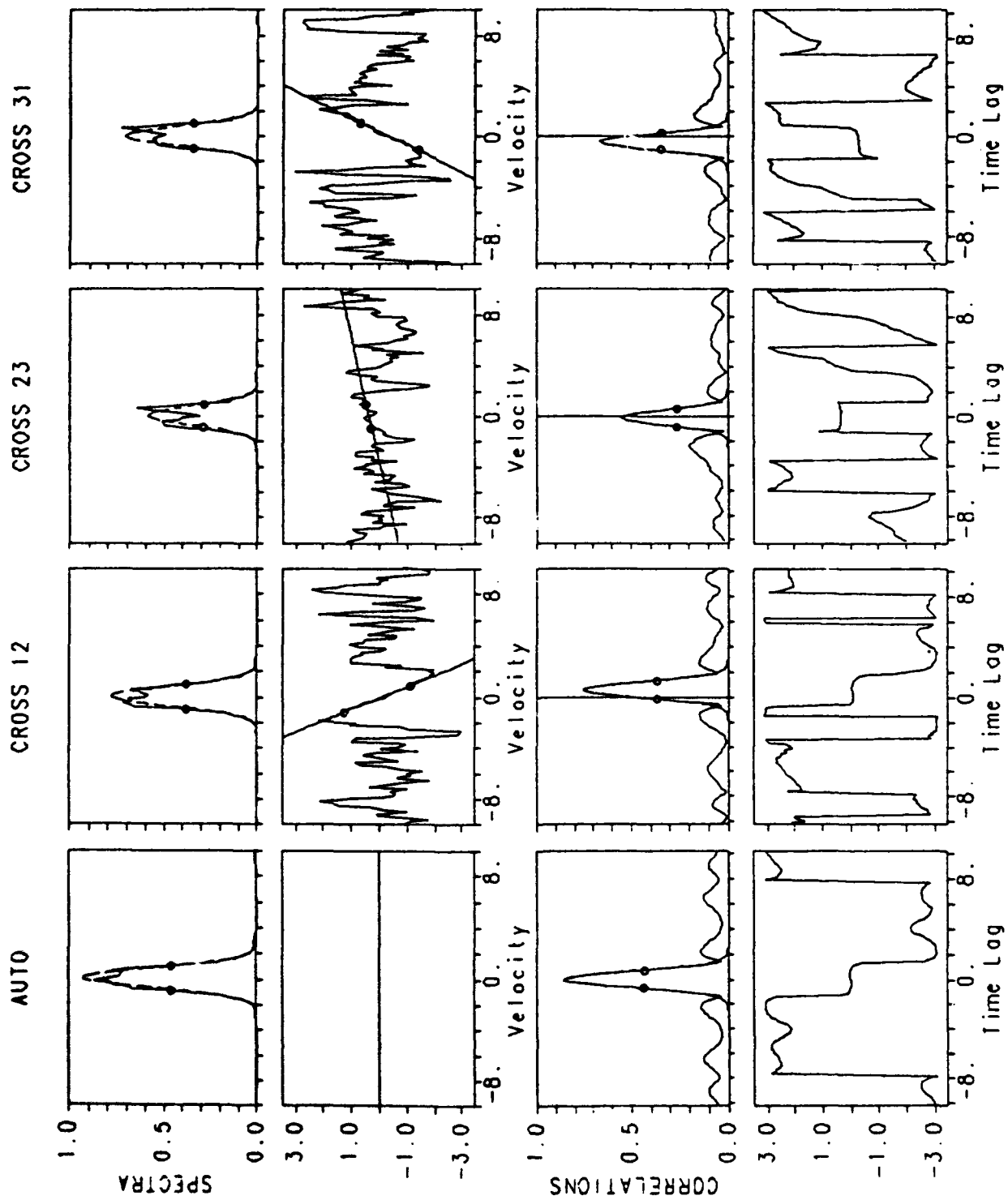
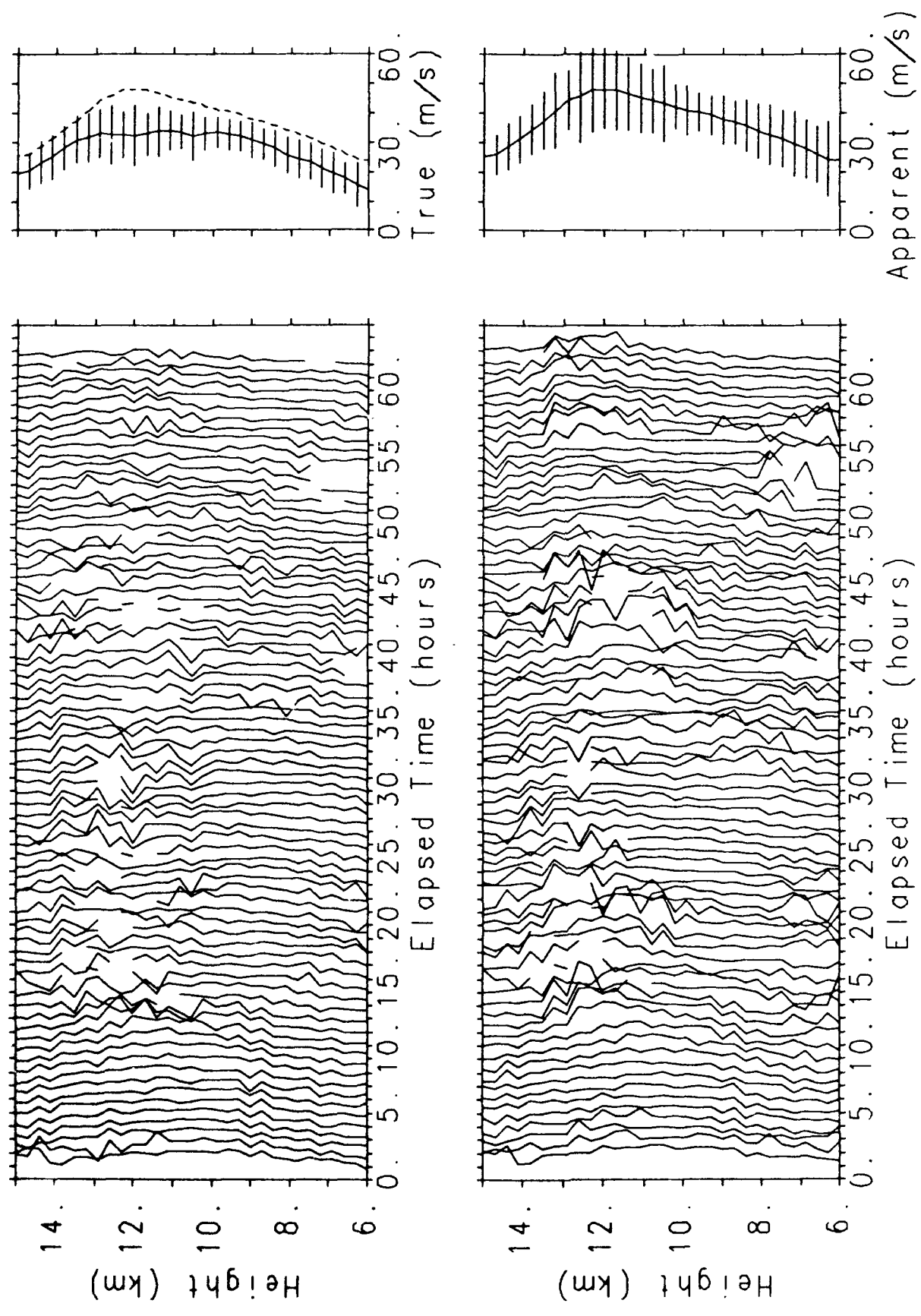
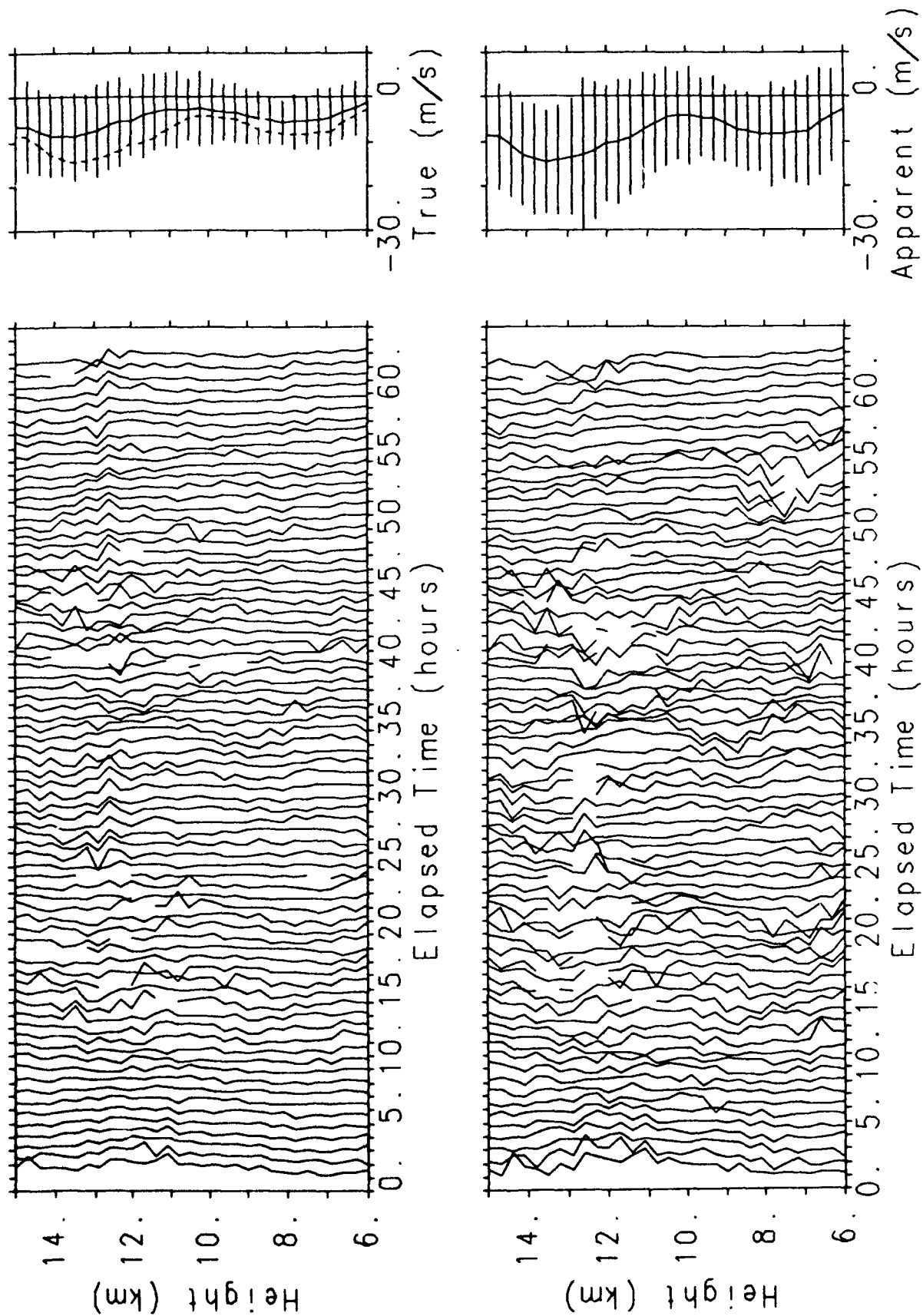
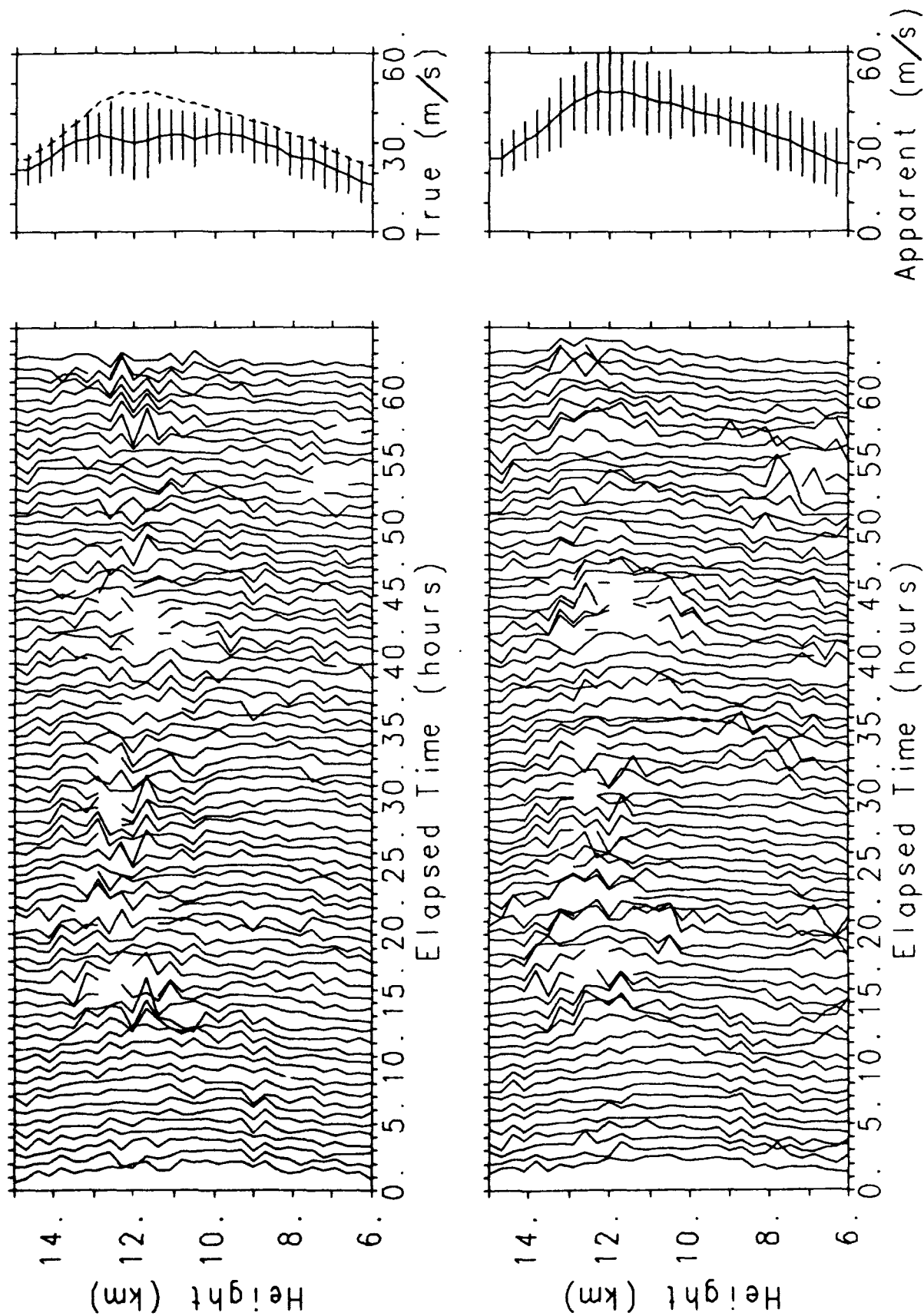


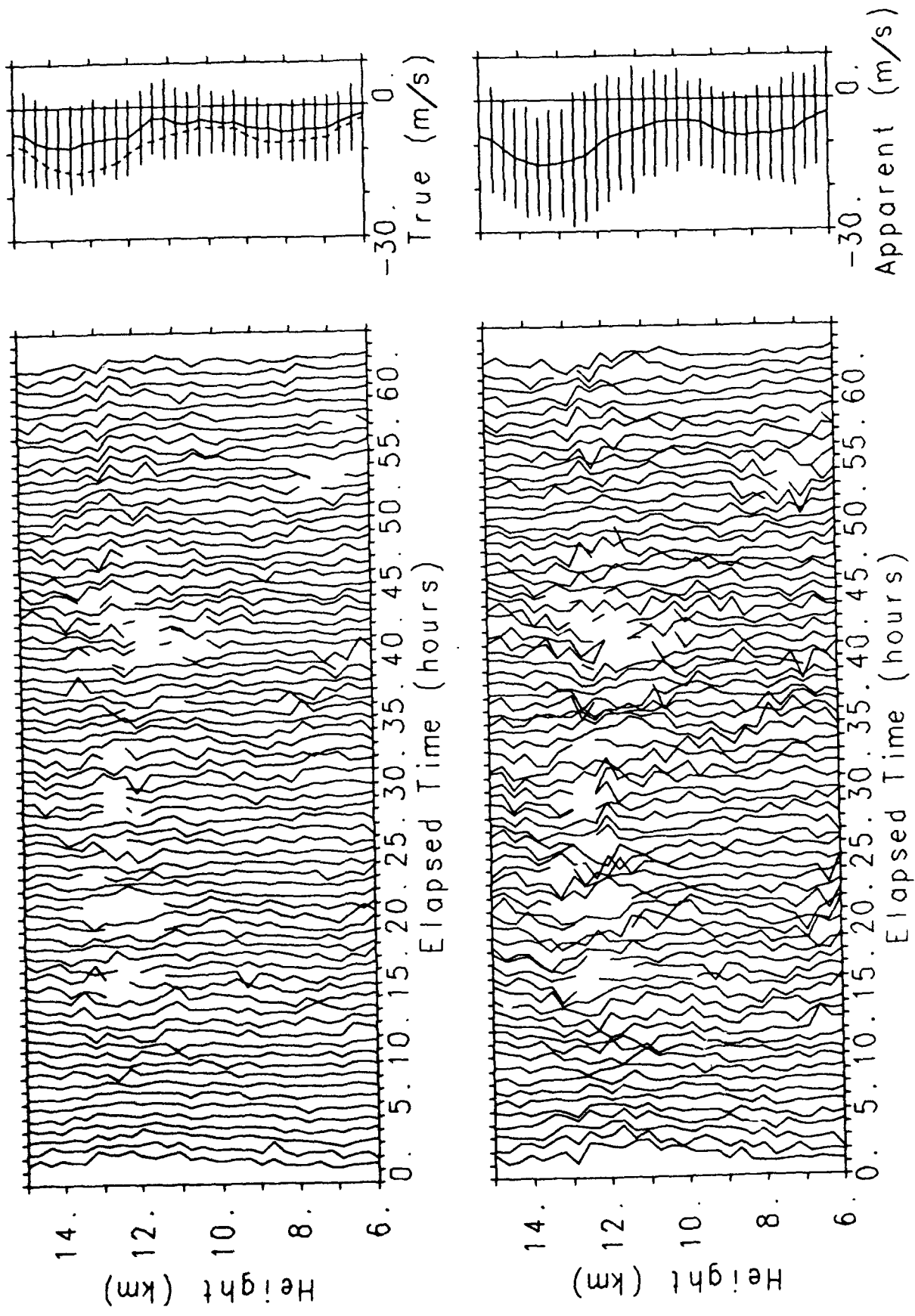
Fig 2

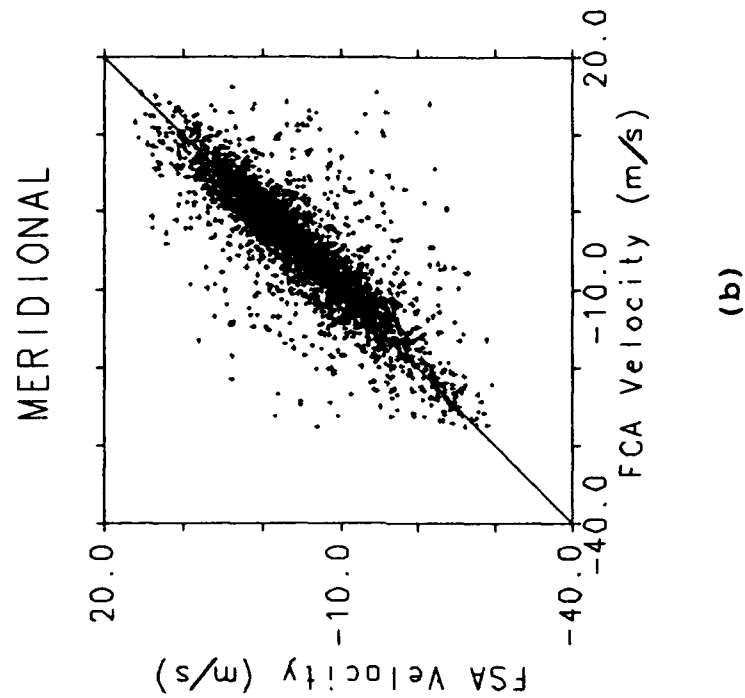
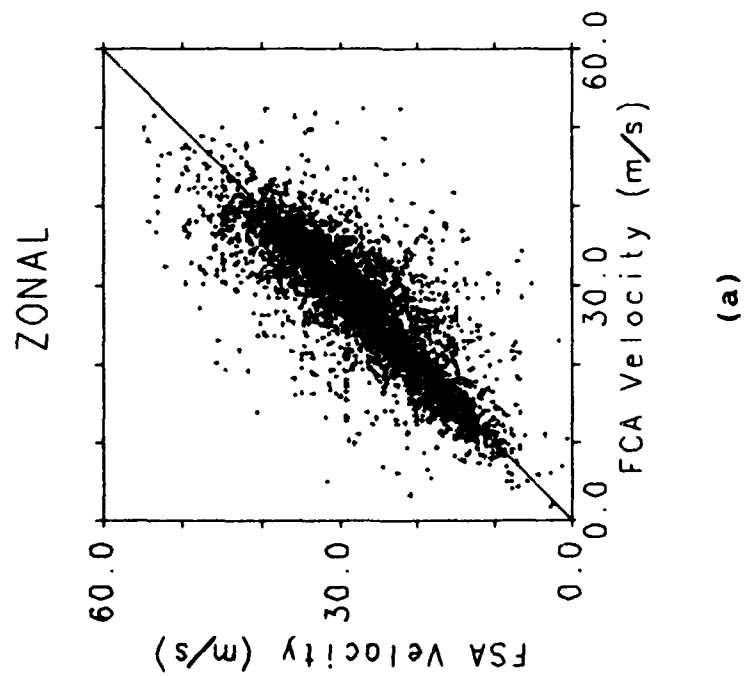
Fig 3a

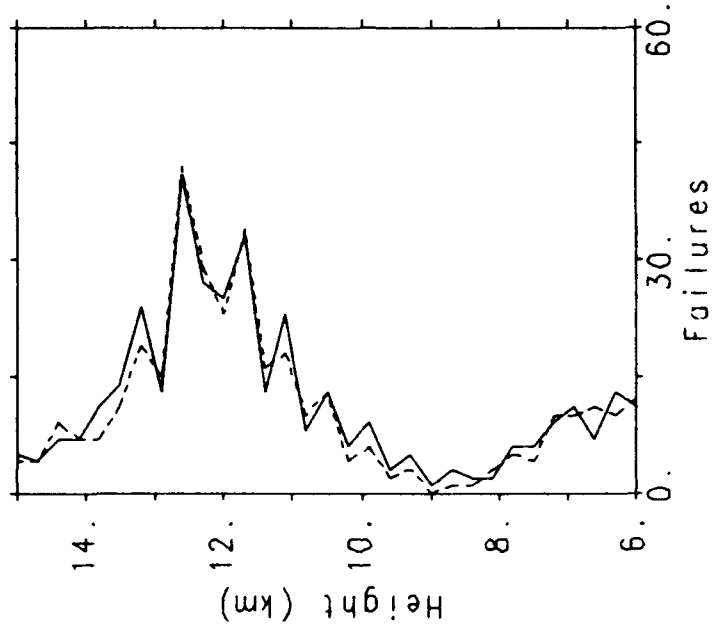




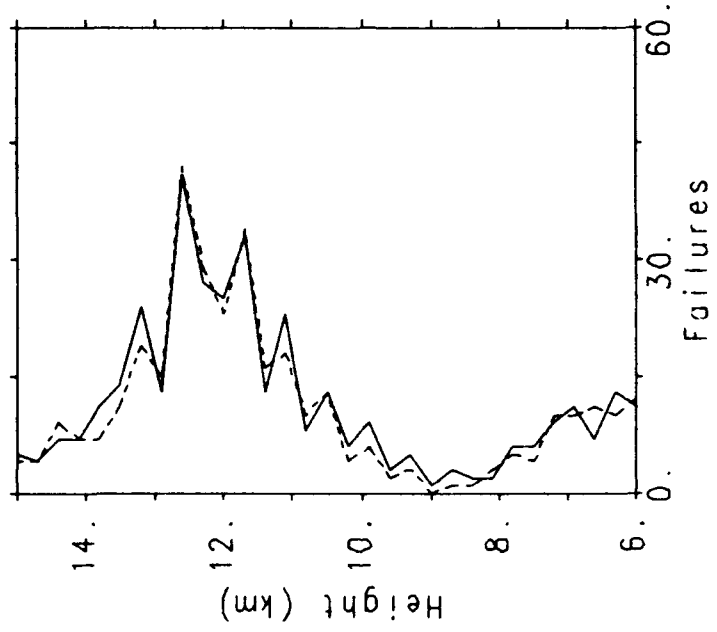








(a)



(b)

VHF Wind-Profiler Data Quality and Comparison of Methods for Deducing Horizontal and Vertical Air Motions in a Mesoscale Convective Storm

J. G. YOE* AND M. F. LARSEN

Department of Physics and Astronomy, Clemson University, Clemson, South Carolina

E. J. ZIPSER

Department of Oceanography and Meteorology, Texas A&M University, College Station, Texas

(Manuscript received 13 October 1990, in final form 23 January 1992)

ABSTRACT

Very high frequency (VHF) Doppler radar measurements of the horizontal and vertical winds are used to examine three procedures to extract mean profiles of horizontal and vertical winds. These are 1) time averaging of first-moment estimates of radial velocity from the high time resolution Doppler spectra; 2) time averaging of radial velocities estimated from a least-squares fitting of either one or two Gaussians to the spectra in order to account for the double peaks corresponding to turbulent and precipitation scattering that appear in the spectra during heavy rain; and 3) consensus averaging of the least-square-fitted radial velocities. Horizontal winds produced by these procedures were compared to each other and to those from two 5-cm radars operating nearby. Least-squares fitting yielded the best wind estimates, although a slight relaxation of the consensus criterion was sometimes found to be necessary in order to avoid the failure to find a consensus. The simple first-moment method produced comparable results, except below the melting level, where it performed more poorly. Vertical winds from the fitted VHF spectra were compared with those derived from the 5-cm-radar data using the extended velocity-azimuth display (VAD) technique. Reasonable agreement was found at heights above the freezing level.

1. Introduction

Doppler radar wind profilers operating mostly at frequencies near either 50 MHz (VHF) or 400 MHz (UHF) have been used increasingly as tools for measuring horizontal winds in the troposphere and lower stratosphere (e.g., see Röttger and Larsen 1990 for a review). A typical wind profiler employs three beam directions. One is usually directed vertically, and the other two are steered away from zenith by a small angle θ_0 at azimuths differing by 90° . Typical zenith angles are 10° – 15° . In the absence of precipitation, the received signal is backscattered from turbulence-generated refractive-index irregularities having spatial scales of one-half the radar wavelength, as discussed, for example, by Woodman and Guillen (1974). Assuming that the scatterers move with the same velocity as the air, the radial Doppler velocity measured along a particular beam direction is

$$V_n = (u \sin \phi_i + v \cos \phi_i) \sin \theta_i + w \cos \theta_i, \quad (1)$$

* Present affiliation: Max-Planck-Institut für Aeronomie, Katlenburg-Lindau, Federal Republic of Germany.

Corresponding author address: Dr. M. F. Larsen, Department of Physics and Astronomy, Clemson University, Clemson, SC 29631.

where u , v , and w are the Cartesian wind components, the subscript i refers to the beam direction, and ϕ and θ are, respectively, the azimuth and zenith angles. At any height z , the volumes sampled by the beams are separated by a horizontal distance $\approx 2z \sin \theta_0$, but the assumption is usually made that the winds do not vary significantly over the sampled region or over the period required to sample the various beam directions. With these assumptions, the horizontal wind components can be calculated by solving Eq. (1) simultaneously for all values of i . In some cases only the two oblique beams are employed, and u and v are calculated with the additional assumption that $w = 0$. The vertical velocity is typically much smaller than the horizontal velocities, but, since the zenith angles are usually small, the contributions of the horizontal and vertical velocities to the radial velocities are generally comparable, so that neglecting the vertical velocities leads to poor estimates of the horizontal winds.

An example of a scheme for estimating the horizontal wind profiles has been 1) to incoherently average the Doppler power spectra over a period of several minutes, 2) to subtract the noise level from the spectrum and to estimate V , as the first moment of the residual spectrum, 3) to obtain hourly averages of the radial velocities for each range gate and beam direction, and 4) to use the average radial velocities, together

with Eq. (1) to calculate the horizontal velocities as a function of height. The average radial velocities are obtained by means of a consensus-averaging technique (Fischler and Bolles 1981), in which the mean of the largest group of V_r values that lie within a prescribed tolerance of one another for the 1-h period is determined. Strauch et al. (1987) have carried out an extensive test of the procedure in clear air over a 1-month period by exploiting the redundancy in data from a five-beam 405-MHz radar. Since only three beam directions are required to estimate the horizontal velocities, two independent hourly estimates of the horizontal wind components could be compared. The standard error of u and v for a three-beam profiler in these conditions was estimated to be 1.3 m s^{-1} .

At UHF, precipitation echoes will dominate the backscattered signals, even for light rainfall rates (see e.g., Larsen and Röttger 1987), so that a UHF profiler senses the motion of precipitation particles rather than that of the air when precipitation is present in the beam. By replacing w in Eq. (1) with the precipitation vertical velocity w_p , and by making the additional assumptions that 1) the horizontal motions of the precipitation and the air are the same, and that 2) w_p is uniform over the area separating the three beams, u and v may still be calculated from the V_r values. Wuertz et al. (1988) analyzed data from a five-beam 405-MHz radar to determine the precision and accuracy of the operational wind-profiling technique described above during periods of precipitation. The errors in hourly estimates of the horizontal wind components were found to be $2\text{--}4 \text{ m s}^{-1}$ when the precipitation was spatially and temporally uniform. For time-varying or inhomogeneous precipitation, however, the inherent assumptions required in using Eq. (1) were not justified, and the errors in the horizontal velocities became large.

VHF measurements of the horizontal winds in the presence of precipitation present a more complicated situation in that the spectra will have contributions from both turbulent scatter and from precipitation as long as the rainfall rates are moderate or heavy (see Larsen and Röttger 1987). Because the projection of the vertical motion along each beam direction is proportional to w for the turbulent scatter component and to w_p for the precipitation scatter component, double-peaked spectra will result as long as the air and precipitation are moving at different velocities in the vertical direction. Double-peaked spectra are characteristic of the heights below the melting level where large negative values of w_p occur. Fukao et al. (1985) observed light stratiform rain with the VHF MU (middle and upper atmosphere) radar in Japan and deduced the wind field by identifying the turbulence contribution of the received signal. Their comparison of the horizontal air motion to that of precipitation showed close agreement. Larsen and Röttger (1987) examined the doubled-peaked spectra associated with a thunderstorm observed with the SOUSY (sounding system)-VHF radar

located in former West Germany and suggested that a combination of VHF and UHF radars could be used for cloud physics research. For example, the vertical air motion obtained from the VHF system would allow the calculation of corrected terminal velocities of precipitation and parameterization of drop-size distributions derived from the UHF radar data. Observations have already been made with a 50-MHz radar located at Urbana, Illinois, and a 915-MHz radar with a small $3\text{-m} \times 3\text{-m}$ antenna to test the merits of combining the low- and high-frequency data for precipitation studies (Currier and Avery 1989). Wakasugi et al. (1986, 1987) calculated drop-size distributions from VHF signals alone by application of a least-squares fitting of the spectra obtained at vertical incidence in stratiform rain with the MU radar. Similar work has been carried out by Gossard (1988) with UHF radar data. Sato et al. (1990) refined the procedure of Wakasugi et al. (1987) and calculated that the derived parameters describing the drop-size distributions were accurate to within 15%.

The earlier studies, with the exception of the work by Wuertz et al. (1988), have focused on the possibilities for extracting information about the precipitation or microphysical processes from the radar profiler measurements. Our goal is to examine the horizontal and vertical winds that can be derived from the radar data in a convective environment. One goal of deploying an operational wind-profiler network is to improve our ability to resolve mesoscale systems with time scales of a few hours to a day. Of particular interest are those systems that produce precipitation. An example is the squall line of 10–11 June 1985, a mesoscale convective system (MCS) that formed during the Oklahoma–Kansas Preliminary Regional Experiment for STORM-Central (OK PRE-STORM). Extensive observations of this system were made using a variety of instruments, including a VHF Doppler radar wind profiler. A preliminary analysis of the wind-profiler data from the event was made by Augustine and Zipser (1987), who compared horizontal wind profiles derived from the Doppler radar data to those from high-time-resolution radiosonde profiles from nearby locations.

In this paper we present a more detailed study of the VHF wind-profiler data for the stratiform cloud portion of the 10–11 June 1985 storm. In section 2 the VHF wind-profiler operation and the MCS are described. The character of the Doppler power spectra, which were affected both by lightning and by precipitation at various times during the course of the observations, is examined in section 3, and the implications of these effects for wind profiling are discussed. Section 4 deals with the results of three different averaging schemes for estimating the horizontal and vertical winds from the profiler data. In sections 5 and 6, respectively, the resulting horizontal and vertical wind estimates are compared to those obtained using a pair of scanning 5-cm Doppler radars that were operated

in the vicinity of the profiler. The conclusions follow in section 7.

2. Operation of the wind profiler and data collection

The OK PRE-STORM campaign was conducted in May and June 1985 to investigate mesoscale meteorological phenomena and to test technologies intended to be included in an operational network for mesoscale observations (Cunning 1986). During the campaign, the mobile SOUSY-VHF Doppler radar (Czechowsky et al. 1984) was installed at McPherson, Kansas, by the Radian Corporation under contract to the National Center for Atmospheric Research (NCAR), for use as a wind profiler. The radar was operated in a three-beam configuration at a frequency of 49.25 MHz. A pulse width of $1 \mu\text{s}$ gave a height resolution of 150 m, with coverage starting at 2.5 km above MSL. The received signals were incoherently added for 0.174 s, and time series of 64 complex points for 133 range gates were made along each beam and written to magnetic tape for off-line processing. A single sampling over all three beams took 41.5 s, including the time required to write the data to tape. The operating parameters of the McPherson profiler are summarized in Table 1.

Two NCAR 5-cm Doppler radars, CP-3 and CP-4, were deployed in the vicinity of the VHF profiler during OK PRE-STORM. The locations of the three instruments are shown in Fig. 1. During most of the 10–11 June 1985 MCS passage, the 5-cm radars operated in a mode consisting of a sequence of conical scans at various elevations up to a maximum of 23° above the horizon (Rutledge et al. 1988). The maximum unambiguous range of 135 km thus provided coverage over a horizontal region with a radius of 120 km, indicated by the heavy circles in Fig. 1. The VHF profiler was well within the coverage of the 5-cm radars when the latter were operated in the scanning mode.

By approximately 2000 UTC 10 June, a squall line had developed over southwest Kansas. The system intensified as it propagated east-southeastward during the next several hours. Augustine and Zipser (1987), Rutledge et al. (1988), and Johnson and Hamilton (1988) have described this system and presented results related to its structure and kinematics.

TABLE 1. Operating parameters for the VHF wind profiler at McPherson, Kansas, during PRE-STORM.

Frequency (MHz)	49.25
Number of beams	3
Orientation of oblique beams (deg)	135/225
Zenith angle of oblique beams (deg)	8
Peak power (kW)	125
Average power (kW)	5
Antenna aperture (m^2)	49×49
Height resolution (m)	150
Number of gates sampled	133

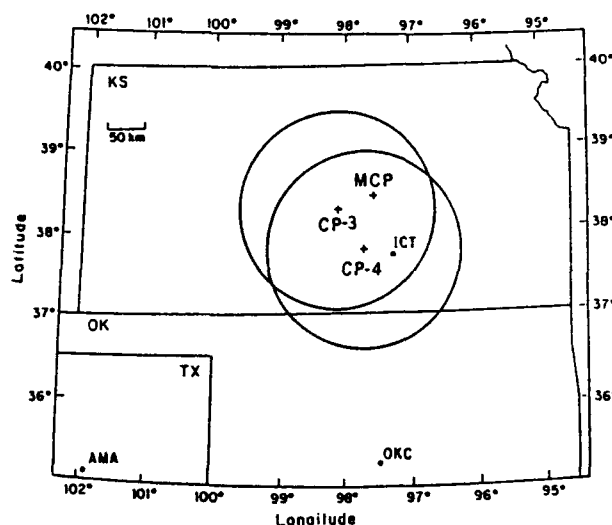


FIG. 1. Map showing the locations of the VHF Doppler radar wind profiler (MCP) and the NCAR CP-3 and CP-4 5-cm radars during the OK PRE-STORM campaign. The heavy circles indicate the 125-km maximum unambiguous horizontal range of the CP-3 and CP-4 radars when scanning azimuthally.

Composite digitized reflectivity data from three National Weather Service radars located at Wichita, Kansas; Oklahoma City, Oklahoma; and Amarillo, Texas, are shown in Fig. 2 for 0200 UTC 11 June, with darker regions denoting higher reflectivities. The leading convective region of the squall line is evident as a narrow,

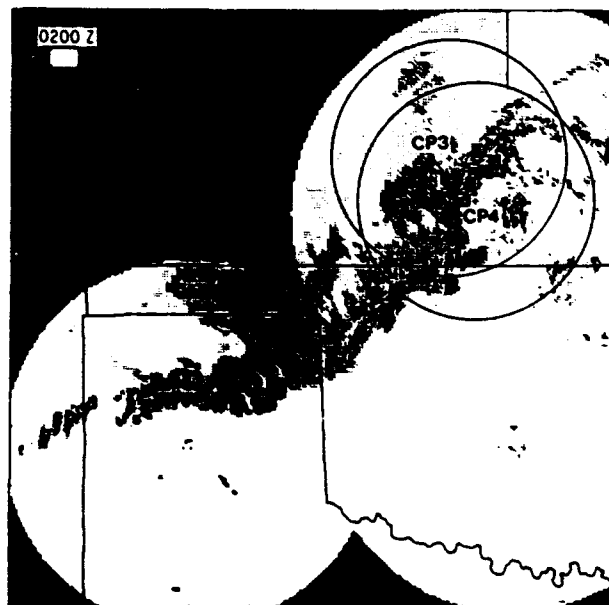


FIG. 2. Composite digitized reflectivity measured with NWS weather radars at Wichita, Kansas; Oklahoma City, Oklahoma; and Amarillo, Texas. Data from 0200 UTC 11 June 1985. Darker shading indicates higher reflectivity (from Rutledge et al. 1988). The 125-km range circles for CP-3 and CP-4 are also shown.

approximately 30-km-wide band of high reflectivities stretching over 700 km in length and oriented roughly from northeast to southwest. A broad 200–300-km-wide trailing region of stratiform cloud cover is apparent as the swath of lower reflectivities behind the convective line. The squall line had reached or surpassed maturity at this time, and the convective region had passed the McPherson profiler and the CP-3 and CP-4 radars. Precipitation in the stratiform cloud region was confined to the region within about 2100 km of the convective line. Operation of the VHF profiler was suspended from 0130 until 0230 UTC on 11 June when the convective region passed the radar site due to the frequency and intensity of lightning strikes in the area. The stratiform cloud region required many hours to pass over the site.

3. Effects of precipitation and lightning on the Doppler spectra

An important difference between the VHF Doppler spectra measured in clear air and those measured during the passage of the mesoscale convective system is that the latter are affected by precipitation and lightning. Lightning, in particular, can severely contaminate the spectra, as we will show in more detail below. Eliminating the contaminated spectra is a critical step in the process of estimating the horizontal winds.

The spectra were obtained from the complex time series of voltages measured with the profiler by application of a fast Fourier transform (FFT). In Fig. 3,

peak-normalized spectra for the vertical beam between 7.0- and 11.4-km altitude are shown for three periods. Each spectrum represents an incoherent average of seven consecutive spectra spanning 4.84 min. The spectra for 2342 UTC 10 June (Fig. 3a) correspond to the period before the squall line reached McPherson and are typical of VHF spectra in clear-air conditions with small vertical velocities. The spectra for 0231 UTC 11 June (Fig. 3b) correspond to the transition from the convective portion of the squall line to the stratiform cloud region and show larger vertical velocities and spectral widths that have increased by a factor of 2–3. The spectra for 0300 UTC 11 June (Fig. 3c) have extremely broad peaks and show little continuity in the Doppler velocity from gate to gate. The seven consecutive sets of spectra from which the averages in Fig. 3c were derived are presented in Fig. 4. Examination of these individual spectra reveals that the averages in Fig. 3c are dominated by the contributions of the second and fifth profiles. The spectra in the remaining five profiles are more nearly comparable to the averages for 0231 UTC. The spectra that dominate the averages for the period have enhanced total power, that is, signal plus noise, in addition to broad peaks and Doppler velocities that vary rapidly with height. Spectra with these characteristics will be referred to as "anomalous."

The anomalous spectra are likely associated with lightning. Similar spectra have been observed during periods of lightning with the SOUSY-VHF Doppler radar system in The Federal Republic of Germany (Larsen and Röttger 1987). The data presented by

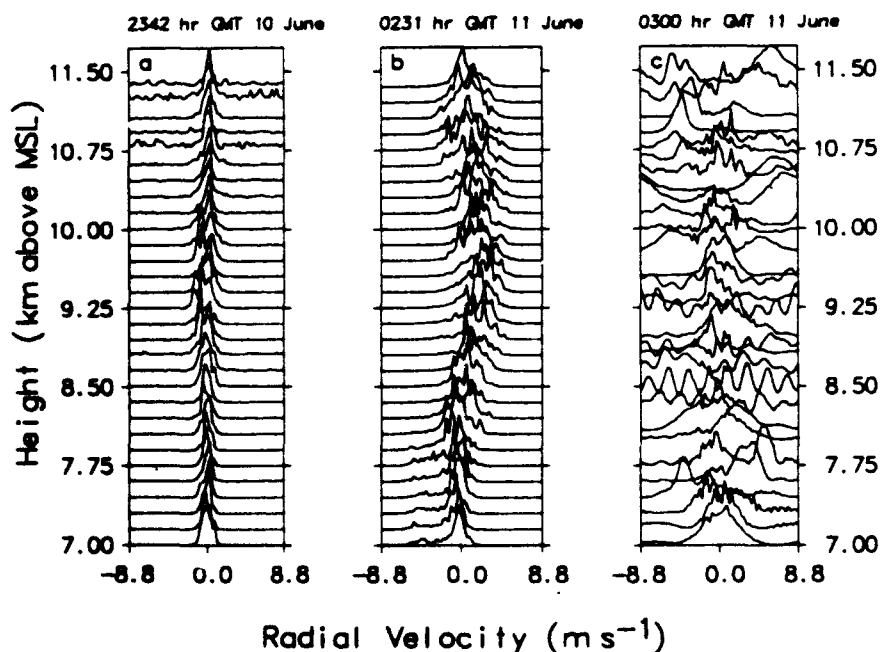


FIG. 3. Doppler power spectra for gates 31–60 for the VHF wind profiler operating at vertical incidence. Each spectrum is the incoherent average of 7 consecutive spectra collected over 4.84 min beginning at (a) 2340 UTC 10 June; (b) 0231 UTC 11 June; and (c) 0300 UTC 11 June.

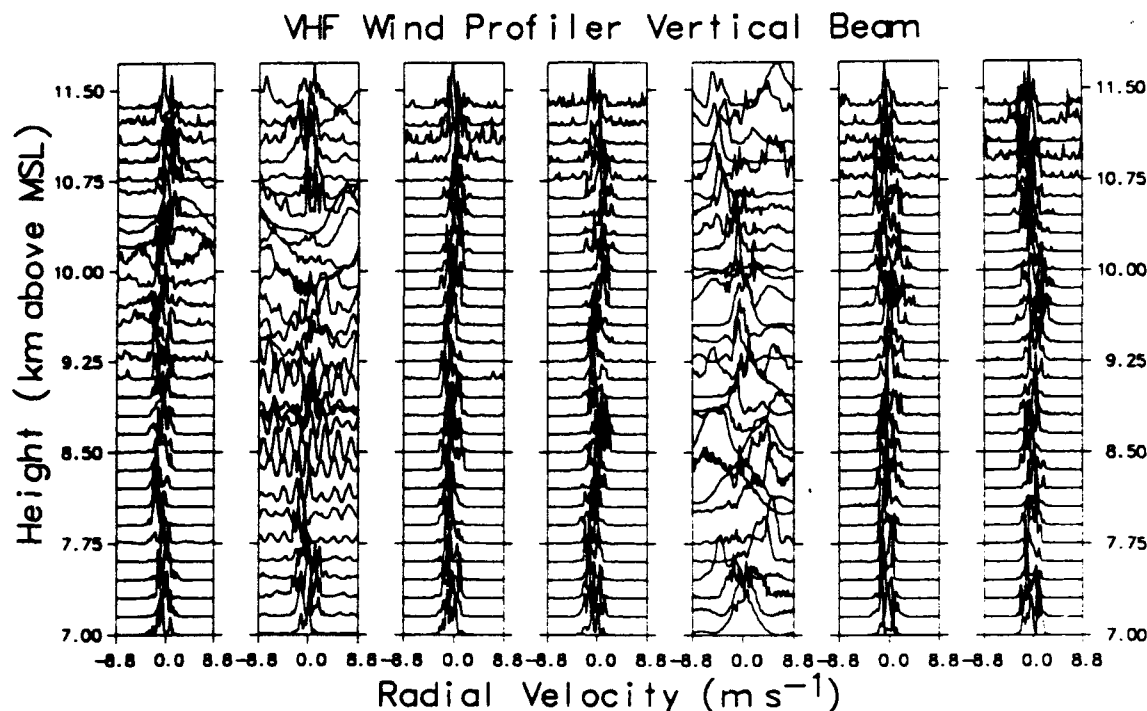


FIG. 4. Seven consecutive profiles of Doppler power spectra for gates 31–60 from the VHF profiler operating at vertical incidence beginning at 0300 UTC 11 June 1985. The spectra have not been incoherently averaged.

Rutledge and MacGorman (1988) show lightning to be present near the profiler throughout the stratiform cloud period. The anomalous echoes, however, will only be observed by the profiler if lightning is present in the main beam or in one of the sidelobes.

Radial velocities estimated from the anomalous spectra will distort the horizontal wind estimates if they are included in the averages. Since the anomalous spectra are characterized by highly variable, and often large, Doppler velocities, one option is to eliminate the radial-velocity outliers. If, however, the spectra are incoherently averaged before first-moment estimation of V_r , too many good data will be contaminated and lost as indicated, for example, by the case shown in Figs. 3c and 4. One solution is to exclude those spectra with excessive spectral widths from the incoherent averages. The criterion was implemented by determining the width of each unintegrated spectrum, after noise subtraction. Only the spectra with widths less than the empirically determined value of 2.00 m s^{-1} were incoherently averaged over a period spanning 6.92 min. Each average included up to ten spectra, less if some of the spectra had excessive widths. We found that the impact of the elimination criterion was minimal, except for the period after 0230 UTC 11 June.

The reflectivities observed in the vertical beam were calculated by subtracting the noise from each 6.92-min-average spectrum and calculating the sum of the power over all Doppler frequencies. The results are

shown in Fig. 5. The profiler was not calibrated, and hence the reflectivity values are given in arbitrary units. The decrease in atmospheric density with altitude causes signal strengths to decrease with height by approximately 2 dB km^{-1} in clear-air conditions. Therefore, the reflectivity contours generally show enhancements at the lower altitudes. The enhanced reflectivities up to 12 or 13 km in altitude before 2200 UTC 10 June are due to an MCS that was dissipating and leaving the area during the early part of the observation period. The enhancements above 6 km after 0100 UTC show a portion of the leading edge of the squall line. There is also a narrow band of higher reflectivities near 14 km due to enhanced aspect-sensitive backscatter characteristic of the heights just below the tropopause (e.g., see Larsen and Röttger 1985). After 0230 UTC 11 June, the specular echoes in the stratiform cloud region in the vicinity of the tropopause are more clearly evident at heights between 15 and 14 km, with the altitude descending approximately 1 km from 0231 to 0630 UTC. Several enhanced reflectivity layers are evident above the tropopause after 2050 UTC. Reflectivity tapered off quickly in the height range from 7 to 13 km between 0230 and 0300 UTC, indicative of the transition from the convective line of the storm to the stratiform cloud region. The spectral-width rejection criterion failed to remove some anomalously strong echoes at heights above 9 km around 0300 UTC and again above 12 km around 0400 UTC, as shown by

June 10–11, 1985

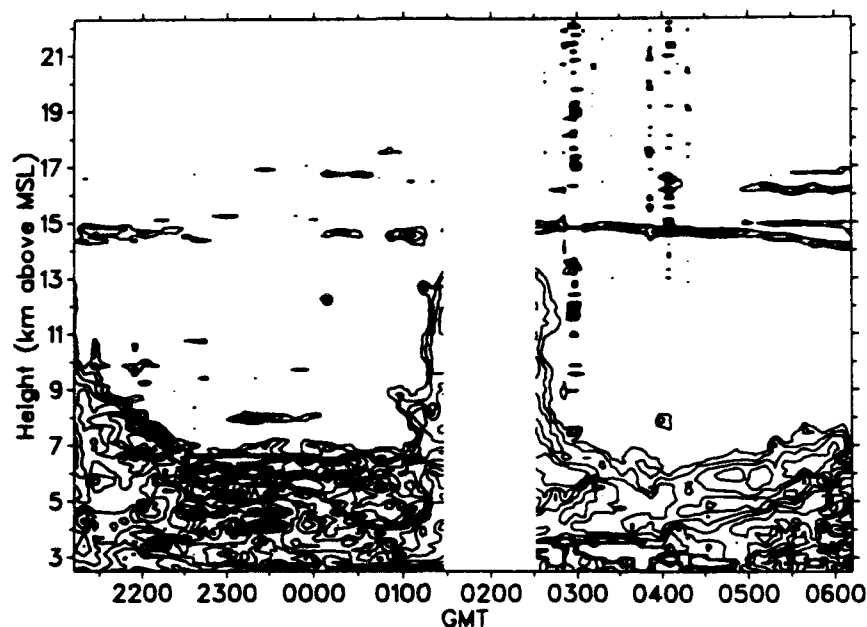


FIG. 5. Reflectivity measured in the vertical beam of the VHF wind profiler at McPherson, Kansas, for the period beginning several hours before the passage of the 10–11 June 1985 squall line until 0612 UTC 11 June. The contour interval is 10 dB with the lowest contour shown 30 dB below the peak value for the entire period.

the vertical bands that appear in the reflectivity contours at those times. A cutoff width sufficiently narrow to remove all the anomalous spectra would, however, have led to rejection of some good data as well, especially between 3 and 4 km where the spectra are consistently wide and double-peaked for much of the period between 0250 and 0405 UTC. Thus, the width criterion was found to work well below ~ 9 km, but not above that height.

4. Procedures for estimating average winds

For routine wind-profiling applications, 1-h averages are usually sought. Of general concern in designing an averaging scheme is the method to be used for eliminating outliers in the wind measurements and possible biases in the averages introduced by the chosen method. Some outliers are no doubt produced by erroneous measurements. For example, various types of clutter can have an effect, or the assumptions inherent in using Eq. (1) may break down at times. Efforts always have to be made to eliminate such values from the averages. In addition, there is a desire to obtain average winds representative of the spatial scales of interest. Studies of mesoscale systems, for example, may require average winds characteristic of a spatial scale on the order of 100 km. Large winds may occur locally near the radar and could produce a significant change in the average

values, but the averages will not be representative of the larger-scale conditions. The problem of determining representativeness is complex and has not been addressed in any detail in studies of wind-profiler data, to our knowledge. Previous studies (e.g., Strauch et al. 1987) have applied a set of criteria to eliminate the erroneous measurements at the outset. Low signal-to-noise ratios are a typical discriminator. In addition, a scheme such as consensus averaging may be applied to eliminate the outliers, that is, the values that differ significantly from the other values included in the averaging interval. It seems likely that consensus averaging has an impact on both the first and the second problems described above, namely, that some erroneous measurements are eliminated and that the spatial scale for which the measurements are representative is affected. The consensus averaging scheme has been used successfully in clear-air conditions (Strauch et al. 1987), although there is no dynamical basis for the method. In this section, we will describe the methods used to estimate the average horizontal and vertical winds for the VHF-profiler data from the stratiform cloud region.

Two methods were used for estimating the radial velocity V_r from the Doppler spectra. The first was the first-moment method (FMM). Noise levels for the spectra were determined by the objective method of Hildebrand and Sekhon (1974) and the noise sub-

tracted prior to the first-moment calculation. The second method of estimating the horizontal wind profiles, to be referred to as the least-squares method (LSM), was based on a determination of V_r by a least-squares fit of either one or two Gaussians. The spectra below the melting level located around 4 km for the period 0250–0405 UTC 11 June consistently showed double peaks, corresponding to turbulence and precipitation scattering. Examples of the spectra and the double Gaussian fits are shown in Fig. 6 for all three beam directions at 0253 UTC 11 June at a height of 3.4 km. The differences in radial velocity for the turbulence- and precipitation-scattering contributions in the examples is close to the maximum difference of about 6 m s^{-1} that was observed, but the goodness of fit is typical. The precipitation contributions are roughly equal in magnitude to the turbulent signals in these examples. The presence of the precipitation peak will bias the simple first-moment estimates of V_r toward negative values for all the beam directions. The motivation for performing the least-squares fitting was to estimate V_r solely from the turbulent-scatter contribution.

The turbulent-scatter peak will be Gaussian in shape if the turbulence is a normal random process (e.g., see Woodman and Guillen 1974). Therefore, a Gaussian was fitted in the least-squares sense to each spectrum that was normalized by the value of its peak component after noise subtraction. When the residual exceeded an empirically determined critical value, a second Gaussian was incorporated in the fit if two distinct peaks could be identified in the spectrum. The algorithm used for the least-squares fitting was adapted from Bevington's (1969) method. Fitting a Gaussian to the secondary peak is not strictly correct since the actual shape

of the curve depends on the size distribution and the terminal velocities of the precipitation particles. Our primary interest, however, was to produce a good fit to the turbulent-scatter signal. Introducing a second Gaussian in the fitting procedure is sufficient for that purpose as long as no unwarranted significance is attached to the fitted values for the precipitation peaks. If neither fit provided a suitably close approximation to the spectrum, the data point was flagged so that a velocity value for that particular gate and time were linearly interpolated from neighboring values. The total number of gates flagged for heights below 10 km amounted to less than 10% of the total data, including the anomalous spectra.

Double-peaked spectra were not as prevalent above the melting level because the reflectivity of snow is smaller than the reflectivity of liquid precipitation. Furthermore, the fall velocity of snow particles is small so that the separation between the turbulent and precipitation scatter peaks in the spectra will be small.

Average horizontal wind profiles were produced by one of two methods. In the first averaging method, the raw mean values of V_r derived either by the FMM or LSM were calculated for each beam direction and range gate for the averaging period. Individual values of V_r differing by more than two standard deviations from the raw mean were assumed to be outliers and excluded from the corrected mean used to calculate the wind components. In the second method, a consensus-averaging procedure was employed for the fitted radial velocities. For each gate and antenna orientation, 48 values of V_r spanning 33.2 min were grouped together. Previous studies (Augustine and Zipser 1987; Rutledge et al. 1988) of the 10–11 June 1985 MCS have shown

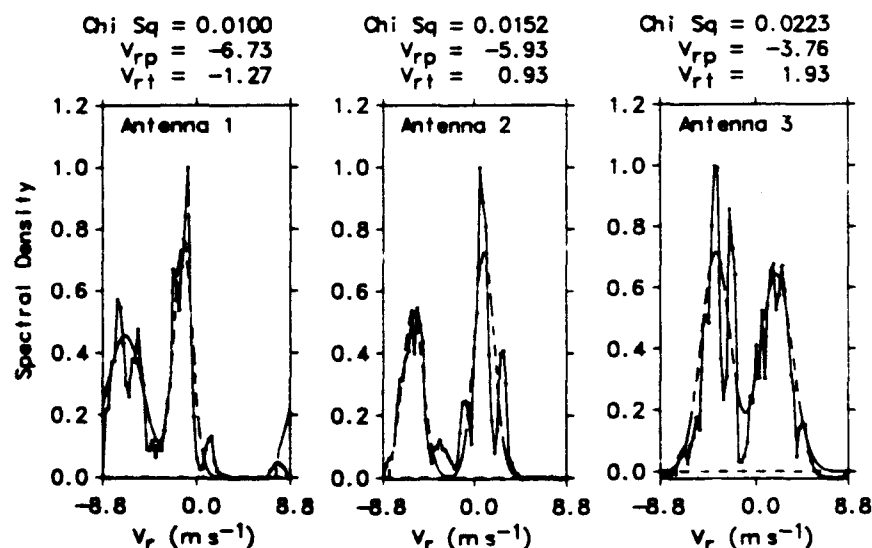


FIG. 6. Observed Doppler power spectra for all three beam directions at 0253 UTC for 3.4 km with double-Gaussian approximations superposed on them. For each spectrum the objectively determined noise level serves as the zero level indicated by the horizontal dashed line, and each spectrum has been normalized by its largest peak after noise subtraction.

that the system's evolution and advection were sufficiently rapid that an appropriate maximum averaging period should be of the order of approximately one-half hour or less. The sampling periods used in the observations made it convenient to use an averaging interval of 33 min. The consensus-average radial velocity is defined as the mean of the largest group of V_r values among the 48 that lie within a given tolerance of one another. Typically, a tolerance of one-sixteenth of the range of Doppler velocities, that is, the range from $-2V_{Ny}$ to $+2V_{Ny}$, where V_{Ny} is the Nyquist velocity, is prescribed. For these data, the corresponding tolerance is 1.1 m s^{-1} . In addition we have calculated consensus averages using a tolerance increased by 50%. The minimum number of values required to provide a consensus average was set to be 16 for the oblique

beams and 24 for the vertical beam. We will refer to the values produced by the two averaging methods as the corrected means and the consensus averages, respectively.

5. Evaluation of horizontal winds

The effect of the outliers associated with the anomalous spectra already described in section 3 on the deduced horizontal winds are illustrated in Fig. 7. Horizontal wind vectors derived from the first moments of Doppler spectra incoherently averaged for 4.84 min, that is, seven consecutive spectra, with no attempt made to exclude the effects of the anomalous spectra are shown in Fig. 7a, which covers a period of approximately 1 h. Many of the vectors indicate unreasonably

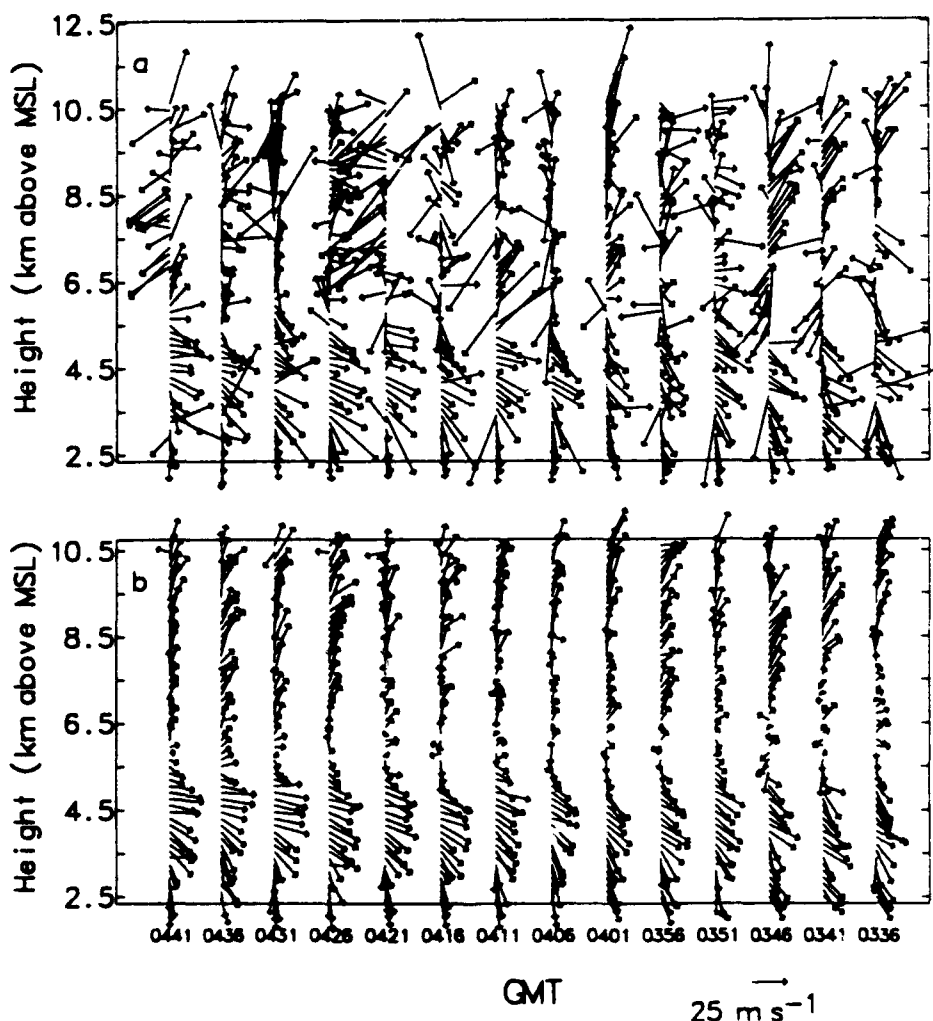


FIG. 7. Profiles of horizontal winds derived from (a) first-moment estimates of the radial velocities calculated from spectra incoherently averaged for 4.84 min, and from (b) the average first-moment estimates of the radial velocities estimated from the unintegrated spectra over the same period, with outliers excluded from the radial-velocity averages. The orientation of the wind vectors is as if plotted on a horizontal map; for example, the scale vector at the bottom of the figure represents a westerly wind.

large speeds and sudden changes in direction in contrast with the steady, well-defined mesoscale flow documented for the system in previous studies (Augustine and Zipser 1987; Rutledge et al. 1988). The winds shown in Fig. 7b were derived by applying the FMM to the unintegrated spectra and the corrected mean calculation for the same periods. Even with the reduced number of values used in each first-moment average, the improvement is immediately apparent, with the excessively large speeds and shifts of direction eliminated. Above ~ 10.5 km the signal-to-noise ratio (SNR) along all beam directions fell below -3 dB, too low to produce reliable wind profiles.

The system-relative horizontal flow derived from 4.84-min averages of the radial velocities determined using the LSM of analyzing the VHF profiler data for the stratiform cloud period is shown in Fig. 8a. The system-relative flow is the component of the horizontal wind from 300° to 120° in azimuth, with the mean speed of 14 m s^{-1} of the convective line toward 120° subtracted. A downward-sloping rear-inflow jet is evident at midlevels with the altitude of the peak inflow increasing from 4.0 to 5.5 km MSL over a 2-h period. In addition, a strong front-to-rear outflow is seen aloft. Earlier studies have shown that the motion of the system was fairly steady over the observation interval being considered. Therefore, the time-height section may be interpreted as a spatial cross section, allowing comparison of the horizontal winds from the profiler with those obtained by the scanning 5-cm Doppler radars. The features noted in Fig. 8a are in general agreement with the range-height indicator (RHI) cross sections from the scanning CP-3 and CP-4 radars at 0414 UTC shown in Figs. 8b and 8c (from Rutledge et al. 1988). The velocity magnitudes are similar in all three sets of observations with peak values of the rear-inflow speed of $10\text{--}15 \text{ m s}^{-1}$. The transition from smoothly varying, generally front-to-rear flow above 6.5 km to the highly variable values above 10.5 km is due to the decrease in SNR. Thus, the apparent velocities in the upper ranges of Fig. 8a are unreliable. If the mean propagation speed of the system is assumed to be constant over the 3.5-h period represented by the profiler data, the corresponding spatial extent would be about 180 km. The portions of the RHI that correspond to the height-time section, if the simple advection transformation holds, are enclosed within the heavy vertical dashed lines in the lower frames. The McPherson profiler's coverage does not extend as far to the rear of the system as the CP-3 or CP-4 coverage. Thus, the rear-inflow jet seen by the profiler does not extend to as high an altitude as shown in the RHI plots. Although the agreement between the two datasets is encouraging, such a comparison should still be viewed with caution. The VHF radar provided vertical profiles at a single location over a period of almost 4 h, during which evolution as well as advection of the mesoscale system was taking place, as indicated by composite radar-data

displays similar to that shown in Fig. 2, but not presented here. In contrast, the data for each of the 5-cm radars was obtained from a single series of conical scans made over 8 min near the temporal midpoint of the profiler observations. A corresponding time-height section of system-relative, 4.84-min-average horizontal motion derived by the FMM showed good agreement with the features in Fig. 8a at all heights and, therefore, is not shown. The largest differences occurred below 4 km between 0230 and 0400 UTC when the FMM winds were generally larger in magnitude than the LSM winds. The FMM values had peak values in excess of 20 m s^{-1} , while the LSM peak values were only slightly in excess of 10 m s^{-1} . The double peaked spectra are more prevalent during the period and in the height range where the largest discrepancies occurred. Of course, the simple first-moment estimates include no attempt to distinguish between the precipitation- and turbulent-scatter peaks, and the radial velocities will be biased toward values between the two peaks.

Figure 9 shows a comparison of a 30-min corrected mean profile of the system-relative horizontal flow derived from the VHF profiler data for 0335 GMT using the LSM, and that measured with CP-3 and CP-4 at 0334 and 0345 UTC, respectively. The extended velocity-azimuth display (EVAD) analysis method (Srivastava et al. 1986; Rutledge et al. 1988) was used to obtain the CP-3 and CP-4 profiles. There is good agreement between all three curves, but particularly between the profiler and CP-3, as may be expected since the profiler was closer to CP-3 in storm-relative coordinates. The line connecting the VHF radar site and the CP-3 site was roughly parallel to the long axis of the system, and both were farther behind the convective line than CP-4 at the time of the comparison. The inflow jet has been shown to slope downward from rear to front in the system, and thus, the peak rear inflow is found at a greater height in the profiler and CP-3 data than in the CP-4 data.

Figure 10a shows the time series of horizontal wind profiles produced by 33.2-min corrected means of the LSM radial velocities. The values agree well with those in Fig. 8a, corresponding to comparable values of relative horizontal flow. The horizontal winds produced by consensus averages of the LSM radial velocities using the standard consensus tolerance of one-sixteenth of the Doppler velocity window are shown in Fig. 10b. The two methods produced comparable results, although somewhat less data survives the consensus-averaging procedure. The result of increasing the window of tolerance for the consensus averaging to three-thirty-seconds of the range of Doppler velocities may be seen in Fig. 10c. Given the relaxed consensus criterion, a consensus value was found for almost every gate and beam orientation, apparently without admitting an excessive number of outliers to the averages. There are, however, still more missing values in the consensus estimates than in the corrected means estimates. As

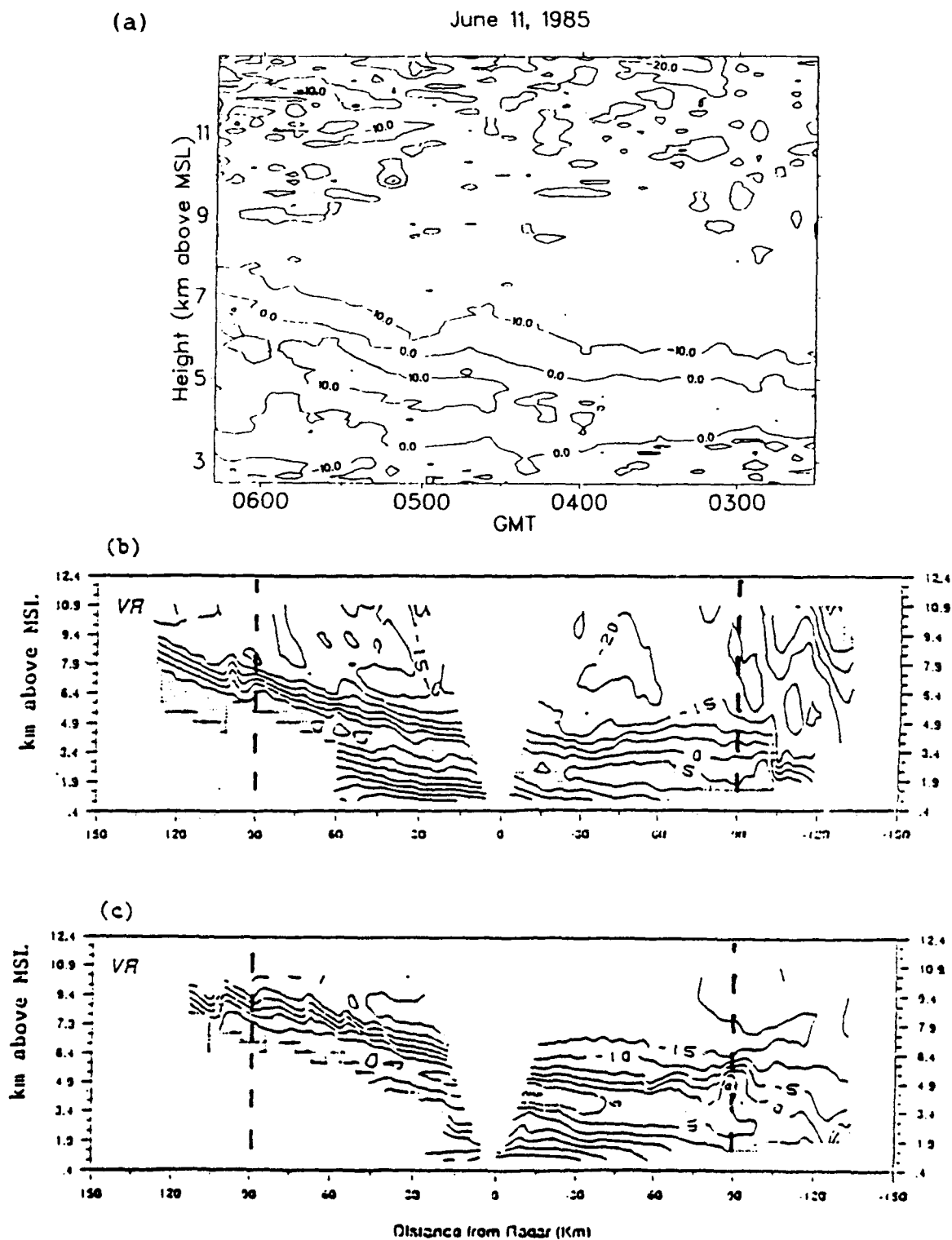


FIG. 8. (a) Height-time section of system-relative horizontal flow (m s^{-1}) derived from the fitted spectra data averaged for 4.84 min; height versus horizontal distance cross section of system-relative horizontal flow measured by (b) CP-4 and (c) CP-3 at 0414 UTC 11 June. Parts (b) and (c) are from Rutledge et al. (1988), with VR referring to system-relative flow. Positive values indicate flow from left to right, along 300° - 120° radial.

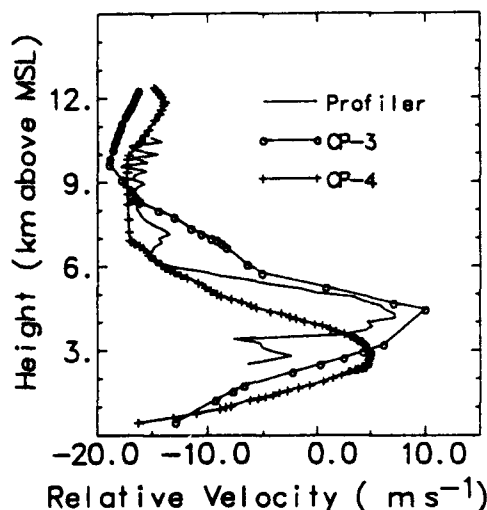


FIG. 9. Vertical profiles of system-relative horizontal velocity from CP-3 data at 0334 UTC, CP-4 data at 0345 UTC, and the VHF profiler data at 0335 UTC. Sign convention is the same as in Fig. 8. CP-3 and CP-4 values were obtained using EVAD analysis and are adapted from Rutledge et al. (1988). Data for the VHF profiler are 30-min averages of radial velocities derived from the fitted spectra.

the consensus criterion is relaxed more, the two methods will eventually give the same results. The fact that a given method leads to more missing values is not a reason per se to judge one of the methods to be inferior. If the values that are eliminated are the ones that correspond to erratic wind directions or magnitudes, then the procedure is working as intended. In the cases shown here, however, the consensus criterion actually introduces wind values that look suspect as compared to the smoothly varying corrected means.

The results indicate that a VHF radar wind profiler can provide representative horizontal wind profiles in conditions such as those associated with the 10–11 June 1985 MCS. The choice of least-squares fitting or first-moment estimation of the radial velocities had little impact above the freezing level, although the first-moment method created a bias below the freezing level during periods of heavy rainfall.

The goal of applying a consensus-averaging procedure is to produce representative hourly or half-hourly winds by eliminating radial outliers through the requirement that the average be formed only from values that differ from one another by less than the prescribed tolerance. In stable conditions in particular, this method of eliminating outliers will likely produce a good estimate of the winds since the number of values that fail the test will be small in most cases. May and Strauch (1989) compared the standard deviations of Doppler velocities derived from the consensus-averaging procedure with those obtained by selecting the median value of the first moment for sets of computer-generated, simulated spectra covering a broad range of SNR. Figure 5 of their article shows that the former

method yields only slightly smaller deviations for SNR in excess of -3 dB, with both methods producing deviations of the order of 0.05 m s^{-1} . For lower SNR, the deviations increase dramatically whichever method is used, although the consensus-average values remain slightly better due to the provision for removal of outliers. Thus, in stable clear-air conditions, when steady winds are expected and variations in the reflectivity are small, consensus averaging is expected to give good results. Wuertz et al. (1988) have already shown some

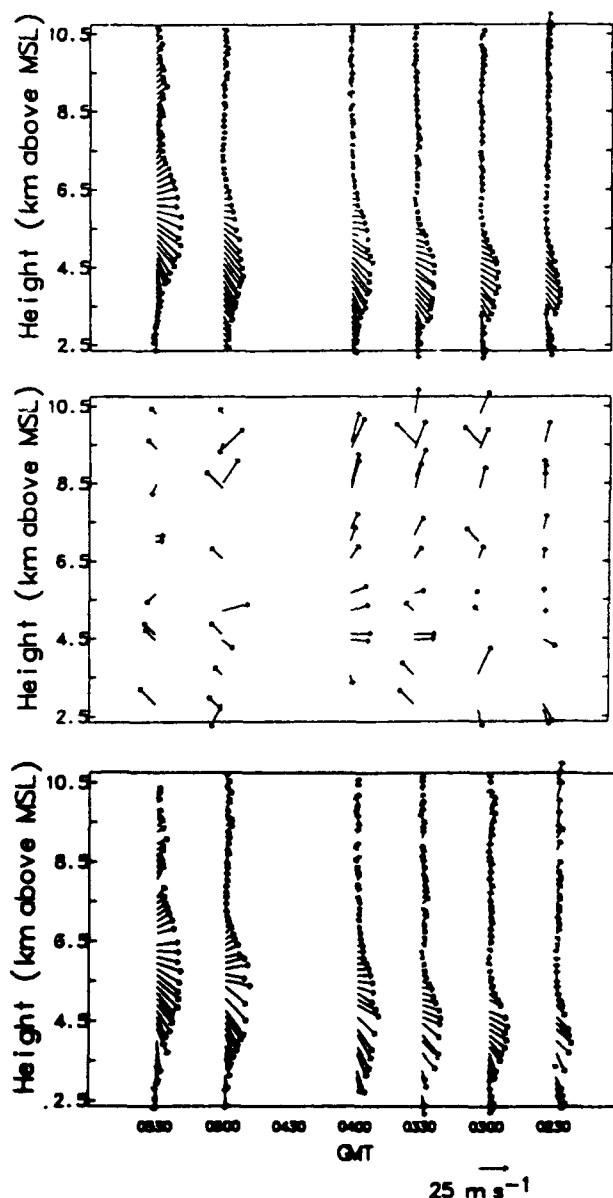


FIG. 10. Vertical profiles of the horizontal wind vectors derived from (a) 30-min corrected averages of the fitted VHF Doppler spectra, from (b) the consensus-averaged radial velocities of the fitted spectra, and from (c) the relaxed consensus-averaged radial velocities, on 11 June 1985.

of the problems encountered in applying the consensus-averaging procedure to profiler observations affected by precipitation. Their study carefully evaluated estimates of the statistical errors based on the requirement of internal consistency in the data. The results indicated that the standard approaches work well as long as the precipitation, as well as the wind field, is horizontally and temporally uniform. The continuity and consistency of our results indicate that these conditions were satisfied for the stratiform precipitation portion of the case study, despite the variability in the velocity-time series. Power spectra of the velocity time series showed enhancements in the high-frequency fluctuations with periods less than an hour ahead of the squall line in the upper troposphere and behind the squall line at all heights below the tropopause sampled by the VHF profiler (Yoe 1990).

Our conclusion must of necessity be somewhat qualitative due to the limited data that are available and the lack of an internal consistency check with the three-beam profiler data. A comparison of the profiles in Figs. 10a-c indicates, however, that methods using the corrected mean of the high-time-resolution radial-velocity data, coupled with outlier removal either by the two standard-deviation criterion or by consensus averaging provides a reliable representation of the kinematics of this system. Computing averages from the first moments of incoherently averaged spectra was also effective, provided that the anomalous spectra discussed earlier were excluded from the incoherent averages, lest good data be contaminated. We have only presented results for a few combinations of radial-velocity estimation schemes and averaging schemes, although many of the various possibilities were examined in the course of the study. The results for combinations other than those that we have presented can be extrapolated from the results that have been presented.

One point that did not emerge clearly from the earlier discussion of the VHF profiler dataset by Augustine and Zipser (1987) is that the winds shown in their time-height sections were not produced by the consensus-averaging procedure. Instead, first-moment estimates of V_r from spectra that had been incoherently integrated for 30 min were used. Individual spectra were excluded from the half-hour incoherent averages if the total power in a spectrum for a given gate was found to be too much in excess of the values found in previous profiles. Since the anomalous spectra that we have described earlier were characterized by large signal power, the latter criterion eliminated most of those spectra. The individual spectra were also eliminated from the averages if the signal-to-noise ratio fell below unity, that is, 0 dB. The noise power was estimated from the average power in the top three range gates where there was no indication of signal at any time during the observations. Comparisons between horizontal wind profiles from Fig. 4 of Augustine and Zipser (1987) with the LSM values with corrected means, the

5-cm radar data, and the available radiosonde wind profiles indicate that the 30-min incoherent averaging tended to produce comparable directions but larger velocities than the other methods. The magnitudes for the rear-inflow jet indicated in Fig. 4 of Augustine and Zipser (1987) are 5 m s^{-1} greater, although the shapes of the profiles are in agreement with those produced by the other analysis methods. The long incoherent averages applied to the spectra in the Augustine and Zipser (1987) study effectively weigh the contributions of the individual spectra by the signal power. Thus, the final averaged spectrum for a given height will be biased toward the Doppler shift for any subinterval characterized by larger reflectivities. The weighting introduced in the spectral averages produced a bias toward larger horizontal velocities.

6. Vertical velocity comparisons

A height-time section of vertical air motion measured by the profiler during the interval 0230-0330 UTC 11 June is shown in Fig. 11a, and the measurements obtained by the CP-4 radar operated at vertical incidence during the same period are shown in Fig. 11b. Only the values from above the melting level are shown. The signals detected by CP-4 radar data will be dominated by precipitation scatter. Therefore, the two sets of values are not expected to be in perfect agreement. A strong updraft is evident during the period from 0233 to 0243 UTC, but there is only a slight indication of a similar feature in the profiler vertical velocity data. The vertical velocities are, however, predominantly positive above 10 km in both datasets. The magnitudes are comparable in both measurements after 0243 UTC, but stronger in the CP-4 data between 0233 and 0243 UTC. The strong updrafts may have been highly localized in this case so that they were only evident at the CP-4 site that was located farther east and south, that is, closer to the convective line.

Figure 12 shows a comparison of vertical velocity profiles measured with the profiler at McPherson at 0335 UTC and with the CP-3 and CP-4 radars at 0334 and 0345 UTC, respectively. The profiler data are 30-min averages derived from the fitted spectra in the vertical beam. The 5-cm-radar data were derived by integration of the horizontal divergence determined from the EVAD procedure. There is generally good agreement between the magnitudes of the vertical velocities measured by all three instruments in the height range from approximately 5 to 10 km, especially when the basic differences in the type of sampling carried out by the different instruments and spatial and temporal fluctuations in the flow are considered. The profiler, however, shows downward velocities between 6 and 8 km, while CP-3 and CP-4 show updrafts. All three profiles indicate downdrafts between 3 and 5 km, although the profiler shows a much larger magnitude. Some of the discrepancies at the lower heights may be due to

June 11, 1985

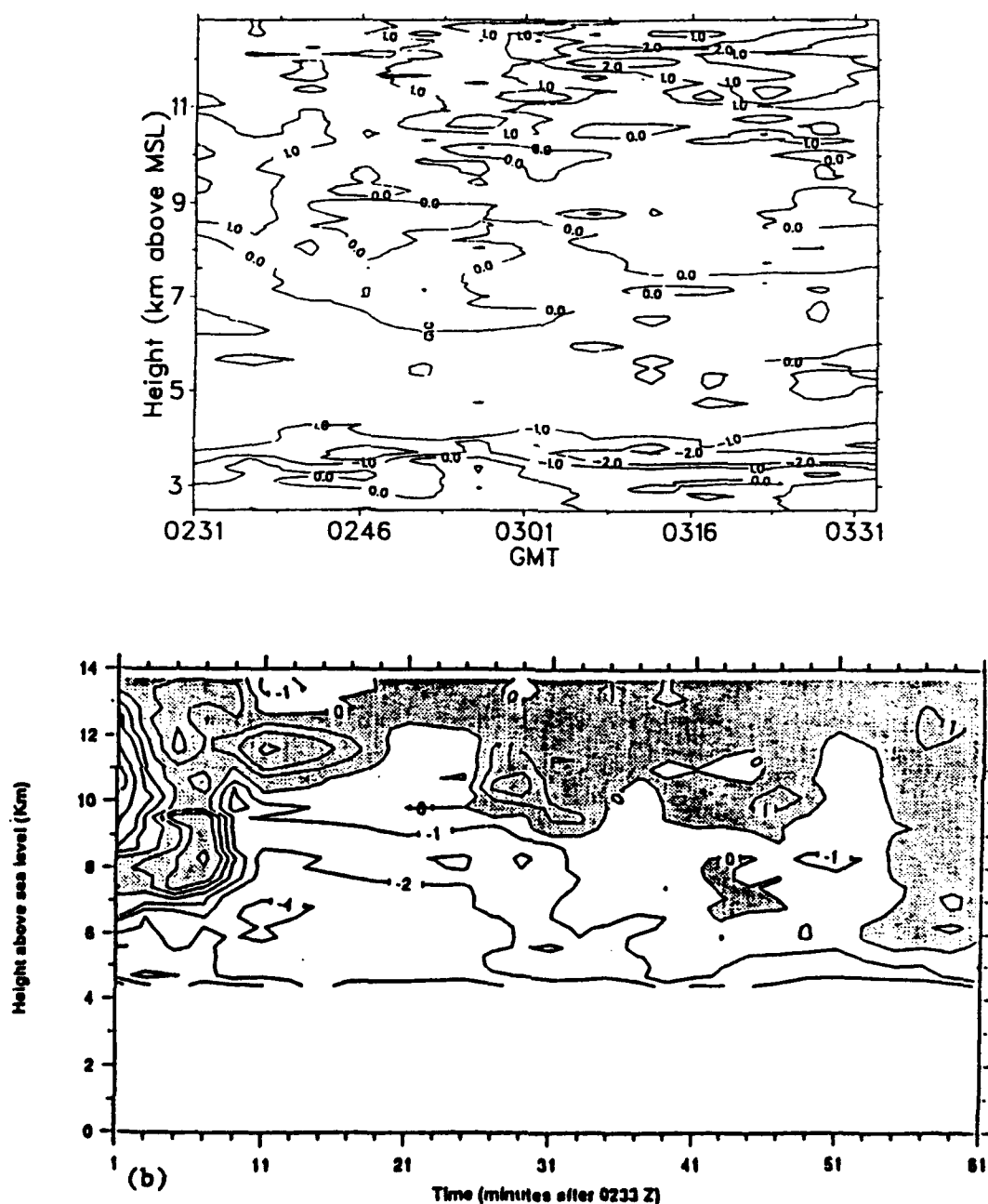


FIG. 11. Vertical velocity (m s^{-1}) for 1 h in the stratiform cloud region of the squall line derived from (a) fitted spectra from the VHF profiler and (b) from CP-4 data when operated at vertical incidence (S. A. Rutledge 1988, private communication). Positive values indicate upward motion.

effects associated with the melting level. In particular, some of the spectra had triple peaks that could not be interpreted easily and that were not fitted well. Furthermore, the lowest five or six gates also suffered from receiver recovery problems that appear to be responsible for the apparent reversal in velocities below 4 km.

Validating the profiler vertical velocity measure-

ments has been a problem because of the lack of standards for comparison. Some studies, such as those by Nastrom et al. (1985) and Larsen et al. (1988), have compared VHF radar vertical velocities to vertical velocities calculated from radiosonde data over a grid. There are, however, many sources of error in such a procedure, and the scales characteristic of the two sets

of values are inherently different. The direct comparison of the two different types of radar measurements suffers less from such problems.

For a dataset such as the one in question, obtaining reliable vertical velocities is critically important for making satisfactory horizontal wind estimates. For example, steady downward velocities observed in the two off-vertical beams of a two-beam radar will produce an apparent horizontal velocity component toward the radar along the direction of the bisector between the two beam directions. In the present case, the oblique beams were pointed toward southeast and southwest, leading to an apparent southerly component, that is, toward north, if no vertical velocity corrections were made. The effect is quantified in Fig. 13, in which the counterclockwise rotation of the apparent wind vector from a true bearing along the 300° – 120° radial is plotted as a function of vertical velocity for a range of system-relative horizontal flow velocities. For all values of system-relative velocity, downdrafts of 0.5 m s^{-1} or more lead to 15° counterclockwise rotation or more of the wind vector. As we have shown in this section, mesoscale downdrafts coexisted with the rear-inflow jet in the stratiform cloud region of the 10–11 June system.

7. Conclusions

It has been demonstrated that the VHF radar wind profiler is capable of providing half-hour-average wind profiles during the passage of a mesoscale system such as the stratiform cloud region associated with the 10–

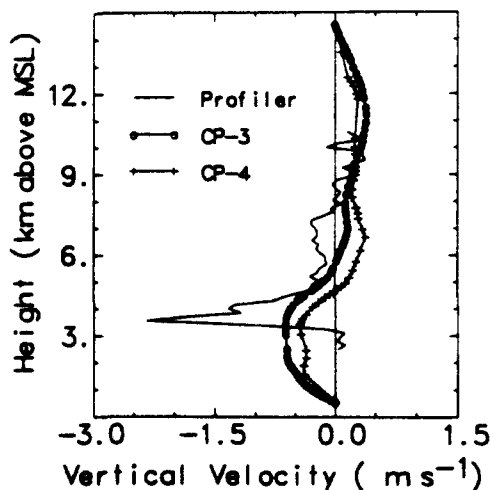


FIG. 12. Single profiles of vertical velocity for CP-3, CP-4, and the VHF wind profiler. Sign convention is the same as in Fig. 14. CP-3 and CP-4 data from EVAD analysis (Rutledge et al. 1988). Profiler data are 30-min averages of fitted spectra obtained at vertical incidence.

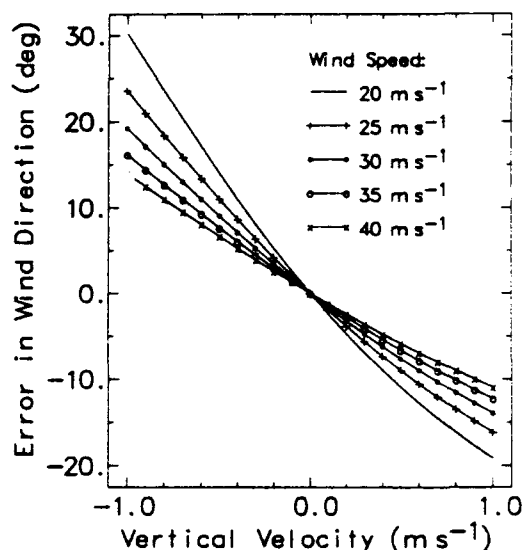


FIG. 13. Expected counterclockwise rotation of wind vector from assumed direction of 300° as a function of (ignored) vertical velocity for a series of horizontal wind velocities. The assumed direction is that of the rear inflow of the system; the range of horizontal velocities includes that observed in the rear-inflow jet of the 10–11 June 1985 MCS.

11 June 1985 PRE-STORM squall line. The measured winds show good continuity temporally and with height. A critical factor in obtaining the averaged profiles was the elimination of the anomalous spectra presumably associated with lightning effects. Also, a simple averaging and consensus averaging with relaxed criteria both gave acceptable results for the high-time-resolution radial-velocity data, but methods in which the Doppler spectra were first incoherently averaged for a short time, followed by a longer temporal average of the radial velocities derived from the spectra, required prescreening to avoid contamination from the anomalous echoes.

In general, the more elaborate Gaussian, least-squares fitting procedure did not produce results that were markedly different from a simpler first-moment estimate, except at certain times when double-peaked spectra are present below the freezing level.

Finally, the overall agreement between the magnitudes and general shapes of the VHF radar vertical velocity profiles and the 5-cm-radar vertical velocity profiles is encouraging, although an understanding of the source of large discrepancies at and below the melting level will require further study.

Acknowledgments. MFL and JGY were supported by the Air Force Office of Scientific Research under Contract F49620-88-C-0121 during the course of this study. We thank the staff at Radian Corporation and Dr. John Augustine of NOAA for their invaluable help in providing the McPherson profiler data tapes. The

comments of the anonymous reviewers served to improve the paper.

REFERENCES

- Augustine, J. A., and E. J. Zipser, 1987: The use of wind profilers in a mesoscale experiment. *Bull. Amer. Meteor. Soc.*, **68**, 4-17.
- Bevington, P. R., 1969: *Data Reduction and Error Analysis for the Physical Sciences*. McGraw-Hill, 204-215.
- Cunning, J. B., 1986: The Oklahoma-Kansas Preliminary Regional Experiment for STORM-Central. *Bull. Amer. Meteor. Soc.*, **67**, 1478-1486.
- Curnier, P. E., and S. K. Avery, 1989: Use of two wind profilers for precipitation studies. *Handbook for MAP*, Vol. 28, 182-184.
- Czechowsky, P., G. Schmidt, and R. Rüster, 1984: The mobile SOUSY Doppler radar: Technical design and first results. *Radio Sci.*, **19**, 441-450.
- Fischler, M. A., and R. C. Bolles, 1981: Random sample consensus: a paradigm for model fitting with applications to image analysis and automated cartography. *Graphics and Image Processing*, **24**, 381-394.
- Fukao, S., K. Wakasugi, T. Sato, S. Morimoto, T. Tsuda, I. Hirota, I. Kimura, and S. Kato, 1985: Direct measurement of air and precipitation particle motion by very high frequency Doppler radar. *Nature*, **316**, 712-714.
- Gossard, E. E., 1988: Measuring drop-size distributions in clouds with a clear-air-sensing Doppler radar. *J. Atmos. Oceanic Technol.*, **5**, 640-649.
- Hildebrand, P. H., and R. S. Sekhon, 1974: Objective determination of the noise level in Doppler spectra. *J. Appl. Meteor.*, **13**, 808-811.
- Johnson, R. H., and P. J. Hamilton, 1988: The relationship of surface pressure features to the precipitation and air flow structure of an intense midlatitude squall line. *Mon. Wea. Rev.*, **116**, 1444-1474.
- Larsen, M. F., and J. Röttger, 1985: Observations of frontal zone and tropopause structures with a VHF Doppler radar and radiosondes. *Radio Sci.*, **20**, 1223-1232.
- , 1987: Observations of thunderstorm reflectivities and Doppler velocities measured at VHF and UHF. *J. Atmos. Oceanic Technol.*, **4**, 151-159.
- , and T. S. Dennis, 1988: A comparison of operational analysis and VHF wind profiler vertical velocities. *Mon. Wea. Rev.*, **116**, 48-59.
- May, P. T., and R. G. Strauch, 1989: An examination of wind profiler signal processing algorithms. *J. Atmos. Oceanic Technol.*, **6**, 731-735.
- Nastrom, G. D., W. L. Ecklund, and K. S. Gage, 1985: Direct measurement of large-scale vertical velocities using clear-air Doppler radars. *Mon. Wea. Rev.*, **113**, 708-718.
- Röttger, J., and M. F. Larsen, 1990: UHF/VHF radar techniques for atmospheric research and wind profiler applications. *Radar in Meteorology*, D. A. Atlas, Ed., Amer. Meteor. Soc., 235-281.
- Rutledge, S. A., and D. R. MacGorman, 1988: Cloud-to-ground lightning activity in the 10-11 June 1985 mesoscale convective system observed during the Oklahoma-Kansas PRE-STORM project. *Mon. Wea. Rev.*, **116**, 1393-1408.
- , R. A. Houze, M. I. Biggerstaff, and T. J. Matejka, 1988: The Oklahoma-Kansas mesoscale convective system of 10-11 June 1985: Precipitation structure and single-Doppler radar analysis. *Mon. Wea. Rev.*, **116**, 1409-1430.
- Sato, T., H. Doji, H. Iwai, I. Kimura, S. Fukao, M. Yamamoto, T. Tsuda, and S. Kato, 1990: Computer processing for deriving drop-size distributions and vertical air velocities from VHF Doppler radar spectra. *Radio Sci.*, **25**, 961-973.
- Srivastava, R. C., T. J. Matejka, and T. J. Lorello, 1986: Doppler radar study of the trailing anvil region associated with a squall line. *J. Atmos. Sci.*, **43**, 356-377.
- Strauch, R. G., B. L. Weber, A. S. Frisch, C. G. Little, D. A. Merritt, K. P. Moran, and D. C. Welsh, 1987: The precision and relative accuracy of profiler wind measurements. *J. Atmos. Oceanic Technol.*, **4**, 563-571.
- Wakasugi, K., A. Mizutani, M. Matsuo, S. Fukao, and S. Kato, 1986: A direct method for deriving drop-size distribution and vertical air velocities from VHF Doppler radar spectra. *J. Atmos. Oceanic Technol.*, **3**, 623-629.
- , ———, ———, and ———, 1987: Further discussion on deriving drop-size distribution and vertical air velocities directly from VHF Doppler radar spectra. *J. Atmos. Oceanic Technol.*, **4**, 170-179.
- Woodman, R. F., and A. Guillen, 1974: Radar observations of winds and turbulence in the stratosphere and mesosphere. *J. Atmos. Sci.*, **31**, 493-505.
- Wuertz, D. B., B. L. Weber, R. G. Strauch, A. S. Frisch, C. G. Little, D. A. Merritt, K. P. Moran, and D. C. Welsh, 1988: Effects of precipitation on UHF wind profiler measurements. *J. Atmos. Oceanic Technol.*, **5**, 450-465.
- Yoe, J. G., 1990: Analysis and comparison of several methods for processing VHF Doppler radar wind profiler data obtained during a mesoscale convective storm. Ph.D. thesis, Clemson University, 132 pp.

DECEMBER 1992	YOE ET AL.	000
DECEMBER 1992	YOE ET AL.	000
DECEMBER 1992	YOE ET AL.	000
DECEMBER 1992	YOE ET AL.	000
DECEMBER 1992	YOE ET AL.	000
DECEMBER 1992	YOE ET AL.	000
DECEMBER 1992	YOE ET AL.	000
DECEMBER 1992	YOE ET AL.	000
DECEMBER 1992	YOE ET AL.	000
DECEMBER 1992	YOE ET AL.	000

VHF radar interferometry measurements of vertical velocity and the effect of tilted refractivity surfaces on standard Doppler measurements

Robert D. Palmer,¹ Miguel F. Larsen,² Ronald F. Woodman,³ Shoichiro Fukao, Mamoru Yamamoto, Toshitaka Tsuda, and Susumu Kato

Radio Atmospheric Science Center, Kyoto University, Uji, Kyoto, Japan

(Received April 16, 1990; revised October 19, 1990; accepted December 3, 1990.)

At VHF wavelengths, aspect sensitivity may result in an apparent beam direction that is off vertical even for a nominally vertically pointing beam direction if the refractivity surfaces responsible for the scatter are tilted with respect to the horizontal plane. Middle and upper atmosphere radar measurements obtained by using the system in a standard multireceiver configuration typical for radar interferometry (RI) and spaced antenna measurements have been analyzed for evidence of such effects. The analysis is based on the linear variation of the cross-spectral phase as a function of the radial velocity in the frequency domain for the RI cross spectra. True-vertical velocity estimates are obtained by using the fact that the phase difference between two antennas should be equal to zero when the echoes are being received from the vertical direction. The tilt angles of the refractivity surfaces were obtained from the phase of the cross-correlation function at zero lag, and the radial velocity in that direction was determined from the cross spectra. The results indicate that the vertical velocity derived from standard Doppler analyses is actually the velocity perpendicular to the refractivity surfaces and thus can be biased by the projection of the horizontal wind along the effective pointing direction.

1. INTRODUCTION

Understanding the vertical circulations in the atmosphere is of fundamental importance for a number of problems in the atmospheric sciences, ranging from long-term vertical transport of trace constituents to short-term weather forecasting. There have been few techniques for measuring vertical velocities directly, although the integration of the mass continuity equation and other indirect methods for estimating the velocities become useful for larger temporal and spatial scales. For smaller scale flows characteristic of the mesoscales and microscales, indirect methods are often not tractable either because many approximations are required in the calculations or dense measurement networks are needed. For these reasons, the potential capabilities of the wind profiling radars or mesosphere-stratosphere-troposphere (MST) ra-

dars for measuring vertical velocities over short time scales are of great interest.

In spite of the interest in the measurements, tests to establish the accuracy or potential biases in the measurements have been difficult to design or implement. A few studies have compared vertical velocities derived from standard radiosonde measurements with the vertical velocities measured by the Doppler technique with VHF radars [Nastrom *et al.*, 1985; Larsen *et al.*, 1988]. While some agreement was found, discrepancies were large enough that detailed quantitative comparisons were meaningless.

So far, the wavelengths used for wind profiling or MST radar studies have been primarily around 6 m in the VHF band or around 70 cm in the UHF band. The longer wavelength has the advantage that the turbulent scatter contribution to the signals is almost always dominant, even in precipitation, unless the rainfall rates become very large. The shorter wavelength signals are dominated by precipitation even for relatively light rainfall rates, and vertical velocity measurements by a direct Doppler method with a vertically pointing beam become impossible. Larsen and Röttger [1986] have discussed the relative reflectivities at the two wavelengths in more detail. Typically, vertical velocities are estimated by pointing the beam of a Doppler radar in the

¹ Now at Department of Physics and Astronomy, Clemson University, Clemson, South Carolina.

² On leave from the Department of Physics and Astronomy, Clemson University, Clemson, South Carolina.

³ On leave from the Jicamarca Radio Observatory, Instituto Geofísico del Perú, Lima.

Copyright 1991 by the American Geophysical Union.

Paper number 91RS00006.

0048-6604/91/91RS-00006\$08.00

vertical direction and processing the received signals, caused by fluctuations in the refractive index of the atmosphere, to obtain the Doppler shift. At VHF frequencies the received signals usually show aspect sensitivity effects, i.e., the reflectivity decreases as the beam is tilted off vertical [e.g., *Tsuda et al.*, 1986]. If the refractivity surfaces are tilted away from the horizontal plane, the aspect sensitivity may cause errors in the estimate of the vertical velocity since the largest contribution to the received signals will come from an off-vertical direction. By finding the center of the aspect sensitivity function, tilt angles estimates with VHF radar were made by *Vincent and Röttger* [1980]. *Röttger and Ierkic* [1985] estimated tilt angles using spatial interferometry. More recently, *Larsen and Röttger* [1991] analyzed the layer tilt angle measurements derived from a data set obtained over 4 days with the sounding system (SOUSY) VHF radar. Their results have provided qualitative evidence that biases in the vertical velocity measurements resulted from the tilted refractive structures.

In this paper we apply the radar interferometer technique to test the relationship between the tilted layers and biases in the velocity estimates. Radar interferometry (RI), also known as spatial interferometry (SI), is based on receiving signals in multiple receiving antennas and has been described in detail by *Woodman* [1971], *Farley et al.* [1981], and *Adams et al.* [1989]. In section 2 we describe the experimental procedure, which was previously used for an interferometer application [*Palmer et al.*, 1990]. The derivation of the method is presented in section 3. Section 4 shows a comparison of measurements with the Doppler and RI methods. Conclusions are given in section 5.

2. EXPERIMENTAL PROCEDURE

A radar interferometer experiment was conducted on October 24, 1989, 2100–2400 LT using the MU radar located in Shigaraki, Japan (34.85°N, 136.10°E) [*Palmer et al.*, 1990]. The transmitting and receiving antennas are shown in Figures 1a and 1b, respectively. The transmitting antenna can be seen to use only the middle portion of the radar. This was done so that the beam width of the radar could be increased to approximately 6.8° [*Fukao et al.*, 1988], giving a wider range of zenith angles that one could observe. This was accomplished at a loss of sensitivity, due to the decrease in transmitting

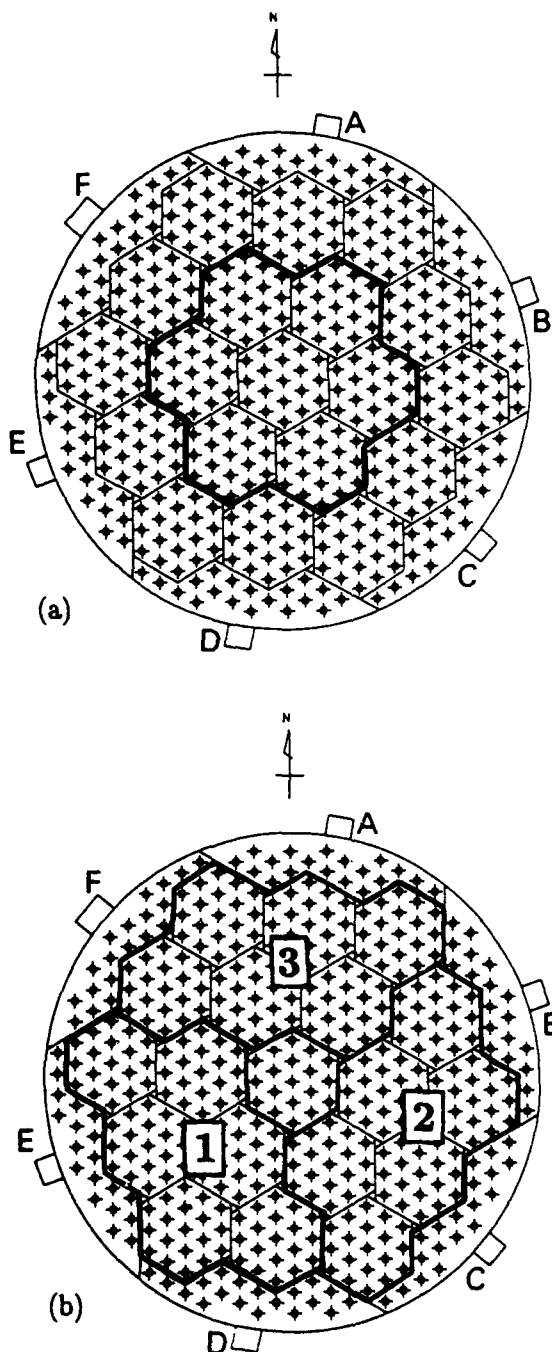


Fig. 1. Antenna configurations used for the interferometer experiment conducted on October 24, 1989, 2100–2400 LT using the MU radar. (a) transmitting antenna, (b) receiving antennas.

power, but was deemed sufficient for tropospheric/stratospheric observations. On reception the antenna was segmented into three equal-area antennas, which are denoted as antennas 1, 2, and 3.

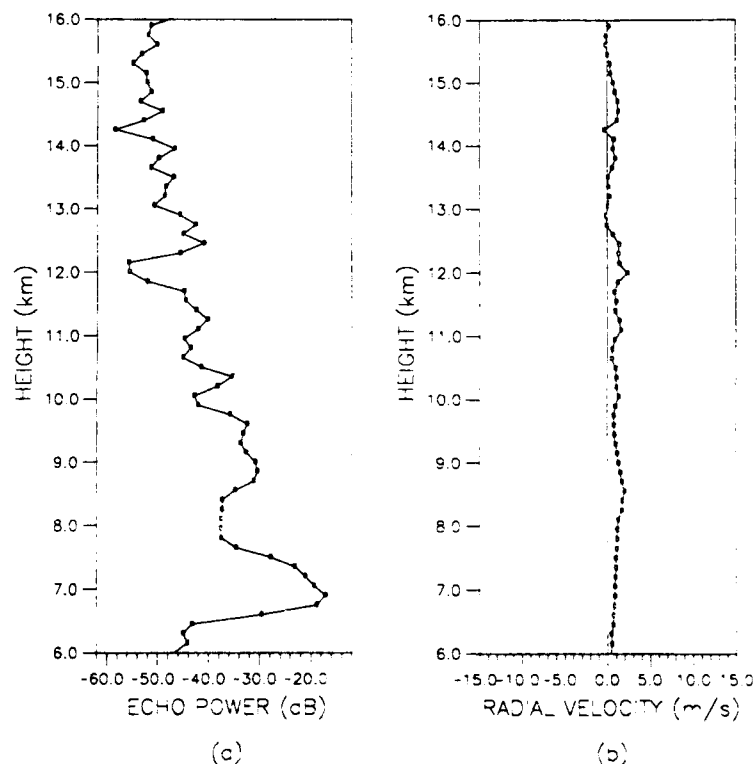


Fig. 2. Standard Doppler measurements at azimuth 0° and zenith angle of 10° , (a) echo power profile, and (b) radial velocity.

The height resolution of this experiment was 150 m, with observations taken from 6.0 to 15.45 km. Pulse compression was used with a flip of the code with every interpulse period (IPP), which in this experiment was set to $400 \mu\text{s}$. Coherent integration was performed with 256 points, giving a sampling interval of 0.1024 s. After this process, 256 points of raw data was stored on magnetic tape, with a small time gap for data processing. Therefore approximately every 30 s, another 256 point data set was stored. Two 30-min averages of autospectra and cross spectra, processed by a rectangular window periodogram, were obtained for all combinations of antennas. These will be used in later sections to illustrate the technique presented in this paper.

Before the RI experiment was conducted a standard Doppler experiment was performed and the radial velocity was estimated by a standard first moment estimate of the Doppler spectra. Figures 2 and 3 show the echo powers and radial velocities for a zenith angle of 10° and azimuth angles of 0° and 90° , respectively. The reflectivity profiles show a typical structure with a decrease of approximately 2

dB km^{-1} . A high reflectivity stratospheric layer is evident around 12.5 km, and the enhancement in the signal strength near the tropopause can be seen at a height just above 10 km. The largest contribution to the radial velocity measured at a zenith angle of 10° is expected to be from the horizontal components. Therefore Figures 2b and 3b imply that almost all of the contribution to the horizontal wind is from the zonal component and that the wind vector is essentially aligned with the baseline between antennas 1 and 2. The uniform wind direction will simplify the analysis discussed later, although the techniques can be applied equally well when the wind direction is not aligned with a baseline.

3. THREE-DIMENSIONAL WIND VECTOR MEASUREMENT USING RADAR INTERFEROMETRY

One way to test for biases in the vertical velocity measurements due to tilted refractivity layers would be to compare the direct vertical beam measurements with the vertical velocity calculated from

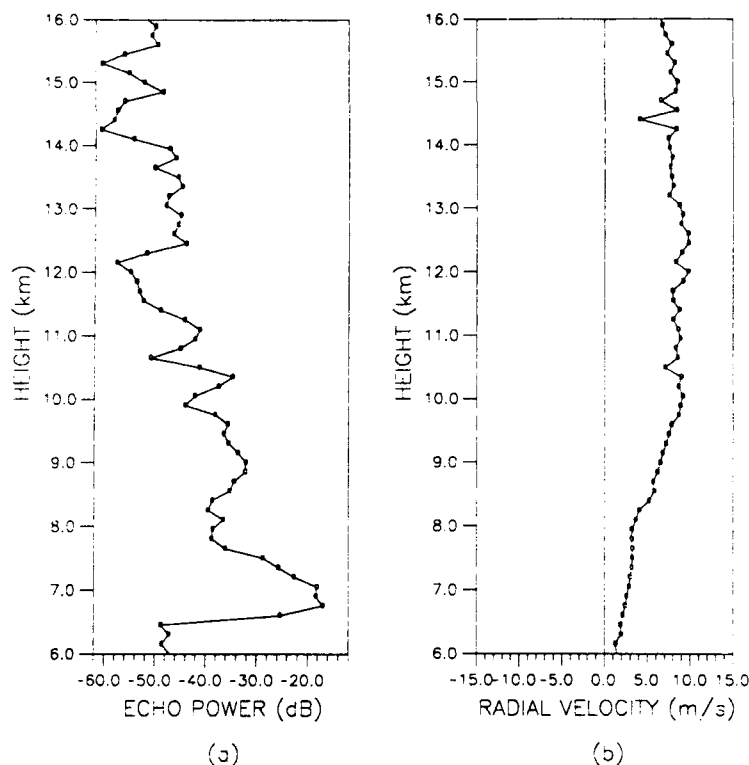


Fig. 3. Same as Figure 2, but with azimuth 90° .

two off vertical beams separated by 180° in azimuth. Differences in the two measurements could then be attributed to aspect sensitivity effects. However, the separation between beams quickly becomes large and can easily be 5–10 km near the tropopause for typical zenith angles of 10° to 20° . The large area over which the velocities are sampled suggests that the horizontal winds and vertical velocities may not be uniform in which case differences in the measurements may be due to either inhomogeneity in the wind field or biases produced by the characteristics of the scattering mechanism.

The RI technique is similar to a many beam-direction, Doppler experiment in that the radial velocity can be obtained as a continuous function of zenith angle, within the beam width of the radar. The RI method for obtaining the three-dimensional wind vector uses only a vertical beam, and the beam steering is accomplished in the data processing stage [Röttger and Ierkic, 1985; Kudeki and Woodman, 1990]. It should be pointed out that an analysis technique, which is similar but more general to the following, has been independently derived by Van Baelen [1990]. The derivation of the

equations relevant to our analysis begins with an equation for the radial velocity

$$v_r = v_H \sin \gamma' + w \cos \gamma' \quad (1)$$

where v_H and w are the horizontal and vertical wind components, respectively. Figure 4 displays the configuration used in this analysis. The angle γ' is the zenith angle in the direction of the wind vector, which would produce a radial velocity of v_r . We would like to find γ' in terms of the zenith angle, which is produced on the baseline, i.e., γ . From Figure 4 it can be seen that

$$\cos(\alpha - \theta) = \frac{\tan \gamma}{\tan \gamma'} \quad (2)$$

where θ and α are the azimuth angles of the wind vector and the baseline, respectively. But, since for an interferometer experiment, the zenith angles are usually very small, the above equation becomes

$$\cos(\alpha - \theta) \approx \frac{\sin \gamma}{\sin \gamma'} \quad (3)$$

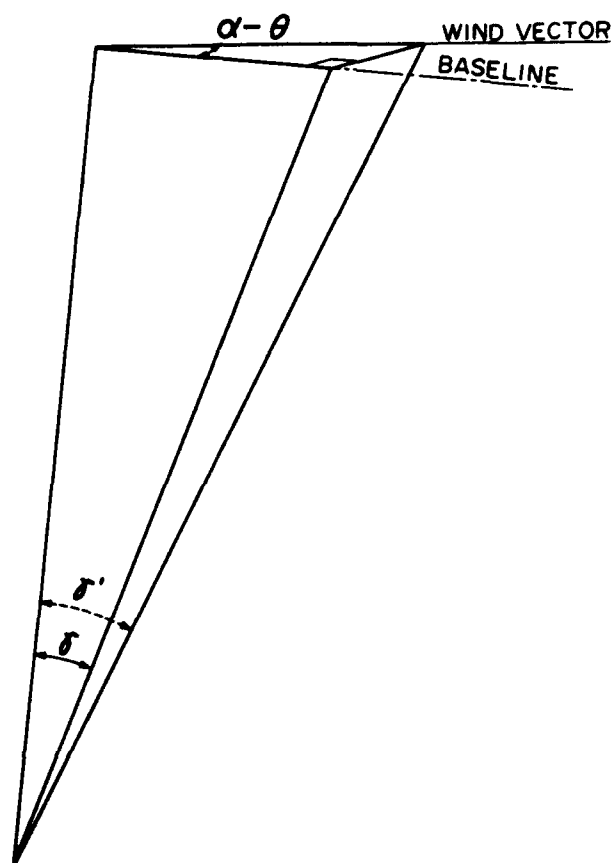


Fig. 4. Configuration of the baseline with respect to the wind vector used for the derivation of the equation of the phase in terms of the radial velocity. The wind vector and baseline have azimuth angles θ and α , respectively. The coefficients γ' and γ denote the zenith angles in the direction of the wind vector and the baseline, respectively.

Substituting for the $\sin \gamma'$ term in (1), and using the fact that $\cos \gamma' \approx 1$, the radial velocity becomes

$$v_r = \frac{v_H \sin \gamma}{\cos (\alpha - \theta)} + w \quad (4)$$

It is well known that the phase difference between two antennas is related to the zenith angle by

$$\phi = kD \sin \gamma \quad (5)$$

where k is the radar wave number and D is the distance between the two antennas, which form a baseline that defines a plane with the vertical in which γ is measured. Using this expression to

substitute the $\sin \gamma$ term in (4) and solving for the ϕ , the following relation is found

$$\phi = \left[\frac{kD \cos (\alpha - \theta)}{v_H} \right] v_r - \left[\frac{wkD \cos (\alpha - \theta)}{v_H} \right] \quad (6)$$

This equation is easily seen to have the form of a line with slope m and intersection b given by

$$m = \frac{kD \cos (\alpha - \theta)}{v_H} \quad (7)$$

$$b = \frac{-wkD \cos (\alpha - \theta)}{v_H} \quad (8)$$

The linear variation of the cross-spectral phase ϕ as a function of v_r has been seen in a number of earlier experiments [e.g., Farley *et al.*, 1981; Röttger *et al.*, 1990] and is expected on physical grounds. Since the phase of the signal is related to the angular position from which the echoes are received, the radial velocity should change linearly for small zenith angles, as the angle changes from positive to negative.

More details of the derivation of (6) have been given by Van Baelen [1990]. A more general equation for the phase of the cross spectra has recently been presented by Liu *et al.* [1990, equation (27)]. In this equation the contribution of the spectral width due to turbulence is assumed to be dominated by the beam-broadening effect, which has been shown to typically be the case [Hocking, 1985]. This is especially true in the troposphere/stratosphere but may not be the case in the mesosphere. The turbulent spectral width is related to the correlation length of the scatterers and is also one source of problems in the SA technique [Briggs, 1984]. As stated by Liu *et al.* [1990], one component of this phase equation can be ignored if sufficient incoherent averaging is performed to insure statistically homogeneous turbulence within the resolution volume. The remaining component of the phase can easily be shown to reduce to (6), and the equation given by Van Baelen [1990] with only the assumption that the magnitude of the horizontal wind is much greater than that of the vertical.

From (7) and (8) we would like to estimate the three components of the wind vector. We will start with a substitution of $v'_H \equiv 1/v_H$, which gives a slope of the form

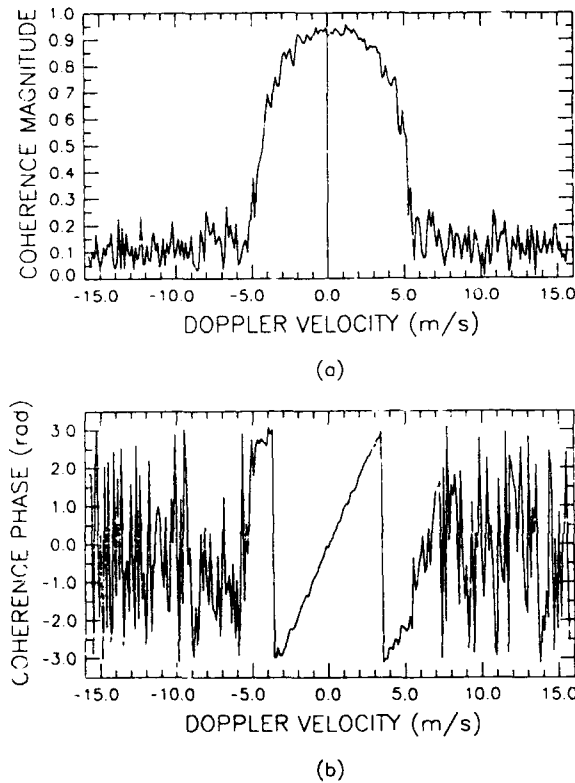


Fig. 5. Typical coherence function, obtained from spatial domain interferometry data, (a) magnitude, and (b) phase with an obvious linear variation.

$$\begin{aligned}
 m &= kDv_H \cos(\alpha - \theta) \\
 &= kD(u' \sin \alpha + v' \cos \alpha)
 \end{aligned} \quad (9)$$

where u' and v' are the zonal and meridional components of v'_H .

From (9) it is evident that u' and v' can be estimated if two independent estimates of the slope m are available from two pairs of receiving antennas, for example. Three antennas are used in the usual interferometer configuration. Therefore three different cross spectra are available. Figure 5 displays the magnitude and phase of a typical normalized cross-spectra, i.e., coherence function. As one can see, there is a linear variation in the phase of the coherence function. In some cases the signals from an antenna pair with a baseline perpendicular to the wind will have low coherence and will be excluded from the calculation of the wind vector. The relationship between u' , v' , and the slopes is given by

the following equation for two independent slope measurements.

$$\begin{pmatrix} \sin \alpha_{12} & \cos \alpha_{12} \\ \sin \alpha_{13} & \cos \alpha_{13} \end{pmatrix} \begin{pmatrix} u' \\ v' \end{pmatrix} = \begin{pmatrix} \frac{m_{12}}{kD} \\ \frac{m_{13}}{kD} \end{pmatrix} \quad (10)$$

where ij denote the baseline formed between antennas i and j . Equation (10) could be extended to include three independent slope measurements, but if one of the cross spectra has low coherence, there is a deterioration in the estimate. Similar problems sometimes arise in SA measurements if one of the antenna pairs is oriented perpendicular to the wind direction. From (10) the u' and v' components of the wind are estimated by

$$u' = \frac{1}{kD\Delta} [m_{12} \cos \alpha_{13} - m_{13} \cos \alpha_{12}] \quad (11)$$

$$v' = \frac{1}{kD\Delta} [m_{13} \sin \alpha_{12} - m_{12} \sin \alpha_{13}] \quad (12)$$

where $\Delta = \sin \alpha_{12} \cos \alpha_{13} - \sin \alpha_{13} \cos \alpha_{12}$.

Once u' and v' have been estimated, the horizontal wind can be obtained by

$$v_H = \frac{1}{\sqrt{(u')^2 + (v')^2}} \quad (13)$$

and the azimuth angle of the wind vector is given by

$$\theta = \arctan \left(\frac{u'}{v'} \right) \quad (14)$$

The vertical velocity can be estimated using (8) once the horizontal component has been computed. However, another approach is to find the radial velocity when the beam is pointing exactly vertically, i.e., $\phi = 0$. Therefore a simple way to estimate the vertical velocity is obtained by letting $\phi = 0$ in (6).

$$w = v_r|_{\phi=0} = -\frac{b_{12}}{m_{12}} \quad (15)$$

When the phase difference between the signals in two adjacent receiving antennas is zero, the contribution must be from the true vertical direction within the accuracy of the mechanical layout of the radar system. The simplicity of (15) is somewhat

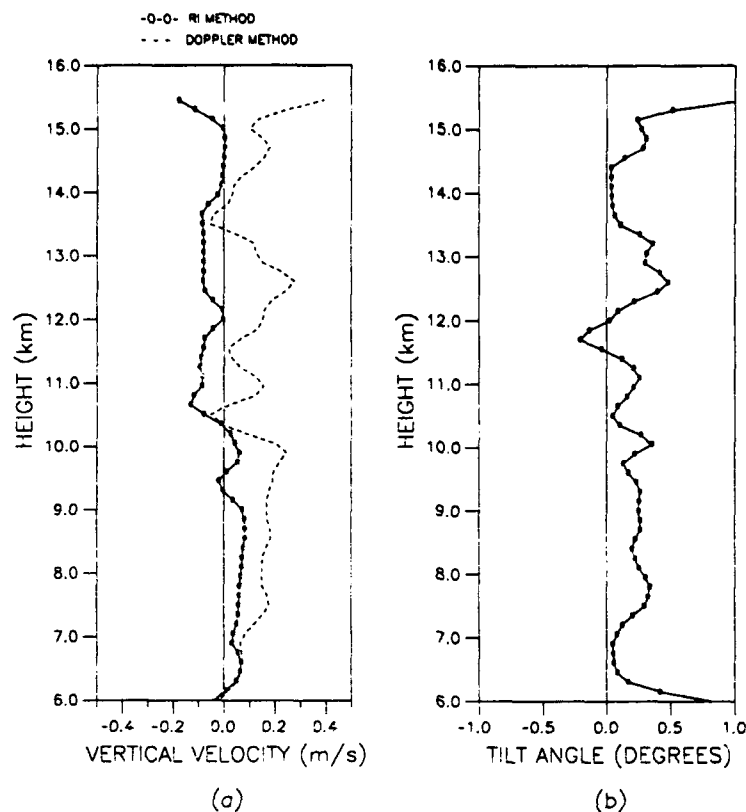


Fig. 6. Data taken from a 30-min average from 2145 to 2215 LT. (a) Comparison of RI and Doppler vertical velocity estimates and (b) estimates of tilt angles obtained from the phase of the cross-correlation function at zero lag.

deceptive. It appears that only one estimate of the slope and intercept are needed in which case one antenna pair is sufficient. However, the apparent beam direction can also be tilted in the direction transverse to the antenna pair baseline so that in the general case, information from at least two antenna pairs must be combined to yield the true vertical velocity. The uniformity of the wind direction with height during our observations has simplified the analysis so that the problem is essentially two dimensional. The general case of the wind vector determination method described in this paper, which includes aspect sensitivity and tilt in all directions, has been derived by *Larsen et al.* [1991].

4. COMPARISON OF THE RI AND DOPPLER TECHNIQUES

Figures 6a and 7a show the profiles of vertical velocity estimated from two independent 30-min averages. The RI estimate was obtained by using

(15), and the Doppler method estimate was obtained by calculating the first moment of the average of the three autospectra obtained from the RI experiment. The two estimates are thus derived from exactly the same data. Only the processing is different. The result is that most of the usual uncertainties associated with temporal or spatial beam separations or differences in sampling schemes are eliminated. The difference between the two curves is clearly significant and amounts to more than 30 cm s^{-1} at some heights. Figures 6b and 7b show the tilt angles inferred from the phase of the cross correlation at zero lag as a function of height [Röttger and Ierkic, 1985; Larsen and Röttger, 1991] from the antenna pair which was aligned along the east/west direction parallel to the wind. A general trend at all altitudes is that the large differences in the vertical velocity estimates occur at those heights where the tilt angles are large.

A further test that can be applied to the data is to

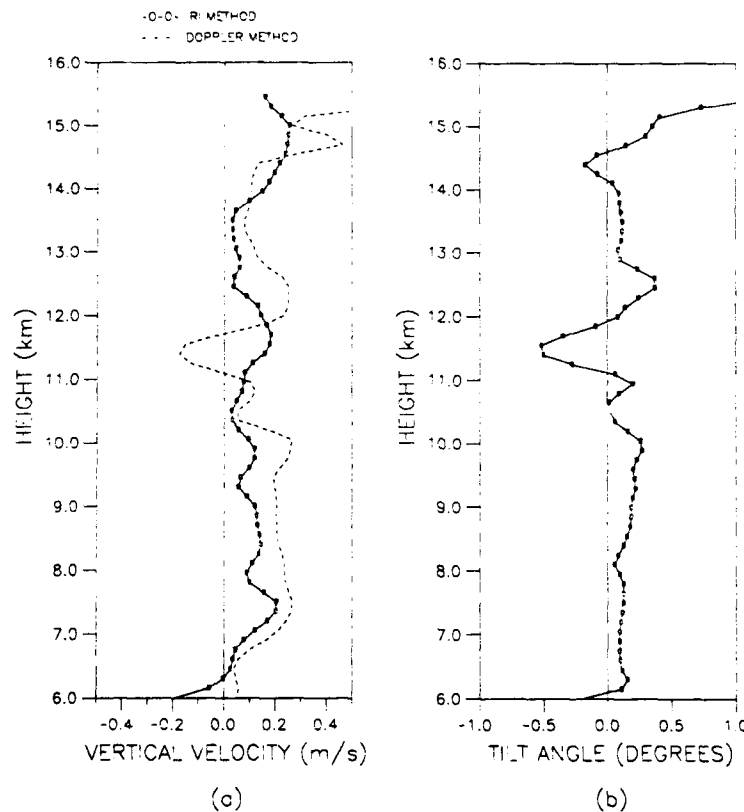


Fig. 7. Same as Figure 6, except for a 30-min average taken from 2215 to 2245 LT.

calculate a predicted difference between the two vertical velocity estimates, which should be equal to the projection of the horizontal velocity along the tilt direction. Figures 8a and 9a show this comparison. The two sets of curves follow each other very closely.

Finally, the velocity perpendicular to the refractivity layers v_{\perp} can be estimated by using the tilt angle information and the cross-spectral phase information together. Instead of isolating the contribution from the true-vertical direction as we did with the curves in Figures 6a and 7a, we now choose a specific off-vertical component along a direction that varies as a function of height. Specifically, the phase corresponding to the tilt angle, obtained from the cross-correlation function, was substituted into (6) and the corresponding value of v_r was calculated.

$$v_{\perp} = v_r \sin \delta_{12} = \frac{kD \sin \delta_{12} - b_{12}}{m_{12}} \quad (16)$$

where δ_{12} is the tilt angle in the baseline formed by antennas 1 and 2. Again, the alignment of the wind vector with the baseline between antennas 1 and 2 made the calculations simple. The perpendicular velocity estimate is compared to the standard Doppler method estimate in Figures 8b and 9b. The agreement between the curves indicates that the Doppler vertical velocities are actually velocity components along the apparent beam direction and are thus biased by the horizontal velocity.

5. CONCLUSIONS

Analysis of interferometer measurements has shown that a bias can exist in standard Doppler estimates of the vertical velocity caused by tilting of refractivity surfaces, at least at certain times and in certain height ranges. Since all the analysis has involved different processing procedures applied to the exact same data set, many, if not all, of the

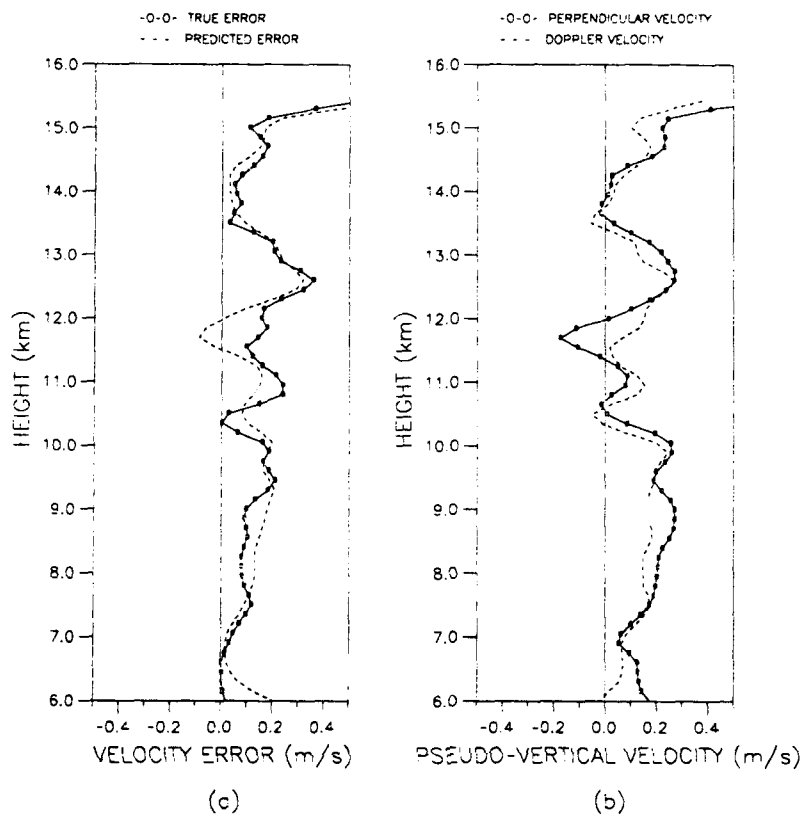


Fig. 8. Data taken from a 30-min average from 2145 to 2215 LT. (a) Comparison of observed error (difference between vertical velocities obtained from the RI and Doppler methods) and the predicted error (obtained from tilt angles and estimates of the horizontal velocity) and (b) Comparison of radial velocities perpendicular to the refractivity layers and the standard Doppler velocities obtained from a vertical beam.

usual uncertainties associated with unknown spatial or temporal variations in the atmospheric medium have been eliminated. The bias is a direct consequence of the aspect sensitivity of VHF echoes received from refractivity surfaces, which when tilted, cause the apparent beam to be tilted away from vertical as illustrated in Figure 10. VHF echoes are known to be aspect sensitive [Tsuda *et al.*, 1986], but the origin of this effect is still an open question. The aspect sensitivity causes the apparent antenna beam to be smaller than the antenna beam of the radar, since the echoes from off-vertical angles will be attenuated. This does not cause a problem with the vertical velocity measurements obtained from the Doppler method, if the refractivity surface which is causing the echo is not tilted. The tilting of the apparent beam toward the perpendicular of the refractivity surface will cause the vertical velocity estimate to be biased by the component of the horizontal wind in the direction of the

tilted beam [Larsen and Röttger, 1991]. If the tilt angle is denoted by δ_T , then the horizontal wind contribution to the vertical velocity is given by the magnitude of the horizontal wind component in the direction of the tilt multiplied by $\sin \delta_T$. Since the tilt angles are usually small, i.e., less than 2° , this contribution is small, but the vertical velocity is also small, and therefore the overall error is significant.

At present, no aspect sensitivity effect has been observed at UHF frequencies, but tilted refractivity layers could still cause a bias in the vertical velocity estimate. This bias could be caused if the wind flow is not horizontal, causing a wind shear within the resolution volume of the radar. But the results presented in the previous section seem to indicate that the flow is horizontal. If the flow was along the refractivity structure, then the perpendicular velocity, shown in Figures 8b and 9b, would be zero.

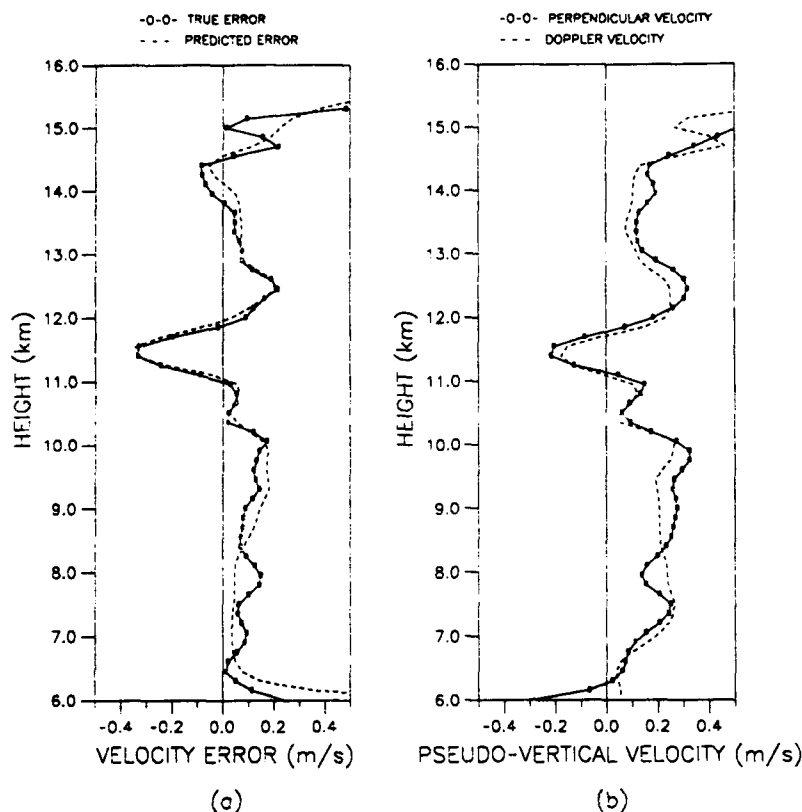


Fig. 9. Same as Figure 8, except for a 30-min average taken from 2215 to 2245 LT.

This is not the case, leading one to believe that the flow is close to horizontal.

The magnitude of the errors indicated both by the data presented here and by the earlier data pre-

sented by *Larsen and Röttger* [1991] can be 200% or more. However, the problems associated with such biases can be eliminated; however, by using multiple receiving antennas and applying the techniques presented in this paper.

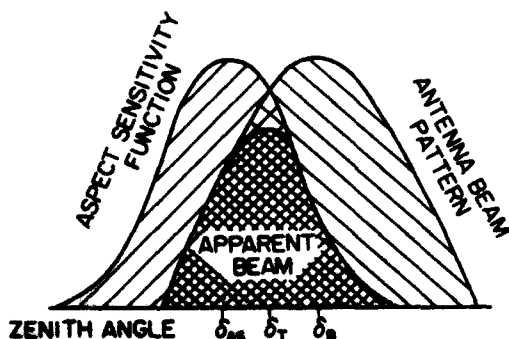


Fig. 10. Depiction of the apparent beam pattern of a VHF radar, when the strongest echoes are received from an off-vertical zenith angle. This effect is due to the aspect sensitivity observed at VHF wavelengths. The aspect sensitivity function has a tilt of δ_{AS} and the desired antenna beam pattern δ_B , which is in this case set to zenith. As a result, the apparent beam is tilted by the angle δ_T (reproduced from *Röttger* [1980]).

Acknowledgments. The research described here was carried out while one of the authors (R. D. P.) was a Japan Society for the Promotion of Science (JSPS) postdoctoral fellow at the Radio Atmospheric Science Center of Kyoto University. M. F. L. was supported by the Japan Ministry of Education, Culture, and Research and by AFOSR contract F49620-88-C-0121. The authors would like to thank J. S. Van Baelen, who pointed out an error in (6). The comments of the anonymous reviewers are gratefully acknowledged. The MU radar belongs to and is operated by the Radio Atmospheric Science Center of Kyoto University.

REFERENCES

- Adams, G., J. Brosnahan, and R. Johnson, Aspect sensitivity of 2.66-MHz radar returns from the mesosphere, *Radio Sci.*, 24(2), 127–132, 1989.
- Briggs, B., The analysis of spaced sensor records by correlation techniques, in *Handbook for MAP*, vol. 13, pp. 166–186,

- SCOSTEP Secretariat, University of Illinois, Urbana, 1984.
- Farley, D., H. Ierikic, and B. Fejer, Radar interferometry: A new technique for studying plasma turbulence in the ionosphere, *J. Geophys. Res.*, **86**(A3), 1467-1472, 1981.
- Fukao, S., T. Sato, P. May, T. Tsuda, S. Kato, M. Inaba, and I. Kimura, A systematic error in MST/ST radar wind measurement induced by a finite range volume effect. 1, Observational results, *Radio Sci.*, **23**(1), 59-73, 1988.
- Hocking, W. K., Measurement of turbulent energy dissipation rates in the middle atmosphere by radar technique: A review, *Radio Sci.*, **20**, 1403-1422, 1985.
- Kudeki, E., and R. Woodman, A poststatistic steering technique for MST radar applications, *Radio Sci.*, **25**(4), 591-594, 1990.
- Larsen, M. F., and J. Röttger, A comparison of thunderstorm reflectivities measured at VHF and UHF, *J. Atmos. Oceanic Technol.*, **4**, 151-159, 1986.
- Larsen, M. F., and J. Röttger, VHF radar measurements of in-beam incidence angles and associated vertical-beam radial velocity corrections, *J. Atmos. Oceanic Technol.*, in press, 1991.
- Larsen, M. F., J. Röttger, and T. S. Dennis, A comparison of operational analysis and VHF wind profiler vertical velocities, *Mon. Weather Rev.*, **16**, 48-59, 1988.
- Larsen, M., R. Palmer, S. Fukao, R. Woodman, M. Yamamoto, T. Tsuda, and S. Kato, An analysis technique for deriving vector winds and in-beam incidence angles from interferometer measurements, *J. Atmos. Oceanic Technol.*, in press, 1991.
- Liu, C., J. Röttger, C. Pan, and S. Franke, A model for spaced antenna observational mode for MST radars, *Radio Sci.*, **25**(4), 551-563, 1990.
- Nastrom, G. D., W. L. Ecklund, and K. S. Gage, Direct measurement of large-scale vertical velocities using clear-air Doppler radars, *Mon. Weather Rev.*, **113**, 708-718, 1985.
- Palmer, R., R. Woodman, S. Fukao, T. Tsuda, and S. Kato, Three-antenna poststatistic steering using the MU radar, *Radio Sci.*, **25**(6), 1105-1110, 1990.
- Röttger, J., Reflection and scattering of VHF radar signals from atmospheric refractivity structures, *Radio Sci.*, **15**(2), 259-276, 1980.
- Röttger, J., and H. Ierikic, Postset beam steering and interferometer applications of VHF radars to study winds, waves, and turbulence in the lower and middle atmosphere, *Radio Sci.*, **20**(6), 1461-1480, 1985.
- Röttger, J., C. Liu, C. Pan, and I. Fu, Spatial interferometry measurements with the Chung-Li VHF radar, *Radio Sci.*, **25**(4), 503-515, 1990.
- Tsuda, T., T. Sato, K. Hirose, S. Fukao, and S. Kato, MU radar observations of the aspect sensitivity of backscattered VHF echo power in the troposphere and lower stratosphere, *Radio Sci.*, **21**(6), 971-980, 1986.
- Van Baelen, J. S., Comparison of clear air atmospheric radar techniques for the study of atmospheric dynamics in the troposphere and the stratosphere, Ph.D. thesis, 191 pp., Univ. of Colo., Boulder, 1990.
- Vincent, R. A., and J. Röttger, Spaced antenna VHF radar observations of tropospheric velocities and irregularities, *Radio Sci.*, **15**(2), 319-335, 1980.
- Woodman, R., Inclination of the geomagnetic field measured by an incoherent scatter radar technique, *J. Geophys. Res.*, **76**, 178-184, 1971.
- S. Fukao, S. Kato, T. Tsuda, and M. Yamamoto, Radio Atmospheric Science Center, Kyoto University, Uji, Kyoto 611, Japan.
- M. F. Larsen and R. D. Palmer, Department of Physics and Astronomy, Clemson University, Clemson, SC 29631.
- R. F. Woodman, Jicamarca Radio Observatory, Instituto Geofísico del Perú, Apartado 3747, Lima, Perú.